In vitro modelling of cellular haemozoin and inhibition by β-haematin inhibitors and their derivatives

Roxanne Openshaw

Thesis presented for the degree of

DOCTOR OF PHILOSOPHY

in the Department of Chemistry

University of Cape Town

January 2020

Supervisor: Professor Timothy J. Egan

For my best friend, role model and late grandfather,

Antony Rudolph Botha

1940-2018

Plagiarism Declaration

I, Miss Roxanne Openshaw, declare the following that;

1. The thesis entitled, "*In vitro* modelling of cellular haemozoin inhibition by β-haematin inhibitors and their derivatives", is my own work, both in carrying out the necessary experiments and proving the concepts outlined, along with the guidelines of my supervisor.
2. Where third parties work has been used, it has been acknowledged and referenced appropriately.
3. This thesis was submitted through an internet plagiarism detection platform, Turnitin.
4. No part of this thesis or work has been submitted for another degree as this or any other university.
5. I grant the University of Cape Town full authority to reproduce this work for future research.

I hereby present this work for the degree of Doctor of Philosophy (PhD) in chemistry for examination which was signed at the University of Cape Town.

Signed by candidate

Miss Roxanne Openshaw

Student Number: OPNROX001

Date: 29 January 2020

Abstract

The discovery of new β-haematin inhibitors has become one focus for researches in response to the resistance of *P. falciparum* malaria parasites that emerged towards well-known antimalarials. While hundreds of new β-haematin inhibitors have been discovered using detergent mediated high-throughput screening methods, a crucial aspect is understanding exactly how these β-haematin inhibitors behave in the malaria parasite and inhibit the formation of haemozoin. What is known, is that well-known β-haematin inhibitors like chloroquine cause increased amounts of exchangeable haem in the parasite digestive vacuole and form a Fe(III)PPIX-inhibitor complex by accumulating at high concentrations which consequently inhibits parasite growth. Another important focus is on understanding the digestion of haemoglobin and its role in haemozoin formation. This research investigates the *in vitro* modelling of cellular haemozoin and inhibition by various β-haematin inhibitors across different scaffolds and the role of haemoglobin degradation in *P. falciparum* malaria parasites.

The investigated β-haematin inhibitors resulted in micromolar IC_{50} (NF54) values and decreased parasite growth with increases in concentration. Using a pyridine-based parasite haem fractionation plate method, these β-haematin inhibitors were shown to target haemozoin formation by causing increased amounts of exchangeable haem that corresponded to decreasing amounts of haemozoin in chloroquine-sensitive parasites. The amounts of exchangeable haem were shown to be inversely proportional to the percentage of parasite growth in the presence of these β-haematin inhibitors. It was apparent that there was a tendency for parasite growth inhibition activity to decrease as the amount of exchangeable haem present in chloroquine sensitive parasites increased, although, the trend was not statistically significant. Moreover, it was observed that experimental cellular accumulation ratio values were low in comparison to chloroquine and amodiaquine. Based on the experimental cellular accumulation ratio values, it was deduced that the accumulation of these β-haematin inhibitors was not primarily due to pH trapping and more complex than previously proposed. Further investigations into the exchangeable haem amounts as a function of intracellular test compound amounts at the IC_{50} values of these β-haematin inhibitors highlighted that there was an apparent 1:1 relationship with the amount of intracellular exchangeable haem, indicative of complex formation.

Transmission electron microscopy images were obtained for untreated parasites that showed intact parasites inside red blood cells with clearly visible haemozoin crystals dispersed throughout the parasite digestive vacuole, whilst, treated parasites showed less defined

haemozoin crystals as a result of inhibition. Moreover, electron energy-loss spectroscopy revealed that untreated parasites exhibited a strong iron signal which was associated with haemozoin in the parasite digestive vacuole with a weaker signal attributed to the red blood cell cytoplasm. Similarly, a strong iron signal was shown in the digestive vacuole of treated parasites which was associated with less defined haemozoin crystals. A halo around these haemozoin crystals was observed and was suggested to be indicative of the build-up of exchangeable haem. Additionally, a strong bromine signal attributed to a bromine-containing β-haematin inhibitor, test compound **1**, was also observed in the same region as the haemozoin crystals. Overlaid signal distribution maps for iron and bromine showed direct evidence of Fe(III)PPIX and test compound **1**, suggesting complexation. High-quality Raman spectra were obtained for the Fe(III)PPIX species in red blood cells, chloroquine sensitive parasites and synthetically prepared samples for the Fe(III)PPIX porphyrin dominated spectral region of 1700-500 cm^{-1} at an excitation wavelength of 532 nm. From the spectra, a putative Fe(III)PPIX-test compound **1** complex was identified and shown to be similar to the synthetically prepared counterpart, haematin-test compound **1** mixture. It was highlighted that a unique peak at 1080 cm^{-1} indicated π- π interactions between the pyrrole-imidazole ring and thus confirming that the formation of this putative Fe(III)PPIX-inhibitor complex occurs. The confocal Raman true mapping technique proved to be efficient and reliable for imaging the signal distribution of haemozoin at the Raman peak of 754 cm^{-1} and 1080 cm^{-1} for the Fe(III)PPIX-test compound **1** complex which co-localized in the digestive vacuole of chloroquine sensitive parasites. Moreover, oxy- and deoxy-haemoglobin was observed to be localized to the red blood cell, where, deoxy-haemoglobin was located on the outer parts of the parasite. Principle component analysis, based on the Raman peak positions, exhibited significant differences in the spectra for Fe(III)PPIX species in red blood cells, chloroquine sensitive parasites and synthetic samples where clusters were observed to separate mainly along principle component 1. These data proved that the spectra of the Fe(III)PPIX-test compound **1** complex was the same as its synthetically prepared counterpart but different from the remaining Fe(III)PPIX species. In comparison to the Fe(III)PPIX-test compound **1** complex, the cluster separations were observed to be significant, where, no significant separation was observed for the Fe(III)PPIX-test compound **1** complex and the haematin-test compound **1** mixture. Based on this, it was evident that a Fe(III)PPIX-test compound **1** complex existed in the digestive vacuole of treated chloroquine sensitive parasites.

To fully understand the inhibition of haemozoin, the development of a haem pathway model is necessary, but, requires certain prerequisites. Bioinformatics data from PAXdb and

ExPASy revealed that chloroquine resistance (Dd2) parasites, containing 1337 previously identified proteins with an average abundance-weighted molecular weight of 40,483 ± 77 g/mol. With this, the protein mass per cell for red blood cells, chloroquine-sensitive and -resistant parasites were consistent across three protein quantification methods was measured and revealed that chloroquine resistant parasites had a significantly higher protein mass per cell than chloroquine sensitive parasites and in turn a higher total number of protein molecules per cell. Aspartic proteases are 4-fold higher in concentration than cysteine proteases with histo-aspartic protease having the highest concentration in chloroquine resistant parasites. Along with these data, a time point quantification for chloroquine sensitive parasites throughout the blood-stage showed that the amount of haemoglobin decreased in a sigmoidal manner and corresponded to a linear increase in the amount of haemozoin and relatively constant exchangeable haem amount. This was consistent with Giemsa smears that showed that for early time points, large initial decreases in the amount of haemoglobin were observed between the early trophozoite to late trophozoite stage.

Publications and conference proceedings

Parts of the research carried out in this thesis were published;

1. L'abbate, F.P., Müller, R., Openshaw, R., Combrinck, J.M., de Villiers, K.A., Hunter, R. and Egan, T.J. (2018) Haemozoin inhibiting 2-phenylbenzimidazoles active against malaria parasites. Eur. J. Med. Chem. **159**. 243-254.

Part of the research carried out in this thesis was presented at the following conference proceedings;

1. **2015**: 17th SACI Inorganic Chemistry Conference held at/ in Grahamstown at Rhodes University on/ in June.

Poster Presentation: Assay of cellular haemozoin inhibition by β-haematin inhibitors and their derivatives discovered by high-throughput screening.

2. **2015:** Young Chemists Symposium held at University of Western Cape, Cape Town in September.

Oral and Poster Presentation: Assay of cellular haemozoin inhibition by β-haematin inhibitors and their derivatives discovered by high-throughput screening.

3. **2016:** H3D Symposium held at Goudini Spa, Worcester, Cape Town in November.

Poster Presentation: Relationship of cellular haemozoin inhibition and the relative intra-cellular drug accumulation of β-haematin inhibiting antimalarials.

4. **2017:** 18th SACI Inorganic Chemistry Conference held at/ in the Arabella Country Estate, Hermanus, Cape Town in June.

Poster Presentation: *In vitro* modelling of cellular haemozoin and inhibition by β-haematin inhibitors and their derivatives.

5. **2017:** 18th International Conference on Biological Inorganic Chemistry held in Florianopolis, Brazil in August.

Oral Presentation: Exchangeable haem levels are equal to intra-cellular drug amounts for β-haematin inhibiting antimalarials and is present as a Fe(III)PPIX-drug complex **(Prize: Best Oral Presentation)**

6. **2018**: 43rd National Convention of the South African Chemical Institute, held in Pretoria at the CSIR-ICC in December 2018.

Oral Presentation: Spectroscopic evidence of co-localization and a possible haem-drug complex within *Plasmodium falciparum* parasites.

Acknowledgements

I would like to extend my sincere appreciation to the following people who contributed in many ways therefore allowing the following work to be carried out;

Professor Timothy John Egan for all his support, patience, guidance and brilliant knowledge on the topic of this research. He has not only provided me with the best mentorship during my time in his group but also always had an "open door" policy, pushed me to be the best I can be, helped me to be confident in myself and my research as well as gave me the opportunity to travel and attend conferences here and abroad. I will always be very grateful for what I have learnt from you but also for how you have shaped me into the researcher I am today.

The Haem team and my colleagues, in the chemistry department; Dr Ana de Sousa and Dr Jill M. Combrinck for all their support in the laboratory, especially during the long nights. I would also like to thank members that are no longer a part of the Haem team; Dr Nicola Kuter, Dr John Woodland, Dr Aneesa Omar, Stefan J. Benjamin, Dr Fabrizio, P. L'abbate, Dr Kathryn Wicht and Dr John Okombo with a special mention to Dr D. Kuter for all his support.

The Stellenbosch team who we often collaborated with for the NIH project; Dr Katherine de Villiers, Miss Sharne-Mare Fitzroy and Miss Chandre Jade Sammy. Special mention to Miss Chandre Jade Sammy for all her support during my research, friendly welcomes whenever we saw each other and for the unforgettable memories in Grahamstown and at the Arabella Country Estate.

The Division of Pharmacology colleagues, at Groote Schuur Hospital, specifically referring to Mrs Sumaya Salie and Mr Virgil Verhoog for all their support and guidance in the tissue culture lab. I will always be grateful for all the techniques, experiments and the exposure to various equipment that I learnt whilst working alongside you.

The Electron Microscopy Unit in the New Engineering Building at the University of Cape Town, with special mention to Mr Mohamed Jaffer for all his assistance with the parasite microscope imaging and Mrs Miranda Waldron for all her assistance with the Raman microscope.

Dr Danni Ramduth from BD Bioscences for the training and assistance for the flow cytometry work done in this thesis.

Mr Mogamat Tohier Salie for all his support during this stressful journey and always telling me that anything is possible if I put my mind to it. ***Miss Celema Koti*** for all her support, late nights spent working in her office, encouragement to keep going when things got hard and always being there to offer a shoulder to cry on. ***Miss Stephanie Lynn Paterson***, all the way from Durban, thank you for your loving support, kind and uplifting words that helped me get through the tough times.

My PhD journey would have not been possible without my family. I would especially like to thank my wonderful parents, ***Colin Openshaw*** and ***Schanelle Openshaw***. They have always done everything to help me succeed, provided me with on-going support, love, guidance, and forever willing to drive a thousand miles just to bring me home. A special thank you to my room-mate and brother, ***Calvin Openshaw***, for all the times I was struggling with "home sickness" and just for being the best brother anyone could ask for because no sibling would do what you did for me. This thesis is dedicated to my grandfather, ***Antony Rudolph Botha*** whom was my best friend and role model for the simple fact that he was my whole world. For the 8 years that I lived away from home he always cried when I had to leave and now that he is gone I thank him even more for all he did that made me the person I am today.

Lastly I would like to mention my gratitude for the following funding organizations whom made it possible to achieve what I did in this project; ***National Institutes of Health (NIH)*** for all the financial support throughout this project (Grant number: R01AI110329) and the ***National Research Foundation (NRF)*** and the ***University of Cape Town*** for additional financial support.

List of Abbreviations

ACT - Artemisinin combination therapy
APAD - 3-acetylpyridine adenine dinucleotide
HEPES - 4-(2-hydroxyethyl)-1-piperazineethanesulfonic acid
AQ - Amodiaquine
ART - Artemisinin
Atov - Atovaquone
BCA – Bicinchhoninic acid
BD - Becton Dickinson
BSA - Bovine serum albumin
CAR - cellular accumulation ratio
CCD - Charge-coupled device
CD - Circular dichroism
CI - Confidence interval
Co(II) - Cobalt
CQ - Chloroquine
CQR - Chloroquine-resistance
PQ - Primaquine
CQS - Chloroquine-sensitive
CT - Charge transfer
DFT - Density functional theory
DHA/PPQ - Dihydroartemisinin-piperaquine
DMSO - Dimethyl sulfoxide
DNA - deoxyribonucleic acid
DV - Digestive vacuole
EELS - Electron energy-loss spectroscopy
ESI - Electron spectroscopic imaging
FACS - Flow cytometry cell sorter
Fe - Iron
Fe(III)PPIX - ferriprotoporphyrin IX
fg - femtograms
FQ - Ferroquine
GSK - GlaxoSmithKline
HAP - Histo-aspartic protease
HDP - Haem detoxification protein
HF - Halofantrine
HRP II - Histidine rich protein II
HTS - High throughput screening
IC_{50} - 50% inhibitory concentration
iRBC - infected red blood cell
ISQ - Isoquine
k_{cat} - Turnover constant
K_m - Michealis-Menten constant
LDH - Lactate dehydrogenase
LF - Lumerfantrine
MMV - Medicines for Malaria Venture
MQ - Mefloquine
MSF - Malaria SYBR green-I fluorescence
NBT - Nitroblue tetrazolium chloride
NP40 - Nonidet P-40
p-LDH - parasite lactate dehydrogenase
PBS - Phosphate buffer solution
PCA - Principle component analysis
***Pf*CRT -** *Plasmodium falciparum* chloroquine resistant transporter
Phiβ - Ferrihemochrome
Plm - Plasmepsin
PPQ - Piperaquine
PV - Parasitophorous vacuole
QD - Quinidine
RBC - red blood cell

RNA - ribonucleic acid

βHIA - β-haematin inhibition activity

RERS - Resonance Enhanced Raman Spectroscopy

rpm - revolutions per minute

SAR - structure activity relationships

SDS - Sodium dodecyl sulfate

SEM - Scanning electron microscopy

TEM - Transmission electron microscopy

QN - Quinine

TMD - Transmembrane domains

VICB - Vanderbilt University Institute of chemical biology

WHO - World Health Organization

Table of Contents

1

Literature review and Introduction

1.1 Malaria overview

Malaria is a human infectious disease that has infected hundreds of millions and claimed the lives of hundreds of thousands annually over the past decades, where, up to 90% of these deaths occur in Sub-Saharan Africa with children and pregnant women being the most vulnerable [1-2]. Malaria is caused by the *Plasmodium* protozoan parasite that is transmitted to the human host through the bite of an infected female *Anopheles* mosquito. Currently, there are five reported *Plasmodium* species which are; *P. vivax*, *P. ovale*, *P. knowlesi*, *P. malariae* and *P. falciparum* [1, 3-4]. The *P. falciparum* species, specifically, has been reported to be responsible for threatening up to one third of the World's population as it has been classified as the most frequently fatal malaria parasite to humans [5-7]. Historically, for the treatment of *P. falciparum* associated malaria the most widely used antimalarial drug that was used is chloroquine (CQ). During this time, CQ had proven to be the most cost effective, efficient and reliable antimalarial drug which decreased the number of malaria related infections and deaths. However, within a period of ten years of its introduction, CQ-resistant *P. falciparum* parasites first emerged and then the drug gradually became less effective over the following three decades [8-9]. Scientists even went on to develop CQ analogues that would possess the same advantages of being cheap to manufacture, reliable and show effectiveness against CQ-resistant *P. falciparum* [10-12]. Since then, mortality rates have decreased and the spread of resistance has slowed down but still poses as a major threat to public health world-wide. To counteract this problem, the World Health Organization (WHO) introduced the use of artemisinin-based combination therapies (ACTs) over twenty years ago as the first-line treatment for *P. falciparum*. These ACTs included the use of previously discovered antimalarial drugs such as amodiaquine (AQ), mefloquine (MQ), piperaquine (PPQ) and various artemisinin's (ART), where an example is artesunate (AS) [13-14]. These ACTs have been very effective, contributing to reducing the number of malaria related deaths by 44% with reported cases of 99.7% in the African regions, 62.8% in South-East Asia, 69% in Eastern Mediterranean and 71.9% in Western Africa. However, there have been reports of *P. falciparum* resistance towards artesunate-MQ, dihydroartemisinin-PQ and AS itself [15-21]. Even though the effectiveness of certain ACTs have been compromised, WHO has reported 219 million cases of malaria and 435 000 deaths for the year, 2018, a large improvement over 2000 [16]. During this time, a non-profit organization Medicines for Malaria Venture (MMV) had been established and aims to develop new efficient

and cost-effective antimalarial drugs in the hopes to be able to completely eradicate malaria from at least 60 countries by 2030 (***Figure 1-1***) [22-23].

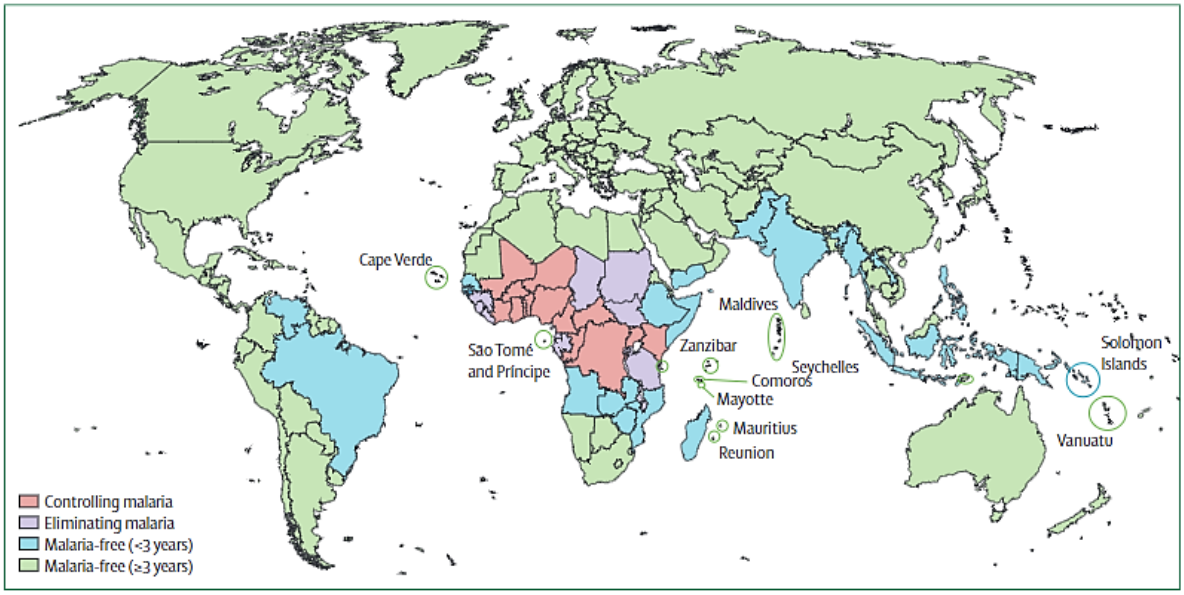

Figure 1-1: Categorisation of countries as malaria-free, eliminating malaria, or controlling malaria, 2020 projection. Elimination date projections are based on current national and regional goals as well as epidemiological progress as documented in WHO's annual World Malaria Report. For those countries that do not currently have clearly defined national or regional goals, elimination dates have been projected based on documented country-level efforts to reach pre-elimination status, recent epidemiological trends, geographical settings such as islands, and the necessary degree of ambition and optimism essential to achieve global eradication within a generation. Reprinted from: The Lancet, 387 (10029), Newby, G., Bennett, A., Larson, E., Cotter, C., Shretta, R., Phillips, A.A. and Feachem, R.G., The path to eradication: a progress report on the malaria-eliminating countries, pp.1775-1784., Copyright (2016), with permission from Elsevier [23].

1.2 Life cycle of *P. falciparum* parasites

The lifecycle of the *P. falciparum* parasite is divided into three different stages that can be defined as the hepatic stage, the intraerythrocytic asexual stage and the sexual mosquito stage [24-27]. The cycle starts with the malaria infected female *Anopheles* biting the human host and upon withdrawing blood through the capillaries of the host's skin, injects sporozoites that are contained in their saliva. For 2-3 hrs, these sporozoites can remain at the site of injection prior

to entering the blood stream via the dermal cell barrier and then traverse to the liver, where they proceed to enter hepatic cells [28-31]. For a period of 6-7 days, these sporozoites multiply into roughly 30 000 merozoites each. By their own mechanism, these merozoites rupture from the hepatic cells in small merosomes and are released into the blood stream of the host [32]. At this stage, they are temporarily exposed to the host's antibodies before invading red blood cells (RBCs) [24]. After the RBC invasion by one merozoite, the parasite begins to egress and transform into three distinct stages which include the ring, trophozoite and schizont stage which lasts for a period of 48 hrs. This is typically called the intraerythrocytic stage [7].

After 48 hrs, 16-20 merozoites are produced in one infected RBC through the cell division of the parasite. With this, the mature schizont ruptures and releases these merozoites as well as RBC debris. These merozoites are then able to then invade fresh non-infected RBCs. At this stage, the host begins to show visible symptoms that include fevers, fatigue, diarrhoea and nausea to name a few [24]. Two examples of severe malaria are placental and cerebral, where the latter is the deadliest caused by *P. falciparum* [33-34].

The cycle of merozoites invading RBCs is repeated several times before the sexual lifecycle begins. This involves some of these blood stage parasites transforming into male and female gametocytes. These gametocytes further develop into gametes which are re-ingested by a non-infected female *Anopheles* when biting and withdrawing blood from the infected host. In the newly infected *Anopheles*, the gametes fuse together and form zygotes that have the ability to pass through the gut wall. In the gut, these zygotes mature into invasive ookinetes which pass through the midgut and develop into oocysts. Over a period of 10-22 days, these oocysts release migratory sporozoites that accumulate in the lobes of the salivary glands which are ready to be injected into another human host during its next blood meal (***Figure 1-2***) [7,33,35].

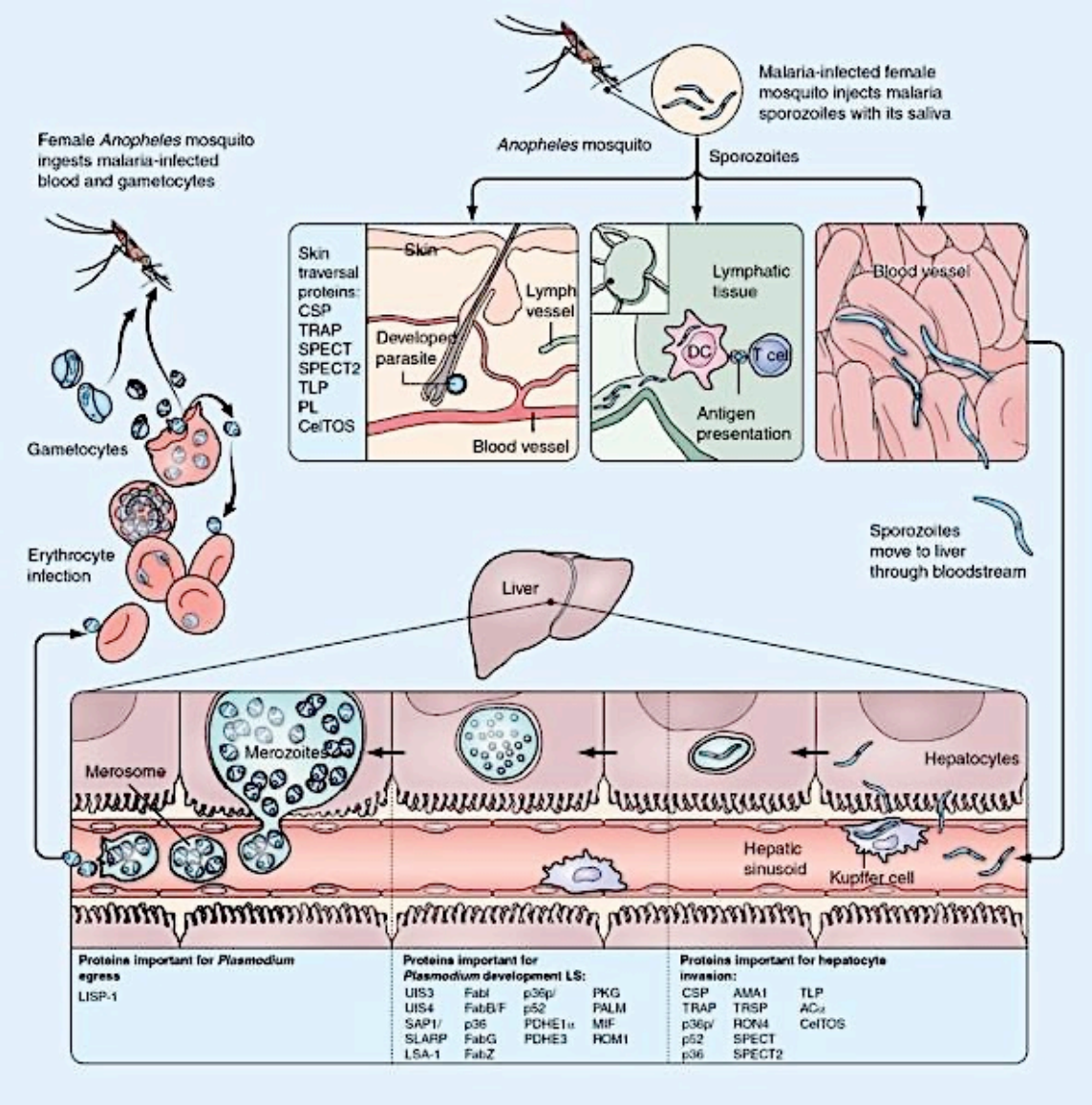

Figure 1-2: Life cycle of *P. falciparum* parasites in the human host. Reproduced from Duffy, P.E., Sahu, T., Akue, A., Milman, N. and Anderson, C., 2012. Pre-erythrocytic malaria vaccines: identifying the targets. *Expert review of vaccines*, *11*(10), pp.1261-1280., Copyright (2012), with permission from Taylor & Francis Online [36].

Throughout the stages of the life cycle, each stage is associated with different vaccine targets that can be targeted with various subunit vaccines. The aim of these vaccines is to induce antibody and T-cell responses [37]. For instance, during the highly metabolically active hepatic stage subunit pre-erythrocyte vaccines, such as Hepatitis B-based ones, are commonly used [36,38]. These vaccines target sporozoites and liver stage parasites which have been seen to be important in eliminating the ability of the parasite to egress and develop into the intraerythrocytic stage. This is an important drug target for two main reasons. The first, being

that at this stage the number of infected hepatic cells range from dozens to hundreds. Second, the *P. falciparum* parasite is known to incubate in hepatic cells for a period of two weeks before infecting RBCs which offers ample time and opportunity to eliminate this disease [39-40]. For the intraerythrocytic stage, subunit vaccines such as those targeting glutamate rich protein and merozoite surface protein-3 (MSP-3) as well as *P. falciparum* erythrocyte membrane protein-1 (*Pf*EMP-1) have been extensively assessed as potential vaccines for this stage. However, all these potential vaccines still require further investigations [37,41-42]. More recently, studies into effective transmission blocking vaccines using improved gametocyte activity screening assays have also been carried out. These have proved to potentially reduce the chance of malaria transmission by targeting the sexual stage of the parasite, specifically the sexual gametocytes [43-47].

With that said, antimalarial drugs remain the only effective means to treat malaria infections. The mechanism of action of β-haematin inhibitors and their derivatives against the inhibition of haemozoin formation during the intraerythrocytic stage of the *P. falciparum* parasite is the focus of this literature review.

1.3 Intraerythrocytic asexual cycle of *P. falciparum* parasite

The intraerythrocytic asexual cycle is important for understanding how the parasite causes apparent symptomatic signs in the host, such as fevers. This cycle has also become the focal point for developing new antimalarial drugs in the efforts to kill the parasite. There are four distinct stages which occur; the merozoite stage, the ring stage, the trophozoite stage and the schizont stage (***Figure 1-3 a-d***) [24].

Merozoite stage

The cycle begins with the smallest stage, the merozoite stage, which involves invasive merozoites being released into the blood stream of the host which capture and invade RBCs. These invasive merozoites have a distinctive shape that has been previously described as "lemon-shaped" (***Figure 1-3 a***). This lemon-shape is attributed by the various membranous vesicles for contents secretion, ribosomes, nucleus, a mitochondrion and plastid contained in the merozoites [48-51]. They are also coated in a thin merozoite surface protein-1 containing

filament which facilitates in the capturing of RBCs. However, this thin filament is cleaved during the process of RBC invasion. They attach to RBCs with a random orientation, re-orientate themselves to be in close proximity to the RBC membrane and start to invade the RBC. Whilst invading the RBC, an invasion pit is created whereby the merozoite becomes encapsulated in a membrane-lined cavity known as the parasitophorous vacuole (PV) [52-54]. Upon entering the RBC, the merozoite forms dense knob-like features within its apical cytoplasm which increases its size. The main function of these dense knob-like features is to allow for contents to be transferred from the merozoite into the PV. This facilitates the transformation of the merozoite into flat thin discoidal cup shaped rings, known as the ring stage [48,55-56].

Ring stage

At this fairly low metabolically active ring stage, also referred to as the early trophozoite stage, a thick cytoplasmic rim containing various components forms while the center is quite void. This thick rim in the ring contains the nucleus, mitochondrion, plastid, ribosomes and endoplasmic renticulum which are necessary for the progressive growth of the parasite. At the surface of the parasite, small globules of the RBC cytosol are consumed through the parasites cytostome. With these RBC-containing globules, portions of the PV membrane and plasma membrane are digested within the parasite vacuoles [57-62]. As the parasite develops, these small digesting vacuoles fuse together to form one single vacuole, known as the digestive vacuole (DV). During this fusing process, the PV membrane increases in size and the parasite transforms into an irregular-shaped trophozoite (***Figure 1-3 a***).

Trophozoite stage

While this highly metabolically active stage has the same functionality as the ring stage, it is distinctively different in terms of its shape and size (***Figure 1-3 b***). During this stage, the parasite continues to feed on the host RBC while changing the physiology of the host RBC. This occurs as a result of the parasite exporting an increased amount of proteins into the host RBC cytoplasm [51]. Coincidentally, large amounts of haemoglobin from the cytosol of the host RBC are transported into the DV and are digested in an orderly manner by various proteases [63]. As a result of this haemoglobin digestion, toxic haematin and globin fragments are released, the latter being further digested into amino acids that are exported from the parasite. On the

other hand, the toxic haematin is converted into inert crystals called haemozoin. Subsequently, the size of the parasite enlarges and forms irregular bulges and deep tubular invaginations, seen as knobs and Maurer's clefts at its surface [64-65]. At this point there is an increase in the size of the endoplasmic reticulum, the number of free ribosomes and the complexity of the Golgi complex as a direct response to increased protein synthesis. With this increase in protein synthesis, proteins are exported to the surface of the host RBC by proceeding through the Golgi complex into cytoplasmic vesicles by means of an energy-dependent process into the PV [58,66-67]. Other proteins form into dense aggregates or in Maurer's clefts that are able to penetrate through the PV membrane and bind to the surface of the RBC membrane [51]. The parasite begins to undergo multiple nuclear divisions which is identified as a feature of the schizont stage.

Schizont stage

At the schizont stage, both the process of proteins being exported and haemozoin forming as a consequence of depleting RBC haemoglobin are continued (***Figure 1-3 c-d***). As a result of the continued export of proteins, the cytoskeleton and membrane of the host RBC becomes distorted and angular in shape, whereas the haemozoin crystals are densely compacted into a single mass [51]. During this endomitotic process, the parasite nucleus divides and produces about 16-20 single nuclei containing chromosomes and mitotic spindles which move to the surface of the parasite [48,55,68-69]. This is followed by the formation of the daughter merozoite centre, which in itself involves a number of stages that starts with the apical organelles [53,69-71]. From here, a nucleus, mitochondrion and plastid is added from the schizont cytoplasm after which the merozoite coat forms. As a result of the secretion process of the apical organelle, the host RBC ruptures and releases the daughter merozoites into the host's blood stream along with the haemozoin. The daughter merozoites are then able to invade new host RBCs.

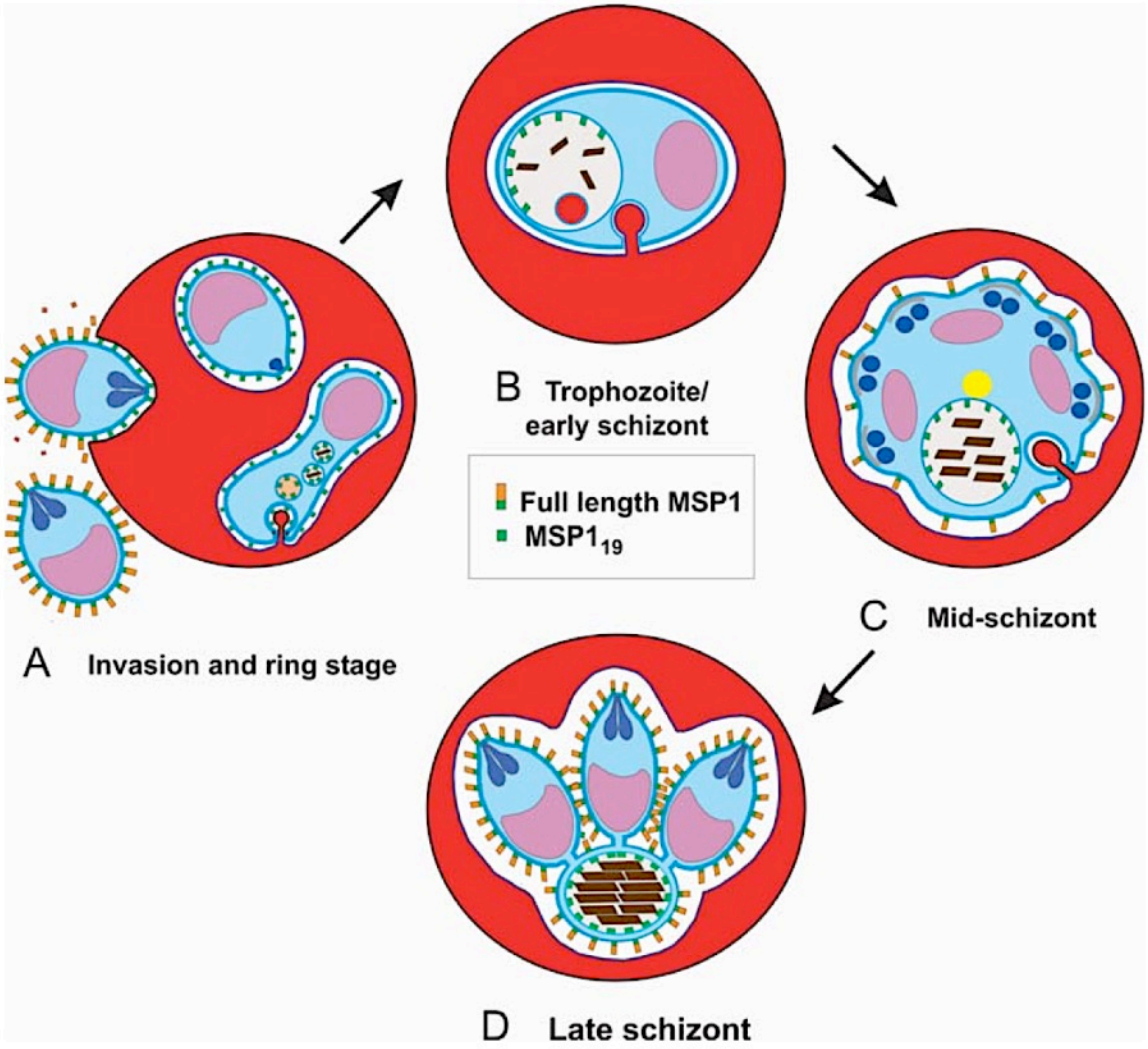

Figure 1-3 a-d: Intraerythrocytic asexual cycle of *P. falciparum* parasite representing (a) merozoite and ring stage, (b) trophozoite stage, and (c-d) schizont stage. Reprinted from: Dluzewski, A.R., Ling, I.T., Hopkins, J.M., Grainger, M., Margos, G., Mitchell, G.H., Holder, A.A. and Bannister, L.H., 2008. Formation of the food vacuole in Plasmodium falciparum: a potential role for the 19 kDa fragment of merozoite surface protein 1 (MSP119). *PLoS One*, *3*(8) [25].

1.4 Haemoglobin degradation

1.4.1 Haemoglobin digestion

According to literature, haemoglobin being the main protein in RBCs, has a concentration of 5 mM in the RBC which constitutes 95 % of the total cell protein. Thus haemoglobin, contained

in the RBCs cytoplasm, is the most important component needed for the survival of the malaria parasite, *P. falciparum*. During the intraerythrocytic life cycle of the parasite, haemoglobin is ingested via the parasite cytostome and transported into the DV by double-membrane vesicles [72-73]. Therefore, once inside the DV, digested haemoglobin provides a large number of amino acids which provide a source of nutrition utilized for self-generation of new proteins. At the same time the parasite has to maintain osmotic stability within the infected RBC (iRBC). It does this by exporting the amino acids from the iRBC [74-75]. Research into the degradation process of haemoglobin, has become relevant for not only understanding the process of haemoglobin degradation within the DV, but also to design protease inhibitors as potential new drugs. Known protease inhibitors, such as pepstatin and E-64 inhibit the proteases which are responsible for this process, albeit non-selectively [76].

The digestion process of haemoglobin by the parasite is complex. Haemoglobin undergoes a degradative catabolic reaction which occurs due to the presence of a series of proteinases within the DV [77]. The proteinases, localized specifically to the DV, include; four main aspartic proteases, plasmepsin (Plm) I, II, IV and histo-aspartic protease (HAP), constituting the protein products of four of the ten main Plm genes [78]; cysteine proteases (falcipains); a metalloprotease (falcilysin); a dipeptidyl aminopeptidase (*Pf*DPAP1) and neutral amino peptidases [77,79-82]. According to early studies by Francis *et al*, Gluzman *et al* & Goldberg *et al*, within the DV aspartic and cysteine proteases account for 60-80% of haemoglobin degradation as well as the degradation of globin fragments, while other enzymes account for only 20-40% [76, 83-84].

From ***Figure 1-4***, it can be seen that this catabolic degrading reaction is initiated by Plm I and II, such that these enzymes cleave native haemoglobin along the α-chain at the amino acid residues, specifically at αPhe_{33} and αLeu_{34} [79]. This is the cleaving point in native haemoglobin which is also referred to as "the α-helical hinge region" [76,79,85-86]. But, according to Luker *et al*, the cleavage site at which these Plms cleave native haemoglobin is more specific such that Plm I tends to cleave haemoglobin at the αPhe_{33} whereas Plm II, cleaves at the αLeu_{34} site both in the P1 position, which tends to be more hydrophobic in character [85]. This cleavage not only causes the dissociation of the tetrameric structure of haemoglobin but also allows for the exposure of other possible cleavage sites. It has also been found that even though Plm I and Plm II are of the same group of proteases, they have different periods at which they appear in the intraerythrocytic stage of the malaria parasite [87]. Plm I is first synthesized during the ring stage of the parasite and is continuous throughout the trophozoite stage. Francis *et al* has stated that this is an indication that the activity of Plm I activity is minimal in the haemoglobin

degradation process. On the other hand, Plm II, has been shown to be mainly active in the trophozoite stage, where it has been shown to be at its highest concentration [87]. After this initial catabolic cleaving of haemoglobin, two main products, toxic haem and globin fragments are released [79]. Concentrating on the resulting globin fragments, they are broken down to large globin fragments by a combination of enzymes which include mainly; falcipain II & III as well as Plm I, II, IV and HAP [75,88-90]. Bjelic *et al* has mentioned that HAP, due to the 60% similarity shared with Plm I, Plm II and Plm IV, would exhibit the same activity as an aspartic protease [91].

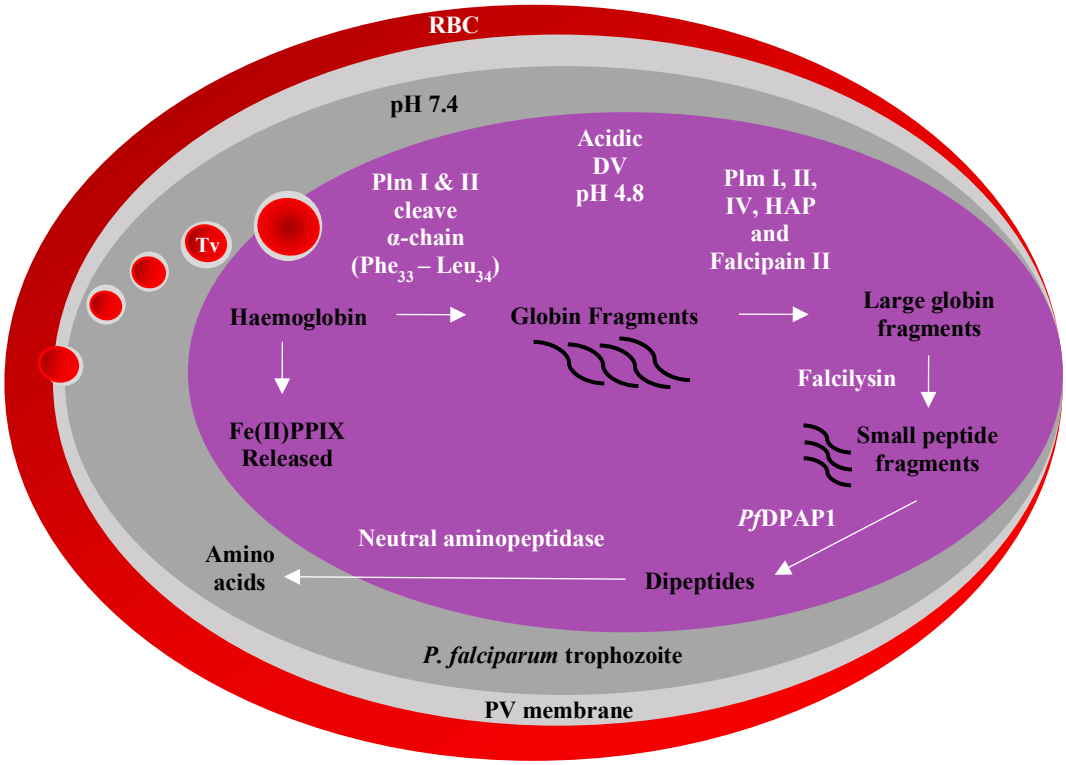

Figure 1-4: Catabolic reaction process of haemoglobin degradation. RBC = red blood cell; PV = parasitophorous vacuole; Fe(II)PPIX = haem; Plm = plasmepsin; HAP = histo-aspartic protease; DV = digestive vacuole; Tv = transport vesicles [72,92].

The third phase of haemoglobin degradation involves these large globin fragments, which are susceptible to further degradation, being cleaved by the hydrolysis of a metalloprotease falcilysin. The metalloprotease falcilysin mainly targets polar and charged smaller side chain residues within these large globin fragments therefore releasing small peptide fragments [92]. In 2004, Klemba *et al* reported that a dipeptidyl aminopeptidase (*Pf*DPAP1) had also been identified in the DV of the *P. falciparum* parasite. *Pf*DPAP1 is part of a set of homologous

gene sequences including, cathepsin C lysosomal exopeptidase. As indicated in ***Figure 1-4***, it is known to be active in the fourth phase of the haemoglobin degradation process and is capable of digesting these smaller peptide fragments into dipeptide residues [93]. According to Gavigan *et al*, these dipeptide residues are removed from the DV and digested in the cytoplasm of the parasite to amino acids by a group of neutral aminopeptidases [94]. These neutral aminopeptidases include; M1-family alanyl aminopeptidase (*Pf*M1AAP - transmembrane protein) and M17-family leucyl aminopeptidase (*Pf*M1LAP) that are found in the *P. falciparum* genome [95-96]. The mechanism as to how this process occurs is still unknown, however, research done by Skinner-Adams *et al*, Grembecka *et al* and Gavigan *et al*, show that there is a direct correlation with the inhibition of these neutral aminopeptidases and the complete process of haemoglobin degradation for the survival of the parasite [94,97-98].

1.4.2 Kinetics of aspartic and cysteine proteases

In order to further understanding the process of haemoglobin degradation, research into the kinetics of each of these proteases has also been carried. These kinetic analyses have included looking at both native and recombinant forms of these proteases using various assays and equipment in order to obtain the Michealis-Menten (K_m) and turnover (k_{cat}) constants.

The proteome of the *P. falciparum* parasite DV has been widely studied using techniques such as sodium dodecyl sulfate polyacrylamide gel electrophoresis (SDS-PAGE) and liquid chromatography–mass spectrometry (LC-MS) [99]. Experiments have also been done with recombinant Plm I, which were expressed in *E. coli* BL21 (DE3) cells at 37 °C and characterized using techniques including SDS-PAGE and Q-Sepharose column chromatography. Lolupiman *et al*, collected K_m and k_{cat} constants (***Table 1-1***) and tabulated them for different studies with recombinant Plm I [100]. Unfortunately, they could not be directly compared as the methods by which the constants were obtained, differed in terms of the substrates and assay conditions that were used. The kinetics of the recombinant sample **1** (***Table 1-1***) were analysed in the presence of a fluorogenic (FRET) peptide as a marker, (emitted fluorescence is based on the conformational change of the fluorogenic peptide), in this case DABCYL-Glu-Arg-Nle-Phe*Leu-Ser-Phe-Pro-EDANS specifically at pH 4.5. Recombinant samples **2-4** (***Table 1-1***) were analysed using another FRET peptide, DABCYL-GABA-Glu-Arg-Met-Phe*Leu-Ser-Phe-Pro-GABA-EDANs at pH 5.0. However for samples **2** and **4** purified, naturally occurring Plm I were used. The later samples (**5-8**) were analysed

in the presence of a chromogenic peptide (Leu-Glu-Arg-IIe-Phe*Nph-Ser-Phe), in which a change in the colour of the solution was observed when interacting with proteolytic enzymes such as Plm I. It was suggested that the lower K_m values that were obtained (***Table 1-1, samples 1-3***) could be due to the recombinant samples having a higher degree of interaction between the FRET peptides and the hydrophobic portions of Plm I. Lolupiman *et al* also stated that with the charge of the Glu residue being reduced in the FRET peptide at pH 4.5, this could have been the cause for lower K_m values being obtained [100].

***Table 1-1*:** Comparison of kinetic parameters of recombinant Plm I from various studies [100].

	K_m (µM)	**k_{cat} (s^{-1})**	**Reference**
1	0.092 ± 0.004	0.344 ± 0.050	[100]
2	0.917 ± 0.144	0.473 ± 0.172	[101]
3	0.49 ± 0.12	2.3	[85]
4	13 ± 1	0.24	[85]
5	8	16	[102]
6	10	2.1	[102]
7	8.6 ± 0.2	2.6 ± 0.1	[103]
8	10	1.3	[104]

Additional studies by Moon *et al*, were carried out where the kinetics of recombinant Plm I and II were studied in the presence of two chromogenic peptide substrates with a sequence, Leu-Glu-Arg-Xaa-Phe*NPhe-Ser-Phe (NPhe = nitrophenylalanine), where Xaa is IIe and Val respectively. The kinetic analyses were done under pH conditions of 4.4 at 37 °C and are displayed in ***Table 1-2*** [104].

***Table 1-2*:** Kinetic analysis of recombinant Plm I and II in the presence of two chromogenic peptide substrates [104].

Substrate	**Enzyme**	**K_m (µM)**	**k_{cat} (s^{-1})**
Xaa = IIe	Plm I	10	1.3
	Plm II	25	15.2
Xaa = Val	Plm I	30	1.6
	Plm II	20	8.9

The values obtained in the study were comparable with those obtained in Dunn *et al*, where hydrolysis was carried out using proteases from various vertebrate and fungal species [105]. The comparison with other aspartic proteases showed that Plm II gave observations that were in close agreement to these, whereas Plm I gave lower values. It was also noted that Plm II results in a much higher k_{cat} values than Plm I for both substrates thus proving the efficiency of Plm II relative to Plm I [104-106] . According to Banerjee *et al* as well as studies mentioned above, immuno-electron microscopy showed that Plm II, IV and HAP were found in the same regions of the DV as haemozoin whereas Plm V, IX and X were located in the external parts of the DV [80-81]. Plm IV has been shown to result in higher affinity values (K_m = 0.33 μM) than those reported for Plm I and II. HAP, on the other hand, has similarities with that of Plm I, II and IV as mentioned above, but when recombinant HAP studies were carried out in *E.coli* it was found that there was no significant haemoglobin cleavage. It was suggested that this could have been due to the fact that this protease lacks the ability to activate itself like the other proteases [81]. But kinetic data has been published for HAP where a K_m value 0.29 μM (***Table 1-3***) was obtained which corresponds to a higher affinity value than those of Plm I and II. It was also proved that even though a higher affinity was obtain for HAP the k_{cat} proved to be much slower, 0.05 s^{-1} (***Table 1-3***) showing that HAP may not play that much of a role in the cleaving of haemoglobin [85]. When comparing Plm IV and HAP, Plm IV was observed to be more catalytic efficient as mentioned by Banerjee *et al* [81]. Experiments, where Plm IV was incubated overnight, were carried out and proved that Plm IV digests globin residues much more in native haemoglobin, but is somewhat less efficient than Plm II when digesting globin fragments. However, the combination of these two enzymes resulted in much more efficient cleavage of haemoglobin [81].

Table 1-3**:** K_m and k_{cat} values for PM I, II, HAP and PM IV [81].

	K_m (μM)	**k_{cat} (s^{-1})**	**Reference**
Plm I	0.49 ± 0.12	2.3	[85]
Plm II	2.6 ± 0.9	11	[85]
HAP	0.29 ± 0.04	0.05 ± 0.002	[80]
Plm IV	0.33 ± 0.04	1.05 ± 0.03	[80]

Studies by Francis *et al* and Rosenthal *et al.*, have obtained kinetic data (K_m and k_{cat}) for both native and recombinant falcipain [83,106-107]. In this study the native samples were obtained by

methods of haemoglobin denaturing assay whilst the recombinant samples were obtained from Francis *et al* and Rosenthal *et al* [83,106-108]. The recombinant samples that were used were the forms VLR (Z-Val-Leu-Arg-AMC) and FR (Z-Phe-Arg-AMC) in order to obtain kinetic data for comparison (***Table 1-4***).

***Table 1-4*:** Kinetic analysis of falcipain [83].

	K_m (µM)	k_{cat} (s^{-1})
Recombinant VLR	3.7	0.25
FR	2.8	0.018
Extracted VLR	4.0	0.017
FR	15.7	0.43
Native VLR	4.9 ± 1.2	0.011 ± 0.001
FR	43 ± 16	0.086 ± 0.11

According to Francis *et al*, the values that were obtained in ***Table 1-4*** were similar to those obtained in previous studies which were done in whole trophozoite lysates as well as isolated DV [83]. However, it was found that the values obtained using the baculoviral expressions system were substantially different to the results that were obtained by Salas *et al*, for the recombinant falcipain samples expressed in the ring stage [106,108]. This was said to be due to the recombinant falcipain producing two major products that proved to have a different method of action to that of the native form. It was further proved by Rosenthal *et al*, that the recombinant form did not have the same conformation as the native form [106-107].

Kinetic studies with dipeptide-digesting neutral aminopeptidases have also been carried out. Vander *et al* determined the K_m for three soluble aminopeptidases in *P. falciparum* parasites which included L-Alanine-*p*-nitroanilide, L-Leucine-*p*-nitroanalide and L-Leucine-7-amido-4-methylcoumarin, where L-Alanine-*p*-nitroanilide resulted in the highest K_m [109]. A more recent study by Teuscher *et al* determined that the aspartyl aminopeptidase, *Pf*M18AAP, is localized to the parasite cytosol and trafficked out of the parasite to the parasite PV. With this, they measured the K_m and k_{cat} for the hydrolysis effect of the enzymes H-Asp-NHMec and H-Glu-NHMec by recombinant *Pf*M18AAP in the absence and presence of cobalt (Co(II)). In the presence of 1 mM Co(II), the k_{cat}/K_m values were increased by 8- and 30-fold for H-Asp-NHMec and H-Glu-NHMec respectively [110].

Nonetheless, the kinetics of both aspartic and cysteine proteases would be useful in developing a haem pathway model which may provide a better understanding of the *P. falciparum* parasite and the development of antimalarials that target the haemoglobin degradation pathway.

1.5 Haemozoin

1.5.1 Structure of Haemozoin

Early in the 18th century, haemozoin was first discovered and later led to the discovery of the malaria parasites life cycle in humans [111-113]. While Brown *et al* identified that haemozoin contained haematin as the chromophore in 1911, very little attention was paid towards haemozoin [114], until 76 years later, when Fitch *et al* published a study which showed that haemozoin consists of the insoluble aggregated form of haem ferriprotoporphyrin IX (Fe(III)PPIX) [115-116]. With this, it was shown that a haemozoin crystal contains roughly 80 000 haem molecules where each crystal has a length of 100-200 nm [117]. A few years later, Slater *et al* proved that while the chemical structure of haemozoin is related to haem, there are no proteins included in its structure. It was also reported that the spin state of the central iron (Fe) of haemozoin was different to that of the spin states of haematin and haemin which had high spin state ferric centers [118]. This contradicted the observations of Ghosh and Nath whom showed that haemozoin was only comprised of Fe(III)PPIX which had an identical composition as haematin [119]. Bremard *et al* agreed with this and showed that the Fe of haemozoin existed in the 3+ state which is characteristic of a high spin state, similar to haematin [120]. In a related study, Slater and colleagues were able to show with the use of infrared and X-ray spectroscopy that the haemozoin crystal was characteristic of Fe(III)PPIX molecules that are bonded through an iron-carboxylate bond [115,118]. In support of this, Pagola *et al* showed that there are two distinct bonds in the crystal structure of haemozoin, an iron-carboxylate bond which was thought to extend the Fe(III)PPIX chain and a hydrogen bonded carboxylic acid linkage between Fe(III)PPIX units of different chains through a propionate groups which provides rigidity to the structure by cross-linking [121-122]. In haemozoin, this iron-carboxylate bond was estimated to be short with a distance of 1.92 Å. Later it was shown that haemozoin is in fact a dimer and is neutral in the form of Fe(III)PPIX which involves the ionization of one propionic acid group of each haematin molecule coordinated to the Fe centre of the other with hydrogen bonds between propionic acid groups of neighbouring dimers and strong π-π interactions in the

crystal [121]. As illustrated in ***Figure 1-5***, haemozoin crystals localize in the parasite DV and have a lath-like shape [123-126].

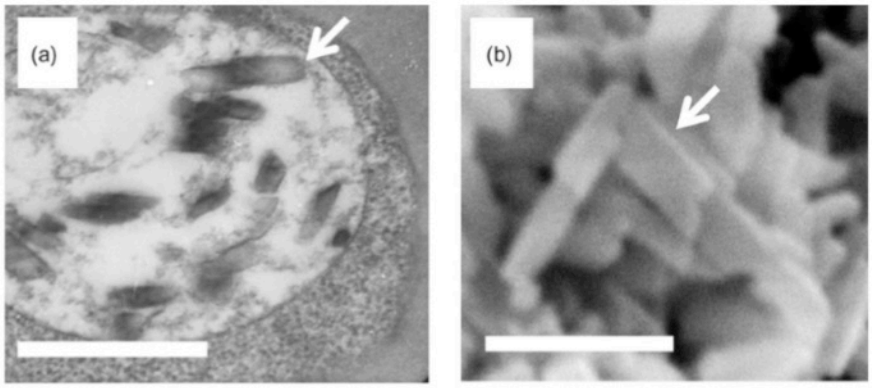

Figure 1-5: Micrographs obtained by transmission electron and scanning electron microcopy of (a) *P. falciparum* iRBCs showing haemozoin crystals inside the DV (white arrow), and, (b) isolated haemozoin crystals. Reprinted from: *Molecular and biochemical parasitology*, 157 (2), Egan, T.J., Haemozoin formation, pp.127-136., Copyright (2007), with permission from Elsevier [123].

The structure of haemozoin is identical to its synthetic ferriprotoporphyrin counterpart, β-haematin. This was originally recognized from observations that insoluble haemozoin formed in the parasite DV at a pH of 5 and under physiological conditions, both which are the favorable conditions for β-haematin formation [116,127-128]. Bohle *et al* showed that β-haematin has a high spin ferric center similar to that of haemozoin [122]. This was supported by earlier findings published by Koenig *et al* in 1965 [129]. The structure of β-haematin and haemozoin was at first proposed to be a polymer of Fe(III)PPIX units linked by coordination of the propionate group of one Fe(III)PPIX molecule to the Fe(III) center of the next as mentioned earlier [118]. Slater *et al* was able to prove using X-ray adsorption spectroscopy that the composition and the ordered microcrystalline structure of haemozoin reported in the study by Fitch *et al*, in fact identical to β-haematin [115,118]. At first, haemozoin/β-haematin was routinely referred to as a polymer until 2000, when Pagola *et al* proved otherwise. Indeed, this incorrect description is still occasionally encountered in the literature. Having first established that the powder X-ray diffraction pattern of β-haematin was identical to that of whole dried iRBCs, the crystal structure of β-haematin was determined from the powder diffraction data obtained with synchrotron radiation using Rietveldt refinement. Haemozoin and β-haematin were determined to be made up of cyclic dimers of Fe(III)PPIX with the propionate of one Fe(III)PPIX coordinated to the Fe(III) center

of the other. Dimers are linked to each other by hydrogen bonding of propionic acid groups [121,130]. From the comparison of the single-phase microcrystalline powder of β-haematin and whole dried iRBCs, it was also shown that β-haematin and haemozoin have the same triclinic unit cell and are isostructural at an atomic level (***Figure 1-6***) [130-131].

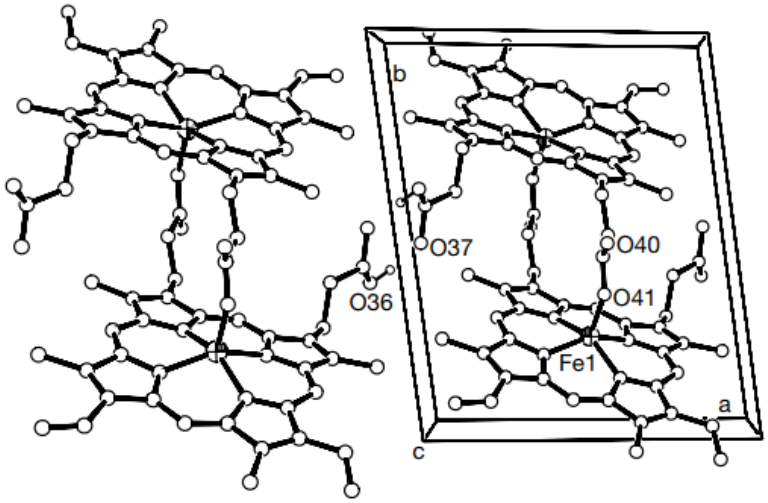

Figure 1-6: The dimer crystal structure of haemozoin/β-haematin formed through the Fe1-O41 bond which are viewed along the fastest growing face (001). All hydrogen bonds have been omitted. Reprinted by permission from Macmillan Publishers Ltd: [Nature Publishing Group], Pagola, S., Stephens, P.W., Bohle, D.S., Kosar, A.D. and Madsen, S.K., 2000. The structure of malaria pigment β-haematin. *Nature*, *404*(6775), p.307., Copyright (2000) [121].

1.5.2 Intracellular Haemozoin formation

Looking at the overall process, the parasite ingests up to 80 % of the host RBC haemoglobin in the DV. During this haemoglobin digestion, Fe(II)PPIX is released along with globin fragments. It has been presumed that in the presence of oxygen (O_2), Fe(II)PPIX is oxidized into Fe(III)PPIX which is known to be toxic to the parasite. Indeed, superoxide has also been assumed to be produced as a result of the rapid oxidation process of oxy-haemoglobin at acidic pH values [123]. The parasite is then able to convert this toxic Fe(III)PPIX to haemozoin ensuring that it does not damage the membrane of the parasite or cause lysis of the RBC host. The conversion of this toxic Fe(III)PPIX is in fact a rapid process that less than about 1 % of the total haem present in the parasite would be in the form of toxic Fe(III)PPIX [132]. The parasite detoxifies this toxic haematin by producing the insoluble inert microcrystalline dimer haemozoin by a process of haem detoxification (***Figure 1-7***) [115,121,133-134]. In line with this

theory, even though there has been extensive research into determining the exact pathway of haemozoin formation and its structure, a comprehensive model has yet to be developed.

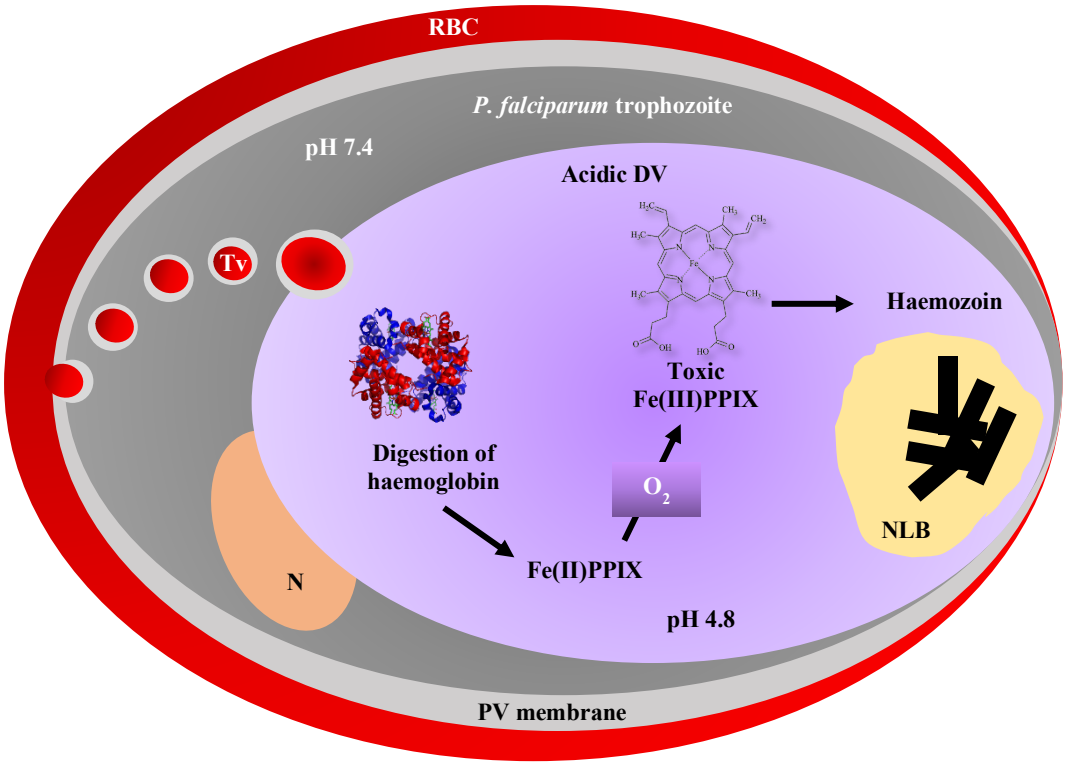

Figure 1-7: Haemozoin formation pathway [123]. RBC = red blood cell; Tv = transport vesicle; N = nucleus; NLB = neutral lipid body; DV = digestive vacuole; PV = parasitophorous vacuole.

There have been many theories that try to explain the mechanism by which haemozoin forms during the trophozoite stage. These theories include: the combination of Fe(III)PPIX molecules by a process of "haem polymerization" catalyzed by a haem polymerase [135]; catalysis by histidine-rich protein II (HRP II) which is specific to the *P. falciparum* parasite and highly concentrated in the DV during the blood stage of the parasite [136-138]; mediation by neutral lipid bodies [139] and more recently; by haem detoxification protein (HDP) [140-142]. Initially, it was proposed by Slater *et al* that haemozoin was a polymer [118]. This led to the second proposal by Slater and Cerami *et al* that haemozoin was formed due to the presence of a haemozoin forming enzyme. They termed this haemozoin forming enzyme, "haem polymerase" [135]. Following this, Egan *et al* and Dorn *et al* disagreed with this theory of haemozoin formation and it was rather suggested by Dorn *et al* to be an autocatalytic process [143-145]. In the same year, it was suggested that the haemozoin/β-haematin used in the process was contaminated with lipids and that this was the reason for the autocatalysis [146]. This was later supported by Dorn *et al* [144].

A second theory for the mechanism by which haemozoin is formed involved the protein HRP II. HRP II is a 30 kDa protein which has previously been found to have 51 repeats of the tripeptide His-His-Ala [147-148]. It was demonstrated with protein immunoblot analysis and indirect immunofluorescence with a monoclonal antibody that showed HRP II was localized in the DV of the parasite. In addition, it was shown that HRP II is able to bind to haem and promote β-haematin formation in a haem-binding titration experiment. However, it was uncertain whether the function of HRP involved a binding-releasing process or a nucleation role [136]. In relation to the location of HRP II, Papalexis *et al* showed in more detail that the primary location of HRP II was in the RBC cytoplasm with a sub-population of this protein existing in the parasite DV [149]. This findings agreed with that of Akompong *et al*, who reported that the parasite transports 97% of HRP II to the RBC, leaving only 3% that could facilitate haemozoin formation [150]. In fact, parasite mutants lacking HRP II were shown to produce haemozoin normally. Later, this HRP II mediated haemozoin formation theory was proven not to be the sole cause but was facilitated by the presence of lipids in the parasite DV by Pandey *et al* [151]. This agreed with later studies by Fitch *et al* [152].

Studies have also shown that the involvement of neutral lipid bodies in the DV of *P. falciparum* parasites could mediate the formation of haemozoin [153]. It was first shown by Coppens and Vielemeyer that haemozoin was enclosed within neutral lipid bodies by using electron microscopy [154]. These neutral lipids included mono-, di- and tri-acylglycerols, where tri-acylglycerol has been determined to accumulate in iRBCs but is difficult to detect [155-156]. In support of this, Pisciotta *et al* showed that in the parasite DV during the early trophozoite stage that the haemozoin crystals were entrapped within neutral lipid bodies using transmission electron microscopy (TEM). Furthermore, these lipid bodies were identified to have a specific composition that was made up of mono- and di-glycerols, monostearic, monopalmitic, dipalmitic, dioleic and dilinoleic glycerol in a 4:2:1:1:1 ratio [139]. In a similar study with electron microscopy, it was also shown that these haemozoin crystals form within neutral lipid bodies in the parasites DV which facilitate the formation of haemozoin [154,157]. It has been reported that lipids are sourced through the degradation of the inner membrane of haemoglobin transport vesicles by phospholipases once inside the parasite DV [61]. Ambele and Egan supported the lipid mediated hypothesis by demonstrating that the neutral lipids associated with haemozoin formation mediate the formation of β-haematin under the same physiological conditions as those in the parasite [153]. Hoang *et al* was also able to provide evidence of the partitioning of Fe(III)PPIX into neutral lipid bodies using a Nile red fluorescent probe, which is lipid specific [158]. With the use of the same fluorescent probe and TEM, Jackson *et al* showed that these

neutral lipid bodies were roughly 100 nm in size which was in the size range of the parasite DV [159]. In a related study, it was shown that these neutral lipid bodies are surrounded by a monolayer comprised of a phospholipid, glycolipid or sterol [154]. In support of this theory, Stiebler *et al* investigated the contribution of phospholipids in both chemical and biological haem crystallization. They demonstrated that unsaturated glycerophospholipids are true catalysts of fast and efficient synthetic haemozoin formation [160]. In addition, Kapishnikov *et al* demonstrated the properties of these neutral lipid bodies that are required for the formation of haemozoin in the DV. They also provided evidence of the molecular interactions of these lipophilic bodies with haem that promote the nucleation and formation of synthetic haemozoin [161]. These studies were also in agreement with the findings of Stiebler *et al* and Oliveira *et al*, who also strongly indicated that neutral lipids and phospholipids are major catalysts of haemozoin formation but involved hydrophilic-hydrophobic interfaces [160,162]. In 2012, Kapishnikov *et al* used cryogenic soft x-ray tomography and three-dimensional electron microscopy to explore the nucleation process of haemozoin. They found no evidence that the nucleation of haemozoin occurred within neutral lipid bodies but rather that a thin layer of these lipid containing bodies may remain between adjacent crystal interfaces [161]. However, it was then proposed that haemozoin crystals form on an acylglycerol lipid film rather than a lipid body which is absorbed onto the inner phospholipid membrane of the DV. In a relating study, they reported that the haemozoin crystals were orientated parallel along their needle *c* axes x-ray diffraction patterns. This essentially allows for the {100} faces of haemozoin to be exposed to curved surfaces like the acylglycerol lipid surface [163].

More recently, haemozoin formation has been shown to be assisted by the presence of a HDP in *P. falciparum* parasites. Jani *et al* showed that HDP is found in the RBC cytosol from where it is co-transported with haemoglobin into the parasite DV. With its unique trafficking route and 2.7 Fe(III)PPIX binding sites, HDP was found more potent at converting haemozoin with concentrations of 1500-2000-fold lower than neutral lipids. From here, it was suggested that HDP is involved in the formation of haemozoin dimers and transports them into neutral lipid bodies which leads to the formation of haemozoin crystals [140]. The observations by Chugh *et al* agreed with these findings and showed a multiprotein haemoglobin degradation/haemozoin formation complex in the DV of *P. falciparum* parasites. It was also shown that a cysteine protease, falcipain-2, was associated with HDP [141]. This haemoglobin degradation and haemozoin formation was supported by the findings of Kapishnikov *et al*, who used correlative X-ray fluorescence microscopy and soft X-ray tomography to highlight that haemoglobin digestion and haem crystallization via the HDP are closely associated [142].

1.6 Chemotherapy for *P. falciparum*

1.6.1 Past

For decades, various antimalarial drugs have been discovered or synthesized for the treatment of malaria. One of the first naturally occurring antimalarial drugs that was discovered came from the bark of the Cinchona tree in South America, namely quinine (QN) [26,164-166]. In the 1800's, QN was used to heal the intermittent fevers that were associated with malaria and this drug was highly effective during World War I. Following this, QN was considered to be the main treatment for *P. falciparum* malaria for many years [167]. By the 1930's, a group of German scientists at Bayer Chemicals discovered a 4-aminoquinoline antimalarial compound that was chemically somewhat similar to QN and was initially named Resochin. Later, this compound was renamed, CQ, which was used as a substitute for QN [168-171]. It was eventually found that CQ exerted its antimalarial effect during the blood stage of the *P. falciparum* parasite by disrupting haemozoin formation, which at that time, was termed "haem polymerization" [135]. In the 1950's, CQ was announced as the first-line of treatment for *P. falciparum* by the newly established WHO, which not only saved millions around the world but cured many people suffering from this disease. However, with the frequent use of this antimalarial drug (in some countries CQ was even added to the salt supplies) the *P. falciparum* parasite developed a resistance to CQ which was first reported in the year of 1957 [167]. This resistance is now known to be associated with mutations in DV transport proteins lowering the concentration of CQ at its target site [172]. Over time, CQ resistance became widespread which lead to the introduction of CQ analogues, like AQ. Being one of the first CQ analogues to be synthesized, AQ was assumed to behave similarly in terms of the mode of action of CQ [167]. However, by 1980 some *P. falciparum* parasites were reported to be resistant towards AQ and led to the development of AQ analogues, isoquine (ISQ) and ferroquine (FQ). These AQ analogues showed an increased activity and proved to be effective against CQ-resistant parasites (CQR) [173-176].

During the 1970's and 1990's, numerous other antimalarial drugs were developed and include; PPQ, MQ, halofantrine (HF), lumefantrine (LF) and primaquine (PQ), to name a few. PPQ, a bisquinoline antimalarial drug was first introduced in the 1960's and synthesized with the intention to replace CQ. In China, this particular compound was used as the primary treatment for *P. falciparum* during 1970's to 1980's, but with its frequent use became ineffective due to resistance [177-181]. Around the mid 1980's, the US Military synthesized MQ

as a substitute antimalarial drug for QN in an effort to treat patients with CQR malaria. It was thought that MQ acted against the schizont stage of the *P. falciparum* parasite but its mechanism of action was still debatable. Although its mechanism of action was not apparent, an advantage to MQ was that it remained in the patient's body for long periods of time. Ultimately, though, this was seen to be a disadvantage since the long half-life was thought to be the reason why parasites became resistant to it relatively quickly [167]. Another antimalarial drug that was observed to be active against the intraerythrocytic stage of the *P. falciparum* parasite was, HF. HF is a phenanthrene-methanol compound that was developed for the purpose of aiding countries facing multi-drug resistant *P. falciparum* parasites. In spite of the fact that HF was highly effective it was observed to cause irregularities in patient heart beats, specifically for those who were suffering from heart diseases already [167,182]. With a similar name, LF was developed by the Chinese Academy of Military Medical Sciences in the 1970's. This compound was cleared for use as an antimalarial drug and proved to be quite effective against both CQ-sensitive (CQS) and –resistant *P. falciparum* parasites *in vivo* [183]. Nevertheless, a drawback to using LF was that despite its half-life of 3-6 days, it was found not as fast acting when used on its own. Lastly, an 8-aminoquinoline, PQ, was also developed and used to eradicate *P. vivax* malaria in parts of the Southwest Pacific. It was most effective in Indonesia, Colombia and Papua New Guinea but presented adverse effects that included stomach pains and diarrhea (***Figure 1-8***) [167].

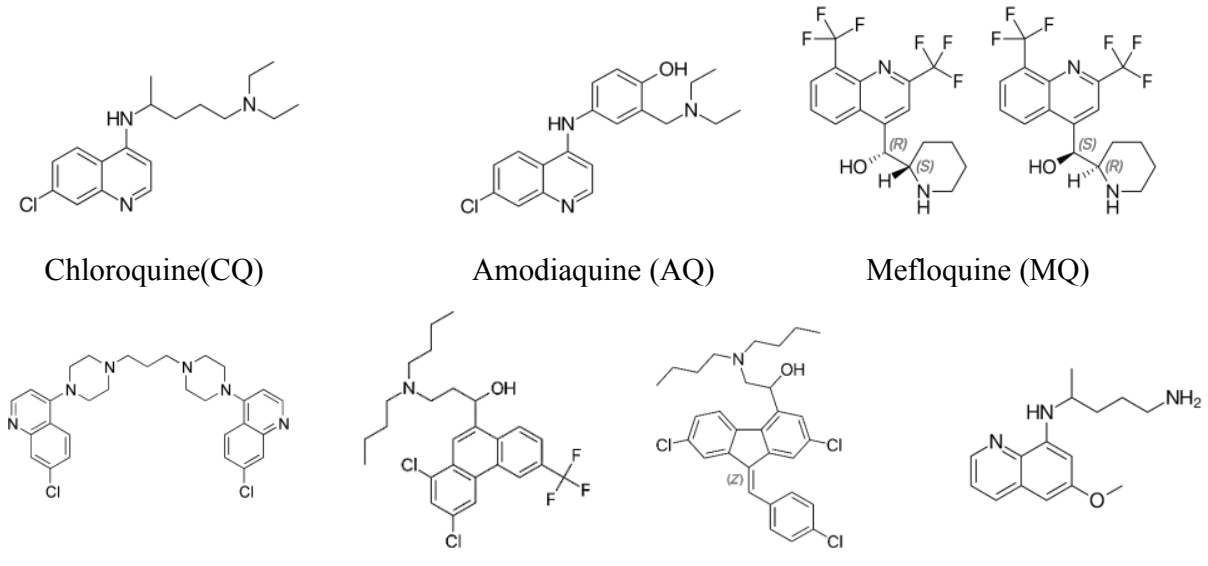

Figure 1-8: Structures of past antimalarial drugs used to treat *P. falciparum*.

1.6.2 Present

For the last few years, WHO has recommended the use of combinations of past antimalarial drugs with ART derivatives for the treatment of uncomplicated *P. falciparum* malaria [16]. These Acts first came about after the discovery of ART in 1971 by Tu Youyou, who was recently awarded the Nobel Prize in 2015 [184]. This particular compound was found to be effective against multi-drug resistant *P. falciparum* parasites. Semi-synthetic derivatives of this compound have been also synthesized and included; AS, artemether and arteether (***Figure 1-9***).

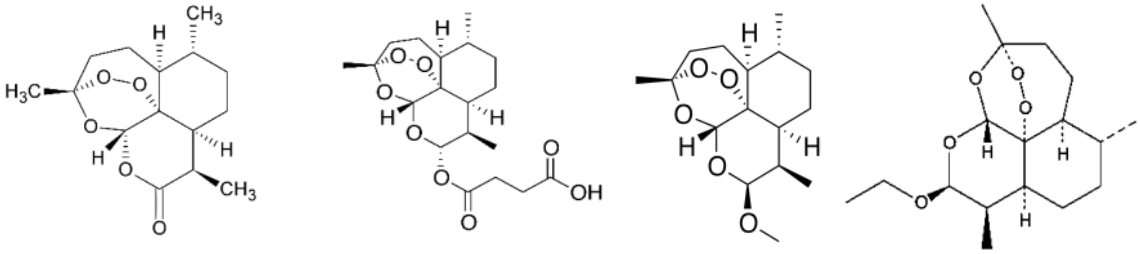

Artemisinin (ART) | Artesunate (AS) | Artemether | Arteether

Figure 1-9: The structure of some ART derivatives.

There are limiting factors that are associated to the use of these derivatives, however, in that they rapidly breakdown and have high clearance rates from the hosts plasma [167,185]. Therefore, ACTs entail using a previously discovered antimalarial drug, like AQ or MQ, with ART. However, these antimalarial drugs must have a different mode of action, suitable pharmacokinetic and pharmacodynamic properties, be effective against resistant parasites and have no undesirable or toxic effects [185]. This results in the possible inhibition of two stages of the parasite simultaneously, therefore reducing the possibility of resistance emerging from the parasite. It has been theorized that ART exhibits its antimalarial effect by being activated by haem generated from haemoglobin digestion which results in free radicals that damage parasite proteins which are essential for its survival [186-188]. Others have also reported that ARTs block the ring stage as well as the gametocyte stage [189]. Additionally, various observations have been reported between 2013 and 2015 to try and understand the mode of action of ART, where it was shown that ART is first activated the iron centre in Fe(III)PPIX and then, subsequently, inhibits the function of the calcium pump *Pf*ATP6, leading to parasite death [190-192]. Recently, there have been an increasing numbers of reports of *P. falciparum* resistance to ACTs

specifically in the regions of Southeast Asia, where the dihydroartemisinin-piperaquine (DHA/PPQ) combination has been used. This has been greatly concerning due to the fact that ACTs play a pivotal role in the treatment of *P. falciparum* malaria [193-194].

1.7 *P. falciparum* chloroquine resistant transporter

For many years, CQ was the most effective and reliable antimalarial drug used for the treatment of *P. falciparum* infections. CQ, a diprotic weak base compound [195], in its neutral form is known to be highly membrane permeable which makes it easier for CQ to cross parasite membranes. Moreover, CQ becomes protonated in the low pH environment of the DV, becoming membrane impermeable and accumulating at high concentrations [196-197]. CQ is thus able to exert its antimalarial effect and inhibit the formation of haemozoin and cause subsequent death of *P. falciparum* parasites [198]. CQ was used for almost two decades before CQ resistant *P. falciparum* emerged initially in South-east Asia and South America in the 1950's and 1960's. After this, CQ resistant *P. falciparum* began to spread throughout the globe. By the 1970's, CQ resistance was detected to have spread to Sub-Saharan Africa [199]. To counter the effects of this resistance, antimalarial drugs such as sulfadoxine with pyrimethamine and MQ were introduced, however, as a result of the increased surge of *P. falciparum* resistance they have since become ineffective [200]. Over the years, this not only caused the morbidity and mortality rates to increase but also brought about concerns of how to circumvent the resurgence of this life-threatening disease for the sake of the public health world-wide [201] (***Figure 1-10***).

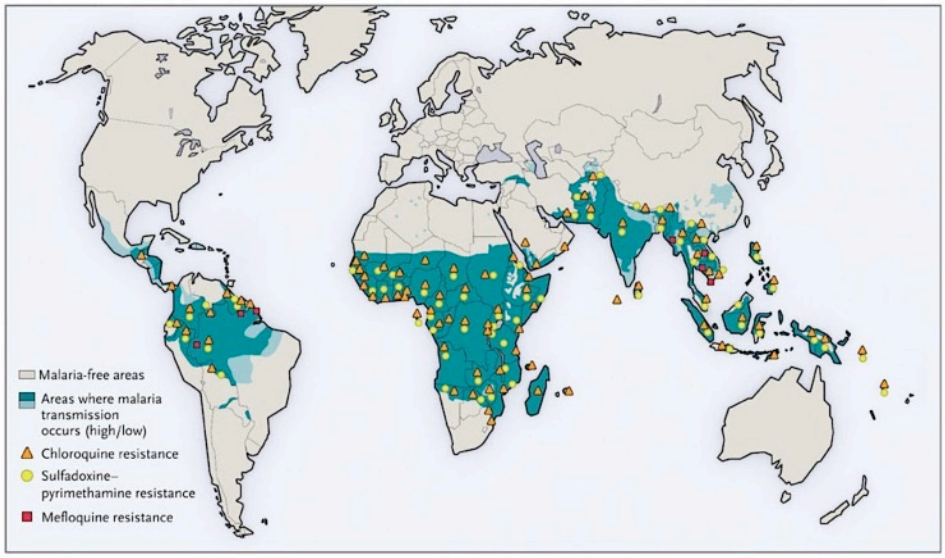

Figure 1-10: World map showing the spread of CQ, sulfadoxine-pyrimethamine and MQ resistant *P. falciparum* parasites. Reproduced from: Okie, S., 2008. A new attack on malaria. *New England Journal of Medicine*, *358*(23), pp.2425-2428 [202].

A striking observation with CQ resistant *P. falciparum* parasites was the decreased amount of accumulated CQ as a result of the reduced net uptake of CQ, compared to CQS parasites [203-204]. There have been several theories that have been reported in the efforts to understand the mechanism by which CQR parasites cause a reduction in the amount of accumulated CQ. Some of these theories include the efflux of CQ out of the parasites DV and increased detoxification of the CQ-haematin complexes which decreases the amount of CQ uptake and in turn decreases complex formation [205-208]. In 2000, it was initially observed by Fidock and colleagues that CQ resistance was primarily caused by the mutation of a specific protein, called the *Plasmodium falciparum* Chloroquine Resistance Transporter (*Pf*CRT). This specific transporter protein was identified to have ten α-helical predicted transmembrane domains (TMD) and localized in the parasites DV membrane (***Figure 1-11***) [172,209].

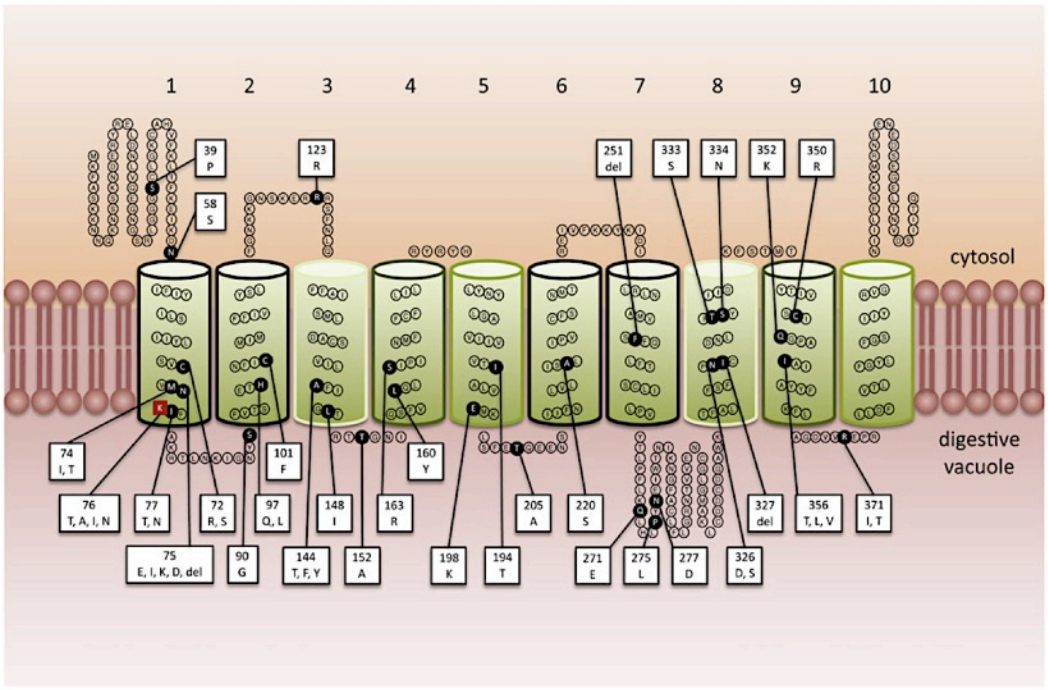

Figure 1-11: Arrangement of known polymorphic residues in *Pf*CRT. *Pf*CRT is predicted to contain 10 α-helical transmembrane domains (TMDs) and to be orientated in the DV membrane with the N- and C-termini extending into the parasite cytosol. The positions of the polymorphic residues are indicated with black circles. The key CQ resistance-associated mutation (K76T) is represented as a red square. The box attached to each polymorphic residue lists the (non-wild-type) amino acid(s) known to occur at that position. The predicted roles of the TMDs are as follows: 4 and 9 (outlined in dark green) are implicated in the binding and translocation of substrates, TMDs 3 and 8 (boxed in light green) are thought to assist in the binding and translocation of the substrate and may also influence the substrate-specificity of the transporter, TMDs 1, 2, 6, and 7 (boxed in black) are involved in recognising and discriminating between substrates, and TMDs 5 and 10 (outlined in mid-green) play a role in the formation of homo-dimers. Reproduced from: Cellular and Molecular Life Sciences, Know your enemy: understanding the role of *Pf*CRT in drug resistance could lead to new antimalarial tactics, 69, 2012, 1967 – 1995, Summers, Robert L., Megan N. Nash, and Rowena E. Martin, (Springer Basel AG 2012)., with permission of Springer [210-211].

The mechanism by which *Pf*CRT is able to reduce CQ accumulation and thus render it ineffective in killing the parasite has been extensively studied over the years. First, *Pf*CRT was thought to reduce the ability of CQ to traverse parasite membranes and accumulate in the DV of parasites by altering the pH of the DV [199]. With this, it was proposed by Yayon *et al* and

Ginsburg *et al* that the steady state reduction in CQ accumulation in CQR parasites could be as a result of CQR parasites maintaining a more acidic DV which was related to a much lower pH in comparison to CQS parasites [196,212]. This was ostensibly confirmed by observations reported by Bennett *et al*, who reported that CQR parasites have a more acidic DV with a pH of 5.2 compared to CQS parasites with a DV pH of 5.7 [213]. In other attempts to confirm this theory, Dzekunov *et al* and Ursos *et al*. used a fluorescent dye acridine orange to monitor the changes in the intensity of fluorescence between CQR and CQS strains. They observed a much more intense fluorescence signal in CQR strains compared to CQS which they deduced to be as a result of a more acidic DV [214-215]. However, these studies were later found to be incorrect by the independent studies carried out by Bray *et al* and Wissing *et al*, who proved that the use of acridine orange to monitor DV pH was unreliable and pH was found to be hardly changed [199,216].

An alternative theory is that *Pf*CRT transports CQ out of the parasites DV in CQR strains in an efflux process which occurs in an energy independent manner [204,217]. In related studies, it has been shown that this involves a polymorphic change in the transmembrane domain of *Pf*CRT at position 76. At this position, the positively charged lysine residue is substituted for a threonine residue, K76T that is uncharged. This occurs in conjunction with a series of other mutations that evidently are required to preserve function. While the normal physiological function of *Pf*CRT is unknown, but it has been suggested that it is used by the parasite to effectively transport peptides and amino acids out of the DV [218-219]. It has been directly shown that the mutated *Pf*CRT is able to transport CQ in its doubly protonated form down its electrochemical gradient in injected *Xenopus laevis* oocytes.

Chemosensitizing agents have been investigated in an effort to reverse *P. falciparum* resistance. These include the calcium channel blocker verapamil and antidepressants and antihistamines such as imipramine, azatadine and chlorpromazine. These chemosensitizers are believed to interact with hydrophobic and negatively charged pockets within the protein sequence, inhibiting CQ transport [220]. In this regard, Juge *et al* showed that verapamil could inhibit CQ transport in a *Pf*CRT-liposome assembly [221]. It has been suggested that these chemosensitizers have the ability to bind to *Pf*CRT close to residues 72-76 which as previously stated is believed to be primarily responsible for CQ resistance [199]. From this, it has been hypothesized that these chemosensitizers bind and compete with CQ. Indeed, Johnson *et al* have reported increased CQ accumulation in CQR strains upon treatment with amantadine [222]. Combination studies have also been reported showing that the use of CQ combined with verapamil or chlorpromazine inhibits parasite growth. Specifically, it was observed that the

concentrations of CQ that are used to treat CQS parasites had a similar effective against CQR parasites [204,223-224]. However, a drawback to using these chemosensitizers to substantially reverse CQ-resistance is that they all require high doses which are not clinically acceptable [225-226].

1.8 High-throughput screening for the identification of novel antimalarial drugs

Over the last two decades, high-throughput screening (HTS) tools have been the forefront for identifying new and effective antimalarial drugs. These well-established HTS tools are frequently used as an approach for drug discovery in pharmaceutical and biotechnology industries world-wide including companies such as Novartis and GlaxoSmithKline (GSK) [227-229]. The HTS approached makes use of robotic automated systems to rapidly identify large numbers of potentially active compounds against a specific biomolecular pathway or whole cells, with success rates of up to 55% [230-231]. This process uses miniaturized *in vitro* assays which require low volumes of samples being tested [232-233]. Hit compound classes, also referred to as scaffolds, are identified from this process and are used as starting points for the development of new compounds.

In an early application of this approach, Kurosawa *et al* used a haematin "polymerization" assay which involved the use of radio-labeled haematin that incorporated into β-haematin under the pH conditions mimicking that of the parasite DV. They were able to screen more than 100 000 compounds from the Roche compound library, SPECS, NCC, microbial broths and chemical combinatorial chemistry libraries. Eight novel compound scaffolds were identified as active against haemozoin formation with 50% inhibitory concentrations (IC_{50}) of less than 50 μM. The scaffolds that were identified included triarylcarbinols, piperazines, benzophenones, imides, hydrazides, indoles and isoxazoles, from which they found that the triarylcarbinol Ro 06-9075 and piperazine Ro 10-3428 showed consistent antimalarial activity after being administered orally in mouse models [234].

In 2009, Rush *et al* adapted a previously developed colorimetric pyridine ferrihemochrome (Phiβ) assay to a high-throughput screening method to screen 16 000 compounds for possible β-haematin inhibitory activity. The assay utilized a robotic liquid handling system which was carried out in 384-well microtiter plates. From this, 600 hit compounds were identified, with 17 found to be active against both CQS and CQR strains, 3D7 and Dd2 respectively [235].

Around the same time, Huy *et al* developed a fast, simple and reproducible HTS assay based on haem adsorption in β-haematin formation with the use of Tween 20 as a β-haematin inducer. A group of 9600 selected compounds were chosen from the chemical library of The Drug Discovery Initiative, Tokyo University (http://www.ddi.u-tokyo.ac.jp/en/#5) which contains more than 200 000 compounds. First, 394 compounds were identified from the HTS assay and showed activity, however, these were further refined using a dose-response assay to exclude false positives. From the dose-response assay, 224 HIT compounds were correctly identified having IC_{50} values not exceeding 5 µM [236].

Between 2008 and 2010, Novartis, GSK and a research group that was based at the St. Jude Children's Research Hospital, performed HTS for potential antimalarials using a phenotypic screening approach. Novartis screened a total of 1.7 million compounds from which 5973 compounds were identified as hit compounds [227], while the St. Jude Children's Research Hospital group screened only 309 474 compounds. From the St. Jude Children's Research Hospital group screening, only 561 hit compounds were identified [237]. GSK screened the largest number of compounds (2 million) from their existing libraries against *P. falciparum*, identifying 13 533 hits that inhibited parasite growth at concentrations of up to 2 µM and were subsequently grouped and named the Tres Cantos Antimalarial set (TCAMS) [228].

More recently, Sandlin *et al* adapted a β-haematin formation assay to a 384-well HTS plate method, employing the lipophilic detergent, Nonidet P-40 (NP40) was used a surrogate lipid for *in vitro* β-haematin formation under physiological conditions. They were able to screen 38 400 small molecules at a concentration that was similar to the IC_{50} of AQ (19.3 µM). From this, they identified 161 compounds that were active against β-haematin formation with a reported 0.42% hit rate. After this prescreening process, they used a malaria SYBR green-I fluorescence (MSF) assay to determine the parasite growth inhibition activity of these hit compounds against a CQS (D6) and multi-drug resistant (C235) strain. Following this, they were able to identify 48 (D6) and 40 (C235) compounds that had parasite growth inhibition activity of more than 90%. Of these compounds, 25 resulted in IC_{50} values lower than 5 µM, and only 8 showed nanomolar parasite growth inhibition activity in the D6 strain [238-240].

In a follow-on study, they used the same NP40 β-haematin formation was used to perform a target-specific screen on 144 330 compounds that were chosen from the Vanderbilt University Institute of Chemical Biology (VICB) library. The target-specific screen resulted in 729 identified preliminary hit compounds which showed more than 80% inhibitory activity against β-haematin formation. Using a "cherry-picking" approach and a threshold of 27 µM, they were able to test for false positives from which they identified 530 of these compounds to be hits.

To further refine these hit compounds, they used a MSF assay to screen for parasite growth inhibition activity against D6 strain parasites. This resulted in the identification of 171 hit compounds that exhibited activity that resulted in more than 90% parasite growth inhibition, 73 and 25 which showed micromolar and nanomolar activity, respectively. The latter 25 nanomolar hits were subjected to further testing against the multi-drug resistant C235 strain and found 21 to be active against this strain [240-241]. The mode of action of the hit compounds was confirmed *in vivo* using a haem fractionation assay developed by Combrinck *et al* which measures the amount of haemozoin and exchangeable haem as a function of increased dosage of a compound. All hits were shown to cause decreasing amounts of haemozoin with increasing amounts of exchangeable haem, indicating that they targeted haemozoin formation [241-242].

1.9 Mechanism of action of antimalarials

1.9.1 Haemozoin Inhibition

Haemozoin formation is unique to the *P. falciparum* parasite and remains one of the most attractive targets for antimalarials even with *P. falciparum* resistance to known antimalarials emerging. The reason for this is that the Fe(III)PPIX concentration in parasites can reach up to 200-500 mM if not detoxified into haemozoin. This is far above levels toxic to the parasite and, being a pathway unique to the parasite, makes it a viable target [26]. The formation of haemozoin has also been shown to be unaffected by *Pf*CRT and other membrane proteins which makes haemozoin inhibitors the key to possibly eradicating malaria [210]. Researchers have made a considerable effort to understand the mechanism by which β-haematin inhibitors that have been discovered by HTS tools inhibit haemozoin formation within the parasite and subsequently cause parasite death. In 1970, CQ was known to target Fe(III)PPIX and showed only to be active during the intraerythrocytic stage of the parasite [243]. Several other theories for the mechanism of action of CQ have also included inhibition of haemoglobin proteases and inhibition of glutathione dependent degradation of haem in the parasite cytosol [76,135,244-246]. It has also been shown that CQ has the ability to bind to deoxyribonucleic acid (DNA) therefore inhibiting DNA replication and ribonucleic acid (RNA) synthesis in the parasite. This, however, only occurs at concentrations far higher than the IC_{50} against the parasite [247-249]. In support of the haemozoin inhibition hypothesis, CQ has been shown to inhibit the formation of β-haematin *in vitro*. This has led to the many studies in which researchers have attempted to verify newly discovered β-haematin inhibitors as potential haemozoin inhibitors [135,143,145,250-

[255]. While various investigations have been reported on the ability of quinoline-containing compounds to inhibit β-haeamtin formation, how they are able to achieve this in *P. falciparum* parasites and its relation to haemozoin inhibition is still inconclusive [256-259].

Initially, Dorn *et al* investigated the β-haematin inhibition activity (termed haematin polymerization activity at the time) of a group of quinoline-containing compounds using a haem "polymerization" assay that incorporates the use of carbon-14 radio-labeled haemin. Their findings revealed that β-haematin inhibition activity (βHIA) was correlated to parasite growth inhibitory activity in CQS NF54 strain parasites. Included in this correlation was a compound that they synthesized, namely the bisquinoline Ro 48-6910, which showed the best βHIA and lowest IC_{50} value [144-145] (***Figure 1-12***).

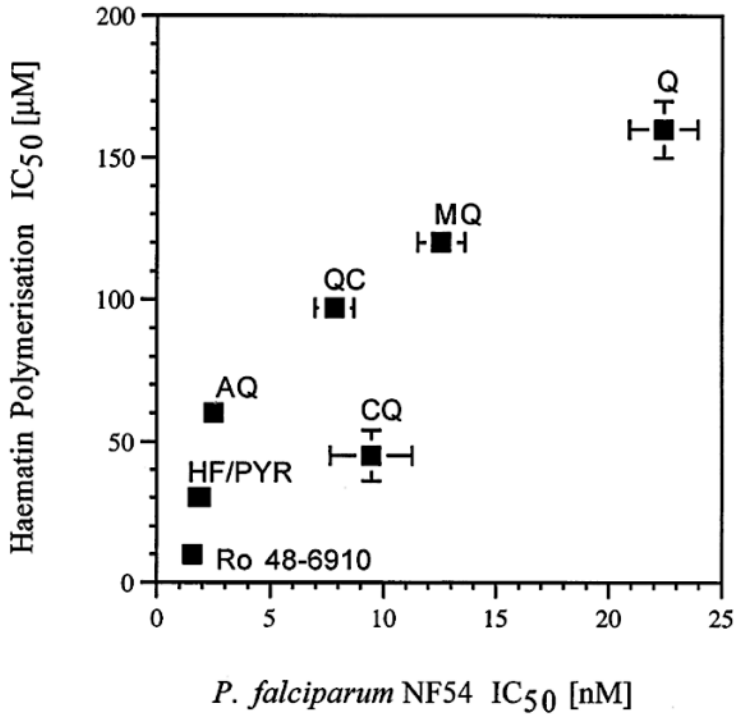

Figure 1-12: βHIA versus parasite growth inhibition activity in NF54 CQS strain *P. falciparum* parasites for various quinolone-containing compounds. Reprinted from *Biochemical pharmacology*, 55 (6), Dorn, A., Vippagunta, S.R., Matile, H., Jaquet, C., Vennerstrom, J.L. and Ridley, R.G., An assessment of drug-haematin binding as a mechanism for inhibition of haematin polymerisation by quinoline antimalarials., pp.727-736., Copyright (1998), with permission from Elsevier [144].

In a related study, βHIA values were normalized with the association constants of these compounds and haem. From this, Vippagunta *et al* illustrated a better correlation between the

βHIA values and parasite growth inhibition activities in comparison to Dorn *et al* [144,260]. It was also highlighted from this correlation that the parasite growth inhibition activity of CQ and its analogues was influenced by the binding strengths of these compounds to haem. On the other extreme, Kashula *et al* investigated the structure activity relationships (SARs) of CQ analogues, where it was observed that the chloro-group at the 7-position was important for β-haematin inhibition and therefore haemozoin inhibition. No distinct correlation between βHIA and parasite growth inhibition activity values could be obtained unless the vacuole accumulation factor (α) was included (***Figure 1-13***) [261].

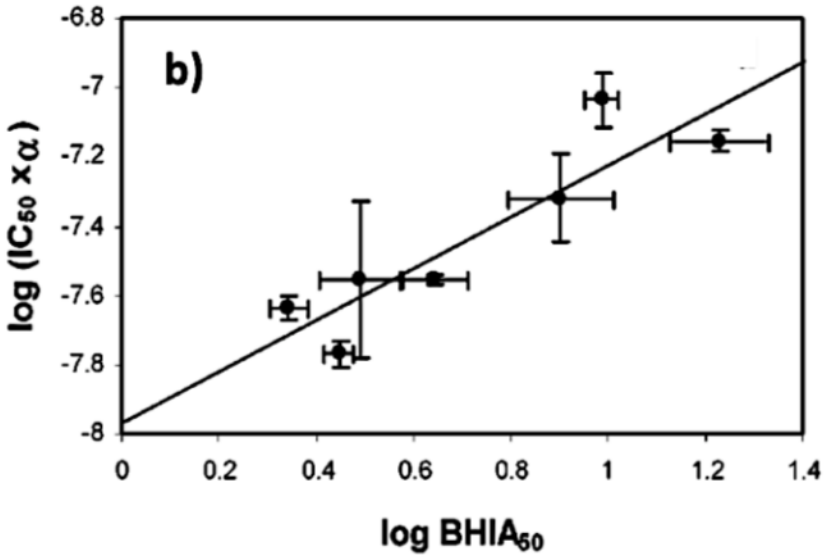

Figure 1-13: Linear correlation between log IC_{50} × α plotted as function of log βHIA_{50}. Reprinted with permission from Kaschula, C.H., Egan, T.J., Hunter, R., Basilico, N., Parapini, S., Taramelli, D., Pasini, E. and Monti, D., 2002. Structure− activity relationships in 4-aminoquinoline antiplasmodials. The role of the group at the 7-position. *Journal of medicinal chemistry*, *45*(16), pp.3531-3539. Copyright (2002) American Chemical Society [261].

A similar trend was observed by Ncokazi and Egan, who developed a fast, cheap and reliable ferrichrome method that incorporates the use of pyridine to measure β-haematin inhibition to re-examine the βHIA of the same compounds as Kashula *et al* [261-262]. In another study, Gligorijevic *et al* determined the effect of CQ on parasitized RBCs over a time period of 37 hrs using spinning disk confocal microscopy. From the reconstructed z-stacked images they were able to show that CQ inhibits the formation of haemozoin during the time points 22-29 hrs which was during the early trophozoite stage. The same was observed in both CQS and

CQR strains, however, was dependent on the concentration of CQ. Furthermore, a linear correlation between haemozoin inhibition and percentage parasite growth inhibition was observed for both CQS and CQR strain parasites. Verapamil- and CQ- treated parasites too conformed to the linear correlation (***Figure 1-14***) [205].

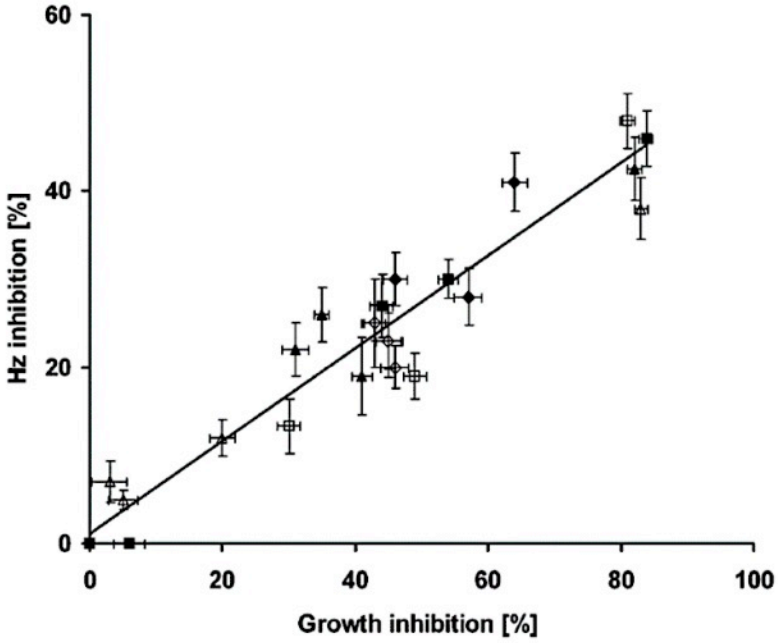

Figure 1-14: Linear correlation of percentage haemozoin inhibition as a function of parasite growth inhibition for HB3 strain parasites (empty markers) with verapamil (triangle), without verapamil (squares), combination of verapamil and CQ (diamond) and Dd2 strain parasites (filled markers). Reprinted with permission from Gligorijevic, B., McAllister, R., Urbach, J.S. and Roepe, P.D., 2006. Spinning disk confocal microscopy of live, intraerythrocytic malarial parasites. 1. Quantification of hemozoin development for drug sensitive versus resistant malaria. *Biochemistry*, *45*(41), pp.12400-12410. Copyright (2006) American Chemical Society [205].

With this knowledge, Combrink *et al* went on to be the first to demonstrate direct evidence of haemozoin inhibition in *P. falciparum* parasites. Using a haem fractionation method, they were able to measure the individual haem species within D10 strain parasites as a function of increasing doses of CQ. From the data, it was observed that CQ caused a dose-dependent increase in the levels of haem and dose-dependent decrease in the levels of haemozoin. In addition, a direct correlation between increasing haem levels and decreasing percentage parasite growth was observed (***Figure 1-15***) [242].

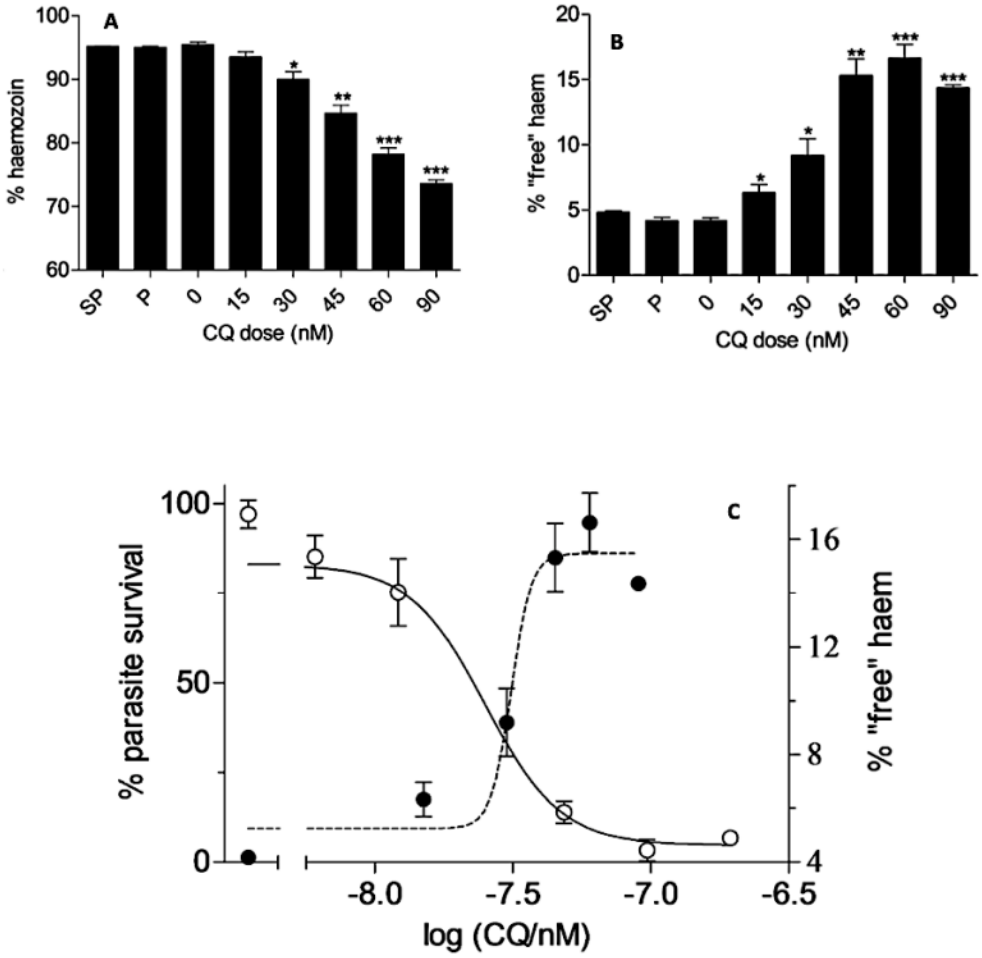

Figure 1-15: Bar graphs showing (a) decreasing haemozoin levels and (b) the increasing "free" haem levels as a function of increasing CQ doses including the negative controls, pyrimethamine (P) and sulfadoxine (SP). Decreasing percentage parasite growth with increasing percentage "free" haem is represented in (c). Statistical significance was determined using a two-tailed t-test and is indicated, relative to the control (95% confidence interval (CI)), by the asterisks where; * p = <0.05; ** p = <0.01 and *** p = <0.001 etc. Reprinted with permission from Combrinck, J.M., Mabotha, T.E., Ncokazi, K.K., Ambele, M.A., Taylor, D., Smith, P.J., Hoppe, H.C. and Egan, T.J., 2012. Insights into the role of heme in the mechanism of action of antimalarials. *ACS chemical biology*, *8*(1), pp.133-137. Copyright (2012) American Chemical Society [242].

Following this, Combrinck *et al* optimized the method into a multi-well higher throughput colorimetric plate assay. This improved throughput colorimetric plate method was adapted to a 24-well plate which was faster by 6-fold and used less starting materials (24-fold). The study

showed that while AQ behaved similarly to CQ, the antifolate pyrimethamine and atovaquine (Atov) did not [263].

1.9.2 Intracellular accumulation

Historically, it has been assumed that haemozoin inhibitors like CQ have the ability to transverse into the parasite DV by permeating through the DV membrane, accumulating and exerting their antimalarial activity. For the weak diprotic base CQ, it has been shown that CQ selectively accumulates at high concentrations and is localized to the DV rather than normal tissue [264-266]. The accumulation of CQ is also linked to its parasite growth inhibition activity [127,133,139,267]. There is strong evidence which has shown that the accumulation of CQ is dependent on two factors: (i) their physiochemical properties; and (ii) the pH-gradient between the external and internal compartments within the parasite [203,268].

As a weak base, CQ accumulation can be explained by the phenomenon of pH trapping. The pH-dependent accumulation of CQ involves both its neutral and protonated (CQH_2^{2+}) forms. Neutral CQ, being highly membrane permeable, diffuses rapidly across parasite membranes [127,269-270]. Once inside the parasite DV, neutral CQ becomes protonated at the pH of 4.8-5.2 of the DV and is not able to diffuse out in the protonated state [269,271]. By equilibrium processes, neutral CQ continues to enter the DV until both the internal and external compartments within the parasite are equal. After some time, majority of the accumulated CQ will be in the CQH_2^{2+} form in the DV (***Figure 1-16***) [272].

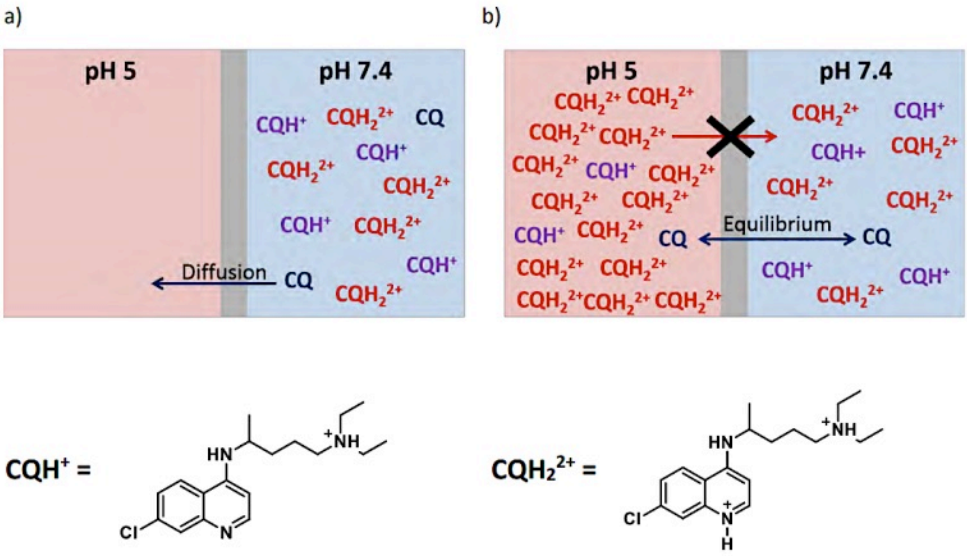

Figure 1-16: The pH-dependent process of accumulation of CQ from the external compartment (cytoplasm) of the parasite (blue) into the DV (red). Reproduced from: Wicht, K.J., 2015. Discovery of benzamides and triarylimidazoles active against Plasmodium falciparum via haemozoin inhibition: high throughput screening, synthesis and structure-activity relationships (*Doctoral dissertation*, University of Cape Town) [273].

Various studies have supported this hypothesis of pH trapping [128,274-278]. Geary *et al* used [^{3}H]-CQ to determine the concentration of CQ that accumulated in the DV as a function of time in various *P. falciparum* strains. With the knowledge that CQS and CQR strains have varying pH values pertaining to their DV, they still concluded that the accumulated CQ was primary due to pH trapping which was driven by the simultaneous process of proton (H^+) uptake and efflux across the membrane of the DV. Also, it was concluded that CQ accumulation was directly related to parasite growth inhibition activity [274]. These data agreed with the conclusions drawn by Fitch *et al* and Diribe *et al* (***Figure 1-17***) [279-280].

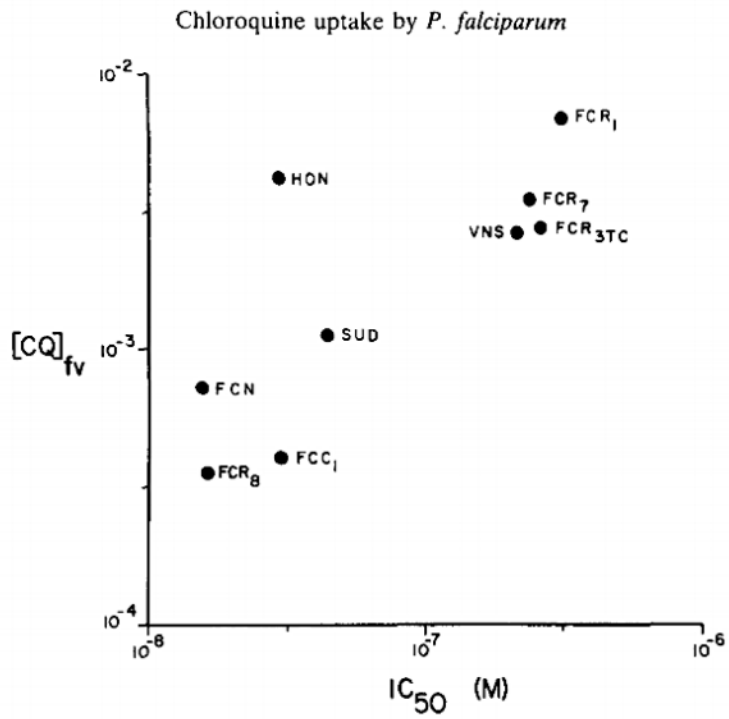

Figure 1-17: Vacuole accumulation of CQ in various *P. falciparum* parasite strains. Reprinted from: *Biochemical pharmacology*, 35 (21), Geary, T.G., Jensen, J.B. and Ginsburg, H., Uptake of [3H] chloroquine by drug-sensitive and-resistant strains of the human malaria parasite Plasmodium falciparum. pp.3805-3812., Copyright (1986), with permission from Elsevier [274].

Geary *et al* devised a model based on the weak base properties of CQ and its accumulation via pH trapping in the DV for CQS and CQR *P. falciparum* strains, where the inoculum size and medium pH were altered. From these data, it was observed that CQ does not raise the pH of the DV which showed that the weak base accumulation does not itself explain parasite growth inhibition activity as had been previously speculated [276]. This contrasted with the study by Ginsburg *et al* that showed a protonophoric effect of various haemozoin inhibitors. MQ and QN were hypothesized to exert their antimalarial effect by transporting protons across the membrane of the DV whilst CQ was claimed to cause an increase in the DV pH which could inhibit parasite growth. They also found that these compounds concentrated at much larger amounts compared to their IC_{50} values [63]. This agreed with the findings previously reported by Yayon *et al*, Krogstad *et al* and Fitch *et al* [61,128,281]. Ginsburg *et al*, however, also emphasized that this depended not only on the DV buffering ability but also on the H^+-gradient pump activity and the basal leak of protons out of the DV along the concentration gradient of these compounds [63].

Since then, a phenomenon that has been frequently used to experimentally determine the cellular accumulation ratio (CAR) of haemozoin inhibitors within *P. falciparum* parasites, is the inoculum effect. The inoculum effect is based on the fact that haemozoin inhibitors accumulate within the DV of the parasite via pH trapping and overall cellular accumulation can be experimentally determined by measuring the change in IC_{50} value as a function of the inoculum size. This inoculum size has been defined as the product of percentage parasitemia and haematocrit. The relative change in the IC_{50} value with changing inoculum sizes has been reported to be linearly correlated, where the absolute IC_{50} at inoculum size 0 can be determined by the extrapolation of the line to the y-intercept. From this linear correlation, the experimental cellular accumulation ratios can be determined, where, ***Figure 1-18*** illustrates an example of this [208,269,276].

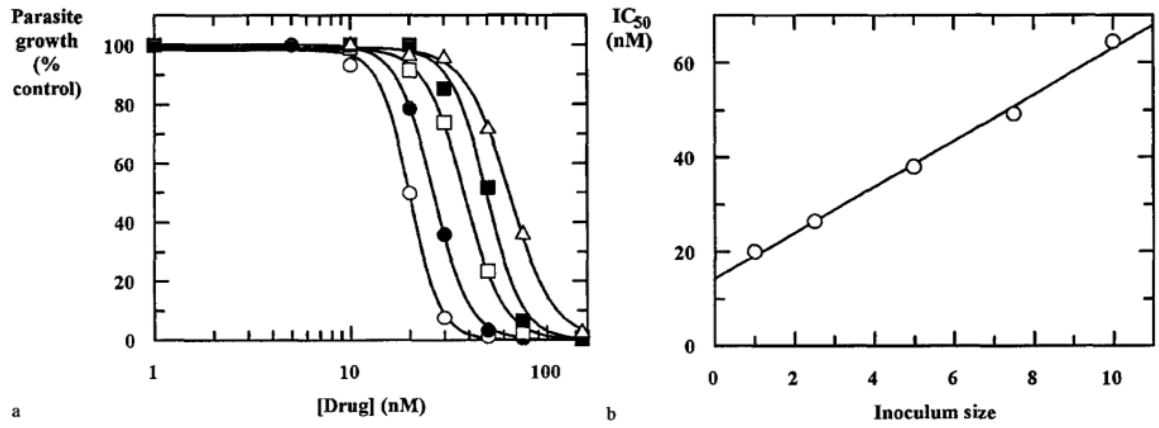

Figure 1-18: An example of measuring the inoculum effect in 3D7 strain cultures that have been treated with an AQ analogue, where (a) represents the change in percentage parasite growth inhibition with increasing inoculum size, and (b) increasing IC_{50} values with increasing inoculum size. Reprinted from: *Biochemical pharmacology*, 52 (5), Hawley, S.R., Bray, P.G., O'Neill, P.M., Park, B.K. and Ward, S.A., The role of drug accumulation in 4-aminoquinoline antimalarial potency: the influence of structural substitution and physicochemical properties. pp.723-733., Copyright (1996), with permission from Elsevier [269].

In relation to the inoculum effect, Hawley *et al* determined the CAR values for various AQ analogues, where they highlighted various structural features that influenced both accumulation and activity of quinoline-containing compounds like AQ. They deduced from their findings that this was due to the presence of specific binding sites for quinoline-containing compounds within the parasite. They showed that out of all the AQ analogues, a *N*-tertbutyl

substituted analogue of AQ (TBQ) had the highest CAR value of 79,456 compared to AQ with a CAR value of 8955 in 3D7 strain parasites [269]. Similarly, Wicht *et al* used the inoculum effect with an antiplasmodial assay to determine the CAR values CQ and AQ of 105,343 and 98,024 in D10 strain parasites, respectively (***Figure 1-19***) [273].

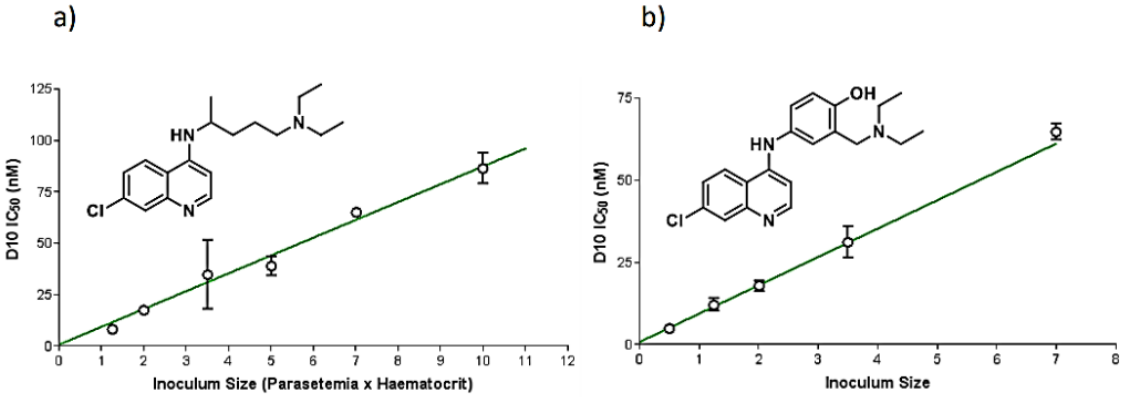

Figure 1-19: Inoculum effect for CQ and AQ. Reproduced from: Wicht, K.J., 2015. Discovery of benzamides and triarylimidazoles active against Plasmodium falciparum via haemozoin inhibition: high throughput screening, synthesis and structure-activity relationships (*Doctoral dissertation*, University of Cape Town) [273].

In 1998, Wünsch *et al* first provided evidence that the reduced uptake of CQ in CQR parasites could be accounted for by the alterations of the sodium-hydrogen (Na^+/H^+) exchanger which was thought to be responsible for the transport CQ through the parasite [282]. This was later disproved by Bray *et al*, who showed that the specificity, accumulation and parasite growth inhibition activity are dependent on the saturable equilibrium binding of CQ and Fe(III)PPIX [208]. A year later, Bray *et al* used ^{3}H-labelled CQ to measure the saturable uptake of CQ in *P. falciparum* parasites and the binding of CQ to Fe(III)PPIX. These data showed that CQ accumulation is in fact dependent on the binding of CQ to Fe(III)PPIX rather than the sodium-hydrogen (Na^+/H^+) exchanger (***Figure 1-20***) [283].

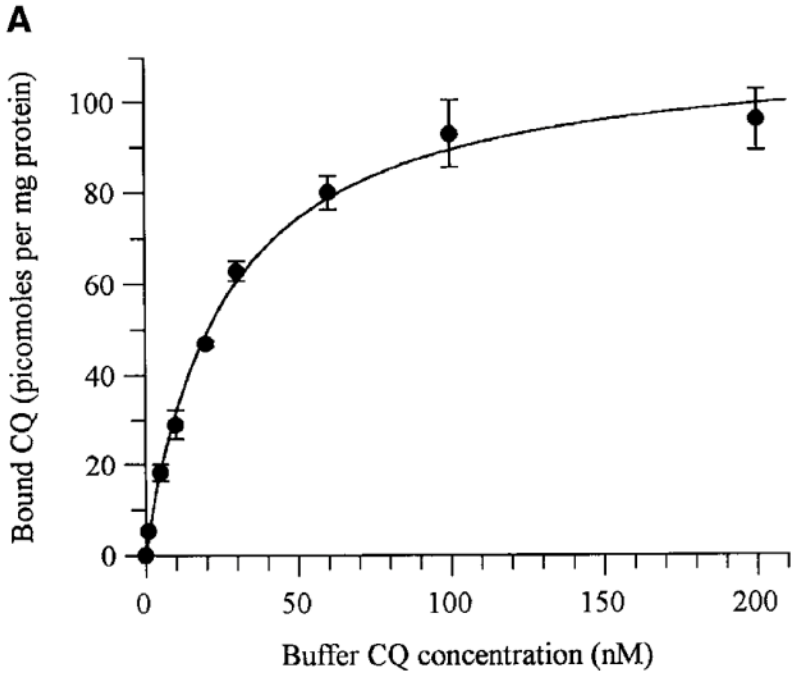

Figure 1-20: Cell-free system of CQ binding to Fe(III)PPIX. Republished with permission by the Journal of Cell Biology, from Bray, P.G., Janneh, O., Raynes, K.J., Mungthin, M., Ginsburg, H. and Ward, S.A., 1999. Cellular uptake of chloroquine is dependent on binding to ferriprotoporphyrin IX and is independent of NHE activity in *Plasmodium falciparum*. 145 (2), pp.363-376.; permission conveyed through Copyright Clearance Centre, Inc [283].

Consequently, accurately determining whether a wide range of haemozoin inhibitors can accumulate might be beneficial to understanding the mechanism of these haemozoin inhibitors.

1.10 Effects on Fe(III)PPIX distribution and localization of antimalarials

With the knowledge that quinoline-containing compounds accumulate to high concentrations in the parasite DV, it is appropriate to discuss their effect on the distribution of Fe(III)PPIX within the parasite. Lipophilic Fe(III)PPIX, released as a consequence of the digestion of haemoglobin during the trophozoite stage, has been known to cause a number of toxic effects in the parasite at micromolar concentrations. These effects include increased osmotic stress in the DV which can lead to interrupted membrane function and destabilization. This further causes lysis of parasite membranes and in extreme cases even the host RBC, eventually causing the parasite to die [76,284-285]. To avoid the toxic effect of haem, the parasite is able to sequester large amounts, more than 95%, of toxic Fe(III)PPIX into haemozoin which was proven in 2002

to be the primary fate of Fe(III)PPIX [286-287]. From this, toxic Fe(III)PPIX has become of a considerable interest for not only understanding the chemical process that occur within the parasites DV and the effect of haemozoin targeting antimalarials, but also for the development of new haemozoin targeting antimalarials [287]. The effect of haemozoin targeting antimalarials on the distribution of Fe(III)PPIX associated Fe and other major haem iron species within the parasite have been previously explored using various spectroscopic techniques that have proven to be useful in both identifying the distribution of Fe(III)PPIX associated iron with other haem iron species and its association with the localization of antimalarial compounds within parasites [72,242,251].

In 2002, Egan *et al* was the first to used electron spectroscopic imaging (ESI) with TEM to identify that the majority of the Fe(III)PPIX associated Fe signal within parasites was attributed to the haemozoin crystals whilst negligible Fe(III)PPIX associated Fe was observed in the rest of the parasite. Additionally, it was observed that small amounts Fe(III)PPIX associated Fe was observed in the RBC cytoplasm coinciding with haemoglobin. From these data, together with Mössbauer spectroscopy and wet chemical colorimetric Fe measurements, they were able to conclude that majority of the Fe(III)PPIX associated Fe (95%) was attributed to haemozoin with the remaining 5% suggested to be available for antimalarials to target [287]. These data, however, disproved earlier reports by Ginsburg *et al* and Loria *et al*, who suggested that more than 70% of the Fe(III)PPIX associated Fe was located in either the parasite cytosol or the parasite DV [244-245]. More recently, Combrinck *et al* used TEM and ESI coupled to electron energy-loss spectroscopy (EELS) to directly observe the effect of CQ on the distribution of haem as a consequence of haemozoin inhibition in CQS strain parasites that were prepared using a chemical fixation method. In accordance with the previous study mentioned above, TEM images revealed that in control parasites the haemozoin was localized to the parasite DV, where the EELS images showed that majority of the Fe signal was attributed to the haemozoin crystals. It was also shown that the rest of the parasite DV showed little or no Fe signal compared to the host RBC. In comparison to the control parasites, CQ treated parasites showed a similar TEM image with the haemozoin crystals inside the DV. However, the EELS revealed that upon treatment with 30 nM CQ the Fe signal increased in the parasite whilst the Fe signal associated with the haemozoin crystals was diminished (***Figure 1-21***) [242].

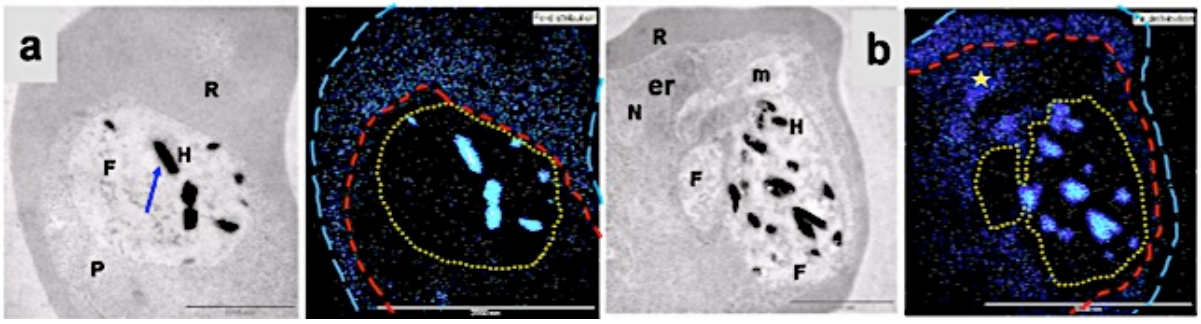

Figure 1-21: TEM images with corresponding EELS images measured with ESI for (a) untreated and (b) CQ-treated *P. falciparum* parasites. Reprinted with permission from Combrinck, J.M., Mabotha, T.E., Ncokazi, K.K., Ambele, M.A., Taylor, D., Smith, P.J., Hoppe, H.C. and Egan, T.J., 2012. Insights into the role of heme in the mechanism of action of antimalarials. *ACS chemical biology*, *8*(1), pp.133-137. Copyright (2012) American Chemical Society [242].

The localization of quinoline-containing compounds has also been explored. In 2012, Bohorquez *et al* used fluorescence microscopy to determine the localization of QN at a subcellular level in CQS and CQR strain parasites, 3D7 and Dd2 respectively. First, they observed with 2D-microscopy and DIC images that QN colocalized with haemozoin. In addition, the fluorescence attributed to QN was observed to appear in the DV as early as one hour into the experiment and was consistent for both parasite strains (***Figure 1-22***) [288].

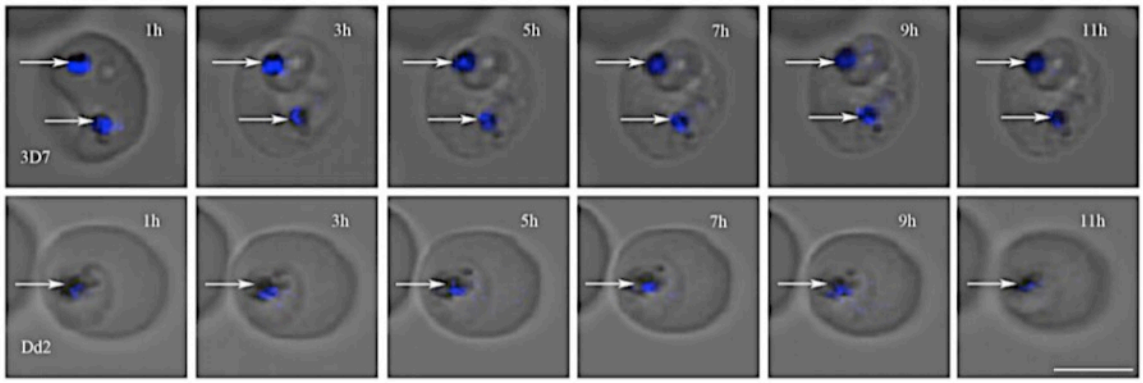

Figure 1-22: Fluorescent microscope images of QN-treated *P. falciparum* parasites over an 11 hr period in both CQS and CQR strain parasites, 3D7 and Dd2 respectively. The haemozoin crystals in the parasite DV are indicated by the white arrows. All images have a scale bar of 5 μm. Reproduced with permission by *Malaria journal*, from Bohórquez, E.B., Chua, M. and Meshnick, S.R., 2012. Quinine localizes to a non-acidic compartment within the food vacuole of the malaria parasite Plasmodium falciparum. , *11*(1), p.350 [288].

To further characterize this QN and haemozoin co-localization, they used a lysoTracker Red DND-99 fluorescent dye to stain the parasite DV and DRAQ5 fluorescent probe that is specific to DNA [289]. From 3D reconstructed z-stacked fluorescent images, they observed that QN did not co-localize with DRAQ5 but rather in an adjacent but separate compartment to the lysoTracker Red. From this, they were not able to definitively state whether QN and haemozoin co-localize as a limitation to this method is that haemozoin cannot be viewed [288]. In another study, Dubar *et al*, used the chlorine (Cl) atom as a tracer for label-free FQ and CQ in H3B strain parasites using ESI to determine their co-localization with haemozoin in the DV. From the results they observed that for untreated iRBCs the DV have a very low Cl signal and a high Cl signal in the rest of the iRBC. For FQ- and RQ-treated parasites, a very high Cl signal was observed in the DV of the parasite, where, they suggested this to be indicative of co-localization with haemozoin. On the other hand, for CQ, the Cl signal was distributed equally throughout the iRBC including the DV, thus giving inconclusive results as to whether it co-localized with haemozoin. From here, they concluded that Cl was not suitable for determining the co-localization of CQ and haemozoin [290]. However, from the distinctively different results that were observed for FQ and RQ compared to CQ, they did suggest that it could be related to the fact that FQ and RQ accumulate at a much faster rate than CQ [251,283]. In a related study, Kapishnikov *et al* showed that bromine (Br) analogue of CQ accumulates at a sub-millimolar concentration and caps haemozoin crystals in the parasite DV using X-ray microscopy. From this, they measured that this bromoquine (BrQ) capping was sufficient enough to disrupt the detoxification process of Fe(III)PPIX and suggested that it could possibly bind to Fe(III)PPIX and form a complex (***Figure 1-23***) [291].

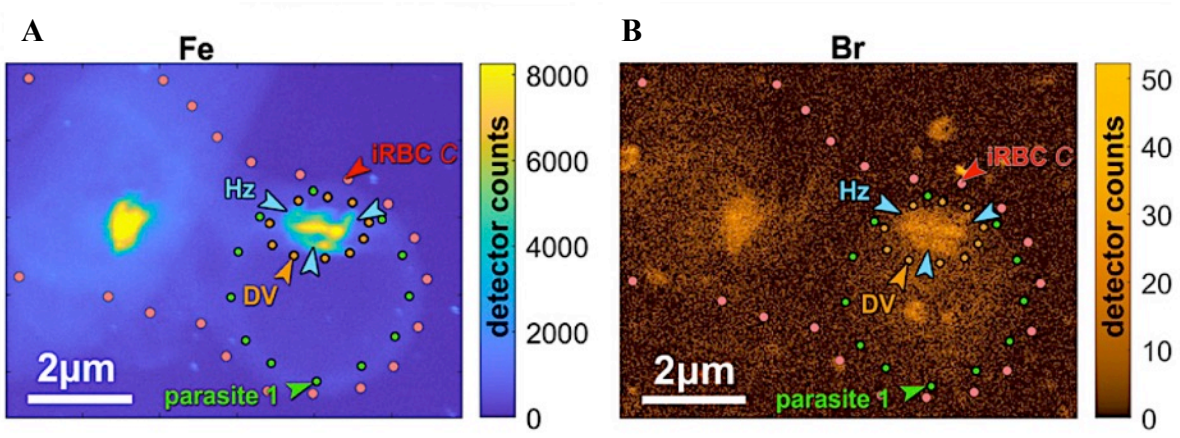

Figure 1-23: X-ray fluorescence maps represented for (a) Fe and (b) Br in *P. falciparum* iRBCs. The BrQ coverage was calculated to be 7 ± 2%. The intensity scale factor $I_{Fe}/I_{Br} \sim 272$ with an estimated uncertainty factor of 15%. Reprinted from Kapishnikov, S., Staalsø, T., Yang, Y., Lee, J., Pérez-Berná, A.J., Pereiro, E., Werner, S., Guttmann, P., Leiserowitz, L. and Als-Nielsen, J., Mode of action of quinoline antimalarial drugs in red blood cells infected by Plasmodium falciparum revealed in vivo. *Proceedings of the National Academy of Sciences*, *116*(46), pp.22946-22952. Copyright (2019) National Academy of Sciences [291].

1.11 Fe(III)PPIX-inhibitor complexes

One theory that has long been proposed for the mode of action of antimalarial compounds is their ability to bind with Fe(III)PPIX, forming a Fe(III)PPIX-inhibitor complex. This proposed theory stems from the fact that quinoline-containing antimalarials are able to accumulate in the parasite DV which is dependent on their ability to bind to monomeric or dimeric Fe(III)PPIX and form a Fe(III)PPIX-quinoline complex via π-π interactions [292-294]. A hypothesis is that these complexes form immediately after the digestion of haemoglobin and release of toxic Fe(III)PPIX but before this toxic Fe(III)PPIX is partitioned into neutral lipid bodies and converted into haemozoin [295]. Moreover, it is thought that these complexes are able to interfere with the function of parasite membranes and subsequently lead to parasite death by causing a build-up of toxic Fe(III)PPIX [145,283,296-297]. In other cases, it has been found that both toxic Fe(III)PPIX and these complexes are able to cause potassium leaks in normal RBCs [298-299].

Several spectroscopic studies have investigated the interaction between antimalarials and Fe(III)PPIX in solution. Blauer *et al* used circular dichroism (CD) and visible light-absorbance spectra to investigate the Fe(III)PPIX-QN complex at a temperature between 26 °C and 27 °C and pH values of 7.4 and 11.5, respectively. They observed from CD titrations that an optically

active Fe(III)PPIX-QN complex was comprised of QN and Fe(III)PPIX in a 1:1 mole ratio at pH 7.4 [300]. A similar effect with CQ on parasite derived Fe(III)PPIX was observed by Balasubramanian *et al* [301]. Fe-Mössbauer spectroscopy has also been used to study the association of CQ, QN, quinidine (QD) and AQ to Fe(III)PPIX as complexes [61,302-304].

Presumably, one would also expect that if these complexes are responsible for parasite death, then they would be tightly bound to Fe(III)PPIX and soluble in order to result in the accumulation of Fe(III)PPIX. This then causes an increased DV osmotic pressure which in turn results in the rupturing of the parasite DV thus killing the parasite [305-307]. In this regard, Dodean *et al* investigated the binding affinities with the assumption that these inhibitors bind in a 1:1 ratio with Fe(III)PPIX. They used UV spectroscopy to monitor the effects of different concentrations of a fluorinated xanthone compound on the intensity and shifts of the Soret band. From this, the fluorine-containing xanthone compounds showed a higher binding affinity to Fe(III)PPIX, with larger K_a values than CQ and a non-fluorinated compound [308-309]. Related to this, is the solubility of these complexes, where the formation of these complexes may be influenced by a pH–dependent solubility [209]. However, up until 2008 no detailed structure of any of these complexes had been presented. It was only in 2008 that de Villiers *et al* used single crystal X-ray diffraction to determine the first crystal structure of a 1:1 complex of the antimalarial HF and Fe(III)PPIX. From the crystal structure, it was observed that HF was able to bind to Fe(III)PPIX by coordinating to the Fe(III) center by a Fe-O bond from its deprotonated alcohol group. In addition, HF was able to π-stack over the haem porphyrin through its phenanthrene ring [124]. A few years later, de Villiers *et al* also published the structures for the Fe(III)PPIX complexes of QN and QD. From these complexes, it was apparent that these compounds bound Fe(III)PPIX in a similar manner to HF (***Figure 1-24***) [310].

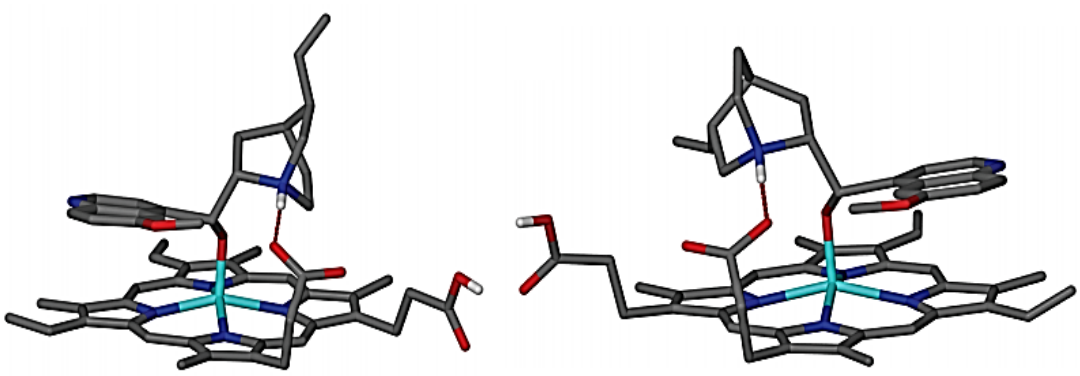

***Figure 1-24*:** The asymmetrical complex structures of QN and QD with Fe(III)PPIX. Each atom has been colour coded; C, gray; H, white; N, blue; O, red; and Fe, cyan with hydrogen bonds indicated with broad dashed lines. Reprinted with permission from de Villiers, K.A., Gildenhuys, J. and le Roex, T., 2012. Iron (III) protoporphyrin IX complexes of the antimalarial cinchona alkaloids quinine and quinidine. *ACS chemical biology*, *7*(4), pp.666-671. Copyright (2012) American Chemical Society [310].

A method that has been well documented and used to investigate Fe(III)PPIX complexes, including Fe(III)PPIX-inhibitor complexes, in *P. falciparum* parasites, is Raman spectroscopy [311-313]. Raman spectroscopy, a fast, label-free and non-invasive technique, is both highly sensitive and selective which makes it suitable for the analysis of biological species such as Fe(III)PPIX complexes in parasites [313-315]. Fe(III)PPIX complexes tend to cause strong Resonance Enhanced Raman Scattering (RERS) when excited at various excitation wavelengths. This results from the highly symmetrical and chromophoric structure of Fe(III)PPIX [316]. RERS can be explained by two terms, type A and B. Type A is dependent on and can be explained by the Frank-Condon principle. This principle is based on the significant overlap of two vibrational wave functions which facilitates an electronic transition in totally symmetric systems. On the other hand, type B can be explained by the mixing of vibrations, where, one transition can be enhanced by the more intense neighboring transition [317-318].

Initially, Ong *et al* used resonance Raman spectroscopy to show that haemozoin could be identified in *P. Berghi* infected parasites [319]. In a similar study, Wood *et al* showed that haemozoin and haemoglobin could be identified in *P. falciparum* parasites using a Raman microscope with an excitation source of 632.8 nm. The spectrum of β-haematin was also recorded and observed to be similar to that of the spectrum for haemozoin, as illustrated in ***Figure 1-25*** [320].

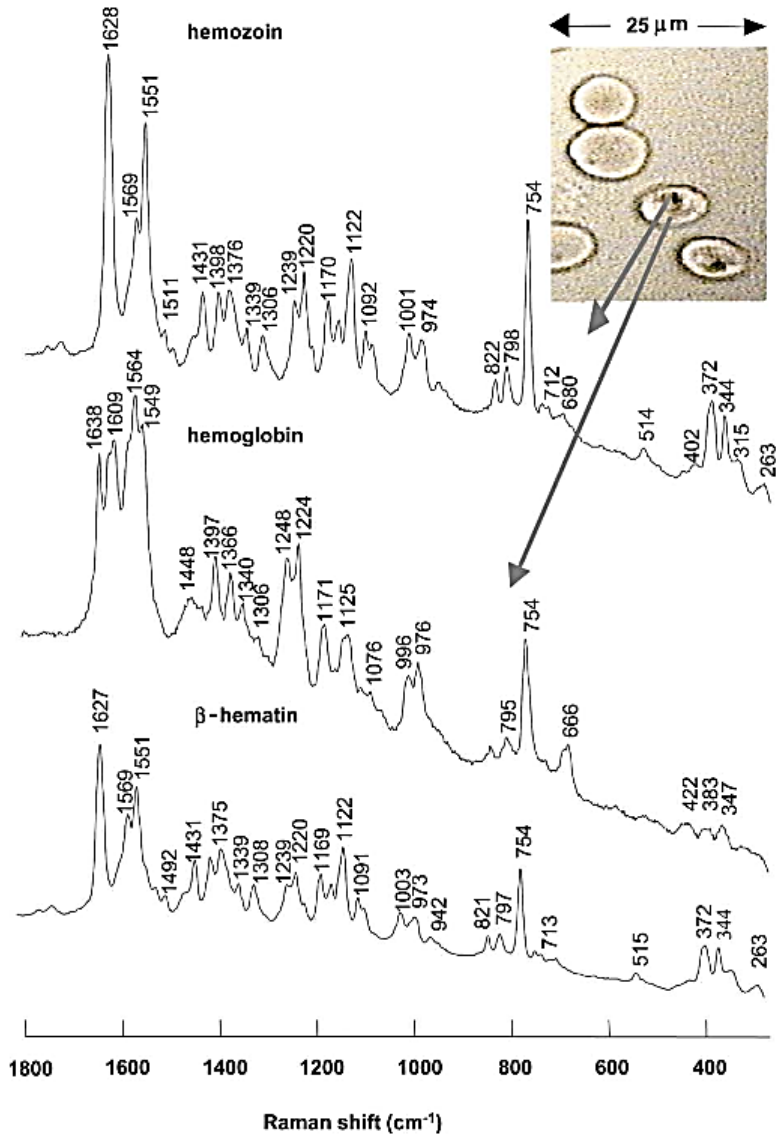

Figure 1-25: Raman spectra recorded for haemozoin and haemoglobin at the late trophozoite stage shown in the inserted photomicrograph. The regions where the corresponding spectra were recorded are indicated by the grey arrows. For comparison, the spectrum of β-haematin was included. Image reprinted with permission from Wiley & Sons for Wood, B.R., Langford, S.J., Cooke, B.M., Glenister, F.K., Lim, J. and McNaughton, D., 2003. Raman imaging of hemozoin within the food vacuole of Plasmodium falciparum trophozoites. *FEBS letters*, *554*(3), pp.247-252. Copyright (2003) [320].

Later, Frosch *et al* used polarization-resolved resonance Raman spectroscopy with an excitation wavelength of 514 nm to investigate the interaction of haematin and CQ in solution. From the spectra, small wavenumber shifts of 2 cm^{-1} were observed and thought to be indicative of the formation of a non-covalent interaction between Fe(III)PPIX-CQ. With this

they also suggested that the spectra of both haematin and the Fe(III)PPIX-CQ complex were similar [311]. Three years later, Frosch *et al* used UV resonance Raman spectroscopy to investigate CQ under conditions that resembled the parasite. With the recorded Raman spectra and density functional theory (DFT) calculations they concluded that CQ was capable of forming a π-π interaction with haemozoin [312]. This agreed with earlier studies with Near IR surface enhanced Raman Spectroscopy measurements [321]. A year later, Webster *et al* used near infrared Raman microscopy to investigate the effect of CQ on haemozoin in iRBCs using a 782 nm excitation source. Initially, they recorded the spectra of the μ-oxo dimer of haematin, haematin and haemozoin from a bright-field image of *P. falciparum* iRBCs for the spectral region of 1700-500 cm^{-1}. What is worth noting, was that the haemozoin spectrum had a poorer signal-to-noise ratio compared to the haemozoin spectrum reported by Wood *et al* at a lower excitation wavelength (***Figure 1-26***) [322]. Then, they recorded the spectra of untreated iRBCs, CQ-treated iRBCs and CQ itself in the same spectral region as the previous samples. They observed a reduction in the intensity of certain bands in CQ-treated iRBCs compared to untreated iRBCs, which are illustrated in ***Figure 1-27*** [322].

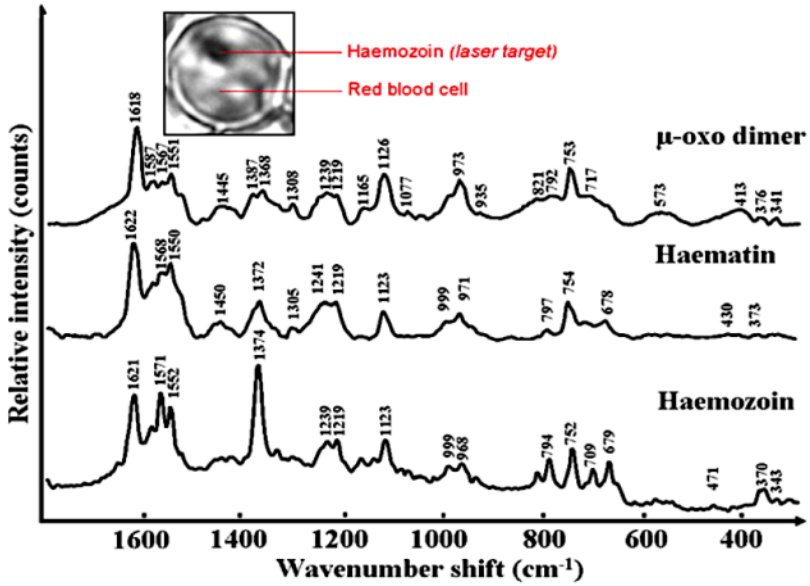

Figure 1-26: Raman spectra of dried samples of the μ-oxo dimer haematin, haematin and haemozoin in live *P. falciparum* iRBCs (inset) at an excitation of 782 nm. The Raman spectra for haemozoin was collected form the dark spot in the image. Reprinted from: *FEBS letters*, 582 (7), Webster, G.T., Tilley, L., Deed, S., McNaughton, D. and Wood, B.R., Resonance Raman spectroscopy can detect structural changes in haemozoin (malaria pigment) following incubation with chloroquine in infected erythrocytes. pp.1087-1092. Copyright (2008), with permission from Elsevier [322].

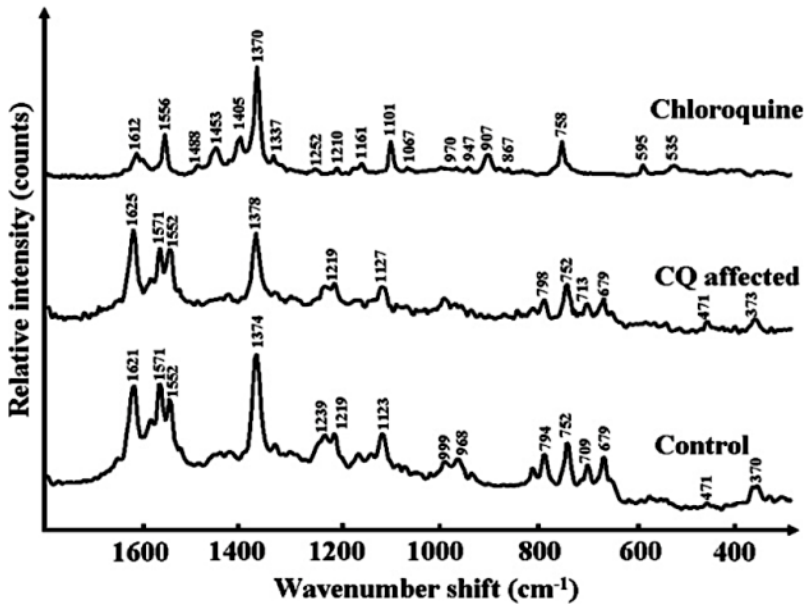

Figure 1-27: Raman spectra of dried CQ samples in comparison to untreated and CQ-treated iRBC samples, analyzed with an excitation wavelength of 782 nm. Reprinted from: *FEBS letters*, 582 (7), Webster, G.T., Tilley, L., Deed, S., McNaughton, D. and Wood, B.R., Resonance Raman spectroscopy can detect structural changes in haemozoin (malaria pigment) following incubation with chloroquine in infected erythrocytes. pp.1087-1092. Copyright (2008), with permission from Elsevier [322].

Small shifts in bands were also observed in this region which was thought to be indicative of molecular changes in the haemozoin environment from drug interaction. To validate these small wavenumber shifts they used a multivariate data analysis tool, namely principle component analysis (PCA). PCA is a commonly used in conjunction with Raman spectroscopy to identify variables or descriptors within Raman spectra. By plotting the individual repeat spectra for a sample, a PCA plot of a chosen number of principle component axes can be used to both reduce the noise factor and re-express the data in a more simplified but detailed manner [323-324]. For the spectral region of 500-1700 cm^{-1}, a differential spectrum of the average spectra for untreated iRBCs and CQ-treated iRBCs (haemozoin) was constructed. From this spectrum, a second derivative function was applied along the principle component 1 (PC1) axis. A PCA plot was constructed and illustrated that there was a significant difference between the spectra for untreated iRBCs and haemozoin in CQ-treated iRBCs along PC1 (***Figure 1-28***) [322].

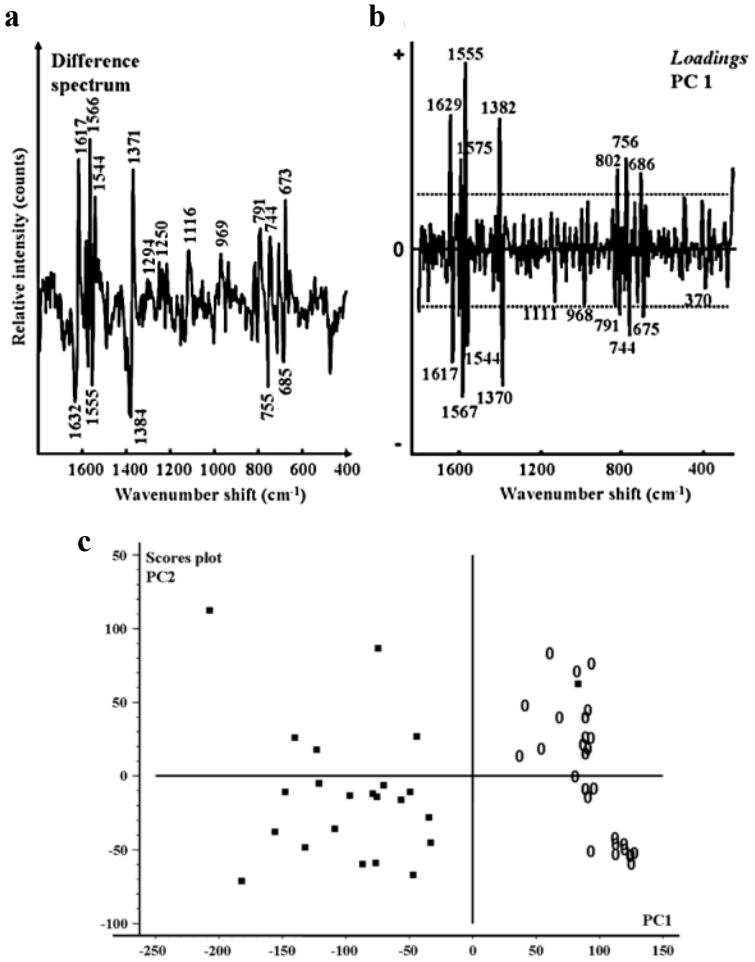

Figure 1-28: Graphs representing (a) differential spectrum of the averaged spectra for both untreated iRBCs and haemozoin in CQ-treated iRBCs, (b) second derivative PCA loadings plot for both untreated iRBCs and haemozoin in CQ-treated iRBCs, and, (c) PCA plot of untreated (open circles) versus CQ-treated iRBCs (squares) which were taken from the corresponding loadings plot along the PC1 axis. Majority of the variance in the data lies along PC1 which was applicable for this study. Reprinted from: *FEBS letters*, 582 (7), Webster, G.T., Tilley, L., Deed, S., McNaughton, D. and Wood, B.R., Resonance Raman spectroscopy can detect structural changes in haemozoin (malaria pigment) following incubation with chloroquine in infected erythrocytes. pp.1087-1092. Copyright (2008), with permission from Elsevier [322].

More recently, Kozicki *et al* investigated the effect of CQ in iRBCs. From the resulting spectra, they observed reductions in the band intensities for the spectra regions of 3300-2600 cm^{-1} and 1700-1300 cm^{-1} upon treatment with CQ (***Figure 1-29***). In addition, PCA plots identified that there was a significant difference in oxygenated (oxy) and deoxygenated (deoxy) haemoglobin in CQ treated and untreated parasites. However, they observed that there was no significant

difference in the spectra of haemozoin in both CQ-treated and untreated parasites which disagreed with the findings by Webster *et al* [322,325].

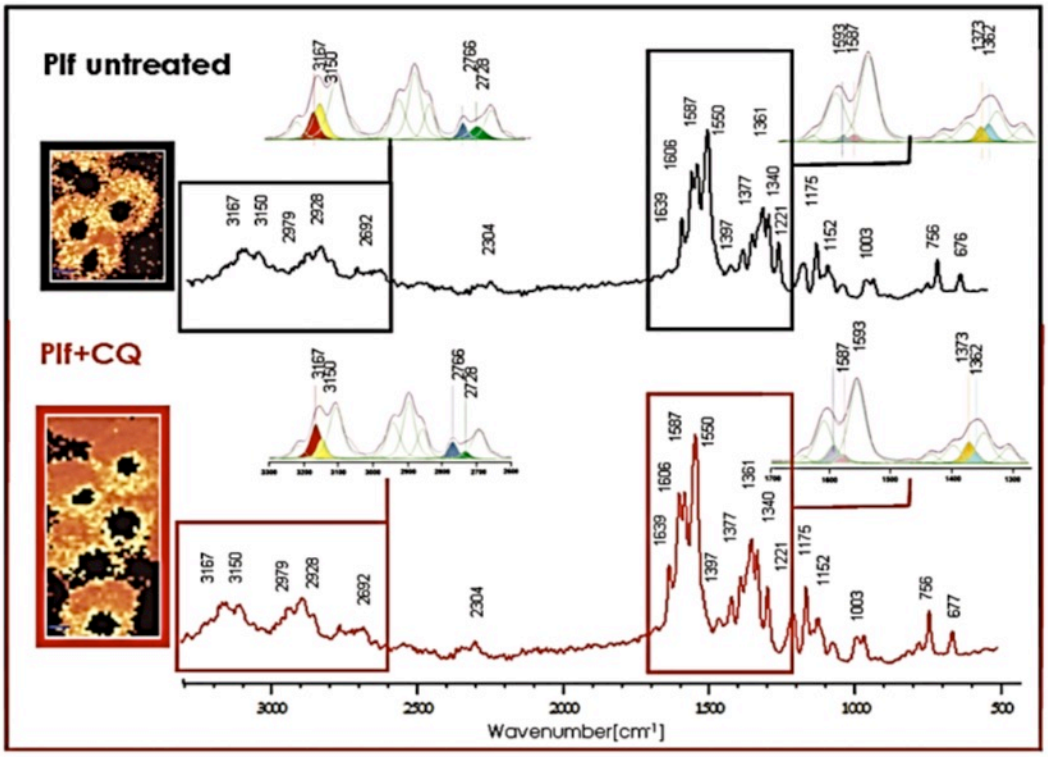

Figure 1-29: Recorded Raman spectra for both untreated and CQ-treated *P. falciparum* iRBCs using a 532 nm excitation wavelength. The insets show both untreated and CQ-treated iRBCs for the spectral ranges, 3300-2600 cm^{-1} and 1700-1300 cm^{-1}. Reproduced with permission from Kozicki, M., Creek, D.J., Sexton, A., Morahan, B.J., Wesełucha-Birczyńska, A. and Wood, B.R., 2015. An attenuated total reflection (ATR) and Raman spectroscopic investigation into the effects of chloroquine on Plasmodium falciparum-infected red blood cells. *Analyst*, *140*(7), pp.2236-2246. Copyright (2015) The Royal Society of Chemistry [325].

1.12 Key remaining questions

The morbidity and mortality rates associated to the virulent *P. falciparum* malaria have decreased dramatically over recent years including the effects on young children despite the wide-spread problem of *P. falciparum* resistant parasites. This has been achieved through the implementation of control measures such as insecticide-treated bed nets and ACTs. On-going HTS searches for new parasite growth inhibitors including β-haematin inhibitors could lead to

potentially new and effective antimalarial drugs, despite the remaining question of the mechanism of haemozoin inhibition of these β-haematin inhibitors in *P. falciparum* parasites. Recently, direct evidence of the behavior of CQ and related quinoline-containing compounds has been published in which these compounds were shown to inhibit haemozoin formation. This was evident from the decreasing haemozoin amounts and increasing exchangeable haem amounts that resulted in the simultaneous inhibition of parasite growth [263,242]. Spectroscopic techniques have also been quite useful in determining the effect and localization of haemozoin inhibitors in relation to haem within the parasite. This haem distribution effect has been suggested to be as a result of the formation of possible Fe(III)PPIX-inhibitor complexes that could be responsible for oxidative stress, membrane damage and eventually parasite death [326-327]. However, this suggestion has not yet been conclusively identified within *P. falciparum* parasites. In that regard, the application of these previously described methods could not only help in understanding the exact mode of action of these β-haematin inhibitors but also provide the necessary determinants for the development of a mathematical haem-pathway model for future development of new antimalarials.

1.13 Aims and objectives

1.13.1 Aim

To investigate the behavior of β-haematin inhibitors and their derivatives in the inhibition of cellular haemozoin formation for the development of a haem pathway model.

1.13.2 Objectives

The following objectives were used to achieve the above aim;

- To investigate ten selected β-haematin inhibitors, measuring their inhibition of the formation of haemozoin, inhibition of parasite growth and accumulation within CQS *P. falciparum* parasites.
- To use spectroscopic techniques to investigate the possible co-localization of Fe(III)PPIX and a β-haematin inhibitor in the parasite DV and further investigation of the possible formation of a Fe(III)PPIX-inhibitor complex.

- To investigate the concentrations of four major haemoglobin digesting proteases and the amount of haemoglobin, exchangeable haem and haemozoin throughout the blood stage of *P. falciparum* parasites for the future development and validation of a haem pathway model.

2

General materials, instrumentation and experimental methods

2.1 General Materials

The materials that were commercially obtained (AR or higher purity grade) and corresponding suppliers are listed below in tables; ***Table 2-1*** to ***Table 2-6***. The materials were used without further purification or sterilization unless otherwise stated in the sample preparation. They are listed in order of the methods first performed where some of the materials were used in multiple methods and those that were purchased from different suppliers are listed separately. Lasec, Millipore, Merck and Becton Dickinson (BD) Science were specific suppliers for the sterile consumables used throughout this study.

De-ionized Millipore® Direct-Q water (d.H_2O) was used to prepare all solvent solutions throughout this study. Test compounds that showed poor solubility in relevant solvents were sonicated and heated in 100% dimethyl sulfoxide (DMSO) for a fixed period of 5 min. Single-channel micropipettes and multichannel micropipettes (Eppendorf) were used for sample dilutions, titrations and aliquoting. For all solutions pH was measured and adjusted using a calibrated Jenway 3510 benchtop pH meter fitted with a 924 007 glass electrode. Calibration of the pH meter was carried out with standard phosphate buffer solutions (PBS) of pH 4.00 and 7.00 before performing measurements.

Table 2-1**:** List of materials for the preparation of controls and β-haematin inhibiting test compounds

Controls and β-haematin inhibiting test compounds	
Material	**Supplier**
DMSO	Sigma-Aldrich/Merck

***Table 2-2*:** List of materials for cell culturing of *P. falciparum* parasites.

Cell culturing of *P. falciparum* parasites	
Material	**Supplier**
O^+ Human Red Blood Cells (RBCs)	Blood Bank (Groote Schuur Hospital)
RPMI-1640 Culture medium powder (with glutamine but excluding sodium bicarbonate (R6504))	Sigma Life Science
Phosphate buffer tablets	Sigma Life Science
D-sorbitol	Sigma-Aldrich/Merck
Hypoxanthine	Sigma Life Science
Albumax II	Gibco
Sodium bicarbonate ($NaHCO_3$)	Sigma Life Science
Giemsa's azur eosin methylene blue solution	Sigma-Aldrich/Merck
Methanol (MeOH)	KIMIX
Microscope immersion oil	Sigma-Aldrich/Merck
D -(+)- Glucose	Sigma Life Science
Gentamicin	Sigma Life Science
N-2-[hydroxyethyl]piperazine-*N*′-2-[ethanesulfonic acid] (HEPES) buffer	Sigma Life Science
Sodium L-lactate (≥ 98%)	Sigma Life Science
Sodium chloride (NaCl)	Sigma-Aldrich/Merck

Table 2-3: List of materials used for parasite antiplasmodial p-LDH assay.

Parasite antiplasmodial p-LDH Assay	
Material	**Supplier**
Triton X-100	Thermofisher
Nitro blue tetrazolium chloride (NBT)	Sigma-Aldrich/Merck
Phenazine ethosulfate (≥ 95%)	Sigma-Aldrich/Merck
3-Acetylpyridine adenine dinucleotide (≥ 85% APAD)	Sigma-Aldrich/Merck
Tris (hydroxymethyl) aminomethane buffer (Trizma® base ≥ 99%)	Sigma-Aldrich/Merck
Calcium L-lactate hydrate	Sigma Life Science
Hydrochloric acid (HCl) 32% wt.	Sigma-Aldrich/Merck

Table 2-4: Materials used for parasite isolation, fixation and cell counting.

Parasite isolation, fixation and cell counting	
Material	**Supplier**
Saponin (1%)	Sigma-Aldrich/Merck
Glutaraldehyde (50%)	Sigma-Aldrich/Merck
BD Trucount^{TM} beads	BD and Company
SYBR green ® I nucleic acid gel stain	Sigma-Aldrich/Merck
DNAse	Sigma-Aldrich/Merck

Table 2-5: Materials used for the solvent-mediated plate method for fractionation of parasite haem species.

Solvent-mediated plate method for fractionation of parasite haem species	
Material	**Supplier**
Pyridine	Sigma-Aldrich/Merck
Dodecyl sulfate sodium salt (SDS)	Sigma-Aldrich/Merck
Sodium hydroxide (NaOH)	KIMIX

Table 2-6: Materials used for ferrihaem standard curve

Ferrihaem standard curve	
Material	**Supplier**
Porcine haematin	Sigma Life Science

2.2 General Instrumentation

Detailed below is the instrumentation that was used throughout this study where specific instrumentation utilized for specific procedures is described.

2.2.1 Centrifuge

Centrifugation of solutions of 10 ml or more was carried out in plastic Greiner falcon tubes using an Eppendorf Centrifuge 5810R or 5804. Microlitre solutions in 24- and 96-well plates were suspended and separated using an Eppendorf deep well plate attachment (A-2-DWP).

2.2.2 Incubator

Both CQ-sensitive and -resistant strain *P. falciparum* cultures were cultured at 37 °C using a Labcon 508IU incubator.

2.2.3 Light Microscope

Synchronicity of cell expressions and parasitemia was viewed from thin films of malaria parasites on Giemsa stained glass microscope slides using a Laborlux 12 Leitz light microscope. The above microscope was also used to determine cell counts by viewing prepared cells on a Sigma bright-line haemocytometer (Z 353, 962-9).

2.2.4 Sonicator

In order to ensure complete dissolution of solid samples in the relevant solvents, a Banelin Sonorex RK100H sonicator was used.

2.2.5 Vortex

For all prepared solutions and samples, a homogenous solution was achieved by using a Scientific Industries Vortex Genie (G560E).

2.2.6 Water bath

A GRANT digital Y6 or YIH DER BL-710 water bath was used for heating and maintaining relevant solutions for parasite culturing, assays, as well as β-haematin formation experiments at a physiological temperature of 37 °C. In order to confirm the required temperature, an external thermometer was used.

2.2.7 Weighing balance

The weighing balance was calibrated with mass standards before weighing of all materials using a Sartorius R200D balance (5 decimals).

2.2.8 UV-Vis spectrophotometer

Absorbance measurements were carried out using a Shimadzu UV1800 spectrophotometer, to quantify the binding constants for ferrihaem and various test compounds. All UV-visible spectra, conducted in a 1 cm pathlength Hellma® quartz cuvette and were monitored for changes in the characteristic Soret band as well as the weaker Q band and charge transfer band. For 96-well absorbance measurements, a SpectraMax 340PC plate reader was used.

2.2.9 Haemocytometer cell counting chamber

A bright-line haemocytometer cell counting chamber, from Sigma, was used to determine cell counts under a light microscope with cover glasses (22 x 26 mm) supplied by Superior Marienfield, Germany.

2.2.10 Flow cytometry

Cell viability, counts, stages and DNA content were determined using a BD FACSCalibur™ along SSC/FL1 with a 530 nm excitation source.

2.3 Software

Analysis and calculations for all data and statistical significance was performed using GraphPad Prism (GraphPad Software Inc.) version (v) 8.2.1 (227) for MacOs [328]. Referencing was carried out using Mendeley Ltd. 2008-2016 v1.16.1. Marvin Sketch v6.2.2 (Windows x86 8.6.2) was used to manually generate molecular structures and calculated molecular weights for all β-haematin inhibiting test compounds in this study [329]. Microsoft Office home and

student 2013 (v 15.0.5093.1001) Excel was used to formulate spreadsheets for the calculations of haem amounts, haemocytometer counts as well as flow cytometry counts [330]. FlowJo LLC 1997-2015 v10.1 [331] was used to analyze flow cytometry data (gated cell counts) collected using BD CellQuest™ Pro analysis software v 5.1 [332]. An annual subscription of FlowJo software was donated by Tree Star Incorporated. SoftMax Pro v4 software was used to acquire absorbance data for 96-well plates [333].

2.4 Preparation of solutions and samples

2.4.1 β-haematin inhibiting test compounds and their derivatives

Molecular structures for all β-haematin inhibiting test compounds that were investigated throughout this study, unless specified for a particular experiment, are shown in ***Figure 2-1***. The quinoline-containing positive standard CQ was purchased from Sigma-Aldrich. Benzimidazole test compound derivatives **1**-**4** were synthesized and characterized by Dr F. L'abbate, quinazoline test compound derivatives **5**-**7** by Mr S. J. Benjamin, and a benzothiazole test compound **8** and benzoxazole test compound **9** by Miss L. Wainwright. A triarylimidazole test compound **10** and a benzamide test compound **11** were previously synthesized and characterized by Dr K. J. Wicht. For comparison with test compounds **1**-**9**, previously published data by Dr K. J. Wicht for test compound **10**, **11** and AQ were used throughout this study. All stock solutions for the investigated β-haematin inhibiting test compounds (**1**-**9** including CQ) were dissolved in 100% DMSO to a final concentration of 2 mg/ml and stored in sealed Eppendorf tubes at -20 °C until further use. The βHIA values that were determined using a NP-40 detergent mediated β-haematin inhibition assay for all β-haematin inhibiting test compounds, were previously reported based on work in the group [263,334-338].

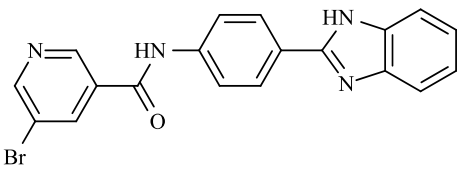

Test compound 1

MW: 393.24 g/mol

βHIA IC_{50} (μM): 32 ± 1

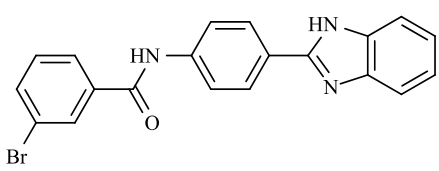

Test compound 2

MW: 392.25 g/mol

βHIA IC_{50} (μM): 24 ± 4

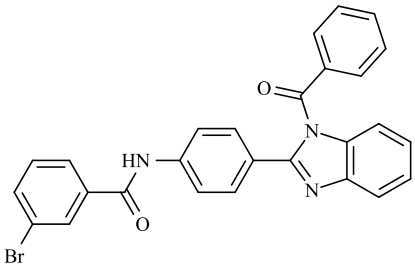

Test compound 3

MW: 496.40 g/mol

βHIA IC_{50} (μM): 80 ± 3

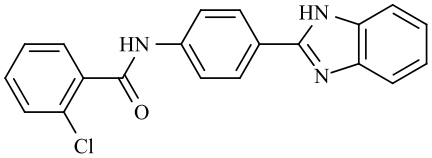

Test compound 4

MW: 347.80 g/mol

βHIA IC_{50} (μM): 38 ± 1

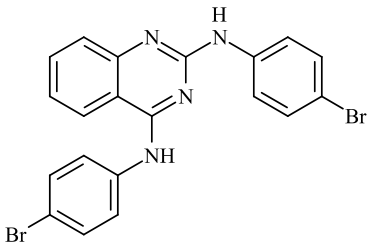

Test compound 5

MW: 470.17 g/mol

βHIA IC_{50} (μM): 20 ± 2

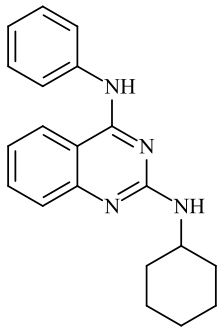

Test compound 6

MW: 318.42 g/mol

βHIA IC_{50} (μM): 26 ± 2

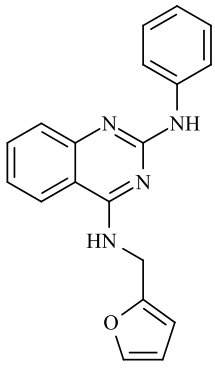

Test compound 7

MW: 316.36 g/mol

βHIA IC_{50} (μM): 23 ± 2

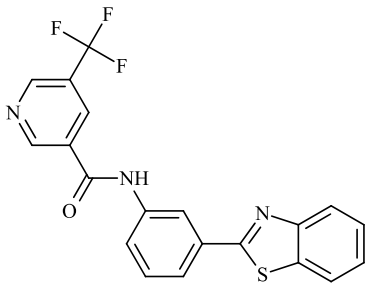

Test compound 8

MW: 397.42 g/mol

βHIA IC_{50} (μM): 30 ± 2

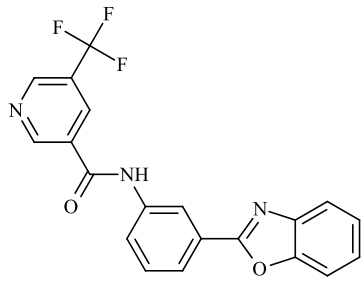

Test compound 9

MW: 381.35 g/mol

βHIA IC_{50} (μM): 22 ± 1

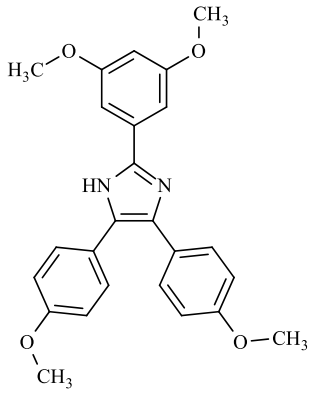

Test compound 10

MW: 416.5 g/mol

βHIA IC_{50} (μM): 14 ± 0.4

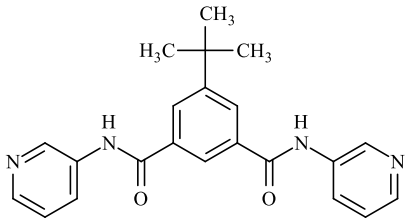

Test compound 11

MW: 373.17 g/mol

βHIA IC_{50} (μM): 7 ± 0.1

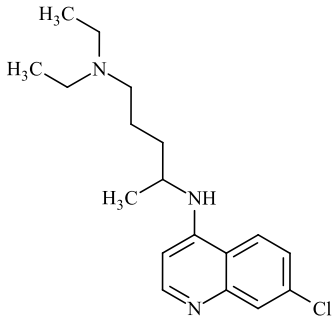

AQ

MW: 355. 86 g/mol

βHIA IC_{50} (μM): 23 ± 3

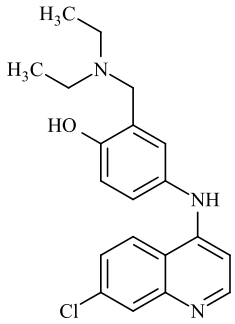

CQ

MW: 515.89 g/mol

βHIA IC_{50} (μM): 39 ± 2

Figure 2-1: Molecular structures for all β-haematin inhibiting test compounds used throughout this study.

2.4.2 Cell culturing of CQS and CQR *P. falciparum* malaria parasites

Incomplete Culture Medium

Incomplete culture medium was prepared by dissolving RPMI 1640 with glutamine (10.4 g/L) but without $NaHCO_3$, D-(+)-glucose (4 g/L), HEPES buffer (6 g/L), hypoxanthine (0.088 g/L), Albumax II (5 g/L) and gentamicin (0.05 g/L) in d.H_2O. The solution was pre-filtered with a

0.45 µm filter then filter sterilized using a 0.22 µm membrane filter. Autoclaved glass bottles were used to store the incomplete medium at 4 °C until further use.

Sodium Bicarbonate

A 0.6 M solution of $NaHCO_3$ was prepared by dissolving 50 g $NaHCO_3$ in 1 L of d.H_2O. Before storing the solution at 4 ºC, the solution was prefiltered through a 0.22 µm membrane filter into autoclaved glass bottles.

Complete Culture Medium

Roughly 17.5 ml of $NaHCO_3$ was added to 400 ml of incomplete culture medium to prepare complete medium. This solution was stored at 4 ºC under sterile conditions until further use.

Prepared O+ Human RBCs

In a sterile centrifuge tube, unwashed human blood was washed by adding 30 ml of complete medium to the centrifuge tube (1:1.5 ratio) and centrifuged at 1200 relative centrifugal force (rcf) for 5 min after which the supernatant was discarded. Before storing the washed RBCs at 4 ºC, this process was repeated for a second time.

Sorbitol

A 0.6 M solution of D-sorbitol was prepared by dissolving 50 g of D-sorbitol in 1 L of d.H_2O. Before storing the solution at 4 ºC, the solution was prefiltered through a 0.22 µm membrane filter into autoclaved 250 ml glass bottles.

Phosphate Buffer Solution (PBS)

A stock solution of PBS (1 tablet = 0.01 M phosphate buffer, 0.0027 M KCl and 0.14 M NaCl) was prepared by dissolving 5 tablets in 1 L of d.H_2O. The solution, pH 7.4, was stored at room temperature. For specific experiments, filtered PBS was prepared by filtering the PBS solution with a 0.22 µm membrane filter.

Giemsa Stain

The stain was prepared by adding 1 ml Giemsa to 9 ml of PBS (1:10) before applying to culture smeared glass microscope slides.

2.4.3 Parasite antiplasmodial assay

Malstat

A 400 ml solution of Malstat was prepared by gently heating 400 µl of Triton X-100 with 8 g of L-lactate, 2.64 g of Tris buffer in d.H_2O. The solution was stirred until dissolved before adding 0.044 g of APAD (pH 9) and stored at 4 ºC until further use.

NBT

A 100 ml solution of NBT was prepared by dissolving 0.16 g NBT salt and 0.008 g of phenazine ethosulphate in 100 ml of d.H_2O and stored at 4 ºC until further use.

2.4.4 Pyridine-based parasite haem fractionation plate method

2.4.4.1 Parasite isolation, fixation and cell counting

Mature trophozoite cultures were isolated using a saponin solution that was stored at 4 ºC and can be kept for a maximum of two weeks. The solution was prepared as a 1% solution (0.5 g) in 50 ml of d.H_2O. Isolated parasites were fixed with a solution of glutaraldehyde that was prepared by vortexing 25 µl of a 50% solution of glutaraldehyde in 10 ml of 0.22 µm membrane filtered PBS. To prevent cells from aggregating, which is necessary for flow cytometry, 50 µl of DNAse was added to the 10 ml of 0.22 µm membrane filtered glutaraldehyde in PBS solution. In preparation of flow cytometry samples, a 10 ml diluted solution of SYBR green® I nucleic acid stain (1:10000) in 0.22 µm membrane filtered PBS was prepared and used as an indicator of cell growth and division. In addition, Trucount™ beads (5 ml) were diluted in a separate tube with 1 ml of 0.22 µm membrane filtered PBS. After thawing of samples and solutions, all were vortexed before each experiment (***Table 2-4***)

2.4.4.2 Solvent-mediated plate method for fractionation of parasite haem species

Various solutions were prepared for the solvent-mediated plate method for fractionation of parasite haem species which are listed in ***Table 2-5*** and include: (i) a 0.2 M buffer solution which was prepared by dissolving 4.76 g of HEPES in 100 ml of d.H_2O and brought to a pH of 7.5; (ii) a 4% anionic protein denaturing detergent solution prepared by dissolving 4 g of SDS in 100 ml of d.H_2O; (iii) a 0.3 M solution of NaCl, by dissolving 1.75 g in 100 ml of d.H_2O; (iv) a 0.3 M solution of NaOH prepared by dissolving 1.2 g in 100 ml of d.H_2O; (v) a

0.3 M HCl solution prepared by dissolving 3 ml (v/v 32 %) in 100 ml of d.H_2O; and (vi) a 25 % pyridine in 0.2 M HEPES (v/v) solution prepared by adding 25 ml of aqueous pyridine to 10 ml of 0.2 M HEPES (pH 7.5) diluting with 65 ml of d.H_2O.

2.4.4.3 Standard ferrihaem curve

Haematin

A 100 µg/ml solution of porcine haematin was freshly prepared by dissolving 0.01 g of haematin in 100 ml of 0.3 M NaOH for each experiment (***Table 2-6***).

2.5 Experimental Methods

Throughout this study, CQS (NF54) and CQR (Dd2 – clone of W2-MEF originating from Indochina [339-340] and K1- and pyrimethamine-resistant clones originally derived from Thailand [341] *P. falciparum* parasite strains) were used. CQS strain, NF54 originally isolated from a patient near Schiphol Airport, Amsterdam [342] was used in the majority of the experimental methods described below, unless stated otherwise.

2.5.1 Cell culturing of CQS and CQR *P. falciparum* parasites

Parasites were cultured using a modified version of Trager and Jensen under a sterile laminar flow hood [343]. Donated trophozoite cultures from a routine culturing laboratory at the Division of Pharmacology, UCT were decanted into sterile 50 ml centrifuge tubes and spun down at 750 revolutions per minute (rpm) for 5 min. The supernatant was aspirated before aliquoting 1 µl of iRBCs onto a glass microscope slide. The droplet was smeared to create a thin film of iRBCs, methanol fixed and completely covered with a 10% Giemsa solution. The stained slide was left for 10 min before rinsing with tap water, air-dried and viewed with an oil immersion light microscope at 100 × magnification. The iRBCs were then checked for the correct stage, parasitaemia and confluency. The remaining iRBC pellet was diluted to 2% haematocrit and 10% parasitaemia, in complete medium and washed O^+ RBC in a sterile 250 ml flat bottom culture flask. For parasite growth, culture flasks were gassed for 1 min with O_2 (3%), CO_2 (4%) and N_2 (4%) before being placed in a CO_2 incubator (37 °C).

After a duration of 24 hrs, the culture flasks (ring stage) were removed from the incubator and centrifuged at 750 rpm for 5 min in a sterile 50 ml falcon tube. The supernatant

was discarded and a Giemsa smear of the culture was prepared as previously mentioned. The ring stage parasites were checked before resuspending the remaining culture pellet in 15 ml of D-sorbitol and incubating in a water bath for 5 min. This was done to synchronize the culture. After 5 min in the water bath, the iRBC pellet was centrifuged at 750 rpm for 5 min, aspirated and diluted in complete medium and washed O^+ RBCs to give 2% haematocrit and 10% parasitaemia. The culture flask was re-gassed (3% O_2, 4% CO_2 and 4% N_2) for 1 min and placed back into a CO_2 incubator. The culturing cycle was maintained at 10% parasitaemia until further use.

2.5.2 Parasite antiplasmodial assay

The parasite antiplasmodial assay, previously described by Makler *et al*., was modified to evaluate the IC_{50} of various antimalarial test compounds by measuring the amount of lactate dehydrogenase (LDH) present in parasites inoculated with a test compound [344]. During the pathogenic blood stage of the malaria parasite, lactate synthesized through the glycolytic pathway can be converted back to pyruvate which is catalysed by parasite lactate dehydrogenase (p-LDH) and is easily distinguishable from human LDH isoforms. The reason is that p-LDH has the ability to use APAD more rapidly and effectively than host LDH isoforms (200-fold) (***Figure 2-2***) [345].

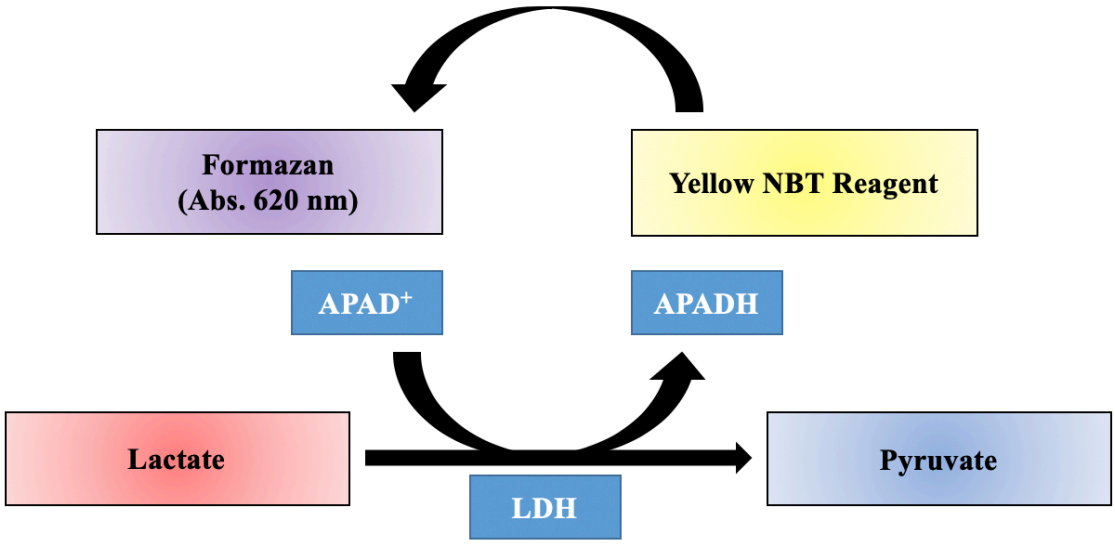

***Figure 2-2*:** The formation of pyruvate in the presence of the APAD coenzyme (Malstat™) produced in viable malaria parasites. APADH formation is colourimeterically observed from the reduction of NBT (yellow) to formazan (purple). The figure was adapted and modified from Combrinck *et al* [346].

Specifically, NAD analogue, APAD, is used during glycolysis instead of NAD in the assay due to its unique uptake by malaria parasites and not RBCs as well as its conversion rate of lactate to pyruvate. During plate development for spectroscopic analysis, iRBCs are suspended in a solution of Malstat™ (containing APAD) allowing the formation of reduced 3-acetylpyridine-adenine dinucleotide (APADH) in viable cells. This rapid formation can be colourmeterically assayed, in the presence of NBT, by the disappearance of the yellow colour and formation of a deep purple solution of formazan salt as the process proceeds. The measured formazan absorbance, recorded at 620 nm, is equivalent to the percent parasite viability at a known concentration of test compound.

Prior to each experiment, test compound solutions of 2 mg/ml were freshly prepared the night before in DMSO (100%) and stored at -20 °C overnight. When preparing for the assay, test compounds were thawed in a water bath at 37 °C and vortexed before diluting to a known starting concentration (1000 ng/ml) in complete medium. Briefly, in columns 3-12 of a 96-well plate, test compound samples were serially diluted further in complete medium, resulting in a DMSO concentration of less than 0.5% (1:2000 dilution). All test compounds were tested in triplicate adjacent to a control test compound (CQ). Column 1 (negative control), contained solely RBCs at a haematocrit of 2%. For the positive control (column 2), iRBCs in complete medium were diluted to 2% haematocrit and 2% parasitaemia where 100 µl was also added to columns 3-12. The plates were covered and sealed in a sterile gassing chamber and gassed with 3% O_2, 4% CO_2 and N_2 before placing in an incubator at 37 °C (***Figure 2-3***).

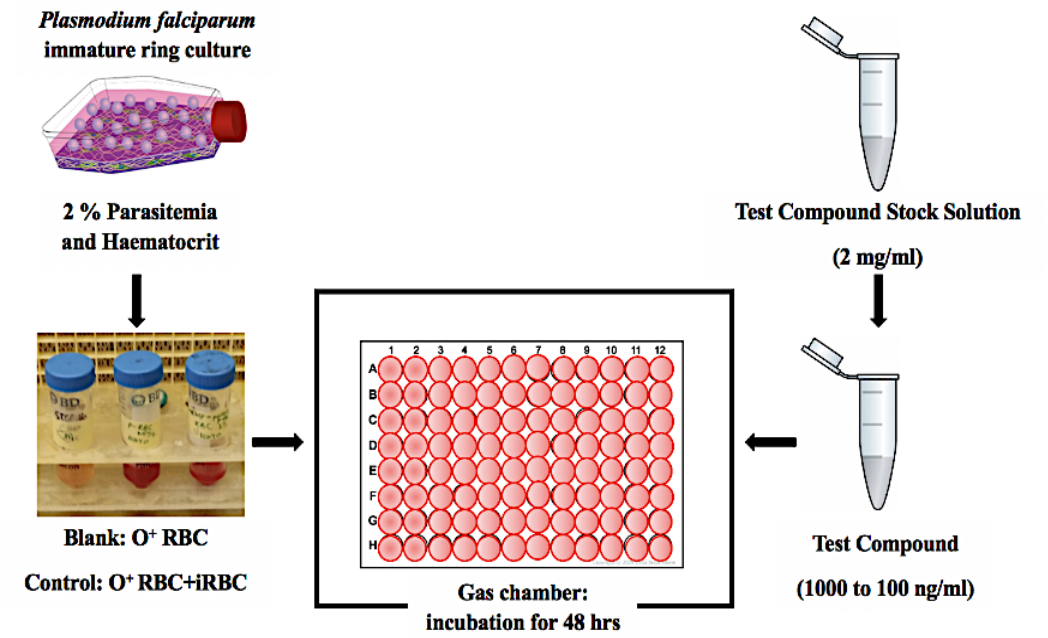

***Figure 2-3*:** p-LDH assay scheme used to determine the IC_{50} of a test compound.

After 48 hrs, the plate was frozen at -20 °C prior to thawing so as to lyse trophozoites for development of the plate. The plate was developed by resuspending 15 µl of lysed trophozoites in 100 µl of Malstat™ and left to stand for 30 min before adding 25 µl of NBT. The measured absorbance was recorded at 620 nm, using a Modulus™ Microplate Multimode Reader (Turner Biosystems), and plotted using sigmoidal dose-dependent curve analysis in GraphPad Prism v8.2.1 software.

2.5.3 Pyridine-based parasite haem fractionation plate method

The pyridine-based parasite haem fractionation method was developed from another method that was first established in 2005 and used as a cheap and reliable means of detecting the inhibition of β-haematin formation [262]. This method is based on the fact that pyridine forms a monomeric low-spin complex with haematin. Dissolved haematin in purely aqueous medium is characterized by a strongly absorbing band, commonly known as a Soret band (389 nm) which is broadened, indicative of an aggregated state of haematin, probably as a result of dimerization [347]. At longer wavelengths, haematin also exhibits a weakly absorbing Q band and is somewhat more prominent charge transfer band (CT). In more detail, in accordance with the Gouterman four orbital model [348] these bands are a result of the transition of an electron between two closely spaced filled porphyrin π orbitals to a low-energy pair of unoccupied

porphyrin π* orbitals of haematin. The Soret band, which is broadened as a result of a vibrationally excited state in the unoccupied π* orbital of haematin is further broadened by aggregation owing to decreased symmetry of the system, which lifts the degeneracy of these orbitals. By forming a monomeric complex, pyridine sharpens the Soret band and gives a consistent extinction coefficient. Nonetheless, upon exposure of haematin to aqueous pyridine, the resulting Soret band is sharpened and significantly increases in intensity along with a characteristic red shift to 405 nm. This increase in intensity is typically due to the presence of monomeric haematin. Simultaneously, a more prominent Q band at 527 nm is observed which is indicative of a low-spin Fe(III)PPIX-pyridine complex where two pyridine ligands are coordinated to the central Fe(III) centre of the haematin porphyrin. The resulting coordination causes the axial water from the haematin Fe(III) centre to be displaced by means of a ligand substitution reaction [262].

Briefly, the colorimeteric multi-well pyridine-based parasite haem fractionation method, previously described by Combrinck *et al*, is a method that involves quantifying haem species present in *P. falciparum* parasites which can be spectroscopically assayed as a low-spin Fe(III)PPIX-pyridine complex [263]. In this chapter, this method was used to determine the effect of nine selected β-haematin inhibitors and their derivatives, including CQ, on the inhibition of haemozoin formation in *P. falciparum* parasites. Resulting haem species; undigested haemoglobin, exchangeable haem and haemozoin present in isolated trophozoites were solvent fractionated and spectroscopically assayed at 405 nm in the presence of aqueous pyridine at pH 7.5 (5% v/v). All absorbance measurements were carried out on a SpectraMax 340PC plate reader.

2.5.3.1 Parasite inoculation plate method (24-well plate)

CQS NF54 strain parasites were cultured according to methods described in ***Section 2.5.1***. Starting with highly synchronous ring stage cultures, iRBCs were confirmed by viewing Giemsa stained smears using an oil immersion objective lens (100×). The ring parasitaemia was determined by calculating the percentage of ring iRBCs in the total number of RBCs and iRBCs (average of 1000 cells counted). The calculated parasitaemia was used to dilute the ring cultures (5% parasitaemia; 2% haematocrit) in 49 ml of complete medium and washed O^+ RBCs. Treated cultures were inoculated, in a 24-well plate (Greiner Bio-One), with increasing multiples of the individual test compound 50% inhibitory concentrations values (0.5, 1.0, 2.0, 2.5, 3.0 × IC_{50}) where the highest volume of test compound used in a single well was 20 µl

(***Figure 2-4***). All dilutions of β-haematin inhibiting test compounds (≤ 0.5% DMSO v/v) in complete medium were prepared prior to inoculation of iRBC cultures, where individual experiments were carried out in quadruplicate. Before incubation at 37 °C for 30-32 hrs, all plates were gassed with 3% O_2, 4% CO_2 and N_2 for a minute in a sterile gassing chamber [263].

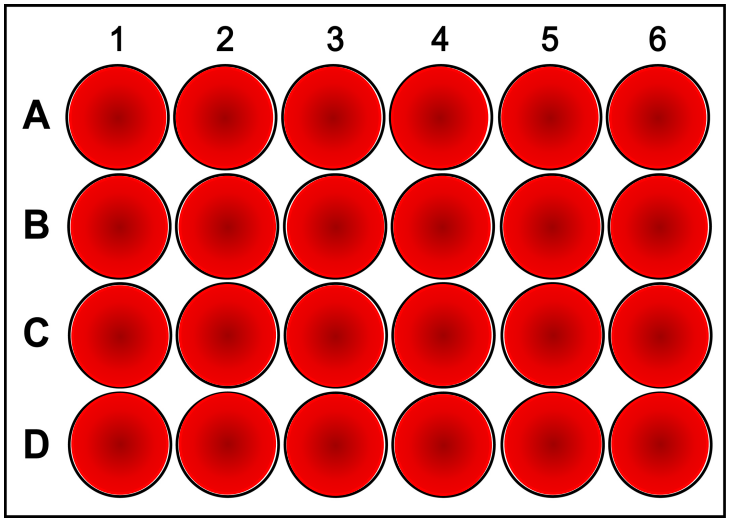

Column:

1. Control-No inhibitor
2. 0.5 x IC_{50}
3. 1.0 x IC_{50}
4. 2.0 x IC_{50}
5. 2.5 x IC_{50}
6. 3 x IC_{50}

Figure 2-4: 24-well plate setup for CQS strain *P. falciparum* parasite (NF54) inoculation assay.

2.5.3.2 Parasite isolation and fixation

Before removing the plates from the incubator, Giemsa stained "scrape" slides were prepared to assess the maturity of the trophozoite culture due to variations in the maturation of *P. falciparum* cultures in the presence of test compounds. In order to attain reliable results, plates were removed from the incubator (37 °C) after roughly 32 hrs and well contents were transferred, under sterile conditions, to the corresponding wells in a 2.5 ml deep well plate. The settled pellet was analysed as a Giemsa stained smear under a light microscope oil immersion lens to view the parasitaemia of trophozoite iRBCs. After the confirmation of trophozoite iRBCs, supernatants were aspirated and parasites isolated by saponin lysis of RBCs by adding 100 µl of 1% saponin in 1.8 ml of PBS (pH 7.5) to 300 µl of iRBC pellet (***Figure 2-5***). The iRBC pellets were resuspended to promote lysis and centrifuged at 1200 rpm for 5 min. After centrifugation, supernatants were aspirated before washing the isolated pellet with 2 ml of PBS. This process was repeated until a clear supernatant was observed in order to remove excess traces of RBCs (undigested haemoglobin), cell debris and associated haemozoin from previous cycles [263]. A 100 µl aliquot of PBS was added to the washed pellet and vortexed to ensure a

homogenous mixture. For cell counting, 10 µl of the resuspended mixture was aliquoted into a separate 96-well plate prior to freezing the remaining pellet at -80 °C (stock plate).

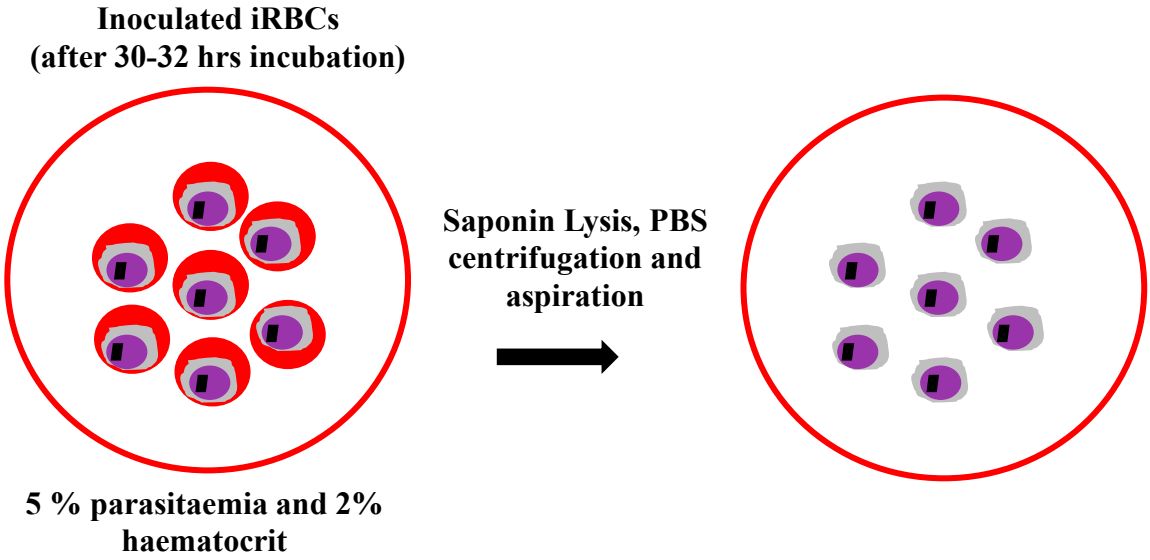

Figure 2-5: Saponin lysis of mature trophozoite cultures from red blood cells.

2.5.3.3 Glutaraldehyde-fixation and cell counting

Cell counting plates were prepared by adding a 10 µl aliquot of isolated trophozoites to 190 µl of 25% glutaraldehyde in PBS (1:20 dilution) and were stored at 4 °C overnight. A bright-line haemocytometer was used to determine the cell count per ml by pipetting 10 µl of glutaraldehyde-fixed trophozoites at room temperature (rt.) onto the counting grid and allowing the cells to settle for 15 min (***Figure 2-6***).

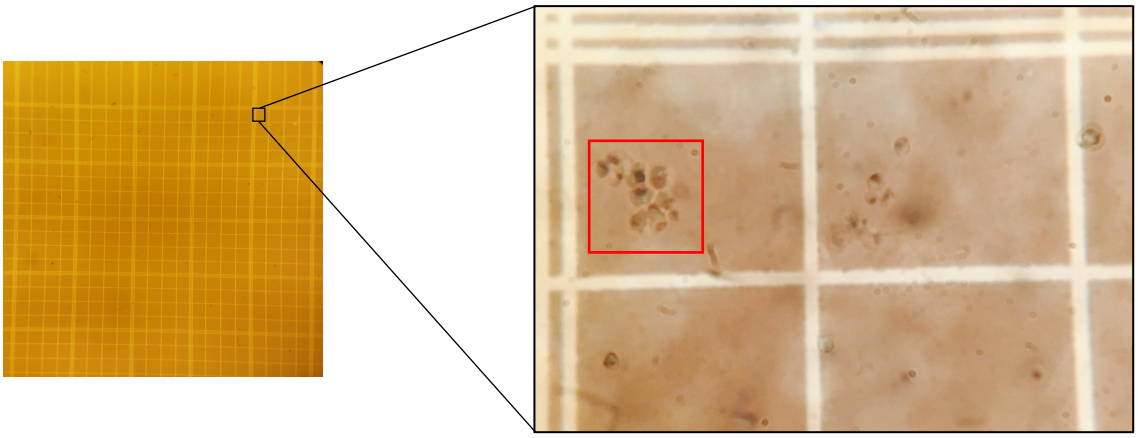

Figure 2-6: Haemocytometer counting grid containing glutaraldehyde-fixed isolated trophozoites (red box).

A minimum of 5 blocks were counted to calculate the number of viable cells per ml in each well using the following equation (Eq.) (***Eq. 1***) [263];

$$\frac{\text{Cells}}{\text{ml}}(H) = T_{CC} \text{ x } T_{BC} \text{ x } D_F \qquad \textbf{\textit{Eq. 1}}$$

Where:

$\frac{Cells}{ml}(H)$ = haemocytometer cell counts per ml in a single well

T_{CC} = total cells counted

T_{BC} = total blocks counted

D_F = dilution factor (10000)

Multiples of the test compound IC_{50} values were individually counted and calculated in order of increasing dosage including the control (no inhibitor present).

For confirmation of haemocytometer counts, cell viability and number of cells per ml in each well were analysed with flow cytometry using a method previously described by Combrinck *et al* [263]. In 5 ml Trucount™ tubes, 100 µl of the glutaraldehyde-fixed trophozoite solution was pipetted into an 800 µl solution of 0.22 µm filtered PBS containing 0.01% SYBR green® I (DNA binding fluorescent dye) spiked with 100 µl of fluorescent trucount beads. Samples were analyzed further on a BD FACSCalibur™ with CellQuestPro software (***Figure 2-7***).

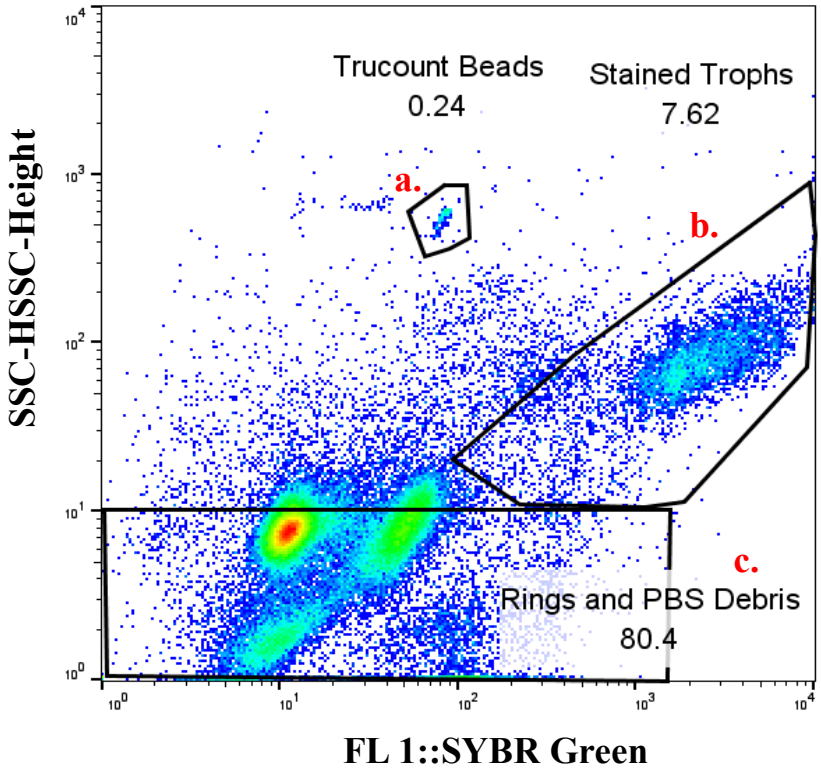

Figure 2-7: A dot plot of side scatter (complexity of cells, SSC) versus the SYBR green® I fluorescent intensity detected on the FL1 detector. Displayed are the predetermined gates for the populations of; a) trucount beads, b) isolated stained trophozoite population fixed with glutaraldehyde after staining with DNA binding fluorescent dye, SYBR green® I and c) ring and PBS debris.

The cell count, relative to fluorescent trucount beads, was used to calculate the concentration of cells per ml in a single well from the number of gated stained trophozoites, gated fluorescent beads and concentration of fluorescent beads per ml provided by the supplier on each package of fluorescent beads. The following equation was used (***Eq. 2***) [263]:

$$[C_c] = \frac{GST}{GFB} \times CFB \qquad \textit{Eq. 2}$$

Where:

C_c = cell concentration per ml

GST = number of gated stained trophozoites

GFB = number of gated fluorescent beads

CFB = concentration of fluorescent beads per ml

2.5.3.4 Solvent-mediated plate method for fractionation of haem species

Fraction 1: Undigested haemoglobin fraction

After 24 hrs, the 96-well round bottom stock plate was removed from the freezer (-80 °C) and left to thaw for 30 min at rt. To the stock solutions, 50 µl of d.H_2O was added and sonicated for 5 min. An additional 50 µl of d.H_2O was added with 50 µl of 0.2 M HEPES (pH 7.5) and centrifuged for 30 min at 3600 rpm. The resulting supernatant was carefully pipetted, on the same plate, into the corresponding adjacent empty wells. To the supernatant, 50 µl of 4% SDS was added and the plate was sonicated for 5 min. Before adding 50 µl of 0.3M NaCl, 25% pyridine and 100 µl of d.H_2O, the plate was left to incubate at room temperature for 30 min. The fraction 1 solution was transferred to a flat bottom 96-well plate (200 µl) where the solutions were re-sonicated before recording the absorbance for the range 350-800 nm (SpectraMax 340PC plate reader) (***Figure 2-8 a***). The absorbance was used to determine the fraction of haemoglobin in a cell [263].

Fraction 2: Exchangeable haem

To the remaining pellet in the stock plate, 50 µl of d.H_2O and 4% SDS was added and mixed well by sonicating the plate for 5 min to ensure complete dissolution of exchangeable haem. For 30 min the solution was incubated at 37 °C prior to adding 50 µl of 0.2 M HEPES (pH 7.5), 0.3 M NaCl and 25% pyridine. The solution was centrifuged at 3600 rpm for 30 min. To the resulting supernatant, 150 µl of d.H_2O was added and mixed using a micro-multichannel pipette. The diluted solution was aliquoted into a 96-well flat bottom plate and spectroscopically assayed, using a SpectraMax 340PC plate reader (350-800 nm), to determine the fraction of exchangeable haem (***Figure 2-8 b***) [263].

Fraction 3: Haemozoin fraction

To the final pellet, 50 µl of d.H_2O and 0.3 M NaOH, to dissolve the haemozoin fraction, was added followed by 30 min of sonication. A colour change was observed from a clear to green solution showing the dissolution of haemozoin crystals present in the isolated pellet. To the

green solution, 50 µl of 0.2 M HEPES (pH 7.5), 0.3 M HCl to neutralize the solution and 25% pyridine was added before diluting with 150 µl of d.H_2O. Aliquots of 200 µl were transferred into a 96-well flat bottom plate and the absorbance was recorded from 350-800 nm (SpectraMax 340PC plate reader) to determine the fraction of the Fe(III)PPIX-pyridine complex corresponding to haemozoin (***Figure 2-8 c***) [263].

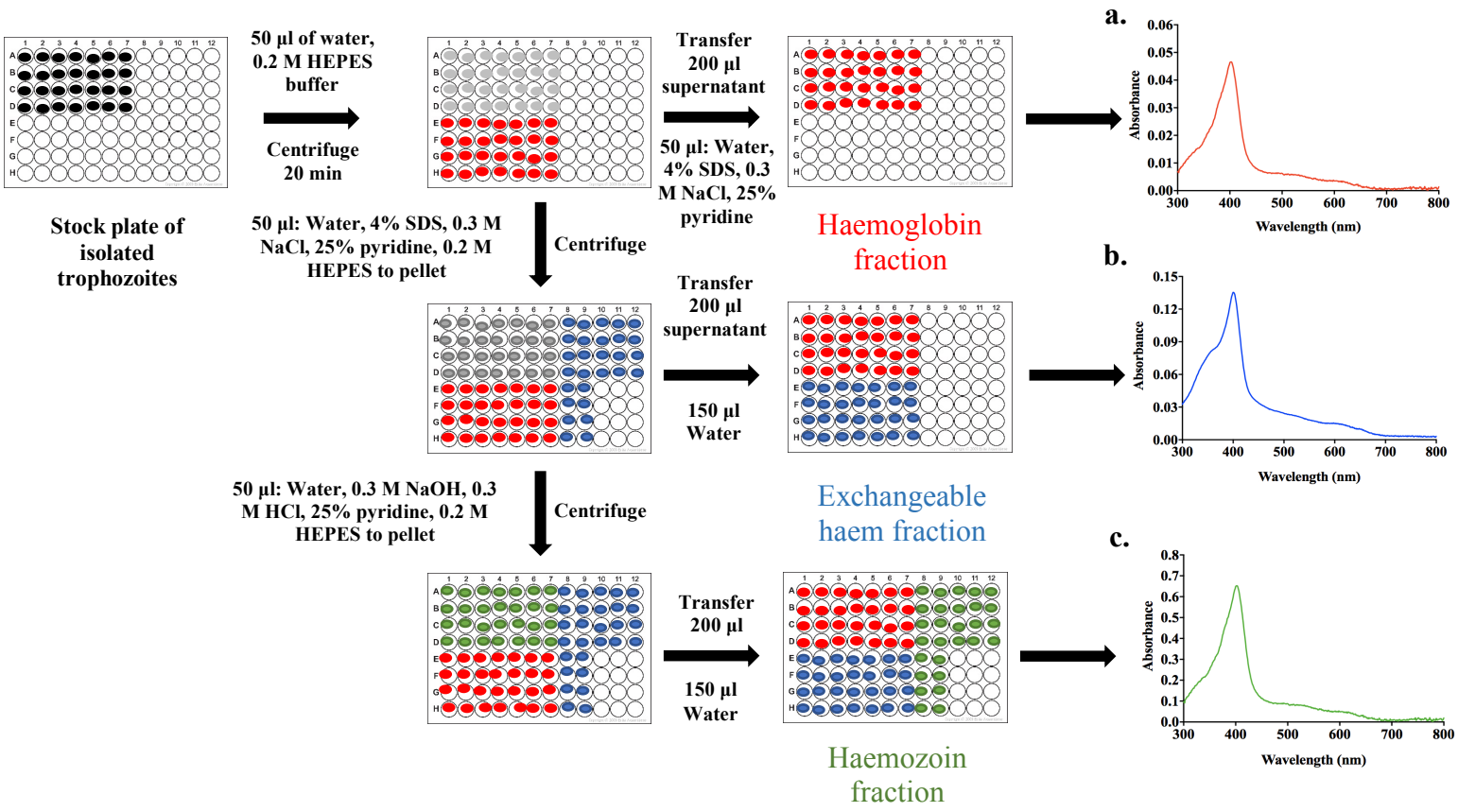

Figure 2-8: Solvent-mediated plate method for fractionation of haem species where Fe(III)PPIX-pyridine complex absorbance spectra represent a) fraction 1: undigested haemoglobin (methaemoglobin), b) fraction 2: exchangeable haem and c) fraction 3: haemozoin, present in *P. falciparum* isolated trophozoites (in the case shown, untreated). This was adapted and modified from Combrinck *et al* [263].

2.5.3.5 Standard ferrihaem curve

A haem standard curve was constructed to determine the total amount of haem in fractionated samples using a 30 µM prepared solution of porcine haematin in 0.3 M NaOH. Briefly, in a 96-well plate, 80 µl of 0.3 M NaOH was added to column 1 as a blank. In the next 6 wells, 80 -2.5 µl of the haematin standard solution (triplicates) was diluted by adding 40 µl of the

following solvent; 0.2 M HEPES (pH 7.5), 4% SDS, 0.3 M NaCl, 0.3 M HCl and 25% pyridine in HEPES and diluting each well to a final well volume of 400 µl with d.H_2O. All wells were mixed using a micro-multichannel pipette before spectroscopically assaying the plate at 405 nm (1 cm pathlength). GraphPad Prism v8.2.1 was used to plot the absorbance of haematin versus haematin concentration to determine the molar extinction coefficient of haematin as a Fe(III)PPIX-pyridine complex (***Figure 2-9***) [263]. The molar extinction coefficient determined (93,726 ± 2221 M^{-1} cm^{-1}) was in close agreement with the value previously reported by Asakura *et al*. This value was used as a reference when calculating the amount of haem per cell expressed as femtograms (fg) of Fe in each fractionated sample (untreated or treated samples) which was determined by dividing the total haem (expressed as Fe mass) by the total haemocytometer cell counts [349].

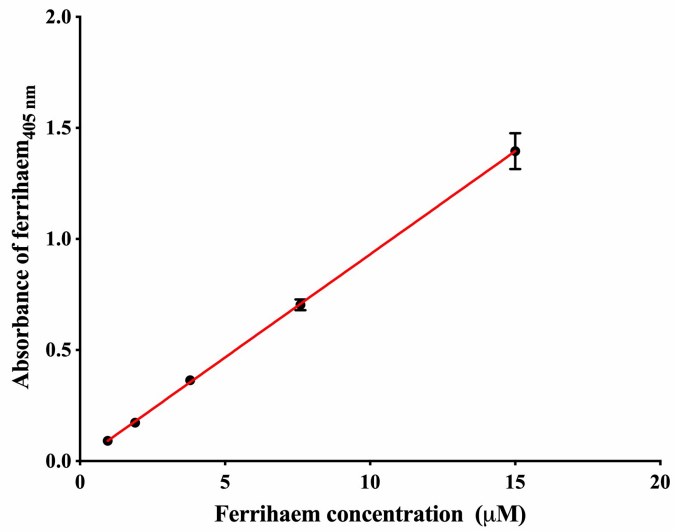

Figure 2-9: The standard curve for the absorbance of haematin at 405 nm at increasing concentrations of haematin, analysed as a Fe(III)PPIX-pyridine complex. The standard curve represents a fit to the mean ± SD for data points obtained from four different experiments. A linear regression analysis was performed using GraphPad Prism v8.2.1 to yield a correlation coefficient, $R^2 = 0.9979$.

2.5.4 Inoculum effect analysis

The inoculum effect analysis was carried out using a modified p-LDH method previously described by Makler *et al* [344]. When preparing for the experiment, test compound stock solutions were thawed in a 37 °C water bath before diluting to a known starting concentration

in complete medium. In brief, test compound solutions were serially diluted in columns 3-12 in complete medium, resulting in a DMSO concentration of less than 0.5% (1:2 dilution). All test compounds were tested in triplicate, adjacent to the positive control CQ. Column 1 (negative control), contained solely RBCs that were diluted to a final haematocrit of 2%. The positive control (column 2) contained iRBCs in complete medium that were diluted to a 2% haematocrit and varying parasitaemia (1 - 5%). 100 µl of the same solution was then transferred to columns 3-12 on the same plate. The parasitaemia was varied according to the inoculum size which ranged from 1-10 which is equivalent to 0.0001-0.001 fractional volume of an iRBC. The plates were covered and sealed in a sterile gassing chamber before gassing with 3% O_2, 4% CO_2 and N_2. Plates were incubated in a 37 °C incubator for 48 hrs.

After 48 hrs, the plates were frozen at -20 °C prior to thawing the lysed trophozoite containing plate to facilitate the rupturing of parasite membranes. The plates were developed by resuspending 15 µl of the lysed trophozoite pellet in 100 µl of Malstat™ and left to stand for 30 min at rt. before adding 25 µl of NBT. The measured absorbance (Modulus™ Microplate Multimode Reader, Turner Biosystems), was recorded at 620 nm and the varying IC_{50} (NF54) values were calculated from the sigmoidal dose-dependent curves plotted using GraphPad Prism v8.2.1 software.

Thereafter, individual experimental CAR values were calculated from a linear plot of IC_{50}(NF54) concentrations plotted as a function of their corresponding inoculum size. Based on the IC_{50} value at each inoculum size, absolute IC_{50} and fractional volume of an iRBC (FV_{iRBC}) the experimental CAR values were calculated using a modified equation adapted from Hawley *et al* (***Eq. 5***) [269];

$$Experimental\ CAR = \frac{IC_{50}\ (NF54) - IC_{50}\ (absolute)}{IC_{50}(absolute) \times FV_{iRBC}} \qquad \textbf{\textit{Eq. 5}}$$

Which can be rearranged to:

$$IC_{50}(NF54) = \{IC_{50}\ (absolute) \times Experimental\ CAR\} \times\ FV_{iRBC} + IC_{50}\ (absolute)$$

Where a plot of IC_{50} values versus FV_{iRBC} is a straight line with;

$$Slope = IC_{50}\ (absolute) \times Experimental\ CAR$$

And,

$$\text{Intercept (y axis)} = \text{IC}_{50}\ \text{(absolute)}$$

From which the experimental CAR value can be directly calculated from the linear plot as follows (***Eq. 6***);

$$\text{Experimental CAR value} = \frac{\text{Slope}}{\text{intercept}} \times 10000 \qquad \textit{Eq. 6}$$

Because, FV_{iRBC} was calculated using the following equation (***Eq. 7***) [269];

$$\frac{\text{IS}}{10000} = \frac{\text{parasitemia (\%)}}{100} \times \frac{\text{haematocrit (\%)}}{100} \qquad \textit{Eq. 7}$$

2.5.5 Total intracellular test compound amounts

The total intracellular test compound amounts per cell were based on the product of experimental CAR values, volume of a RBC and IC_{50}(NF54) values for each individual test compound. The following equation was used (***Eq. 8***);

$$Intracellular\ test\ compound\ amount\ (fmol) = \frac{CAR \times V_{RBC} \times IC_{50}\ (NF54)}{1 \times 10^{6}} \qquad \textit{Eq. 8}$$

Where:
CAR = experimental CAR value
V_{RBC} = volume of a RBC (84.3 ± 5.7 fL) [350]
IC_{50} (NF54) = 50% inhibitory concentration (μM) at inoculum size 4

2.5.6 Propagation of errors

The standard deviation for all calculations were calculated using the propagation of error equation for multiplication and division (***Eq. 9***);

$$y = \frac{ab}{c}$$

Where:

$$\frac{\Delta y}{\mathrm{y}} = \sqrt{\left(\frac{\Delta a}{a}\right)^2} + \sqrt{\left(\frac{\Delta b}{b}\right)^2} + \sqrt{\left(\frac{\Delta c}{c}\right)^2} \qquad \textbf{\textit{Eq. 9}}$$

3

Measuring intracellular haemozoin inhibition in *P. falciparum* parasites in the presence of accumulating β-haematin inhibiting test compounds

3.1 Introduction

Well-known β-haematin inhibitors, CQ and AQ to name two, are known to target and inhibit the formation of haemozoin which was evident from decreasing haemozoin amounts, variable increases in exchangeable haem amounts which have been shown to be detrimental to parasite growth [263,296,334-338,351]. With the recent emergence of CQ resistance, as discussed in Chapter 1, a HTS search for new hit compounds uncovered hundreds of new successful β-haematin inhibitors that may inhibit haemozoin formation have been discovered from the HTS approach method. However, the exact understanding as to how they achieve this in *P. falciparum* parasites is still unclear [143-144,238,262,352-353].

Various investigations have been carried out in the efforts to better understand the mechanism by which CQ and other potential β-haematin inhibitors inhibit parasite growth and haemozoin formation. Ncokazi and Egan developed a simplified method to determine β-haematin inhibition which was cheap, reliable and fast. This method, based on a well-known method commonly known as the ferrihemochrome method (Phiβ), had, however, hardly been used in the study of β-haematin and haemozoin. Limitations to this method included the use of β-haematin inhibitors with poor water solubility. Nevertheless, they were able to show a correlation between β-haematin inhibition and parasite growth inhibition [262]. This was in agreement with the findings of Kashula *et al*, whose studies had investigated SARs for quinoline-containing compounds. With specific reference to CQ, they were able to show that the 4-aminoquinoline nucleus and 7-chloro group were important for β-haematin inhibition as well as parasite growth inhibition [261]. Recently, it has also been shown that a group of benzimidazole-containing β-haematin inhibitors inhibit haemozoin formation and this was suggested to be vital for parasite growth inhibition activity. For these β-haematin inhibitors, their parasite growth inhibition activity was observed to be influenced by the β-haematin inhibition activity and number of hydrogen bond donors [335].

Recently, studies have shown that CQ and other β-haematin inhibitors also target membrane-associated haem, causing a build-up of toxic exchangeable haem inside the parasite's DV, resulting in significant reductions in parasite growth [242,293,354]. Studies by Combrinck *et al* and Fong *et al* have both shown direct evidence of decreasing haemozoin Fe percentages which coincided with increasing exchangeable Fe percentages which have been thought to be the cause of subsequent parasite death for various β-haematin inhibitors [263,354]. In the end, these studies showed that the reliability of using percentage haem values was

questionable and emphasized the importance of utilizing haem amounts conveniently expressed as haem Fe mass per cell values instead. It has also been shown for other β-haematin inhibitors, a group of benzamides and triarylimidazole β-haematin inhibitors, that haemozoin formation was inhibited in a dose-dependent manner causing increasing amounts of exchangeable haem that coincided with decreasing parasite growth [334,338].

Reports have also suggested that the mechanism by which these β-haematin inhibitors inhibit the formation of haemozoin is dependent on their ability to accumulate in the parasite. Fitch *et al* suggested that the selective mechanism for accumulation of CQ to accumulate in iRBCs more than RBCs was due to the binding of CQ to a certain receptor that was unique to the parasite which they later claimed to be haem from the digestion of haemoglobin [203,279,355]. It was also suggested to be as a result of a CQ readily forming a complex with haematin [251,296,356]. To quantify this accumulation, Yayon *et al* and Krogstad *et al* showed with the use of fluorescent probes and labelling procedures that CQ tends to accumulate in the parasite and inhibit parasite growth by raising the pH of the parasite DV [127,128,196,204]. In addition, Yayon *et al* specifically provided evidence that transmembrane proton gradients play a role in the accumulation of β-haematin inhibitors in the parasite DV [196]. Alternatively, the cellular accumulation ratio for a group of β-haematin-inhibiting benzamides known to inhibit the formation of haemozoin were determined by Wicht *et al*. An inoculum effect analysis was used to show that a linear relationship between IC_{50} values and inoculum sizes exists [334]. With close agreement with Hawley *et al* and Warhurst *et al*, the cellular accumulation ratios of these β-haematin inhibitors were suggested to be influenced by their basicity which facilitated their ability to accumulate by the process of pH trapping [269,357-358].

In this chapter, ten selected β-haematin inhibiting compounds were selected for investigation from five different structural scaffolds and their derivatives, for which the synthesis and parasite growth inhibition activity of which have been previously reported [263,334-338]. This was to ascertain their effectiveness in inhibiting *P. falciparum* CQS NF54 strain parasite growth and subsequent ability to interfere with the haemozoin formation pathway from accumulating in iRBCs.

Firstly, a modified antiplasmodial assay, described in Chapter 2, was applied to these test compounds, as well as CQ (as a positive control for comparative reasons) [344]. Decreasing parasite growth at micromolar concentrations was observed and was in agreement with previously reported data [263,334-335,354].

Secondly, a pyridine-based parasite haem fractionation plate method that was modified from a previously established method, was used to quantitatively determine the effects of these test

compounds on haemozoin formation in parasites. In *P. falciparum* CQS parasites, this colorimetric measurement of haem species involved isolating trophozoites treated with increasing parasite growth inhibitory concentrations (0.5, 1.0, 2.0, 2.5 and 3.0 × IC_{50}) for each test compound. Next, the resulting fractionated haem species (undigested haemoglobin, exchangeable haem and haemozoin) were further analysed as Fe(III)PPIX-pyridine complexes, formed as a result of haem complexation with aqueous pyridine (5% v/v pH 7.5) to produce a low-spin state complex, which can be spectroscopically measured at 405 nm [263]. The resulting observations provided insight into the behaviour of these test compounds and clearly showed similar effects on haem species in the parasite to other test compounds; AQ, benzamides and triarylimidazoles [263,334,338]. Sigmoidal profiles of parasite growth inhibition activity and exchangeable haem amounts as a function of increasing concentrations for each test compound proved to be inversely correlated. Specifically, decreasing percentage parasite growth corresponded to increasing exchangeable haem amounts present in the parasite. In spite of this, the relationship does not explain how parasite growth inhibition activity is related to the amount of exchangeable haem which varies between different test compounds. Consequently, the relationship between varying exchangeable haem amounts with parasite growth inhibition activities was explored by constructing a bar plot of the parasite growth inhibition activity with exchangeable haem amounts for all test compounds investigated in this chapter. Additionally, test compounds (**10**, **11** and AQ) investigated in D10 strain parasites were also included for comparison [263,334-338]. Observations provided evidence that parasite growth inhibition activities generally corresponded to equivalent amounts of exchangeable haem present in the parasites for all test compounds.

To better understand the mechanism by which these test compounds in this study result in the inhibition of parasite growth and haemozoin formation, investigations into their ability to accumulate in *P. falciparum* parasites were experimentally determined in CQS (NF54) parasites using a modified inoculum effect analysis [268-269,357,359-360]. Briefly, a modified p-LDH assay was used to determine the IC_{50} (NF54) values of these test compounds at increasing inoculum sizes. This was done by focusing on their accumulation in iRBCs, where, the parasitaemia was varied between 1-5% for the individual inoculum size of 1-10 while the haematocrit was kept at a constant of 2%. A linear correlation analysis was performed where the IC_{50} (NF54) values were plotted as a function of increasing inoculum sizes. From the extrapolation of this linear correlation, the absolute IC_{50} (y-intercept). From this linear correlation, the experimental CAR values, using a modified version of a previously reported equation, were calculated from the slope and y-intercept which takes into account the IC_{50}

(NF54) values at each inoculum size, absolute IC_{50} values and fractional volume of an iRBC as described in Chapter 2.

Further investigations were carried out to explore the relationship between experimental CAR values and exchangeable haem amounts as a result of these test compounds, at their IC_{50} value. A linear correlation plot was constructed by firstly converting the experimental CAR values into their total intracellular test compound amounts for all test compounds which was based on the product of the experimental CAR values, IC_{50} (NF54) values at an inoculum size of 4 and volume of a RBC under standard test conditions. From this, the individual total intracellular test compound amounts, expressed in fmols per cell, was plotted as a function of exchangeable haem amounts at each test compound IC_{50} value. Intriguingly, this plot showed a 1:1 relationship between the total intracellular test compound amounts and exchangeable haem amounts which provided further evidence for understanding the behaviour of these test compounds.

Therefore, this chapter provides effective and reliable methods that contribute to the understanding of the mechanism of action of various β-haematin inhibiting test compounds in *P. falciparum* parasites. Included, is a clear outline that the investigated test compounds inhibit parasite growth and haemozoin formation by causing variable exchangeable haem amounts present in the parasite as a direct result of their ability to accumulate at equivalent amounts.

3.2 Materials, instrumentation and methods

3.2.1 Materials

Throughout this chapter, all commercially purchased materials were of AR grade or higher and used without further purification unless specified below. All general materials that were used throughout this study are detailed in Chapter 2. Haem-containing glassware was cleaned by using 0.2 M NaOH, 1 M HNO_3, with d.H_2O and acetone rinsing in between.

3.2.2 Instrumentation

General instrumentation used throughout this study is discussed in detail in Chapter 2.

3.2.3 Software

The software used to analyse and constructing of graphs for parasite growth inhibition activities, fractionated haem species profiles, experimental CAR values and total intracellular test compound amounts is described in detail in Chapter 2.

3.2.4 Preparation of samples and solutions

The preparation of all samples and solutions is discussed in detail in Chapter 2.

3.2.5 Methods

The general experimental methods used in this chapter is discussed in detail in Chapter 2.

3.3 Results and Discussion

3.3.1 Parasite growth inhibition of *P. falciparum* cultures

A modified antiplasmodial assay (p-LDH), described previously in Chapter 2 (see ***Section 2.5.2***), was used to determine the parasite growth inhibition activity in CQS NF54 cultures for ten selected test compounds including CQ. Test compound **11** and AQ were included for comparison and have been previously reported by Wicht *et al* [334].

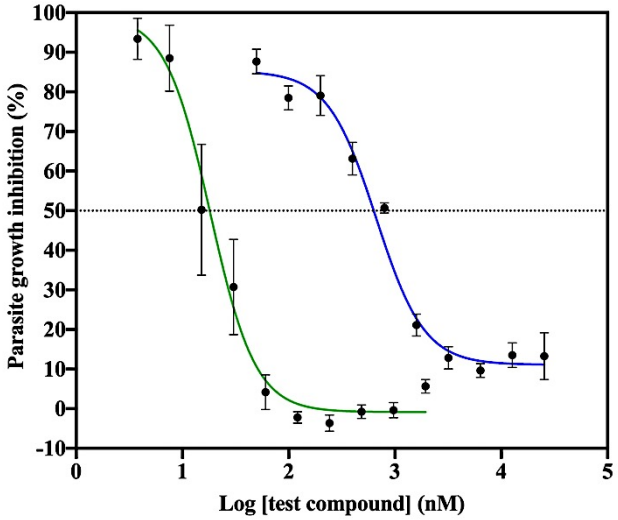

Figure 3-1*:* Parasite growth inhibition curves (mean ± SD) for test compound **1** (blue) and CQ (green) in NF54 strain cultures, generated using GraphPad Prism v8.2.1. All sigmoidal dose response curves were plotted using a non-linear regression function. The dotted line indicates the crossing point at which 50% of parasites are viable.

A typical sigmoidal dose response curve is shown in ***Figure 3-1*** for test compound **1**, showing a decrease in the percentage parasite growth at increasing concentrations of test compound **1** (blue). From this sigmoidal dose response curve, the resulting mean IC_{50} (NF54) value for test compound **1** was calculated to be 0.620 ± 0.005 µM. A parasite growth inhibition curve is also shown for CQ (green) at a lower starting concentration than test compound **1** with a mean IC_{50} (NF54) value of 0.0170 ± 0.0009 µM. This IC_{50} value was in the laboratory reference range and in close agreement with Combrinck *et al* and L'abbate *et al* who previously reported IC_{50} values of 0.019 ± 0.003 µM and 0.016 ± 0.006 µM for CQ, in CQS D10 and NF54 cultures respectively [263,335]. Dose response curves were plotted for the remaining test compounds (**2-**

10), see ***Figure 3-2*** for the structures, and showed a range of IC_{50} values with a benzimidazole-containing test compound (**4**) having the lowest parasite growth inhibition activity (8.5 ± 3 μM). For comparison, test compound **11** and AQ were included and had previously reported IC_{50} values of 0.6 ± 0.1 μM and 0.022 ± 0.003 μM respectively [334]. Test compound **11** resulted in an IC_{50} value that was in the micromolar range, close to the IC_{50} value for test compound **1** whereas, AQ resulted in a similar IC_{50} value to CQ in the nanomolar range. The observed mean IC_{50} values for the remaining test compounds are presented below in ***Table 3-1***.

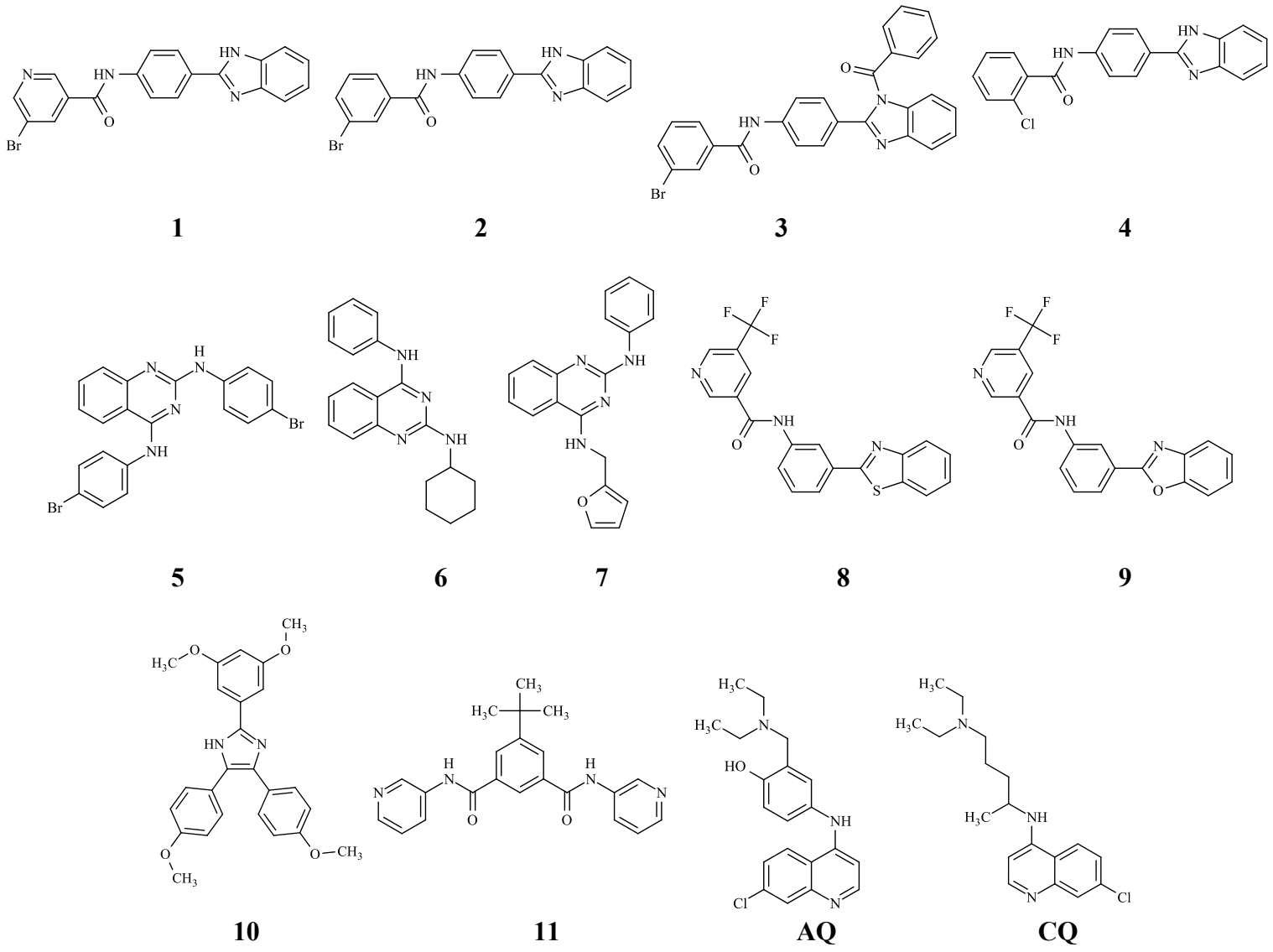

Figure 3-2: The molecular structures, as presented in Chapter 2, for the test compounds (**1-10**) investigated in this study along with previously reported test compounds **11** and AQ.

Table 3-1: The mean IC_{50} (NF54) values and SD for parasite growth inhibition of ten β-haematin inhibiting test compounds and CQ including test compound **11** and AQ, were determined using the p-LDH assay previously described by Makler *et al* [344]. All test compound IC_{50} values were determined in triplicate.

Test compound	Mean IC_{50} value (NF54) ± SD (μM)
1	0.620 ± 0.005
2	1.3 ± 0.09
3	1.7 ± 0.3
4	8.5 ± 3
5	0.19 ± 0.002
6	0.23 ± 0.008
7	0.26 ± 0.003
8	1.4 ± 0.04
9	7.4 ± 0.07
10	1.6 ± 0.0002
11 [7]	0.6 ± 0.1
AQ [7]	0.022 ± 0.003
CQ	0.017 ± 0.0009

A drawback when performing parasite growth inhibition measurements with test compounds that show low water solubility is the large error values in both parasite growth inhibition curves and corresponding IC_{50} values. Low solubility was observed for low parasite growth inhibition activity test compounds (**4** and **9**) where experimental conditions had to be modified. The modified experimental conditions involved maintaining all sample and assay solutions at physiological temperature (37 °C) to ensure complete dissolution prior to performing the experiment.

Parasite growth inhibition activities for the individual test compounds, listed in ***Table 3-1***, were required for subsequent use in the pyridine-based parasite haem fractionation plate method. These IC_{50} (NF54) values were used to determine different multiples of the inhibitory concentrations (0.5, 1.0, 2.0, 2.5 and 3.0 × IC_{50}) for each test compounds needed to inoculate CQS *P. falciparum* cultures. The results for the inhibition of haemozoin formation in the presence of these test compounds are discussed in detail in the section that follows.

3.3.2. Effects of β-haematin inhibiting test compounds on parasite haem species

To determine the effect of individual test compounds on the haem amounts per cell (expressed as fg Fe per cell) for undigested haemoglobin, exchangeable haem and haemozoin in *P. falciparum* cultures, a pyridine-based parasite haem fractionation plate method, previously described in Chapter 2 (see ***Section 2.5.3***), was used [263]. Briefly, test compounds were tested in highly synchronous CQS NF54 strain cultures that were diluted to a 2% haematocrit and 5% parasitemia. Cultures were inoculated at the immature ring stage and incubated for a period of 30-32 hrs. After the incubation period, saponin lysis of mature trophozoites was carried out before exposing the isolated trophozoites to a number of solvent mediated fractionation steps. The resulting fractionated haem species were spectroscopically assayed further as a Fe(III)PPIX-pyridine complex, for which the results are discussed in detail below.

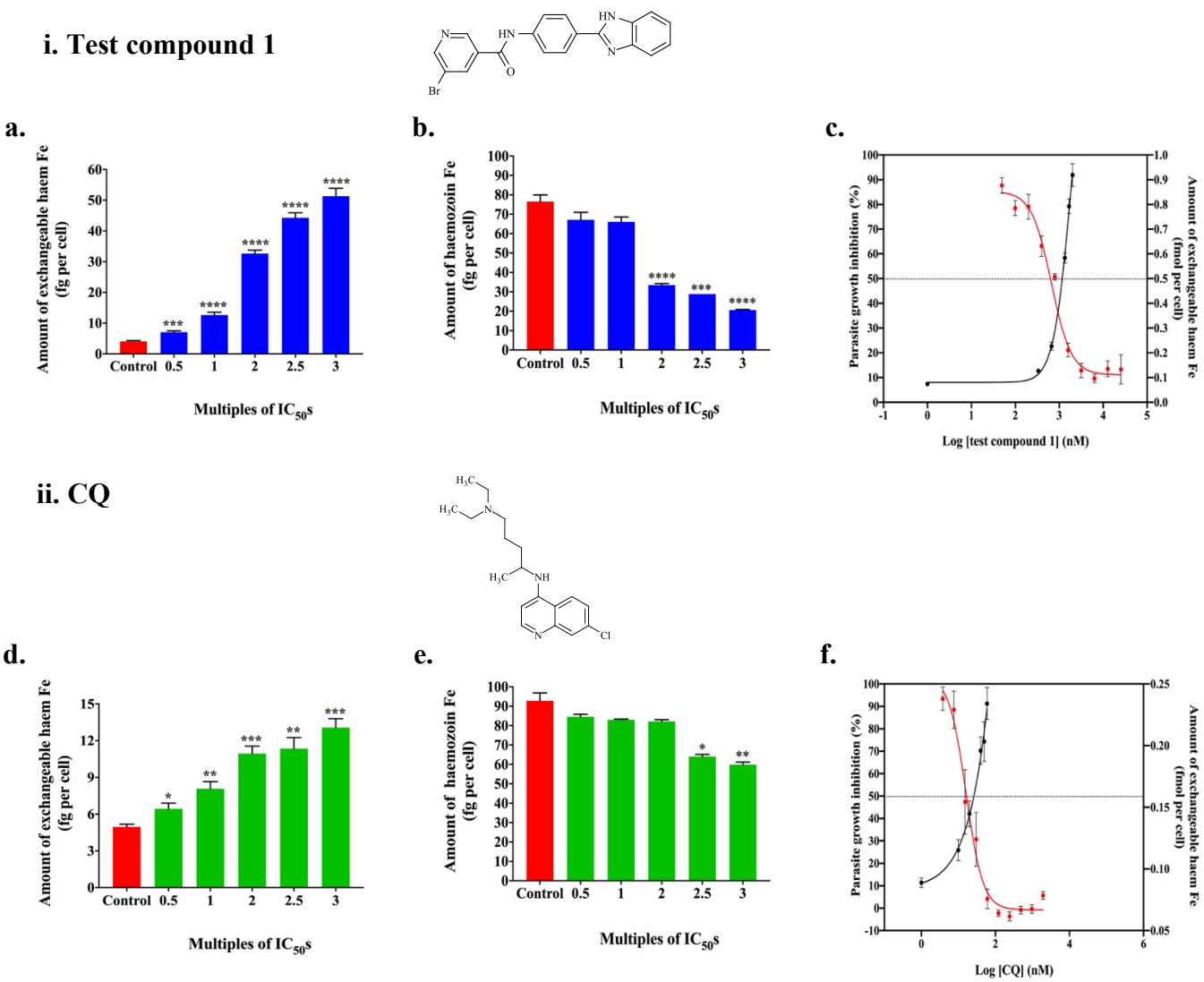

Figure 3-3: Fractionated haem species profiles for i) test compound **1** (blue) and ii) positive control, CQ (green), in synchronous CQS *P. falciparum* cultures. The above profiles represent the mass of haem Fe per cell (fg) that is attributed to (a) and (d) exchangeable haem, and (b) and (e) haemozoin. The percentage parasite growth inhibition curve (red) and exchangeable haem (fmol per cell) (black) profiles overlaid at increasing concentration for (c) test compound **1** and (f) CQ are shown above. Statistical significance was determined using a two-tailed t-test and is indicated by the asterisks, relative to the control (red) at the 95% CI, where; * p = <0.05; ** p = <0.01 and *** p = <0.001 etc.

The effect of a benzimidazole β-haematin inhibiting test compound (**1**), in comparison to CQ, was investigated at increasing multiples of the IC_{50} values. In each case, a control (red) was included, which comprised of untreated iRBCs for determination of statistical significance. In ***Figure 3-3 a*** and ***d***, both test compound **1** and CQ showed a dose-dependent increase in

exchangeable haem which was significant from 0.5 × IC_{50} to 3.0 × IC_{50}. Test compound **1** showed a 7-fold increase in the amount of haem Fe attributed to exchangeable haem with 51 fg per cell at 3.0 × IC_{50}, in comparison to a 2-fold increase for CQ. An accompanying decrease in the amount of haemozoin haem Fe per cell (***Figure 3-3 b*** and ***e***), was observed at increasing concentrations of test compound **1** or CQ, but with a 4-fold greater decrease for test compound **1** compared to CQ. The highest concentration at which parasites could be inoculated was observed to be 3.0 × IC_{50} due to difficulties experienced when fractionating the haem species. This was due to a reduction in the number of cells at a concentration above 3.0 × IC_{50} which also decreased the reliability of the total haem Fe per cell readings and, especially for exchangeable haem and haemozoin.

Figure 3-3 c and ***f*** show an inversely proportional relationship between the percentage parasite growth inhibition and the amount of haem Fe per cell associated to exchangeable haem (fmol) when plotted as a function of increasing concentrations of test compound **1** and CQ respectively. Thus, a decrease in the percentage parasite growth corresponded to an increase in the exchangeable haem amounts in the presence of test compound **1** and CQ. In more detail, at the IC_{50} value for test compound **1** or CQ exchangeable haem amounts of 0.23 fmol and 0.15 fmol per cell respectively corresponded to 50% of parasite still viable showing a clear inversely proportional relationship. This was in close agreement with previous reports [263].

These results showed a clear relationship between percentage decreased parasite growth and exchangeable haem amounts. Finally, the results for test compound **1** strongly suggest that this benzimidazole-containing test compound acts by inhibiting the formation of haemozoin which is similar to that observed for CQ.

Next, the pyridine-based parasite haem fractionation plate method was applied to eight other test compounds (**2-9**) to determine if they act similarly to test compound **1** by inhibiting the formation of haemozoin. These are listed in ***Table 3-1***. All remaining test compounds, excluding test compound **10**, were measured at increasing multiples of their individually determined IC_{50} values (0.5, 1.0, 2.0, 2.5, 3.0 × IC_{50}). Test compound **10** was excluded as the pyridine-based parasite haem fractionation data has been previously reported by Wicht *et al* [338]. The results for the remaining test compounds are discussed below.

i. Test compound 2

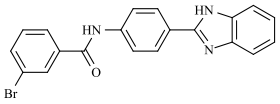

a.

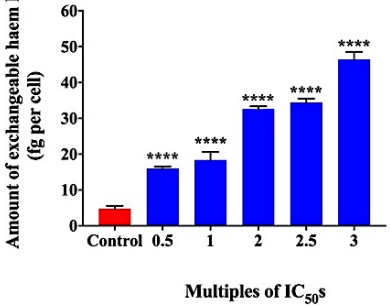

b.

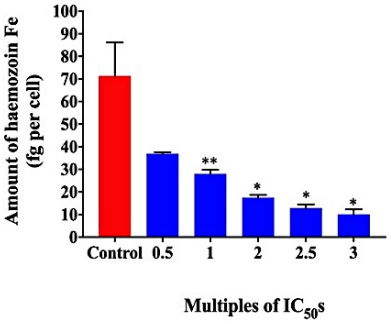

c.

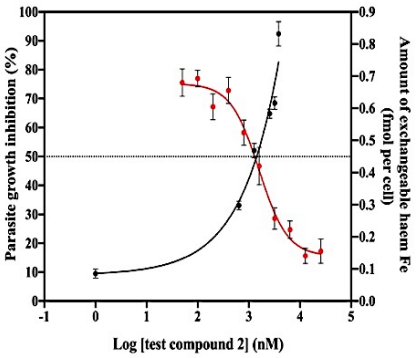

ii. Test compound 3

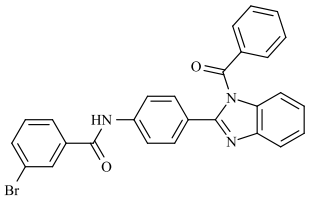

d.

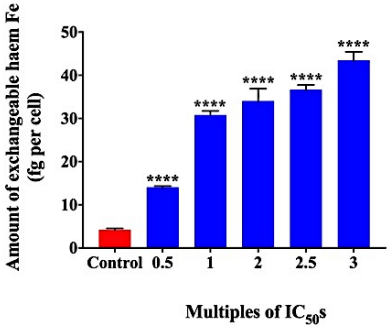

e.

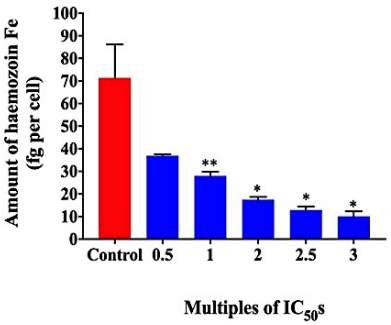

f.

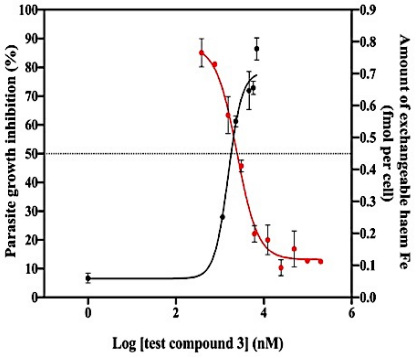

iii. Test compound 4

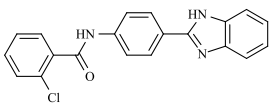

g.

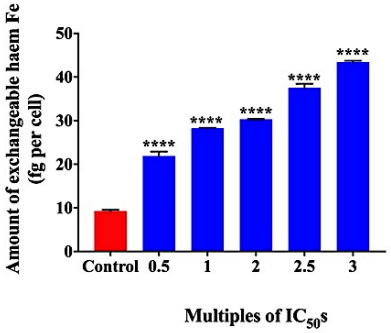

h.

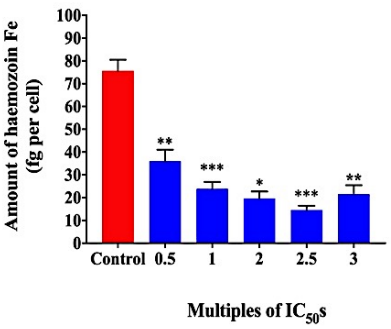

i.

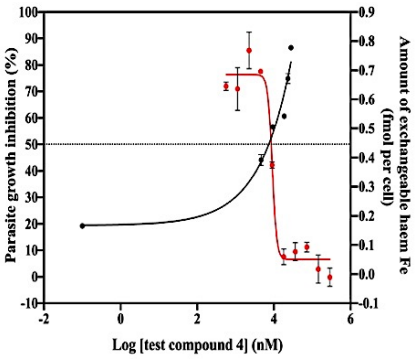

iv. Test compound 5

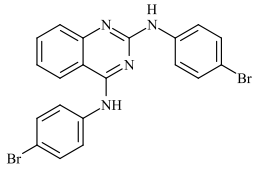

j.

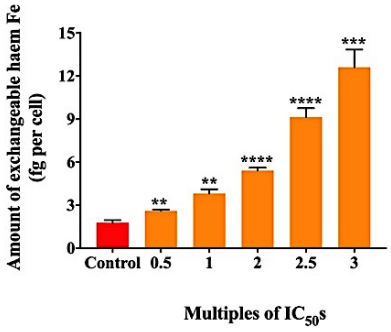

k.

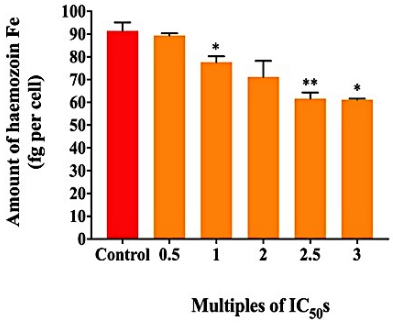

l.

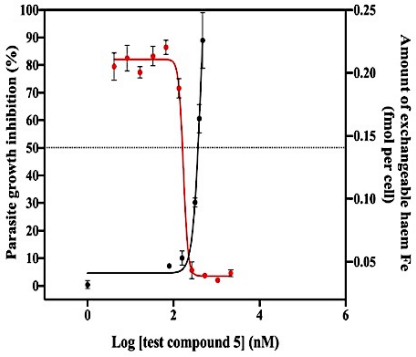

v. Test compound 6

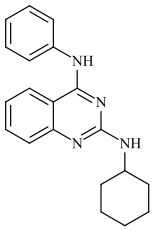

m.

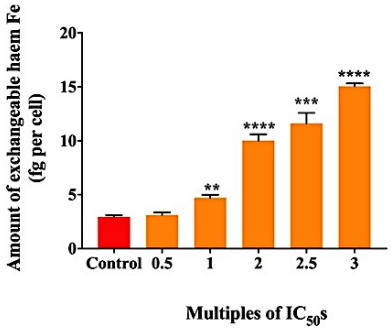

n.

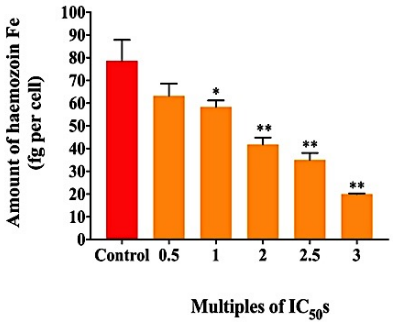

o.

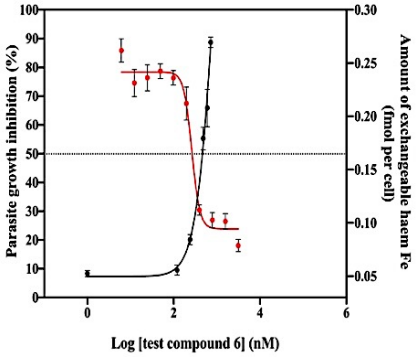

vi. Test compound 7

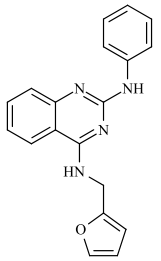

p.

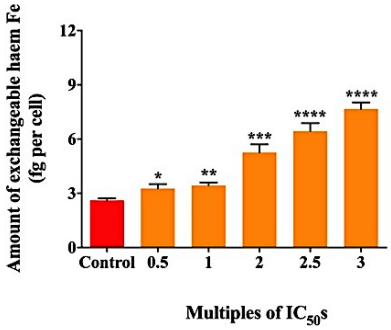

q.

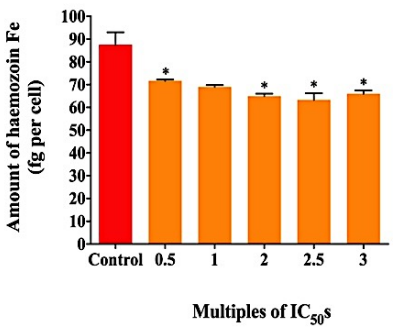

r.

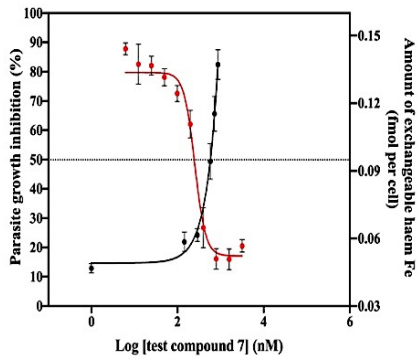

vii. Test compound 8

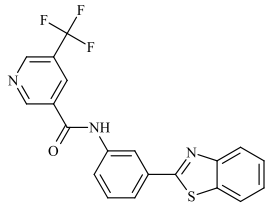

s. **t.** **u.**

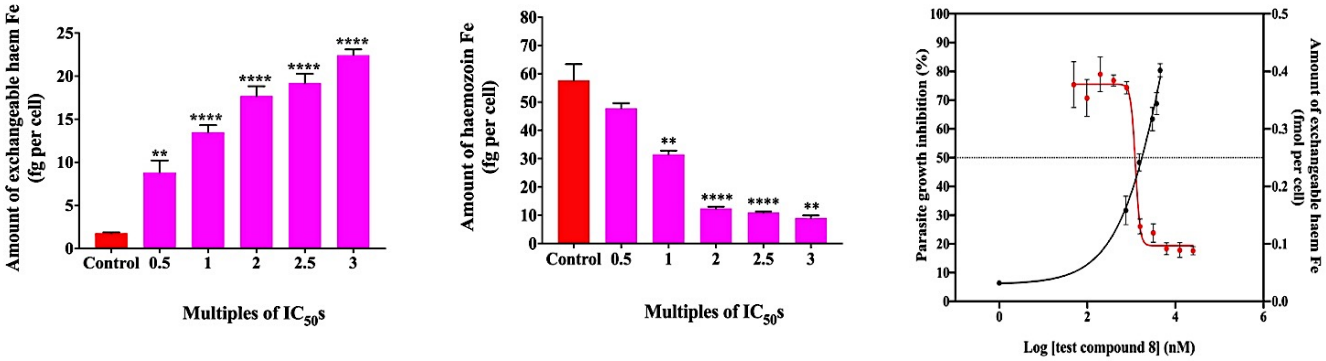

viii. Test compound 9

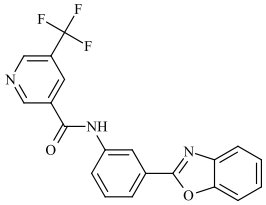

w. **x.**

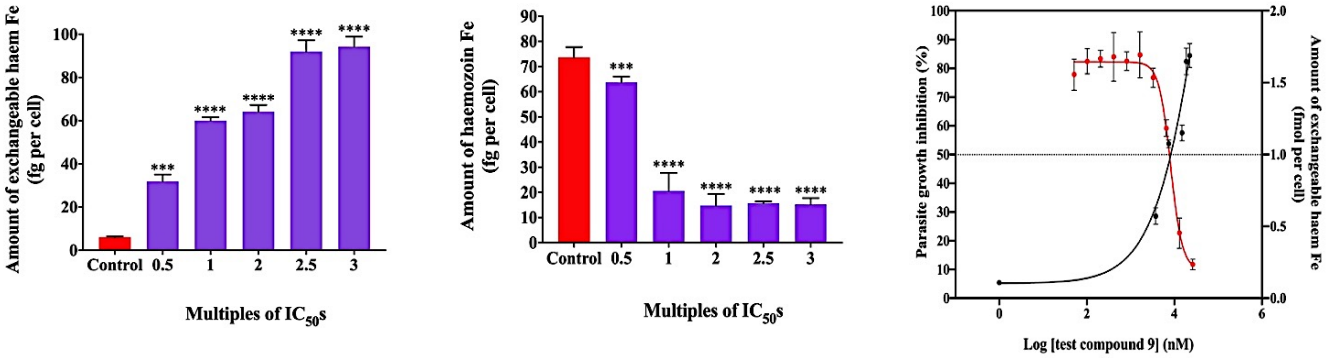

***Figure 3-4*:** Profiles for fractionated haem species for test compounds **2-9** in synchronous CQS *P. falciparum* cultures. The profiles a, d, g, j, m, p, s and v) represent the mass of haem Fe per cell (fg) that is attributed to exchangeable haem and b, e, h, k, n, q, t and w) haemozoin haem Fe per cell relative a control (red). The overlaid sigmoidal profiles c, f, i, l, o, r, u and x) represent percentage parasite growth inhibition (red) and exchangeable haem (fmol per cell) (black) at increasing concentration for test compounds **2-9**. Statistical significance was determined using a two-tailed t-test and is indicated by the asterisks, relative to the control (95% CI), where; * p = <0.05; ** p = <0.01 and *** p = <0.001 etc.

A dose-dependent increase in the amount of exchangeable haem (***Figure 3-4 a, d, g, j, m, p, s*** and ***v***) for all test compounds (**2-9**), relative to the control was observed and similar to that observed for test compound **1**. More specifically, test compounds **2**, **3** and **4** showed significant increases from 0.5 to 3.0 × IC_{50} relative to the control which were similar but lower than test compound **1**. Test compounds **5**, **6** and **7** showed relatively small increases in exchangeable haem amounts compared to the remaining test compounds, demonstrating increases comparable to that of CQ. One specific test compound, test compound **7** showed significant increases from 0.5 to 3.0 × IC_{50} but resulted in the lowest amount of exchangeable haem compared to the remaining test compounds.

The haemozoin haem Fe profiles (***Figure 3-4 b, e, h, k, n, q, t*** and ***w***) for most of the test compounds showed greater dose-dependent decreases in the amount of haemozoin than test compound **1** with the exception of test compounds **5** and **7**. Test compound **4** showed a significant decrease in haemozoin from 0.5 to 3.0 × IC_{50}, however, at concentrations higher than 3.0 × IC_{50}, solubility difficulties were experienced, making it difficult to obtain reliable results. In the case of test compounds **5** and **7**, small decreases in haemozoin from 91 fg per cell in the control to an average of 60 fg per cell at 3 × IC_{50} for both were observed. These results resembled decreases in the amount of observed for CQ. This could possibly suggest that test compounds **5** and **7** could have more than one mode of action. There is a widely accepted theory that quinoline-containing compounds like CQ inhibit the formation of haemozoin but could also result in the inhibition of protein synthesis and the activity of proteases inside the parasite DV which could explain the observed modest decreases in haemozoin amounts for test compound **5** and **7** [361-362].

Unexpectedly for the second least active test compound (**9)**, 60 fg per cell of exchangeable haem was observed at the 1.0 × IC_{50} dosage and the most significant decrease in haemozoin (68 fg per cell) was observed. Despite the results observed for test compound **9**, solubility difficulties were encountered which made it difficult to obtain reliable results. Along with these observations, Giemsa smear microscope images were obtained for both untreated iRBCs (***Figure 3-5 a***) and test compound **9**-treated iRBCs (***Figure 3-5 b***). In ***Figure 3-5 b***, evidence of an unprecedented total absence of haemozoin crystals in the parasites DV compared to untreated iRBCs was observed. This was not the case for test compounds **1-8** and CQ. At this point, test compound **9** could be considered to be more of an effective haemozoin inhibitor than the remaining test compounds including test compound **1**.

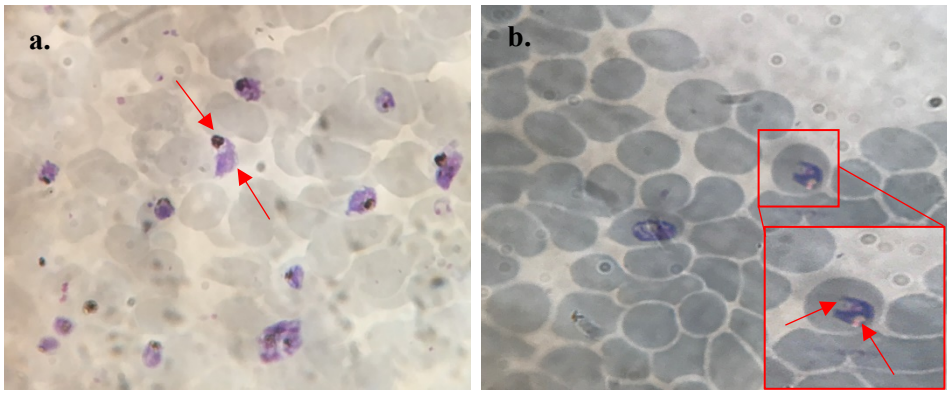

***Figure 3-5*: Giemsa stained microscope images of treated CQS NF54 parasites, showing a) untreated iRBCs (red arrows) and b) test compound **9**-treated iRBCs at the IC_{50} value. Empty parasite DVs are indicated by the red arrows in b.**

The parasite growth inhibition curves overlaid with the exchangeable haem (fmol Fe per cell) as a function of increasing concentrations for the individual test compounds, in ***Figure 3-4 c, f, i, l, o, r, u*** and ***x*** showed that with increasing amounts of exchangeable haem Fe present in the parasites there is a corresponding decrease in the percentage parasite growth. Similar to test compound **1**, exchangeable haem amounts at the IC_{50} value for each test compound (**2-9**) ,with the exception of test compounds **5**, **6** and **7**, corresponded to 50% parasites still viable. For test compounds **5**, **6** and **7**, exchangeable haem amounts at the IC_{50} value was observed to cross the percentage parasite growth inhibition at a much lower percentage of parasites still viable.

This pyridine-based parasite haem fractionation plate method proved to be a reliable and efficient method for determining whether these β-haematin inhibiting test compounds, like CQ, inhibit the formation of haemozoin. These results strongly suggest that these test compounds, from a range of scaffolds, act by inhibiting the formation of haemozoin. What is also clear, is that parasite growth inhibition activity does not occur at a single given amount of exchangeable haem in the parasite. Indeed the observations with test compound **9**, emphasize this.

3.3.3 Relationship between parasite growth inhibition activity and exchangeable haem amounts.

Given the observations in ***Section 3.3.2***, a key question was whether parasite growth inhibition activity is related to the amount of exchangeable haem in the parasite. For this reason, the mean IC_{50} value of each test compound (**1-9**) was plotted next to the amount of exchangeable haem expressed in fmol Fe per cell at its IC_{50} value. Previously reported haem species data for test

compounds **10**, **11** and AQ was included in the plot below for comparison to the test compounds investigated in this study.

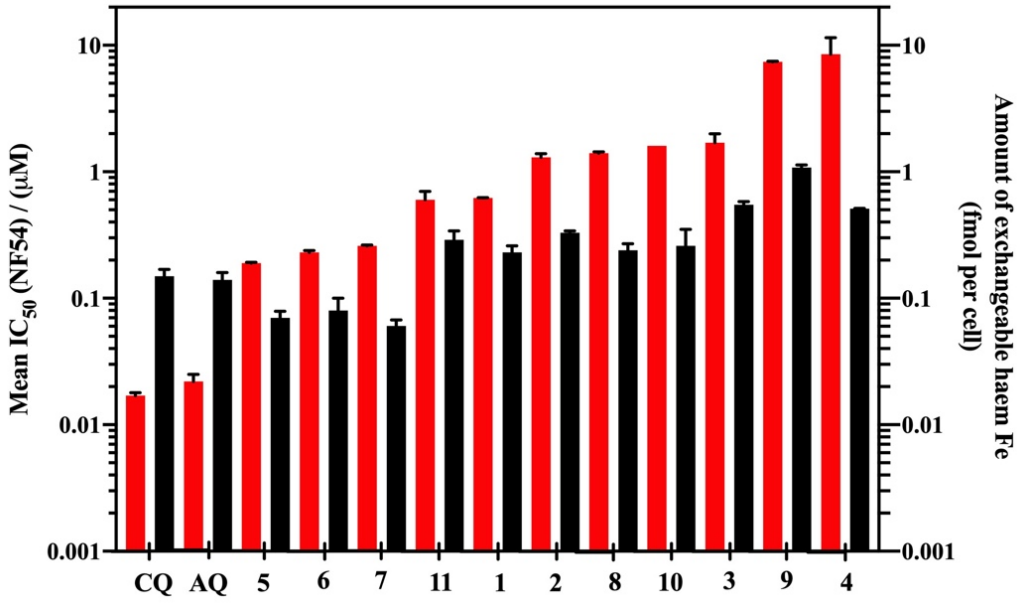

Figure 3-6: Bar plot of mean IC_{50} value (red) and corresponding amount of exchangeable haem in fmol per cell (black) present in treated CQS *P. falciparum* isolated trophozoites for all compounds (**1-9**) tested including test compound **10**, **11**, AQ and CQ in order of increasing IC_{50} values.

A bar plot for the full series of test compounds (**1-9**) investigated in order of increasing IC_{50} values in this chapter, including CQ and comparative test compounds **10**, **11** and AQ is shown in ***Figure 3-6***. A rough trend of increasing IC_{50} values (decreasing parasite growth inhibition activity) with corresponding increased amounts of exchangeable haem at the individual IC_{50} value for all test compounds was observed.

In more detail, test compounds with lower IC_{50} values, like test compound **5**, resulted in smaller amounts of exchangeable haem whereas test compounds with higher IC_{50} values, like test compound **4**, resulted in higher amounts of exchangeable haem. On the other hand, test compounds **5**, **6** and **7** showed higher IC_{50} values that corresponded to lower amounts of exchangeable haem, opposite to similar quinoline-containing test compounds CQ and AQ in which lower IC_{50} values corresponding to significantly higher amounts of exchangeable haem present in the parasite.

Lastly, previously published test compounds (**10**, **11** and AQ) that were investigated in other CQS *P. falciparum* strains (D10 and NF54 respectively) were included for comparative reasons (***Figure 3-6***) [334,338]. These test compounds too conformed to this trend of increasing

IC_{50} value with corresponding increasing amounts of exchangeable haem present in parasites, therefore further suggesting that this trend is genuine, even if not statistically significant.

3.3.4 Inoculum effect analysis

From the observed results in ***Section 3.3.1-3.3.3*** above, the ability of these test compounds to accumulate in iRBCs was investigated, excluding test compound **4** and **9** due to previously mentioned solubility difficulties with the solubility of these test compounds. This was carried out by measuring the experimental CAR values in CQS NF54 strain parasites using the inoculum effect analysis. As discussed in Chapter 1, cellular accumulation can be determined from the linear relationship of decreasing parasite growth inhibition activity (increasing IC_{50} values) with increasing numbers of inoculated parasites [269,361]. According to previous reports by Hawley *et al*, Bray *et al* and Brook *et al*, this linear relationship of increasing IC_{50} values can be further explained by the decreasing concentration of test compound in the extracellular complete medium as an increasing concentration of test compound is taken up by parasites [269,283,359]. This increasing number of inoculated parasites can be defined by what is known to be an inoculum size, where each inoculum size is a product of the varying percentages of parasitaemia and haematocrit. As outlined in Chapter 2 (see ***Section 2.5.4***), to ensure that the optimal amount of these test compounds is taken up solely by iRBCs, the parasitaemia was varied (1-5%) at a constant haematocrit (2%) throughout this study.

Secondly, the experimental CAR values were determined from this linear relationship using a modified equation, shown in ***Section 2.5.4*** (***Eq. 6***), which takes into account the IC_{50} values at each inoculum size, absolute IC_{50} values and the fractional volume of an iRBC [269,363]. In more detail, the absolute IC_{50} value (test compound IC_{50} value at the limit of infinite dilution of iRBCs) was predicted from the extrapolation of this linear relationship to an inoculum size of zero (y-intercept). The fractional volume of an iRBC can be calculated from the division of the inoculum size by 10000 (see ***Section 2.5.4, Eq. 7***). The results are discussed below.

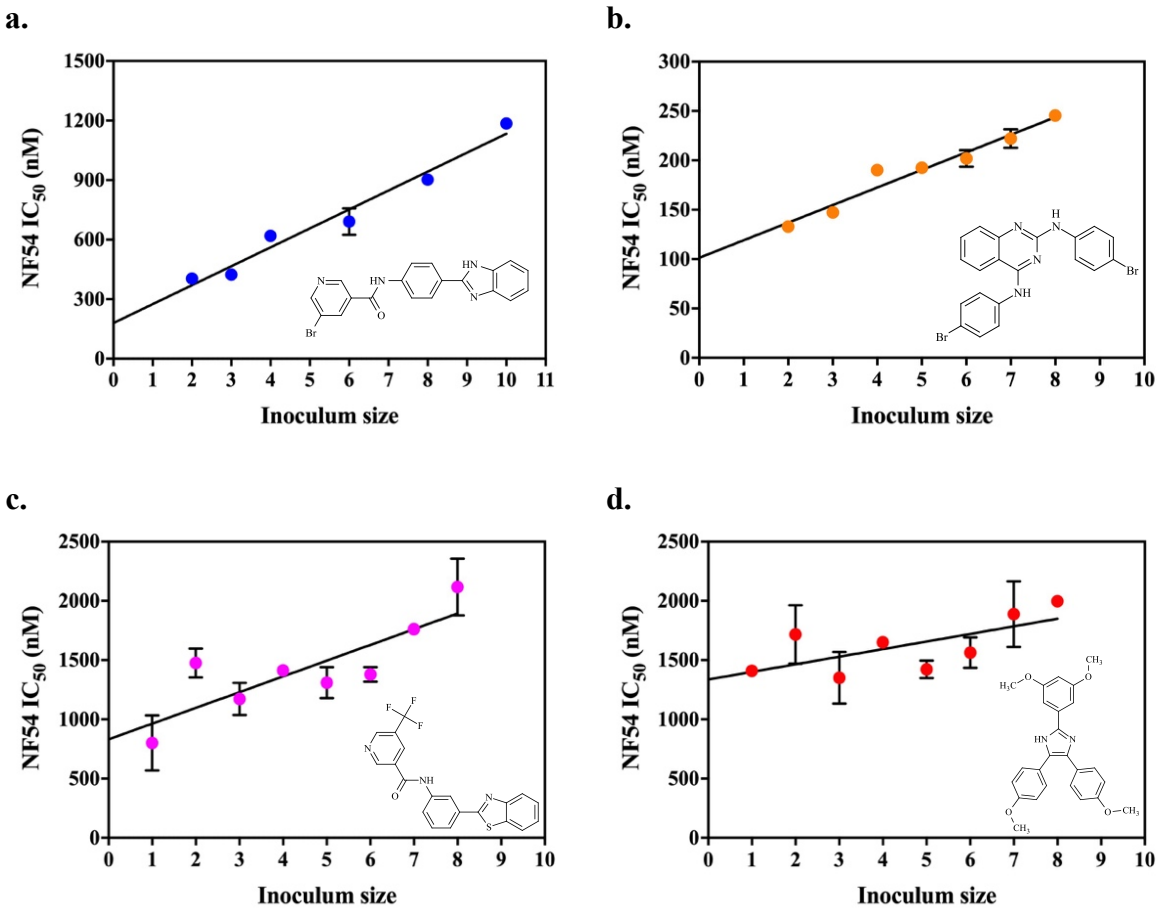

Figure 3-7: Linear relationship plots for the inoculum effect analysis in CQS (NF54) strain parasites for (a). test compound **1** (blue), (b) test compound **5** (orange), (c) test compound **8** (pink) and (d) test compound **10** (red) that resulted in experimental CAR values of 5305 ± 1079, 1757 ± 242, 1599 ± 552 and 479 ± 223 respectively. A linear regression function, using GraphPad Prism v8.2.1, was used to fit the above curves resulting in correlation coefficients, $R^2 = 0.9466$,$R^2 = 0.9524$,$R^2 = 0.6974$ and $R^2 = 0.4489$ respectively. Each inoculum size was tested in triplicate.

Figure 3-7 a-d illustrates the linear relationship plots for the inoculum effect analysis for four test compounds (**1**, **5**, **8** and **10**). For all these test compounds, a general trend of increasing inoculum size corresponded to increasing IC_{50} values. This agreed with previous observations by Hawley *et al*, Wicht *et al* and O'Neill *et al* with similarly behaving test compounds [269,334,363]. Test compound **1** showed a more significant increase in IC_{50} value of 3-fold ($R^2 = 0.9466$) in the micromolar range (***Figure 3-7 a***) over the range measured compared to a 2-fold increase for test compound **5**, **8** and **10**. It was also observed, specifically for test compound **8** and **10** that there were much lower increases in IC_{50} values ($R^2 = 0.6974$ and $R^2 = 0.4489$ respectively).

The remaining test compounds (test compound **2-3** and **6-7**) showed similar increases in IC_{50} values with increasing inoculum size where, test compound **3** specifically showed a 3-fold increase in IC_{50} value which was comparable to that of test compound **1**.

Certain limitations were noticed when using the p-LDH method to carry out the inoculum effect analysis which included: (1) unreliable IC_{50} values were found for the inoculum size 1 and 10, where, for an inoculum size 1 there were too few parasites to give a strong enough reading. The opposite was observed for inoculum size 10, where a much reduced effect on the parasite growth due to the number of parasites being too low for the amount of test compound being too high which resulted in complications in obtaining reliable IC_{50} values; (2) the absolute IC_{50} values were observed to be highly dependent on how close the intercept was to zero, therefore, resulting in extremely high errors and experimental CAR values tending to infinity where the intercept was too low; (3) solubility difficulties were also encountered when performing this experiment, especially at the inoculum size 10, where test compounds would precipitate out of solution even after maintaining all solutions at physiological temperature (37 °C). This is the reason why all test compounds that were investigated in this study, except for test compound **1**, only resulted in accurate IC_{50} values for inoculum sizes in the range 2-8.

Table 3-2: Experimental CAR values (mean ± SD) for all test compounds in CQS NF54 trophozoite cultures, including previously reported test compounds **11**, AQ and CQ.

Test compound	Experimental CAR value
1	5305 ± 1079
2	1912 ± 276
3	2039 ± 757
4	N/A
5	1757 ± 242
6	1823 ± 381
7	1746 ± 206
8	1599 ± 552
9	N/A
10	479 ± 223
11 [7]	5934 ± 945
AQ [7]	98024 ± 15296
CQ [7]	105342 ± 3365

* N/A, could not be determined

Illustrated in ***Table 3-2*** are the experimental CAR values which were determined using the individual slope and y-intercept values (***Eq. 6***) from the inoculum effect analysis plot for each test compound (**1-10**), excluding test compounds **4** and **9**. Previously reported test compounds (**11**, AQ and CQ) determined in CQS NF54 cultures were also included [334]. Of the series of test compounds investigated, test compound **1** was observed to be about 5305 times more concentrated in iRBCs compared to the external at its IC_{50} value, the highest experimental CAR value of the test compounds measured in this study.

Varying experimental CAR values for the remaining test compounds were observed, albeit, much lower than test compound **1**. Indeed, a 3-fold decrease in the experimental CAR values was observed for the remaining test compounds, indicating that these test compounds would be expected to be much less concentrated in iRBCs. Test compound **10**, a triarylimidazole derivative resulted in the lowest experimental CAR value of the series. This could be due to suggestions that have been previously published where, for triarylimidazole-

containing test compounds like test compound **10**, certain groups that allow for the coordination or hydrogen bonding with haem are lacking [338].

On the other hand, comparing these test compounds to previously published test compounds **11**, AQ and CQ, much lower experimental CAR values were observed, except for, the benzamide-containing test compound (**11**) which was similar to test compound **1**. It was also assumed that quinoline derivatives (test compound **5**, **6** and **7**) would have experimental CAR values close to that of AQ and CQ, but this was not the case. AQ is known to accumulate more than CQ in parasites and this was not observed. The experimental CAR for AQ (98,024 ± 15,296) was lower than the experimental CAR value for CQ which was 105,342 ± 3,365 which did not agree with results published by Hawley *et al* [269]. However, Wicht *et al* and Krogstad *et al* have previously suggested that varying experimental CAR values could be as a result of differences in the pH ranges (4.8-5.0) of the parasite DV across different *P. falciparum* strains which could affect the experimental CAR values when considering the accumulation of these test compounds to be as a direct result of the mechanism of pH trapping [128,334]. It has also been suggested that binding of quinolines, like CQ, to haem across different parasite strains may also be the reason for varying experimental CAR values as seen for CQ and AQ and the test compounds investigated here [208,356,364].

Hence, with the variations observed in the experimental CAR values, it could be concluded that the mechanism by which these test compounds accumulate could be driven by pH trapping, even if pH trapping is a small contribution to this equilibrium process of accumulation in parasites [269]. However, this lack of correlation could also suggest that the accumulation process of these test compound in CQS NF54 parasites is more complex than only pH trapping and would need further investigations. This was in agreement with the observations reported by Wicht *et al* [334]. A leading candidate for accumulation could be that haem binding may be the primary cause for the amount to which these test compounds accumulate in the parasite, which is in agreement with previous reports [128,208,269,283,334].

Therefore, the experimental CAR values for all test compounds, including test compound **11**, AQ and CQ, were converted into their individual total intracellular test compound amounts within iRBCs and comparisons made to the observed amounts of exchangeable haem in the parasite.

3.3.5 Relationship of total intracellular test compound and exchangeable haem amounts present in CQS iRBCs.

The total intracellular test compound amounts for all test compounds (**1-10**), excluding test compounds **4** and **9** were investigated. In brief, the intracellular test compound amounts (fmol per cell) were calculated based on the product of their experimental CAR values, IC_{50} values and the volume of an iRBC (see ***Section 2.5.5, Eq. 8***). The values are listed in ***Table 3-3*** where test compound **11**, AQ and CQ were also included for comparative reasons.

Table 3-3: Total intracellular test compound amounts per cell (mean ± SD) for all test compounds in NF54 cultures.

Test compound	Total intracellular test compound amount (fmol per cell)
1	0.27 ± 0.06
2	0.21 ± 0.04
3	0.4 ± 0.2
4	N/A
5	0.028 ± 0.004
6	0.037 ± 0.008
7	0.042 ± 0.006
8	0.20 ± 0.07
9	N/A
10	0.07 ± 0.03
11	0.30 ± 0.07
AQ	0.18 ± 0.03
CQ	0.17 ± 0.01

* N/A, could not be determined

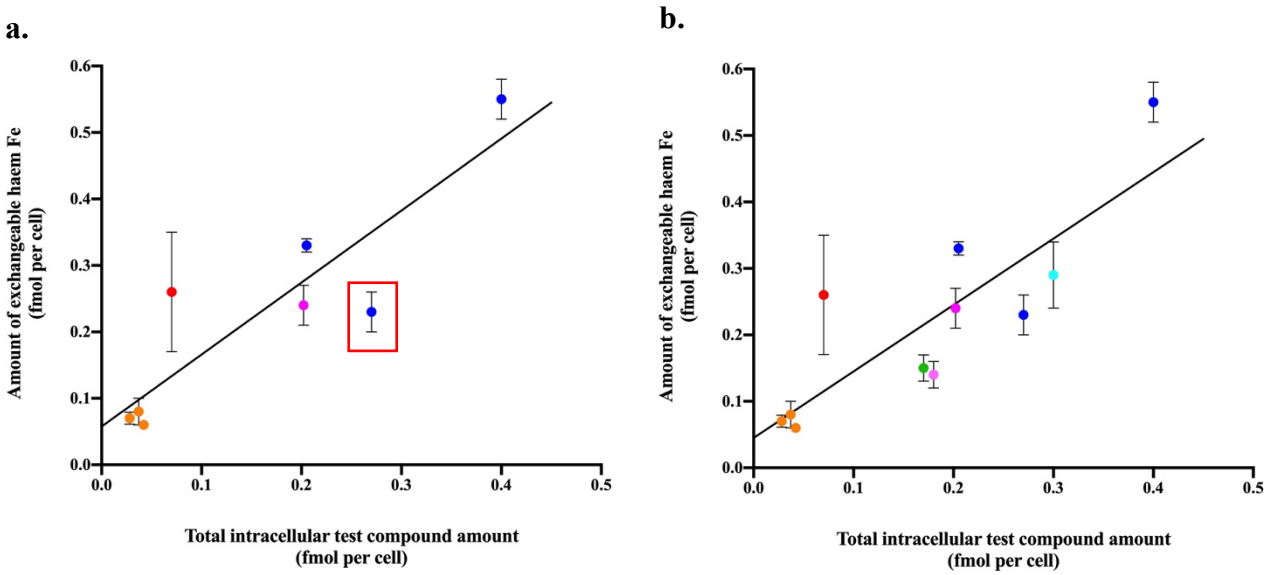

Figure 3-8: Linear correlation plots of total intracellular test compound amount (fmol per cell) plotted as a function of the amount of exchangeable haem at the IC_{50} (fmol per cell) present in treated *P. falciparum* CQS (NF54) isolated trophozoites for (a) all test compounds excluding test compound **4** and **9**, and (b) including comparative test compounds **11**, AQ and CQ. A linear regression analysis, using GraphPad Prism v8.2.1, was performed to fit the above curve resulting in a correlation coefficients (95% CI) of $R^2 = 0.7884$ and $R^2 = 0.7055$ respectively.

Linear correlation plots were constructed where the individual exchangeable haem amounts were plotted as a function of total intracellular test compound amounts at the mean IC_{50} value for all test compounds excluding **4** and **9** (***Figure 3-8 a***) and including comparative test compounds **11**, AQ and CQ (***Figure 3-9 b***).

In ***Figure 3-8 a***, an apparent 1:1 relationship was observed where for example test compound **1** (red square) was shown to have a moderate total intracellular test compound amount which corresponded to a moderate amount of exchangeable haem at its IC_{50} value present in each parasite and is indicated in the red square. This was true for the remaining test compounds and resulted in a correlation coefficient of $R^2 = 0.7884$ ($p = 0.0032$). Interestingly, test compound **3**, a relatively active test compound with a mean IC_{50} value of 1.7 ± 0.3 µM, showed the second highest amount of exchangeable haem in the parasite which related to the highest total intracellular test compound amount (blue). On the other extreme, more active test compounds like test compounds **5-7** (orange) resulted in very small amounts of exchangeable haem that corresponded to small total intracellular test compound amounts present in parasites.

Finally, in an effort to establish whether or not this trend was applicable to different test compounds determined elsewhere, test compounds **11**, AQ and CQ were included in this linear correlation plot (***Figure 3-8 b***). Observations showed that these test compounds too followed this apparent linear correlation and still resulted in a statistically significant plot with a correlation coefficient of $R^2 = 0.7055$ ($p = <0.0012$).

The findings from these linear correlation plots further explains how these test compounds are able to inhibit the formation of haemozoin, causing a build-up of exchangeable haem by accumulating at a 1:1 equivalence in the parasite. The equivalence in amount strongly suggests that these test compounds could accumulate via Fe(III)PPIX-binding which in turn allows for the formation of Fe(III)PPIX-inhibitor complexes in CQS NF54 parasites. Lastly, it was suggested from these data that pH trapping, to a certain extent, plays a role in the ability of these test compounds to accumulate in the parasite, specifically for quinoline-containing test compounds like AQ and CQ [204,265,272,293,365].

3.4 Summary and conclusions

In summary, the inhibition of parasite growth, haemozoin formation and cellular accumulation of ten chosen β-haematin inhibiting test compounds (**1-10** and CQ) to accumulate in *P. falciparum* CQS cultures was successfully investigated and compared to previously published test compounds (**11** and AQ) in this study.

Most of the test compounds were observed to decrease parasite growth in a dose-dependent manner, similar to CQ, but had micromolar IC_{50} values. It was also observed that when performing p-LDH experiments for test compounds showing low water solubility, certain modifications were required.

Use of a pyridine-based parasite haem fractionation plate method to determine the mass of haem Fe per cell profiles in CQS NF54 trophozoite cultures treated with test compound **1** showed a 4-fold increase in exchangeable haem amounts and 3-fold decreases in the amounts of haemozoin compared to CQ. This meant that test compound **1**, at a higher IC_{50} value, could be equivalent to that of CQ at inhibiting the formation of haemozoin. Similarly, the remaining test compounds (test compound **2**-**9**) that were investigated proved to behave like test compound **1**, excluding two of the quinazoline-containing test compounds (test compounds **5** and **7**). Interestingly, one of the least active test compound (test compound **9**) resulted in the most significant decrease in haemozoin amounts at the IC_{50} value with evidence of empty parasite DVs with no observable haemozoin crystals. These results confirmed that like a well-known β-haematin inhibiting test compound CQ, the mode of action for all compounds tested in this study was to inhibit the formation of haemozoin, with the exception that quinazoline-containing test compounds may have more than one mode of action. Besides, overlaying plots of decreasing percentage parasite growth and increasing exchangeable haem amounts as a function of dose-dependent increasing test compound IC_{50} multiples further confirmed their target of action to be the formation of haemozoin.

A bar plot of parasite growth inhibition activity and exchangeable haem amounts as a function of individual test compounds exhibited a trend in which amounts of exchangeable haem tended to increase with the mean IC_{50} values observed for all test compounds (**1**-**9**) including test compounds (**10**, **11** and AQ) that were determined elsewhere. However, this trend was not definitive and is counterintuitive given that higher levels of exchangeable haem would be expected to be more toxic. It thus does not reveal how the parasite growth inhibition activity relates to the observed amount of exchangeable haem present in the parasite.

With the knowledge of haemozoin formation being the major pathway within the parasites DV and evidence of these test compounds being involved in its inhibition, they were considered to be efficient haemozoin inhibitors. It has long been suggested that the cellular accumulation of haemozoin inhibitors, like CQ, within the parasites DV is vital in their ability to inhibit the formation of haemozoin and this may involve haem-binding [265,270,355-356,366].

This led to further investigations to determine the cellular accumulation of these haemozoin inhibiting test compounds in CQS *P. falciparum* parasites. Experimental CAR values were determined using a previously published inoculum effect analysis for all test compounds. Linear correlation plots were observed whereby increasing IC_{50} values as a function of increasing inoculum size was used to quantitatively determine the experimental CAR values. The experimental CAR values were much lower for most of these test compounds relative to the test compounds **11**, AQ and CQ, which were previously determined by Wicht *et al* using a similar procedure [334]. Less basic test compounds do not accumulate primarily due to pH trapping which suggests that other influencing factors, like haem-binding, may play a primary role which then leads to the suggestion that accumulation of these compounds in CQS NF54 strain parasites may be more complex than initially believed, probably involving both pH trapping and haem-binding.

Further calculations were carried out to determine the total intracellular test compound amounts for these compounds as well as, test compounds **11**, AQ and CQ. A linear correlation plot of the exchangeable haem amounts plotted as a function of total intracellular test compound amount present in parasites at the IC_{50} values of these test compounds was constructed. Observations showed an apparent 1:1 relationship, and addition of test compound **11**, AQ and CQ to the plot maintained the linear correlation showing that these test compounds too conformed to this relationship.

In conclusion, it could not be clearly explained from the above data if parasite growth inhibition activities are dependent on either the total intracellular test compound amount, amount of exchangeable haem present in parasites or both. Although, it was apparent that the ability of these test compounds to accumulate in iRBCs is vital for the build-up of exchangeable haem and thus inhibiting the formation of haemozoin. It has, however, been previously suggested that haem-binding by the co-localization of haem and test compound in the DV of the parasite allows for the interaction between test compounds and haem. This co-localization has been suggested to be from a possible haem-inhibitor complex forming inside the parasite and could be responsible for the ability of these compounds to accumulate at the site of action thus inhibiting the formation of haemozoin [279,355]. This is investigated further in Chapter 4.

4

Spectroscopic evidence of a Fe(III)PPIX-inhibitor complex in *P. falciparum* parasites

4.1 Introduction

A widely suggested theory for understanding the behavior of haemozoin inhibiting antimalarials is centered around their association with Fe(III)PPIX in *P. falciparum* parasites. According to this hypothesis, the method which they achieve this is by membrane impermeable accumulation of the protonated form in the DV, which concentrates the drug, driving equilibrium binding of these haemozoin inhibitors to Fe(III)PPIX. In turn, the build-up of Fe(III)PPIX or Fe(III)PPIX-inhibitor complex inside the parasite interrupts parasite membrane function, causing subsequent parasite death [283,293,297,367-370].

Researches have used spectroscopic techniques and diagnostics tools to detect the distribution of Fe(III)PPIX and to attempt to provide evidence of a Fe(III)PPIX-inhibitor complex that has been suggested to exist in parasites [311,325,371]. In 2002, Egan *et al* used electron microscopy with electron spectroscopic imagining techniques together with chemical measurements of the Fe content of cellular fractions to show that > 90% of the total Fe present in untreated parasites is presented as Fe(III)PPIX that was attributed to haemozoin. This study also used, Fe-Mössbauer spectroscopy of freeze-dried isolated trophozoites to confirm that more than 95% of Fe was haemozoin that was located in the parasites DV [287]. Related studies detected, with the use of TEM and ESI, that the Fe associated Fe(III)PPIX signal in untreated parasites was mainly attributed to haemozoin with evidence of negligible Fe in the parasites' cytoplasm [242,287]. In addition, parasites treated with CQ were observed to result in a substantial amount of Fe in the form of Fe(III)PPIX in the parasites' cytoplasm which was suggested to be as a direct result of haem partitioning into lipid environments [287,372]. This was also in agreement with the previous findings that were reported by Schmitt *et al* and Bendrat *et al* in 1993 and 1995 respectively [146,284].

Another non-destructive technique that has long been used to identify structural and chemical variations in the speciation of Fe in Fe(III)PPIX complexes is Raman spectroscopy [315,373]. In 2008, Tarcea *et al* studied the spectra of haematin and parasite extracted haemozoin, where for haemozoin, certain peaks were observed to be enhanced using varying excitation wavelengths. They concluded that the most suitable excitation wavelength was 647 nm for the study of the structures of Fe(III)PPIX complexes [374]. Wood *et al* had previously reported spectra consistent with high-spin Fe(III) electronic structures of both β-haematin and haemozoin at the excitation wavelengths of 780 nm and 830 nm. From this, they inferred that the enhancement of certain Raman peaks, specifically the electron density marker band at 1374 cm^{-1}, could be attributed to excitonic coupling in covalently bonded porphyrins that were

aggregated [320]. They also showed that the spectrum of β-haematin appeared to be similar to that of the spectrum for haemozoin and agreed with the findings of Bohle *et al* [375]. Other studies have also shown that distinctions between oxy- and deoxy-haemoglobin, can be observed using Raman spectroscopy. To explore the variability in the Raman spectra for oxy- and deoxy-haemoglobin, they used a well-known chemometric analysis method, namely PCA. Here, they showed that the scores from the PCA plot exhibited a sigmoidal curve that coincided with the oxygen saturation curve observed in live cells [313]. In 2015, Tempera *et al* explored the interaction of CQ and haemozoin-like crystals and showed increased intensities in parts of the spectra. This was suggested to be indicative of π-π interactions between the pyrrole ring of Fe(III)PPIX and the quinoline ring of CQ. They also showed spectra of haemin, β-haematin and haemozoin where similarities were observed for β-haematin and haemozoin which supported previously published findings by Wood *et al* and Bohle *et al* [313,320,375-376]. Studies by Kozicki *et al* also reported observed increases in intensities of the Raman peaks in the Fe(III)PPIX core and pyrrole-ring stretching regions for CQ-treated iRBCs on a single cell level with an excitation of 532 nm. From this, they were also able distinguish between untreated and CQ-treated parasites using K-mean clustering analysis and PCA, however, they suggested that further investigations were required [325]. Thus, direct evidence of a Fe(III)PPIX-inhibitor complex has remained elusive.

In this chapter, evidence of the localization as well as the Raman spectra of Fe(III)PPIX and a Br-containing haemozoin inhibitor were investigated in an effort to look for evidence for the formation of a Fe(III)PPIX-inhibitor complex.

First, CQS *P. falciparum* cultures (NF54) were treated with a benzimidazole haemozoin inhibitor containing a Br atom (test compound **1**). Briefly, test compound **1**-treated cultures, after 30-32 hrs of incubation, were enriched using a Percoll® density gradient enrichment method [245]. Prior to performing cryofixation, enriched cultures were encapsulated using a polysaccharide gel encapsulation method with agarose [377]. Agarose encapsulated cultures were prepared via cryofixation using a high-pressure freezing, freeze substitution and low temperature embedding protocol [378-380]. From this, the Fe and Br distribution images for both untreated and treated iRBCs were obtained using TEM with ESI that is coupled with EELS. The resulting data showed that the Fe signal associated with Fe(III)PPIX and Br signal associated with test compound **1** co-localized within the DV of treated iRBCs.

Second, Confocal Raman microscopy was used to identify chemical and molecular changes in various Fe(III)PPIX complexes in the presence of test compound **1**. This was carried out in an effort to provide evidence that this co-localization was as a result of the formation of

a Fe(III)PPIX-inhibitor complex. Using aluminium foil covered glass microscope slides, the spectra for different Fe(III)PPIX complexes both in cells (RBC and parasites) and synthetic were successfully recorded for the Fe(III)PPIX porphyrin dominated spectral region of 1700-500 cm^{-1}. The spectrum of a putative Fe(III)PPIX-inhibitor complex was observed and indicated the presence of π-π interactions. Confocal Raman true component mapping images were obtained for untreated and test compound **1**-treated iRBCs, which, revealed that the signal distribution of haemozoin and the Fe(III)PPIX-test compound **1** complex could be imaged at the Raman peaks at 754 cm^{-1} and 1080 cm^{-1}. From this, it was apparent that the signal distributions for both haemzoin and the Fe(III)PPIX-test compound **1** complex co-localized in the parasites DV, where the Raman peak at 1080 cm^{-1} was unique to the Fe(III)PPIX-test compound **1** complex and considered to be a marker band for this complex

With small variations in the position and intensities of peaks observed in comparison to the remaining Fe(III)PPIX complexes, it was difficult to make definite conclusions by direct inspection of spectra. Therefore, PCA was used to assess the variability in the Raman spectra of all Fe(III)PPIX complexes based on their peak positions. The resulting PCA plots demonstrated separations along PC1 for all Fe(III)PPIX complexes being compared including comparisons to the Fe(III)PPIX-inhibitor complex. With this, the significance of these separations was further analyzed statistically using a Welch's t-test. These data showed that the proposed Fe(III)PPIX-inhibitor complex in the parasite was significantly different to all other Fe(III)PPIX complexes analyzed except its synthetically prepared counterpart. This analysis was also applied to oxy-haemoglobin and haemozoin in treated iRBCs in order to test the reliability of these data. These data proved that this analysis was reliable and could be used for future investigations.

Thus, this chapter provides insights into the location and distribution of Fe associated Fe(III)PPIX in the presence of a haemozoin inhibitor as well as strongly supporting evidence for the existence of a Fe(III)PPIX-inhibitor complex in CQS *P. falciparum* parasites. It also supports the theory that haemozoin inhibitors, like test compound **1**, accumulate within the parasite causing variable exchangeable haem amounts via co-localization with Fe(III)PPIX that is facilitated by the formation of a Fe(III)PPIX-inhibitor complex which inhibits the formation of haemozoin and likely causes parasite death.

4.2 Materials, instrumentation and methods

4.2.1 Materials

General cell culturing and fixation materials are listed in ***Table 2-2*** in Chapter 2. Materials and their suppliers, that were specific to this particular chapter, are listed below (***Table 4-1*** to ***4-3***). All the materials were of AR grade or higher and used without further purification, unless specified. A haemozoin inhibiting test compound, **1**, was used throughout this study. Its synthesis and characterization have been previously reported [335]. Haem-containing glassware was cleaned by using 0.2 M NaOH, 1 M HNO_3, with d.H_2O and acetone rinsing in between.

Table 4-1: Materials used for the preparation of TEM and EELS samples

TEM and EELS samples	
Material	**Supplier**
Percoll®	Sigma-Aldrich/Merck
Low melting point agarose	Sigma-Aldrich/Merck
1-Hexadecane	Sigma-Aldrich/Merck
Liquid Nitrogen	Afrox
Spurr's epoxy resin (low viscosity)	Agar Scientific
Osmium tetraoxide	Agar Scientific

Table 4-2: Materials used for the preparation of samples for Confocal Raman microspectroscopy

Confocal Raman microspectroscopy	
Material	**Supplier**
Heavy-duty aluminium foil (commercial grade)	Aro
Clear Nail Polish	Revlon

Table 4-3: Materials used to for β-haematin formation

β-haematin formation	
Material	**Supplier**
Haemin (≥ 97% Fluka)	Sigma Life Science
Glacial Acetic acid (AcOH)	Sigma-Aldrich/Merck
Sodium acetate trihydrate ($C_2H_9NaO_5$)	Sigma-Aldrich/Merck

4.2.2 Instrumentation

The instrumentation at the University of Cape Town Aaron Klug Centre for imaging and analysis was used throughout this study

Microcentrifuge

An Eppendorf microcentrifuge 5420 with an aerosol-tight rotor was used for the centrifugation of samples (500-1000 µl) at rpm ranging from 13000-21300.

Microwave

A LG Neochef stainless steel microwave (42 l) was used to prepare agarose gel solution for imaging microscopy and spectroscopy experiments.

Leica electron microscopy high-pressure microsystem (EM HPM) 100 and Leica EM automatic freeze-substitution (AFS) UC7 unit

A Leica EM HPM 100 was used to rapidly freeze agarose-encapsulated samples at a high-pressure of 2100 bar to prevent ice crystal formation in TEM samples. Freeze substitution and low temperature embedding of samples was carried out using a Leica EM AFS UC7 unit.

TEM and ESI coupled with EELS

TEM is a high-resolution electron microscopy technique used to capture images of samples that are minuscule. Coupled to the TEM microscope is an energy filter for ESI which measures the energy-loss of an electron. This is used for the determination of the location and distribution of elements which is achieved by the excitation of core electrons within a sample. All imaging and elemental distribution analysis was performed on a FEI Tecnai 20 transmission electron microscope (200 kV) and Gatan Tridiem 863 UHS. All TEM images were collected using a Gatan charge-coupled-device camera (CCD) (2048 x 2048 pixels) with a slit width of 18 eV

and processed using soft imaging system software. For EELS analysis, the software specifically uses a two-window difference method for calculating the elemental distribution images for each element analyzed. For the Fe distribution images, a slit width of 30 eV and energy offset of 723 eV was used which corresponds to the L_2-absorption edge. For the Br distribution images, slit widths of 10 eV or 40 eV with corresponding energy offsets of 72 eV or 1570 eV were used. These energy offsets correspond to the $M_{4,5}$-absorption edge and L_2-absorption edge respectively.

Confocal Raman microspectrometer

The Confocal Raman imaging and scanning electron microspectrometer (RISE) is a combination of a Scanning Electron Microscope (SEM) coupled to a standalone confocal Raman imaging microspectrometer. Raman spectra were collected using the confocal Raman microspectrometer alpha300 R (WITec GmbH, Germany) that is equipped with a CCD camera that was cooled to -60 °C and three air-calibrated objective lenses (10×, 50× and 100×). For this particular study, all spectra were collected using the 100× objective lens. This Raman microspectrometer uses a Nd:YAG laser (green) which has an excitation wavelength of 532 nm and a laser spot of 1-2 µm with a resolution of 1-2 cm^{-1} that was set at a default grating of 2050. The Raman microspectrometer was controlled using WITec Control FIVE v5.0.0 software. The Raman spectra were further analyzed using WITec Project FIVE v5.0.0.40 software.

4.2.3 Software

Throughout this chapter, the software that was used to analyse the TEM and EELS images were: Microsoft® PowerPoint version 16.16.11(190609) and ImageJ bundled with Java v1.8.0_172 [381]. Raman spectra were collected and analyzed using Control FIVE copyright © 2017 v5.0.0 and Project FIVE copyright © 2017 v5.0.0.40 supplied by WITec GmbH in Germany for Windows 10 (64-bit) [382-383]. All Raman spectra, PCA plots and Welch's t-test calculations were carried using Microsoft® Excel v16.16.11(190609) and GraphPad Prism v8.2.1 (227). Molegro Data Modeller executive v3.0 (Win 32 bit) version MDM 2013.3.0.0, supplied by a bioinformatics software company CLC bio (www.clcbio.com), was used to determine the eigenvalues and eigenvectors for all PCA plots [384].

4.2.4 Preparation of solutions and samples

4.2.4.1 TEM and EELS samples

5 x RPMI-1640: 25% D-sorbitol

The solution was prepared by dissolving 1.05 g RPMI-1640 and 5 g D-sorbitol in 20 ml of d.H_2O (pH 7.4). Before using or storing at 4 ºC, the solution was sterile filtered using a 0.22 µm membrane filter. The solution was stored at 4 ºC until further use.

Percoll® (60%)

A 60% Percoll® solution was prepared in a 6:2:2 (v/v/v) ratio of Percoll®, 5 x RPMI-1640:25% D-sorbitol and complete medium. The solution was stored at 4 ºC.

Percoll® (90%)

A 90% Percoll® solution was prepared by adding 1 ml 5 x RPMI-1640:25% D-sorbitol to 9 ml of Percoll®. The solution was stored at 4 ºC.

2 × PBS

The 2 × PBS solution was prepared by dissolving 1 tablet of PBS in 100 ml of d.H_2O.

1 × PBS

The 2 × PBS solution was further diluted (1:2) with d.H_2O for a 1 × PBS solution.

Glutaraldehyde (5%)

A 5% solution of glutaraldehyde was prepared by adding 1 ml of 50% glutaraldehyde in 9 ml of 1 × PBS

Glutaraldehyde (2.5%)

A 2.5% solution of glutaraldehyde was prepared by adding 0.5 ml of 50% glutaraldehyde to make up to 10 ml in 1 × PBS.

Agarose (4%)

A 4% slurry of agarose was prepared by gently heating 0.04 g of agarose in 1 ml d.H_2O.

4.2.4.2 Confocal Raman microspectroscopy

Test compound 1

A 1 mM solution of test compound **1** was prepared by dissolving 1.97 mg of test compound **1** in 5 ml of 14.1 M DMSO. The solution was stored at -20 ºC.

Haematin

A 1 mM solution of porcine haematin was prepared by dissolving 6.35 mg of haematin in 100 ml of 14.1 M DMSO. The solution was stored at 4 ºC.

Haemin

A 1 mM solution of haemin was prepared by dissolving 6.52 mg of haemin in 100 ml of 14.1 M DMSO. The solution was stored at 4 ºC.

4.2.4.3 Formation of β-haematin in sodium acetate buffer

NaOH

A 0.1 M solution of NaOH was prepared by dissolving 0.399 g in 100 ml of d.H_2O.

NaOH

A 5 M solution of NaOH was prepared by dissolving 19.95 g in 100 ml of d.H_2O.

HCl

A 1 M solution of HCl was prepared by adding 4.91 ml of 32% HCl in 95.09 ml of d.H_2O.

Sodium acetate buffer

A 9.7 M solution of $C_2H_9NaO_5$ (pH 4.8) was prepared by gently heating 23.75 g $C_2H_9NaO_5$ in 10 ml of d.H_2O. After total dissolution, 17.75 ml of acetic acid was added and topped up with 5 ml of d.H_2O. The solution was parafilmed and stored at 4 ºC.

Haemin

A 9.2 mM solution of haemin was prepared by dissolving 30 mg of haemin in 5 ml of 0.1 M NaOH and sonicating for 5 min. The solution was stored at 4 ºC.

4.2.5 Methods

4.2.5.1 TEM and EELS

Untreated and treated CQS NF54 cultures were taken through various preparation procedures prior to cryofixation in order to perform TEM and ESI coupled with EELS (***Table 4-1***). This was carried out for imaging purposes as well as to determine the location and distribution of both Fe(III)PPIX associated Fe and Br attributed to a benzimidazole haemozoin inhibitor containing a Br atom (test compound **1**). A modified version of the method described by Egan *et al* was used throughout this study and is described in what follows [287];

Enrichment and fixation of untreated and treated iRBCs

Sorbitol synchronized NF54 iRBCs (ring stage) were inoculated with test compound **1** at a known concentration that was equivalent to 1 × IC_{50} and incubated at physiological temperature (37 °C) for 30-32 hrs. After incubation, the trophozoite culture was centrifuged (750 rpm for 5 min) and the supernatant was discarded by aspiration. Percoll® density gradient centrifugation, using a modified method reported by Ginsburg *et al*, was used to enrich the trophozoite iRBC sample [245]. This was carried out by gently layering 500 µl of 60% Percoll® on top of 500 µl of 90% Percoll® in a 1.5 ml Eppendorf tube. Roughly 300 µl of the trophozoite pellet was carefully layered on top of the 60% Percoll® layer (***Figure 4-1 a***). Samples were prepared in triplicate by centrifugation for 30 min at 13 000 rpm using a microcentrifuge. After centrifugation, 3 distinct layers were observed as depicted in ***Figure 4-1 b***. Enriched trophozoite pellets were then transferred into 10 ml of complete medium in a 15 ml centrifuge tube and incubated for 15 min at 37 °C. Samples were further centrifuged at 750 rpm for 5 min. The supernatant was removed by aspiration before washing the remaining pellet with 5 ml of complete medium. This washing process was repeated three times to ensure complete removal of Percoll®. The separated black pellet was resuspended in 100 µl of 5% glutaraldehyde and 1 ml of PBS (pH 7.5) for 10 min. After centrifugation (3000 rpm for 1 min), the pellet was resuspended in 1 ml of 2.5% glutaraldehyde in PBS and left to stand at rt. for 10 min. The fixed pellet was stored at 4 °C overnight for polysaccharide gel encapsulation. This method was repeated for untreated CQS NF54 cultures.

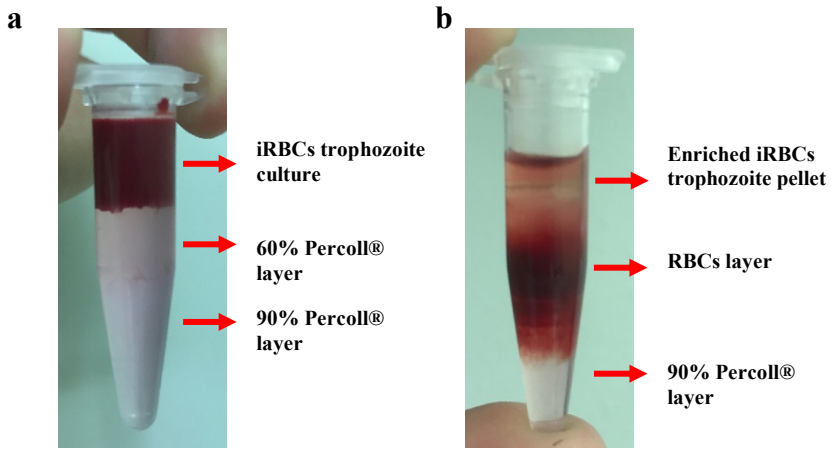

Figure 4-1 a-b: Percoll® density gradient centrifugation method for enrichment of samples, (a) iRBC trophozoite culture before centrifugation, and (b) three distinct layers post-centrifugation.

Polysaccharide gel encapsulation

A 4% agarose gel solution was prepared using a modified microwave method that has been previously described by Koontz [377]. In a 50 ml glass beaker, 4 g of low melting point agarose was dissolved in 10 ml of d.H_2O, using a microwave. To avoid aggregation, the agarose was slowly sprinkled into a stirring solution of d.H_2O. The solution, in a parafilmed glass beaker, was brought to a boil and left to boil for 10 min until the agarose was completely dissolved. A small piercing in the parafilm was made to avoid the parafilm from rupturing within the microwave and reduce the evaporation of d.H_2O. After 10 min of boiling, the solution was allowed to cool to rt. before weighing. Warm d.H_2O was added to bring the solution back to its initial weight. The fixed iRBCs were washed twice with 1 ml PBS before the samples were suspended in 50 µl of the 4% agarose slurry (1:1 v/v). The suspension was allowed to solidify before adding 10 µl of PBS to avoid sample dehydration.

High-pressure freezing, freeze-substitution and low temperature embedding

In order to preserve the native state of the agarose-encapsulated untreated and treated iRBCs, a process of cryofixation by rapid freezing at extremely low temperatures was used. This was performed using a modified high-pressure freezing, freeze-substitution and low temperature embedding method previously described by Yamada *et al* [378-380]. Briefly, agarose-encapsulated iRBCs were removed from the 4 °C refrigerator and left to stand at rt. for 30 min. Agarose-

encapsulated iRBCs were removed from the Eppendorf tubes using a wooden spatula and placed on a clean microscope glass slide. Under a light microscope, samples were cut into thin sections (80-100 nm) using a diamond knife. Thin sections were transferred into the first single-holed copper grid that was placed in the carrier plate of the lower cylinder of a Leica sample carrier (6 mm diameter). The sample was immersed under a small volume of hexane to remove any air bubbles. Using the Leica EM HPM100, the upper cylinder of same Leica sample carrier was placed on top of the lower cylinder and inserted into the system. Samples were rapidly frozen with liquid nitrogen at a pressure of 2100 bar to a temperature of -80 °C within 2 min. High-pressure frozen samples were transferred to a Leica EM AFS embedding system after removing the copper grids from the Leica sample carrier. Samples were embedded at a low temperature of -80 °C in acetone for 24 hrs. After 24 hrs, the acetone was replaced with osmium tetraoxide to maintain lipids and proteins within the sample for an additional 24 hrs. Samples were then left in the Leica EM AFS UC7 embedding system in low viscosity Spurr's resin for an additional 5-7 days, over which the temperature was gradually increased to rt., after which they were analyzed further using TEM and ESI with EELS.

4.2.5.2 Confocal Raman microspectroscopy

Aluminium foil covered glass microscope slides

For these experiments, aluminium was used because of its reduced cost and absence of background fluorescence with minimal interference when recording Raman spectra (***Table 4-2***) [385-390]. Aluminium foil covered glass microscope slides were prepared by adding a drop of clear nail polish onto a clean glass microscope slide and evenly smearing the nail polish to create a thin film. Pre-cut aluminium foil strips (1.5 x 3.5 cm) were carefully placed on the thin nail polish film using thin tipped tweezers. The aluminium foil strips were then carefully pressed, using nitrile gloves, to create a smooth surface.

RBCs

Packed RBCs were smeared (2 µl) onto an aluminium foil covered glass microscope slide and left to dry at rt. for 15 min before analysis.

Untreated and treated iRBC cultures

The parasite cultures were maintained in continuous culture as described in Chapter 2 (see ***Section 2.5.1***) . In brief, CQS NF54 cultures were inoculated with test compound **1** at 1 × IC_{50} in 50 ml culture flask and incubated at 37 °C for 30-32 hrs. Thereafter, trophozoite cultures were removed from the incubator and centrifuged at 750 rpm for 5 min, after which, the supernatant was aspirated. Trophozoite cultures were mixed and decanted into four 15 ml centrifuge tubes (250 µl). The decanted trophozoite cultures were left to stand for 10 min at rt. before mixing and gently smearing 2 µl onto an aluminium foil covered glass microscope slide. The sample slide was left to air dry at rt. for 15 min before analysis. The same was applied for untreated cultures (***Table 4-2***).

β-haematin

Solid crystals were crushed in a glass beaker before placing on an aluminium foil covered glass microscope slide for analysis.

Test compound 1

A 2 µl drop of 1 mM test compound **1** in DMSO was dried onto an aluminium foil covered glass microscope slide using an incandescent lamp at rt. before further analysis.

Haematin and Haemin

A 2 µl drop of 1 mM solutions of haematin or haemin were dried onto separate aluminium foil covered glass microscope slides using an incandescent lamp at rt. before further analysis.

Haematin-test compound 1 mixture

A 1:10 (v/v) mixture was prepared by titrating 5 ml of a 1 mM solution of haematin into 50 ml solution of 1 mM of test compound **1** in a 100 ml glass beaker. In order to correct for dilution, DMSO was added to a final volume of 100 ml. The parafilmed solution was gently heated in a water bath (60 °C) for 30 min and cooled to rt. Roughly 2 µl of the mixture was dried, using

an incandescent light lamp, onto an aluminium foil covered glass microscope slide for further analysis.

4.2.5.2 Formation of β-haematin in sodium acetate buffer

The formation of β-haematin in sodium acetate buffer was carried out using a method previously described by Egan *et al* [143]. Briefly, 30 mg of haemin was dissolved in 5 ml of 0.1 M NaOH in a glass beaker and sonicated for 5 min (stock solution). In a glass vessel, 2.5 ml of the stock solution was added to 0.25 ml of 1 M HCl and 2.31 ml of 9.7 M sodium acetate buffer. The solution was adjusted to pH 4.8 with 5 M NaOH. The glass vessel was then parafilmed and placed on a magnetic stirrer before stirring the solution in a glass titration vessel with a thermostat jacket that was connected to a 60 °C water bath. The solution was allowed to stir for 1 hr. After 1 hr, the solution was removed from the hot plate, quenched with d.H_2O and placed on ice. Once precipitation had occurred, the precipitate was filtered through 8 µm cellulose acetate/nitrate Millipore filter paper using a Buchner funnel. Then, the precipitate was washed multiple time with d.H_2O until a clear filtrate was observed. The precipitate was further dried between two pieces of filter paper before placing the filter paper containing the precipitate in a 15 ml centrifuge tube and into a phosphorous pentoxide desiccator. The β-haematin precipitate was left to dry for 48 hrs until further analysis.

4.3 Data analysis

4.3.1 Confocal Raman microspectroscopy

The Raman spectra for all Fe(III)PPIX complexes were processed using the WITec Control FIVE software. For this study, the Fe(III)PPIX porphyrin dominated spectral region of 1700-500 cm^{-1} was chosen. The excitation wavelength was 532 nm.

To obtain the single scan Raman spectra for the different Fe(III)PPIX complexes, a large area scan (LAS) image Raman spectra was initially performed to determine the particular regions within the sample that are associated with the different Fe(III)PPIX complexes in RBCs, parasites and synthetic Fe(III)PPIX complexes. Every LAS Raman spectrum has a corresponding residual image that is produced where each pixel pertains to a single spectrum. An average of 15 lines per image and 15 points per line for each LAS residual image was

recorded for an average collection time of about 35 min. It was difficult to avoid photo-damage to the cells with this laser exposure time, which has been previously reported to be a common problem when recording images for longer periods [391-392]. The integration times of 0.05 s and 0.1 s at laser powers of 0.1 mW, and 1 mW were used to record the LAS Raman spectra for RBCs, parasite and synthetic Fe(III)PPIX complexes respectively in an effort to minimize damage.

First, the LAS Raman spectrum for each sample was corrected for cosmic rays (filter size 4; dynamic factor 50), smoothed using a Savitzky-Golay algorithm (9 smoothing points; derivative 0), averaged (spectral 9; spatial 0) and subtracted for background correction (shape size 100; noise factor 4). Using a built-in true component analysis tool, the Raman spectra for individual components (e.g. haemozoin) were extracted from the LAS residual image using an auto-setting in order to determine the regions pertaining to the different Fe(III)PPIX complexes in a sample. This process was repeated for 10-15 cells to ensure that the extracted spectra from the respective regions for each Fe(III)PPIX complex were accurate. From here, the spectra for all components selected were averaged with an auto-setting, demixed and extracted. Demixing is important for this process as it is aimed at the removal of any contribution of one components spectrum to another for the selected components within a sample. The spectra were extracted and used as reference spectra for the individual Fe(III)PPIX complexes.

Before recording the single scan Raman spectra, the oscillator was adjusted and calibrated to the aluminium foil covered glass microscope slide to correct for any background signals. This was also to reduce the cosmic ray effect which can cause false peaks in Raman spectra. For all Fe(III)PPIX complexes, experiments were carried out in triplicate. An average of 30 single scan Raman spectra for each Fe(III)PPIX complex, obtained from the previously determined areas of the cell, were recorded from 10 randomly selected cells for RBCs and parasite samples. For synthetic Fe(III)PPIX complexes, the same number of single scan Raman spectra were obtained, however, from 5 randomly selected regions for each slide pertaining to a specific Fe(III)PPIX complex. In addition, each single scan Raman spectrum was collected using a total of 100 accumulations at an integration time of 0.05 s. The spectra for parasite Fe(III) PPIX complexes, including RBCs, were obtained with an optimal laser power of 0.1 mW for high signal-to-noise ratio spectra, at the same time avoiding haemolysis and photo-damage of cells. Cells were also allowed to rest for intervals of 10 min before each scan. Synthetic Fe(III)PPIX complexes were analyzed using a laser power of 1 mW. All individual single scan Raman spectra were corrected for the cosmic ray effect, smoothed, averaged and

background subtracted using the same parameters described above, after which, were plotted in GraphPad Prism v8.2.1 (***Figure 4-2***).

4.3.2 Confocal Raman true mapping images

Similar to the sequential procedure described above for obtaining single scan Raman spectra, separate LAS image Raman spectra were also recorded in order to determine the true mapping images for RBCs, parasites and synthetic Fe(III)PPIX complexes at selected peak positions (754 cm^{-1}, 1080 cm^{-1}, 1090 cm^{-1} and 1642 cm^{-1}).

First, the LAS Raman spectra were recorded and corrected for the cosmic ray effect, smoothed, averaged and background subtracted using the same parameters described above for single scan Raman spectra (see ***Section 4.3.1***). The Raman spectra for individual components (e.g. haemozoin) in a sample were extracted manually from the specific regions pertaining to each Fe(III)PPIX complex that were previously determined for the single scan Raman spectra using the built-in true component analysis tool. Starting with a LAS residual image, each component was extracted, where after each component was extracted there was a remaining residual image and so forth until a residual image corresponding only to background noise is left (i.e. arising from the aluminium foil covered glass microscope slide). In more detail, this process extracts the spectra (in each pixel) pertaining to each component from the LAS residual image separately. From here, the spectra for all the components selected were averaged with an auto-setting, demixed and extracted. With emphasis on demixing, spectra were required to be demixed to ensure that when the signals at different peaks were analyzed no signal contributions from one Fe(III)PPIX was observed in the true mapping image of another Fe(III)PPIX complex. The demixed-component spectra were individually analyzed further with a built-in filter viewer. The filter viewer is a tool that produces images that map out the distribution of the spectra pertaining to an individual component. At specific peak positions that have been assigned to specific vibrations and stretches, a filter width of 1 cm^{-1} was used. This filter width was chosen to reduce the contribution of neighboring peaks, decrease the effect of broad peaks or inclusion of shoulder peaks when obtaining the true mapping images. This process is illustrated in ***Figure 4-2***.

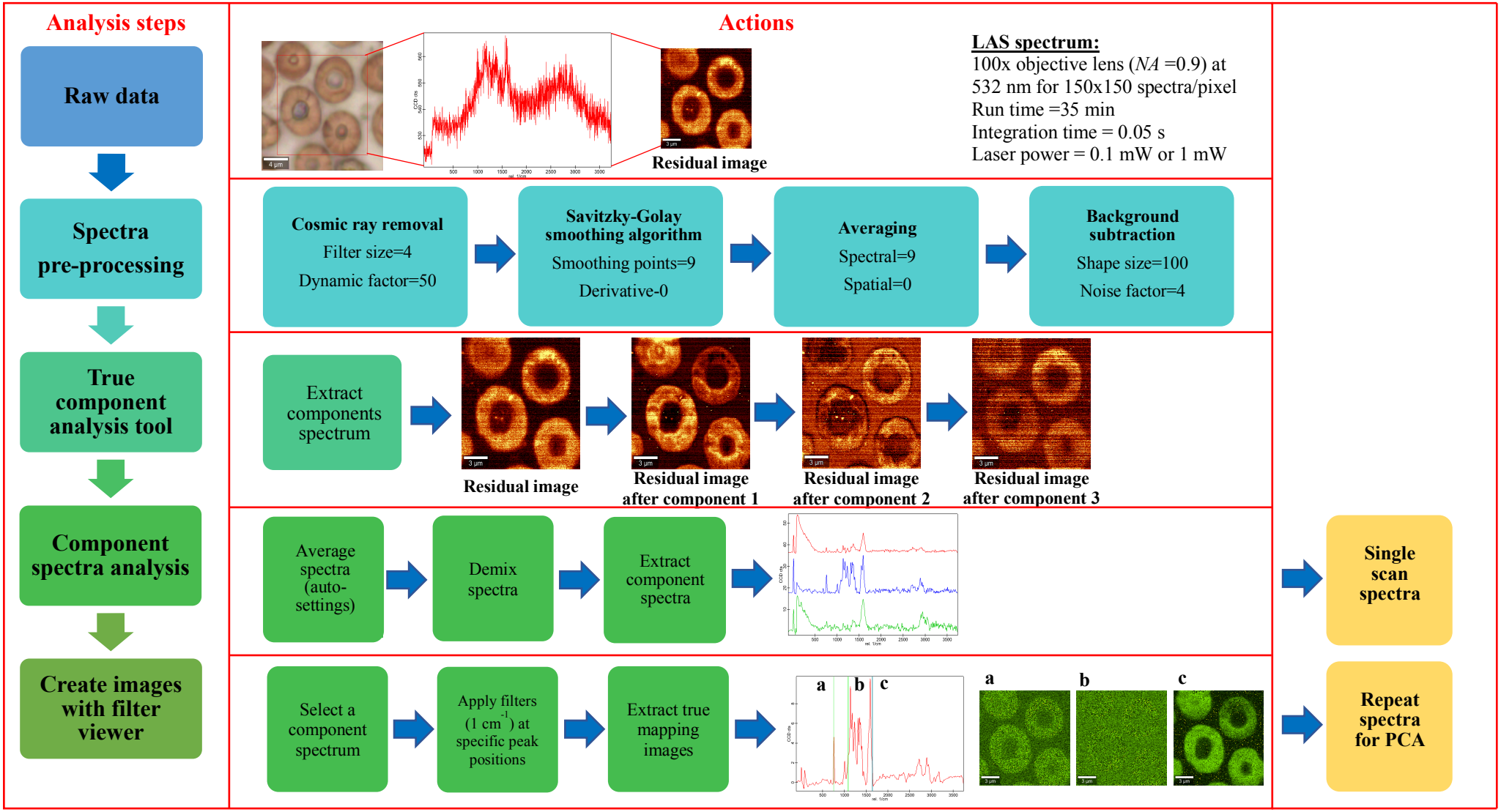

***Figure 4-2*:** A multivariate analysis for confocal Raman true mapping images for individual Fe(III)PPIX complexes in untreated and treated iRBCs [393].

4.3.3 PCA

The peak positions of the recorded Raman spectra for the spectral range of 1700-500 cm^{-1} for all Fe(III)PPIX complexes were separated using PCA (***Figure 4-3***). In more detail, an average of 150-200 spectra were recorded from the relevant true mapping images for each Fe(III)PPIX complex. The obtained repeat spectra for all Fe(III)PPIX complexes were individually corrected for cosmic ray effect, smoothed, averaged and background subtracted as previously mentioned in ***Section 4.3.1***. Thereafter, individual spectra for each Fe(III)PPIX complex were taken through various steps in order to extract the relevant peak positions necessary for this study.

First, spectral intensity was normalized using a modified standard normal variate method which involves subtracting the mean (μ) from each data point (x_i), divided by the standard deviation (std_μ) and subtracting the minima (x_{min}) [394]. The resulting normalized data points (x_N) were calculated using the following equation (***Eq. 1***) :

$$x_N = \left(\frac{x_i - \mu}{std_\mu} - x_{min}\right) \qquad \textbf{\textit{Eq. 1}}$$

Next, the normalized spectra were converted to their corresponding second derivative spectra, using GraphPad Prism v8.2.1, to easily define the relevant peak positions based on their curvature rather than their intensity. The relevant second derivative spectra were then transferred to another Excel document where the data points ($\pm\, a_i$) at each peak position for a second derivative spectra were refined to determine whether or not the resulting data points ($\pm\, a_i'$) were above (***Eq. 2***) or below (***Eq. 3***) the positive ($+p_{0.05}$) or negative ($-p_{0.05}$) 95th-percentile.

$$+a_i' = a_i > +p_{0.05} \qquad \textbf{\textit{Eq. 2}}$$

and,

$$-a_i' = -a_i < -p_{0.05} \qquad \textbf{\textit{Eq. 3}}$$

The resulting data points ($\pm\, a_i'$) were further refined to ensure that only the peak positions with data points ($\pm\, a_i''$) showing maximum or minimum values in comparison to the neighboring data points would be selected (***Eq. 4*** and ***Eq. 5***):

$$+a_i'' = (a_2' > a_1'); (a_2' > a_3'); (a_2' > +p_{0.05}) \quad \textbf{Eq. 4}$$

$$-a_i'' = (a_2' < a_1'); (a_2' < a_3'); (a_2' < -p_{0.05}) \quad \textbf{Eq. 5}$$

Finally, the peak positions (b_i'') of the refined data points ($\pm a_i''$) were selected using ***Eq. 6***:

$$b_i''' = (+a_i'' > +p_{0.05}); (-a_i'' < -p_{0.05}) \quad \textbf{Eq. 6}$$

All resulting peak positions for pairs of Fe(III)PPIX complexes being analyzed (e.g. oxy-haemoglobin versus haemozoin) were transferred to the Molegro Data Modeler Executive software. This software was used to generate the eigenvectors (PC1 and PC2) and corresponding eigenvalues. From here, all PCA plots were plotted using GraphPad Prism v8.2.1.

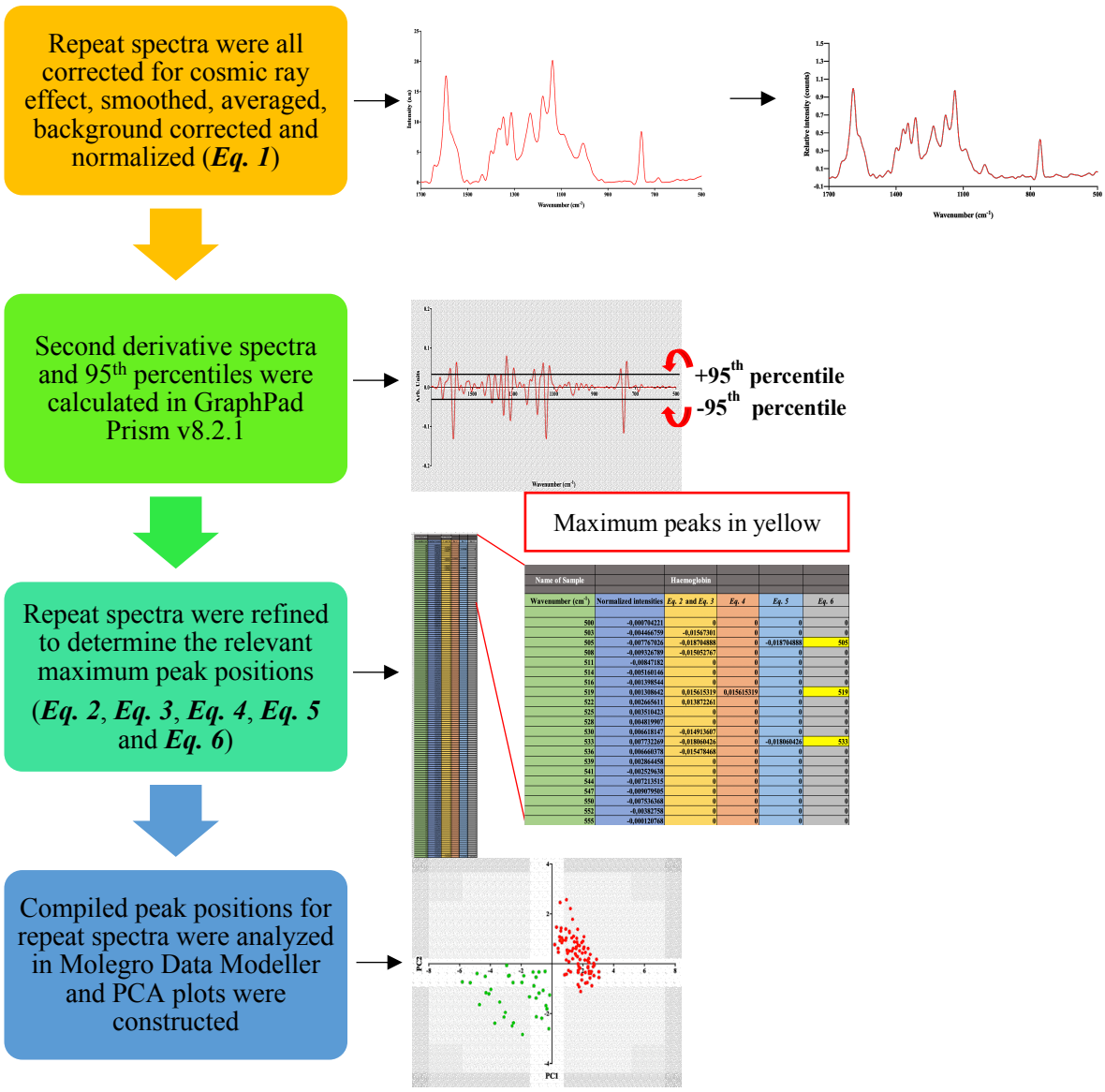

Figure 4-3: Analysis of repeat spectra for individual Fe(III)PPIX complexes for PCA analysis.

4.3.4 Welch's t-test analysis

The statistical significance of the separation of clusters for each PCA plot for pairs of Fe(III)PPIX complexes was analyzed using a Welch's t-test analysis that was performed in GraphPad Prism v8.2.1. In brief, the clusters were shifted so that the one centroid lay at the origin and then transformed so that both centroids lay on the *x* axis (***Figure 4-4 a-d***). This was done using the following equations;

Centroids for cluster I and II are defined by Cartesian coordinates μ_x^a and μ_y^a, $a =$ I or II given by ***Eq. 7*** and ***Eq. 8*** (***Figure 4-4 a-b***):

$$\mu_x^a = \frac{\sum_{i=1}^{n_a} x_i^a}{n_a} \qquad \textbf{\textit{Eq. 7}}$$

$$\mu_y^a = \frac{\sum_{i=1}^{n_a} y_i^a}{n_a} \qquad \textbf{\textit{Eq. 8}}$$

where n_a is the number of points in cluster a. Application of ***Eq. 9*** and ***Eq. 10*** shifts the centroid of cluster I to the origin (***Figure 4-4 c***):

$$\mu_x^{a'} = \mu_x^a - \mu_x^I \qquad \textbf{\textit{Eq. 9}}$$

$$\mu_y^{a'} = \mu_y^a - \mu_y^I \qquad \textbf{\textit{Eq. 10}}$$

The coordinates of all the points are correspondingly shifted according to ***Eq. 11*** and ***Eq. 12***:

$$x_i^{a'} = x_i^a - \mu_x^I \qquad \textbf{\textit{Eq. 11}}$$

$$y_i^{a'} = y_i^a - \mu_y^I \qquad \textbf{\textit{Eq. 12}}$$

The new position of centroid II in polar coordinates is given by ***Eq. 13*** to ***Eq. 16*** (***Figure 4-4 d***):

$$\mu_x^{II'} = R^{II} \cos\theta \qquad \textbf{\textit{Eq. 13}}$$

$$\mu_y^{II'} = R^{II} \sin\theta \qquad \textbf{\textit{Eq. 14}}$$

where,
$$R^{II} = \sqrt{\left(\mu_x^{II'}\right)^2 + \left(\mu_y^{II'}\right)^2} \qquad \textbf{\textit{Eq. 15}}$$

and,
$$\theta = sin^{-1}\left(\frac{\mu_y^{II'}}{R^{II}}\right) \qquad \textbf{\textit{Eq. 16}}$$

Finally, rotation of the axes through angle θ results in a new set of axes x'' and y'' in which both centroids lie on x'' axis with no separation of the clusters along the y'' axis and maximum separation along x''. The position of the points along x'' are given by ***Eq. 17***:

$$x_i^{a''} = x_i^{a'} \cos\theta - y_i^{a'} \sin\theta \qquad \textit{Eq. 17}$$

The statistical significance of the separations of the means $\mu_x^{I''}$ and $\mu_x^{II''}$ was evaluated using a Welch's t-test which allows for unequal variances in the data.

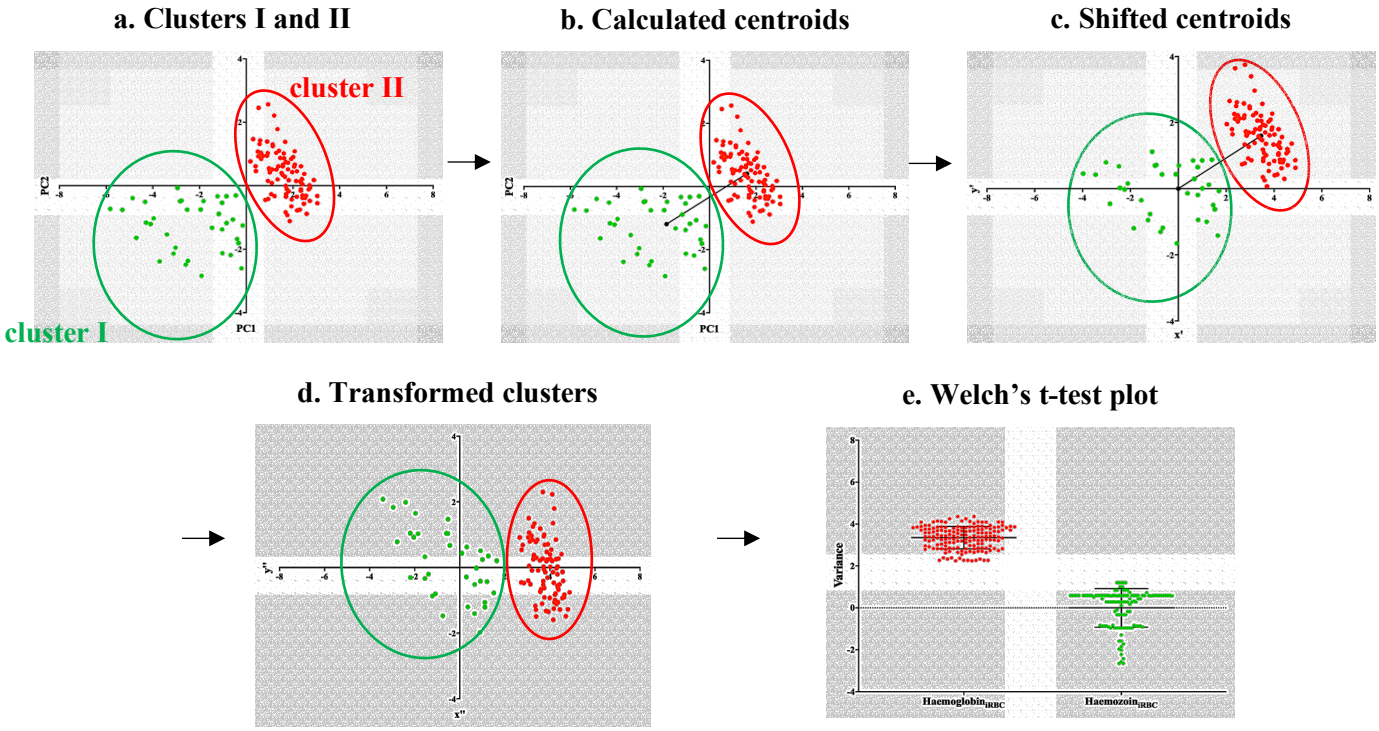

***Figure 4-4 a-d*:** Welch's t-test analysis of PCA plots.

4.4 Results and discussion

4.4.1 Evidence of co-localization of Fe(III)PPIX and test compound 1 in treated CQS *P. falciparum* parasites

In chapter 3, it was shown that an apparent 1:1 relationship exists between the total intracellular test compound amount and the amount of exchangeable haem present in CQS NF54 parasites for the range of haemozoin inhibitors investigated in this study. From here, it was hypothesized that the cause of this observation was the formation of Fe(III)PPIX-inhibitor complexes forming within the parasite DV which would be characterized by co-localization of Fe(III)PPIX and the inhibitor.

Therefore, to examine the possible co-localization of Fe(III)PPIX and a selected haemozoin inhibitor in both untreated and treated CQS parasites, TEM with ESI based on EELS was used (see ***Section 4.2.5***). For this specific experiment, test compound **1** was selected from the series of test compounds investigated in this study because it contains a Br atom. Crucially, (i) it produced a moderate total intracellular test compound amount which coincided with a moderate amount of exchangeable haem present in parasites at its IC_{50} value and thus was more easily detected than CQ which is present in much smaller amounts and gives much lower amounts of exchangeable haem; and, (ii) for microscopy, the difference in L_2 and $M_{4,5}$ excitation edges of Fe and Br respectively makes it possible to distinguish between the two elements in untreated and treated CQS parasites [395-396].

In brief, CQS NF54 cultures were inoculated at the immature ring stage at the IC_{50} value of test compound **1** (616 nM) and incubated for 30-32 hrs. After incubation, cultures were taken through several preparation steps that included; enrichment by Percoll density gradient centrifugation, agarose-encapsulation for cryofixation (high-pressure freezing, freeze substitution and low temperature embedding) (see ***Section 4.2.5.1***). A cryofixation method was chosen as opposed to chemical fixation methods (ethanol) to rule out the possibility of: (i) the test compound **1** leaching out of or being relocated in the parasite; (ii) the formation of artefacts (e.g. water crystals); (iii) improved preservation of ultrafine structures; and (iv) higher signal-to-noise ratio within the parasite which is advantageous for imaging [397-398]. For both untreated and treated iRBCs, the experiments were carried out in triplicate for which representative TEM and EELS images are discussed below.

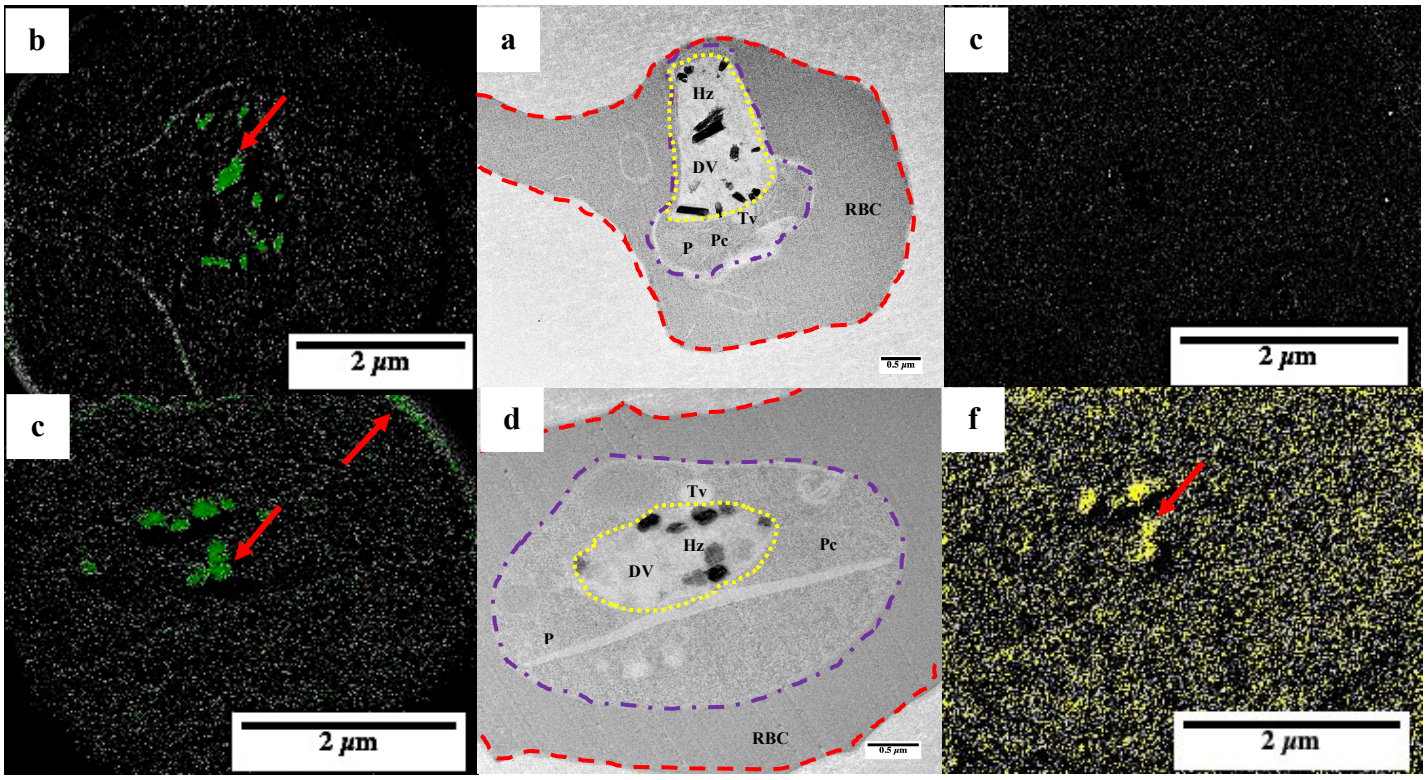

Figure 4-5 a-f: TEM images for samples prepared by cryofixation were obtained for (a) untreated and (d) test compound **1**-treated CQS NF54 parasites. ESI coupled with EELS was used to determine both the Fe (green) and Br (yellow) location and distribution in CQS NF54 parasites for b) untreated parasites showing a strong signal (green) for haemozoin crystals in the parasites DV (red arrow), c) no Br signal for untreated parasites, e) Fe distribution image for test compound **1**-treated iRBCs showing a strong signal for haemozoin crystals in the parasites DV (green) as well as a low Fe signal in the RBC cytoplasm (red arrows), and f) test compound **1**-treated iRBCs showing a low Br signal distributed throughout the iRBC but a much stronger Br signal can be seen inside the parasites DV (yellow) which is indicated by the arrow (red). In a and d; the RBCs are delineated with a red dashed line, the parasite with a purple dashed line and the parasites DV with a yellow dotted line. Abbreviations in (a) and (d) were used and include; RBC = red blood cell, Pc = parasite cytoplasm, P = parasite, DV = digestive vacuole, Tv = transport vesicle and Hz = haemozoin crystals.

For untreated iRBCs, ***Figure 4-5 a*** illustrates the TEM image of a parasite (purple dashed line) inside a RBC (red dashed line). Clearly defined lath-shaped haemozoin crystals localized inside the parasites DV (yellow dotted line) were observed. With this, additional features were also observed and included the parasites cytoplasm and a transport vesicle. This was similar to the

observations published by Love *et al* who showed transport vesicles containing haemoglobin [399]. For the Fe distribution image, a stronger Fe signal (green) within the parasites DV in comparison to a negligible Fe signal in the RBC cytoplasm was observed. This strong Fe signal was attributed to the haemozoin crystals (red arrow) which were shown to be dispersed throughout the DV. It also indicated that in untreated iRBCs most of the Fe(III)PPIX associated Fe was in the form of haemozoin (***Figure 4-5 b***). This agreed with previous findings which showed that in untreated iRBCs about 70-100% of vacuole Fe(III)PPIX Fe is associated to haemozoin [286]. ***Figure 4-5 c*** illustrated that for the Br distribution no signal was observed. This was expected for untreated iRBCs which are expected to contain negligible Br.

Compared to untreated iRBCs, test compound **1**-treated iRBCs resulted in similar observations where the parasite was located in the RBC showing features such as the parasites cytoplasm and transport vesicles. Artefacts as a result of sectioning in untreated iRBC were also observed for test compound **1**-treated iRBC. This was shown by the elongated tube-like feature observed inside the iRBC which is a cutting artefact (***Figure 4-5 d***). This is a common error as previously suggested by Bleck *et al* [400]. In contrast to untreated iRBCs, iRBCs in the presence of test compound **1** resulted in less defined haemozoin crystals within the parasites DV as a result of an electron dense halo around the crystals. This was consistent with the fact that the formation of haemozoin was disrupted and agreed with similar findings previously observed by Combrinck *et al* [242]. ***Figure 4-5 e*** illustrates the Fe distribution image for test compound **1**-treated iRBCs, where, a strong Fe signal (green) was observed from the haemozoin crystals. No Fe signal was observed in the Pc which indicated that no appreciable Fe associated Fe(III)PPIX was distributed out of the DV in the presence of test compound **1**. These observations were different to the finding by Combrinck *et al* and colleagues who showed that Fe(III)PPIX associated Fe had diffused out of the DV into the parasites cytoplasm as a result of CQ treatment [242]. An increased Fe signal was observed in the RBC cytoplasm compared to untreated iRBCs and is indicated by the red arrow. ***Figure 4-5 f*** showed a strong Br signal (yellow), attributed to the Br atom of test compound **1**, for treated iRBCs compared to untreated iRBCs. From this, it was evident that majority of the signal was observed to be located within the DV of the parasite, coincident with the region of the Fe signal. It was, however, not apparent whether the Br signal observed in the parasite was as a result of a poor signal-to-noise ratio and therefore devoid of test compound **1** or test compound **1** was distributed throughout the entire iRBC.

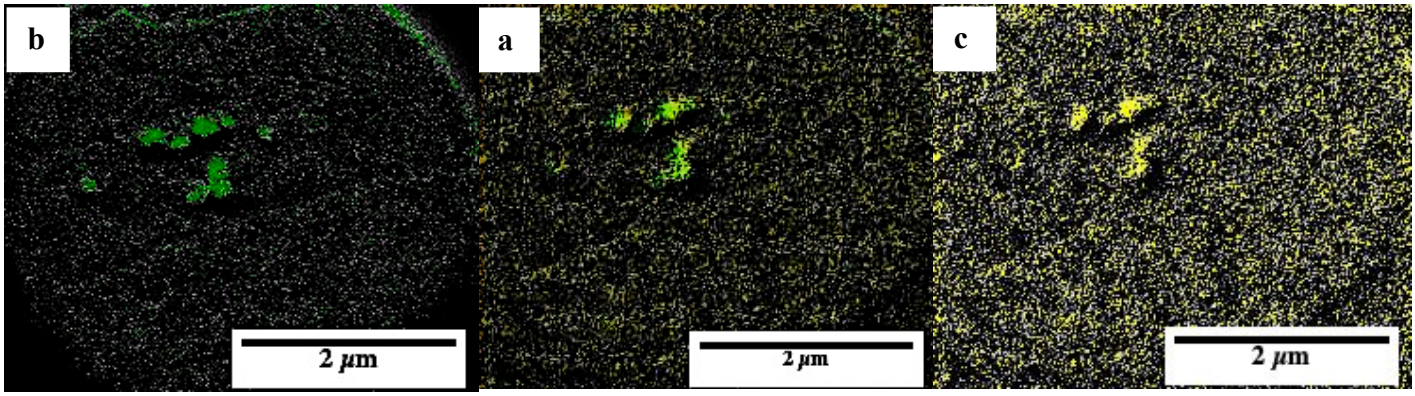

Figure 4-6 a-c: Evidence of the co-localization of Fe(III)PPIX and test compound **1** in the DV of CQS NF54 parasites represented by the (a) overlaid image of the (b) Fe (green), and (c) Br (yellow) distribution images.

To further establish whether Fe(III)PPIX and test compound **1** were in the same region within the parasites DV, the Fe and Br distribution images for test compound **1**-treated parasites were overlaid (***Figure 4-6 a***). Upon overlaying ***Figure 4-6 b*** and ***c***, it was immediately apparent that the Fe(III)PPIX associated Fe signal and Br signal attributed to test compound **1** were both located within the parasites DV in the same specific place. This definitively shows that co-localization does occur between Fe(III)PPIX and test compound **1** which led to further investigations into the possibility that this co-localization is due to the formation of a Fe(III)PPIX-inhibitor complex.

4.4.2 Evidence of a Fe(III)PPIX-inhibitor complex in treated CQS *P. falciparum* iRBCs.

4.4.2.1 Confocal Raman microspectroscopy

Based on the evidence, previously highlighted in ***Section 4.4.1***, it was further proposed that the co-localization of Fe(III)PPIX and test compound **1** was as a direct result of the formation of a putative Fe(III)PPIX-test compound **1** complex in the DV of CQS NF54 parasites. A detailed investigation into this putative Fe(III)PPIX-test compound **1** complex was carried out using a non-destructive, fast and highly sensitive technique, Raman spectroscopy [311,401]. This technique was utilized in order to determine the molecular variations in the vibrational modes in RBC, parasite- and synthetic-based Fe(III)PPIX complexes in an effort to identify the putative Fe(III)PPIX-test compound **1** complex.

For observation of parasite-based Fe(III)PPIX complexes, CQS NF54 parasites (ring stage) were treated at 1 × IC_{50} of test compound **1** (616 nM) and incubated for 30-32 hrs. After incubation, cultures were centrifuged and aspirated. After 24 hrs, cultures were left to stand at rt. for 10-15 min. Cultures were then mixed and smeared (2 µl) onto an aluminium foil covered glass microscope slide. The same procedure was carried out for observing untreated iRBCs. Packed RBCs were prepared as previously described in Chapter 2 (see ***Section 2.4.2***). The untreated and treated parasite Fe(III)PPIX complexes included: oxy-haemoglobin in RBCs; oxy- and deoxy-haemoglobin; haemozoin; and a putative Fe(III)PPIX-test compound **1** complex. For synthetic Fe(III)PPIX complexes, various solutions of 1 mM concentration were prepared in DMSO, dried onto an aluminium foil covered glass microscope slide with an incandescent light before analysis. These included: haematin; haemin; β-haematin; test compound **1**; and a haematin-test compound **1** mixture.

The typical single scan Raman spectra were recorded with varying laser power at an excitation wavelength of 532 nm for the Fe(III)PPIX porphyrin dominated spectral region of 1700-500 cm^{-1} for all Fe(III)PPIX complexes investigated in this chapter (see ***Section 4.3.1***). This specific spectral range was chosen for the reason that it has been previously reported that haemozoin inhibitors, such as test compound **1**, tend to bind to Fe(III)PPIX via π- π interactions with the porphyrin ring of Fe(III)PPIX and therefore would presumably affect this part of the spectrum most strongly [143,322,402-404]. For comparison, all spectra were normalized using a modified standard normal variate method. This was to ensure that peaks of a specific Fe(III)PPIX complex were not excessively different in scale as might occur by normalizing to one specific peak characteristic of another Fe(III)PPIX complex. The observed peak positions, local coordinate, assignments and symmetry terms for the Fe(III)PPIX complexes associated with RBCs and treated iRBCs are listed in ***Table 4-4***. These were adapted from Abe *et al*, Hu *et al*, Szczerbowska-Boruchowska *et al*, Socrates, Dines *et al*, Webster *et al*, Marzec *et al*, Wood *et al*, Suwaiyan *et al*, Mohan *et al*, Weselucha-Birczynska *et al*, Frosch *et al* and Wood *et al* [294,320,322,401,405-414]. The porphyrin symmetry terms of Fe(III)PPIX were designated according to idealized D_{4h} symmetry; ν_1-ν_9 for A_{1g}, ν_{10}-ν_{18} for B_{1g}, ν_{19}-ν_{26} for A_{2g}, ν_{27}-ν_{35} for B_{2g} and ν_{36}-ν_{55} for E_u, where, E_u are IR and Raman active modes. δ, γ, w, m and s were designated to in-plane deformations, out-of-plane deformations, weak, medium and strong peaks relative to other peaks respectively [405-406]. Normal modes are also given in local coordinates (see ***Figure 4-7***). The results are discussed below.

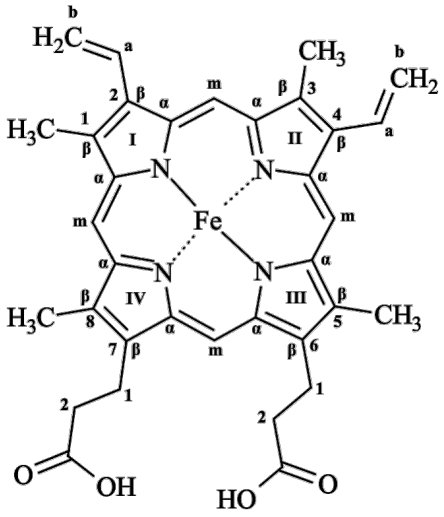

Figure 4-7: D_{4h} structure of Fe(III)PPIX showing the carbon atom type labelling.

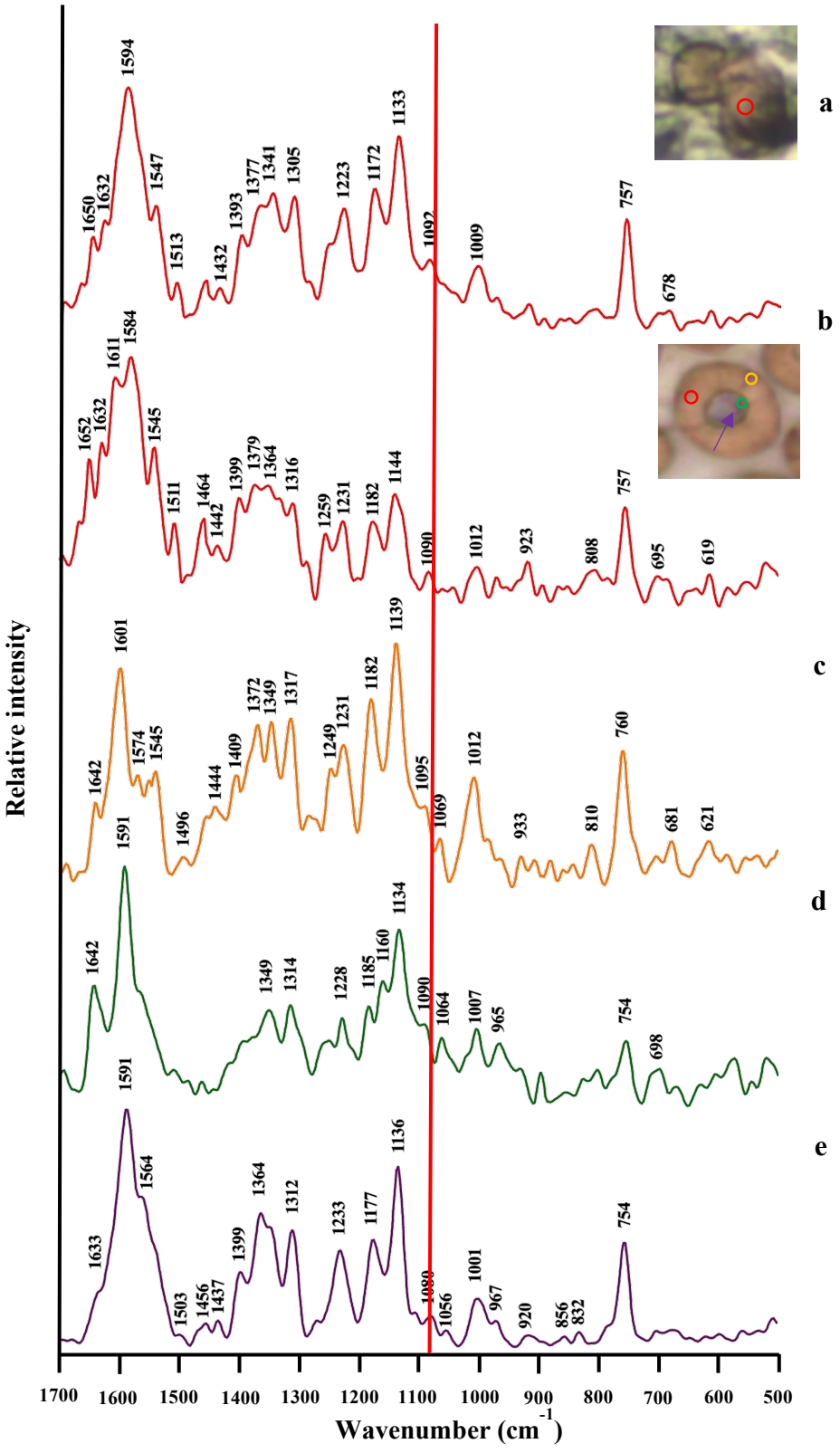

Figure 4-8 a-e: Single scan Raman spectra for the Fe(III)PPIX complexes that are assigned to (a) oxy-haemoglobin in RBCs, and (b) oxy-haemoglobin, (c) deoxy-haemoglobin, (d) haemozoin, (e) putative Fe(III)PPIX-test compound **1** complex in test compound **1**-treated CQS iRBCs. The red line represents the possible marker band for the putative Fe(III)PPIX-test compound **1** complex at 1080 cm^{-1}.

Table 4-4 a-e: The observed peak positions, local coordinates, assignments and symmetry terms for RBC and treated iRBCs Fe(III)PPIX complexes observed at 532 nm excitation [320,322,405-414]. Labels a-e correspond to oxy-haemoglobin in RBCs, oxy-haemoglobin, deoxy-haemoglobin, haemozoin and the putative Fe(III)PPIX-test compound **1** complex in treated iRBCs respectively.

a		**b**		**c**		**d**		**e**		**Local coordinate**	**Assignment**	**Symmetry**
	w		m	1642	w, sh	1642	m, b	-		$\nu(C_\alpha C_m)_{asym}$	ν_{10}	B_{1g}
1632	w, sh	1632	w, sh	-		-		1633	w, sh	$\nu(C_\alpha C_m)_{asym}$	ν_{10}	B_{1g}
-		1611	w, b	-		-		-		$\nu(C_a{=}C_b)$	ν ($C_a{=}C_b$)	
-		-		1601	s,b	-		-		$\nu(C_\alpha C_m)_{asym}$	ν_{19}	A_{2g}
1594	s, b	1584	w, b	1574	w	1591	s	1591	s, b	$\nu(C_\alpha C_m)_{asym}$	ν_{37}	E_u
1547	m	1545	m	1545	w	-		1564	w, sh	$\nu(C_\beta C_\beta)$ and, or δ(N-H)	ν_{11} or ν_{20}	B_{1g}
-		-		-		-		1456	w, b	Aromatic ring vibration, $\nu(C{=}C)_{sym}$	ν_{19}	E_{2g}
1432	w	1442	w, b	-		-		1437	w	$\nu(C_\alpha C_m)_{sym}$	ν_{28}	B_{2g}
1393	m	1399	w	-		-		1399	m	ν(pyr quarter-ring)	ν_{20}	A_{2g}
1377	m, sh	1379	w, b	1372	m, b	-		-		$\nu(\text{pyr half-ring})_{sym}$	ν_4	A_{1g}
-		1364	w, b	-		-		1364	s, b	$\nu(\text{pyr half-ring})_{sym}$	ν_4	A_{1g}
1341	m, b	-		1349	m, b	1349	m, b	-		$\nu(\text{pyr half-ring})_{sym}$	ν_{41}	E_u
1305	m, b	1316	w	1317	m, b	1314	m, b	1312	s	$\delta(C_mH)_{asym}$	ν_{21}	A_{2g}
-		-		1249	w, sh	-		-		$\delta(C_mH)$	ν_{13}	B_{1g}
1223	m, b	1231	m, b	1231	m, b	1228	w	1233	m, b	$\delta(C_mH)$	ν_{13} or ν_{42}	B_{1g}, E_u
1172	m, b	1182	m, b	1182	s	1185	w	1177	m, b	$\nu(\text{pyr half-ring})_{asym}$	ν_{30}	B_{2g}
-		-		-		1160	m, sh	-		$\nu(\text{pyr half-ring})_{asym}$	ν_{30}	B_{2g}
1133	s, b	-		1139		1134	s	1136	s	$\nu(C_\alpha N)$ and, or $\nu(\text{pyr half-ring})_{asym}$	ν_{22}	A_{2g}
1092	w, b	1090	w, b	1095	w, sh	1090	w, sh	-		$\nu(C_\beta C_1)_{asym}$ and, or $\gamma(=C_bH_2)_{sym}$	ν_{23}	A_{2g}
-		-		-		-		1080	w, b	$\nu(C_\beta C_1)_{asym}$, possible marker band	ν_{23}	A_{2g}
1009	w, b	1012	w, b	1012	m, b	-		-		Phenylalanine		
-		-		-		1007	w, b	1001	m, b	$\nu(C_\beta\text{-methyl})_{asym}$	ν_{45}	E_u
-		-		-		965	w, b	967	w	$\delta(\text{pyr deform})_{asym}$	ν_{46}	E_u
-		-		-		-		832	w	$\gamma(C_mH)$	γ_{10}	B_{1u}
757	m	757	m,b	760	s	754	w, b	754	s, b	$\nu(\text{pyr breathing})_{asym}$	ν_{15}	B_{1g}

ν , stretch; δ, in-plane deformation; γ, out-of-plane deformation; pyr, pyrrole; deform, deformation; asym, asymmetric; sym, symmetric; α, β, m, carbon positions on haem porphyrin; w, weak peak relative to others; m, medium peak relative to others , and, s, strong peak relative to others. Local coordinates, assignments and symmetry terms for the haem labelling scheme were adopted from references 320,322,405-414.

The spectrum of oxy-haemoglobin in RBCs was recorded from the microscope image in the region indicated by the red circle, presented in ***Figure 4-8 a, inset***. Poor signal-to-noise ratio with weak broad peaks were observed in the region of the asymmetric stretches of the porphyrin ring which were assigned to ν_{10} (ν $(C_\alpha C_m)_{asym}$) and include peaks at 1650 cm^{-1} and 1632 cm^{-1} (***Table 4-4 a***). A strong but broad peak in the core size region of the spectrum at 1594 cm^{-1} (ν_{37} (ν $(C_\alpha C_m)_{asym}$)) relative to other peaks was observed compared to a weaker carbon-carbon (C-C) stretch in the porphyrin ring at 1547 cm^{-1} (ν_{11} (ν $(C_\beta C_\beta)$). Weak and medium peaks at 1432 cm^{-1}, 1393 cm^{-1}, 1377 cm^{-1}, 1341 cm^{-1} and 1305 cm^{-1} were observed in the symmetric and deformed pyrrole-ring stretching region which were assigned to ν_{28} (ν $(C_\alpha C_m)_{sym}$), ν_{20} (ν (pyr quarter-ring)), ν_4 (ν (pyr half-ring)$_{sym}$), ν_{41} (ν (pyr half-ring)$_{sym}$) and a methine deformation mode, ν_{21} (δ_{asym} (C_mH) respectively. Broad peaks were observed in the spectral region of 1250-1000 cm^{-1} and included peaks at 1233 cm^{-1}, 1172 cm^{-1}, 1133 cm^{-1}, 1092 cm^{-1} and 1009 cm^{-1} which were assigned to ν_{13} or ν_{42} (δ (C_mH), ν_{30} (ν (pyr half-ring)$_{asym}$), ν_{22} (ν $(C_\alpha N)$) and, or (ν (pyr half-ring)$_{asym}$), ν_{23} (ν $(C_\beta C_1)_{asym}$) and, or $\gamma(=C_bH_2)_{sym}$) and the amino acid phenylalanine, whilst the peak at 757 cm^{-1} was assigned to the pyrrole breathing mode ν_{15} (ν (pyr breathing)$_{asym}$). The peak at 1009 cm^{-1} has been previously assigned to the amino acid phenylalanine in globin and has been known to be indicative of transitions between oxy- and deoxy-haemoglobin [313,316,415-416]. Notably, the observed spectrum for oxy-haemoglobin in RBCs showed similarities in the peak positions previously published by Wood *et al*, but, differed in terms of relative peak intensities and definition in the region of 1700-1500 cm^{-1} [316]. This could be as a result of differences in the resolution of the microscope images as well as excitation wavelengths [320].

In treated iRBCs, oxy- and deoxy-haemoglobin, haemozoin and a putative Fe(III)PPIX-test compound **1** complex spectra are illustrated in ***Figure 4-8 b-e*** with proposed assignments listed in ***Table 4-4 b-e***. All spectra are colour-coded and collected from the regions indicated by the same colour in the microscope image shown in ***Figure 4-8 b, inset***. The spectrum obtained for oxy-haemoglobin (red circle), illustrated in ***Figure 4-8 b***, showed peak positions that were very similar to oxy-haemoglobin in RBCs. This was in close agreement with findings previously reported by Dasgupta *et al* [417]. However, some peaks were observed to have shifted to higher wavenumbers (2-10 cm^{-1}) and there was broadening in the majority of the peaks ascribed to poorer signal-to-noise ratio. Specifically, in the core Fe(III)PPIX porphyrin region peaks at 1652 cm^{-1}, 1632 cm^{-1}, 1584 cm^{-1} and 1545 cm^{-1} were observed and assigned to ν_{10} (ν $(C_\alpha C_m)_{asym}$), ν_{37} (ν $(C_\alpha C_m)_{asym}$) and ν_{11} (ν $(C_\beta C_\beta)$) respectively. The peak at 1584 cm^{-1} was observed to be the strongest peak relative to the other peaks. Additional peaks were observed

in the spectrum for oxy-haemoglobin in treated iRBCs compared to oxy-haemoglobin in RBCs, specifically for the spectral region from 1700-1500 cm^{-1}. This was due to the fact that for oxy-haemoglobin in treated iRBCs, a better resolution was achieved, however, the appearance of these additional peaks was in close agreement with the observations previous reported by Wood *et al* [416]. In this region, similar weak peaks at 1642 cm^{-1}, 1601 cm^{-1}, 1574 cm^{-1} and 1545 cm^{-1} with the exception of 1632 cm^{-1} were observed for deoxy-haemoglobin (***Figure 4-8 c***) which was obtained from the region shown by the orange circle in ***Figure 4-8 c, inset***. These peaks were assigned to ν_{10} (ν $(C_\alpha C_m)_{asym}$), ν_{19} (ν $(C_\alpha C_m)_{asym}$), ν_{37} (ν $(C_\alpha C_m)_{asym}$) and ν_{11} (ν $(C_\beta C_\beta)$) respectively. The absence of the peak at 1632 cm^{-1} agreed with the findings reported by Strekas *et al*, Brunner *et al*, Ozaki *et al*, Venkatesh *et al* and Ong *et al* [319,418-421]. While it has also been reported in previous studies by Asghari-Khiavi *et al*, that the Raman spectrum of oxy- and deoxy-haemoglobin is very similar to the Raman spectrum of met-heamoglobin, this was as a result of the increased oxidation of oxy- and deoxy-haemogloin in RBCs that were fixed with glutaraldehyde which was not used in the present experiment [422]. On the other hand, it has also been previously reported that deoxy-haemoglobin and met-haemoglobin is similar in terms of peaks but differ where met-haemoglobin shows a peak at 1636 cm^{-1}. Therefore, since glutaraldehyde was not used as a fixative in this study the peak at 1636 cm^{-1} was not observed in the above spectrum for deoxy-haemoglobin proving that it was not met-haemoglobin [416]. Haemozoin, shown by the dark region (green circle) in the microscope image resulted in peaks at 1642 cm^{-1} (ν_{10} (ν $(C_\alpha C_m)_{asym}$)) and 1591 cm^{-1} (ν_{37} (ν $(C_\alpha C_m)_{asym}$)) which was similar to peaks observed for deoxy-haemoglobin (***Figure 4-8 c***). The latter peak position was the strongest in haemozoin and has been attributed to excitonic coupling as a result of the propionate linkage of the Fe(III)PPIX porphyrin units in haemozoin [322,423]. The putative Fe(III)PPIX-test compound **1** complex (purple arrow in ***Figure 4-8 c, inset***) showed peaks at 1633 cm^{-1}, 1591 cm^{-1} and 1564 cm^{-1}, where the peak at 1564 cm^{-1} was shifted to a higher wavenumber (17-19 cm^{-1}) compared to the other Fe(III)PPIX complexes (***Figure 4-8 d***). Peak assignments pertaining to ν_{10} (ν $(C_\alpha C_m)_{asym}$)), ν_{37} (ν $(C_\alpha C_m)_{asym}$)), ν_{11} (ν $(C_\beta C_\beta)$) and, or ν_{20} (δ(N-H)) respectively, were made for these peaks.

For the region pertaining to the pyrrole-ring stretches and carbon-hydrogen (C-H) deformations, oxy-haemoglobin resulted in peaks at 1442 cm^{-1}, 1399 cm^{-1}, 1379 cm^{-1}, 1364 cm^{-1}, 1316 cm^{-1} which were assigned to ν_{28} (ν $(C_\alpha C_m)_{sym}$), ν_{20} (ν (pyr quarter-ring)), ν_4 (ν (pyr half-ring)$_{sym}$) and ν_{21} (δ $(C_m H)_{asym}$) respectively. Deoxy-haemoglobin showed peaks at 1372 cm^{-1} and 1317 cm^{-1} with the exclusion of 1349 cm^{-1} which was shifted to lower wavenumbers. These peaks were assigned to ν_4 (ν (pyr half-ring)$_{sym}$), ν_{21} (δ $(C_m H)_{asym}$) and ν_{41} (ν (pyr half-

ring)$_{sym}$) respectively. Compared to the other Fe(III)PPIX complexes, deoxy-haemoglobin showed a peak at 1249 cm^{-1} which was assigned to ν_{13} (δ (C_mH)). This specific peak was observed to be shifted from 1259 cm^{-1} in oxy-haemoglobin, which has been previously observed to be a distinctive difference when comparing the spectra of oxy- and deoxy-haemoglobin [415-416]. The peaks in this region for deoxy-haemoglobin were also observed to be more pronounced than in oxy-haemoglobin. This has been observed in previous studies and was suggested to be as a result of peaks in this region specifically tending to be sensitive to the oxidation and spin state of the Fe atom [423-430]. Similar to deoxy-haemoglobin, weak and broad peaks at 1349 cm^{-1} and 1314 cm^{-1}, assigned to ν_{41} (ν (pyr half-ring)$_{sym}$) and ν_{21} (δ (C_mH)$_{asym}$) were observed for haemozoin. The putative Fe(III)PPIX-test compound **1** complex had peaks at 1456 cm^{-1}, 1437 cm^{-1} (ν_{28} (ν ($C_\alpha C_m$)$_{sym}$)), 1399 cm^{-1} (ν_{20} (ν (pyr quarter-ring))), 1364 cm^{-1} (ν_4 (ν (pyr half-ring)$_{sym}$)) and 1312 cm^{-1} (ν_{21} (δ (C_mH)$_{asym}$)) which were similar to that observed for the other Fe(III)PPIX complexes with the exception of an additional peak observed at 1456 cm^{-1}. This peak was assigned to an aromatic ring vibration (ν_{19} (ν (C=C)$_{sym}$)).

Towards lower wavenumbers, oxy-haemoglobin showed peaks at 1090 cm^{-1}, 1012 cm^{-1} and 757 cm^{-1} that were assigned to ν_{23} (ν ($C_\beta C_1$)$_{asym}$) and, or γ(=C_bH_2)$_{sym}$), phenylalanine and ν_{15} (ν (pyr breathing)$_{asym}$). Similarly, deoxy-haemoglobin and haemozoin showed peaks at 1133 cm^{-1}, 1095 cm^{-1}, 1012 cm^{-1}, 760 cm^{-1} and 1160 cm^{-1}, 1134 cm^{-1}, 1090 cm^{-1}, 1007 cm^{-1}, 965 cm^{-1} and 754 cm^{-1} respectively. For deoxy-haemoglobin these peaks were assigned to ν_{22} (ν (C_αN)) and, or (ν (pyr half-ring)$_{asym}$)), ν_{23} (ν ($C_\beta C_1$)$_{asym}$) and, or γ(=C_bH_2)$_{sym}$), phenylalanine and ν_{15} (ν (pyr breathing)$_{asym}$), where, peaks for haemozoin were assigned to ν_{22} (ν (C_αN)) and, or (ν (pyr half-ring)$_{asym}$)), ν_{23} (ν ($C_\beta C_1$)$_{asym}$) and, or γ(=C_bH_2)$_{sym}$), ν_{45} (ν (C_β-methyl)$_{asym}$), ν_{46} (δ(pyr deform)$_{asym}$) and ν_{15} (ν (pyr breathing)$_{asym}$). Notably, the peak at 1133 cm^{-1} for deoxy-haemoglobin and 1134 cm^{-1} for haemozoin differed in relative intensity but coincided with similar observed peaks in oxy-haemoglobin in RBCs and the putative Fe(III)PPIX-test compound **1** complex. Reports by Hobro *et al*, reported similar findings where peaks in the region of the pyrrole half-ring stretches for haemoglobin and haemozoin were similar but tended to differ in their relative intensities [431]. In addition, the peak at 1160 cm^{-1} was observed to only appear in the spectrum for haemozoin. It has been suggested by Hobro *et al* that the appearance of this peak could be the reason for the differences in the relative intensities for the neighboring peaks (1185 cm^{-1} and 1134 cm^{-1}) in the pyrrole half-ring stretching region compare to the strong peaks for oxy-haemoglobin, deoxy-haemoglobin and the putative Fe(III)PPIX-test compound **1** complex between 1180-1130 cm^{-1} [431]. The putative Fe(III)PPIX-test compound **1** complex showed peaks at 1136 cm^{-1}, 1080 cm^{-1}, 1001 cm^{-1}, 967 cm^{-1}, 832 cm^{-1}

and 754 cm^{-1}. These peaks, excluding 1080 cm^{-1}, were assigned to ν_{22} (ν ($C_\alpha N$)) and, or (ν (pyr half-ring)$_{asym}$)), ν_{45} (ν (C_β-methyl)$_{asym}$), ν_{46} (δ(pyr deform)$_{asym}$), γ_{10} (γ(C_mH)) and ν_{15} (ν (pyr breathing)$_{asym}$) respectively. With regards to the peak at 1080 cm^{-1} (ν_{23} (ν ($C_\beta C_1$)$_{asym}$), this was not observed in any of the spectra for the other Fe(III)PPIX complexes, shown by the red line in ***Figure 4-8 a-e***. However, it could be that the peak at 1090 cm^{-1} is red shifted to 1080 cm^{-1} which is indicative of a π- π interaction with the pyrrole and imidazole ring. This has been previously observed by Tempera *et al* with CQ where it was also suggested that a similar shift was as a result of the π- π interaction between the pyrrole and quinoline rings [376]. It is also worth noting that the peaks observed at 1349 cm^{-1}, 1314 cm^{-1}, 1228 cm^{-1}, 1185 cm^{-1}, 1090 cm^{-1} and 1007 cm^{-1} in haemozoin appeared shifted in the spectrum of the putative Fe(III)PPIX-test compound **1** complex and included an absence of the peak at 1160 cm^{-1}. In addition, an increased signal-to-noise ratio was observed for the peaks at 1134 cm^{-1} and 754 cm^{-1} in the spectrum of the putative Fe(III)PPIX-test compound **1** spectrum compared to haemozoin. Therefore, these observed changes in the peak position and shape of the spectrum for the putative Fe(III)PPIX-test compound **1** complex compared to haemozoin could also be indicative of changes in the molecular environment of Fe(III)PPIX as a result of a π- π interaction between test compound **1** and Fe(III)PPIX [322,376]. It was, however, apparent that in the spectrum of the putative Fe(III)PPIX-test compound **1**, no prominent peaks attributed to test compound **1** were observed. This is likely the result of haem resonance. Similar observations were reported by Webster *et al* for CQ-treated iRBCs [322].

Next, single scan Raman spectra were recorded for synthetic Fe(III)PPIX complexes. This was in order to determine whether the spectrum of the putative Fe(III)PPIX-test compound **1** complex was unique to test compound **1**-treated iRBCs. The spectra along with the observed peak positions, local coordinate assignments and symmetry terms for all synthetic Fe(III)PPIX complexes are presented in ***Figure 4-9 a-e*** and ***Table 4-5 a-e***. The results are discussed below.

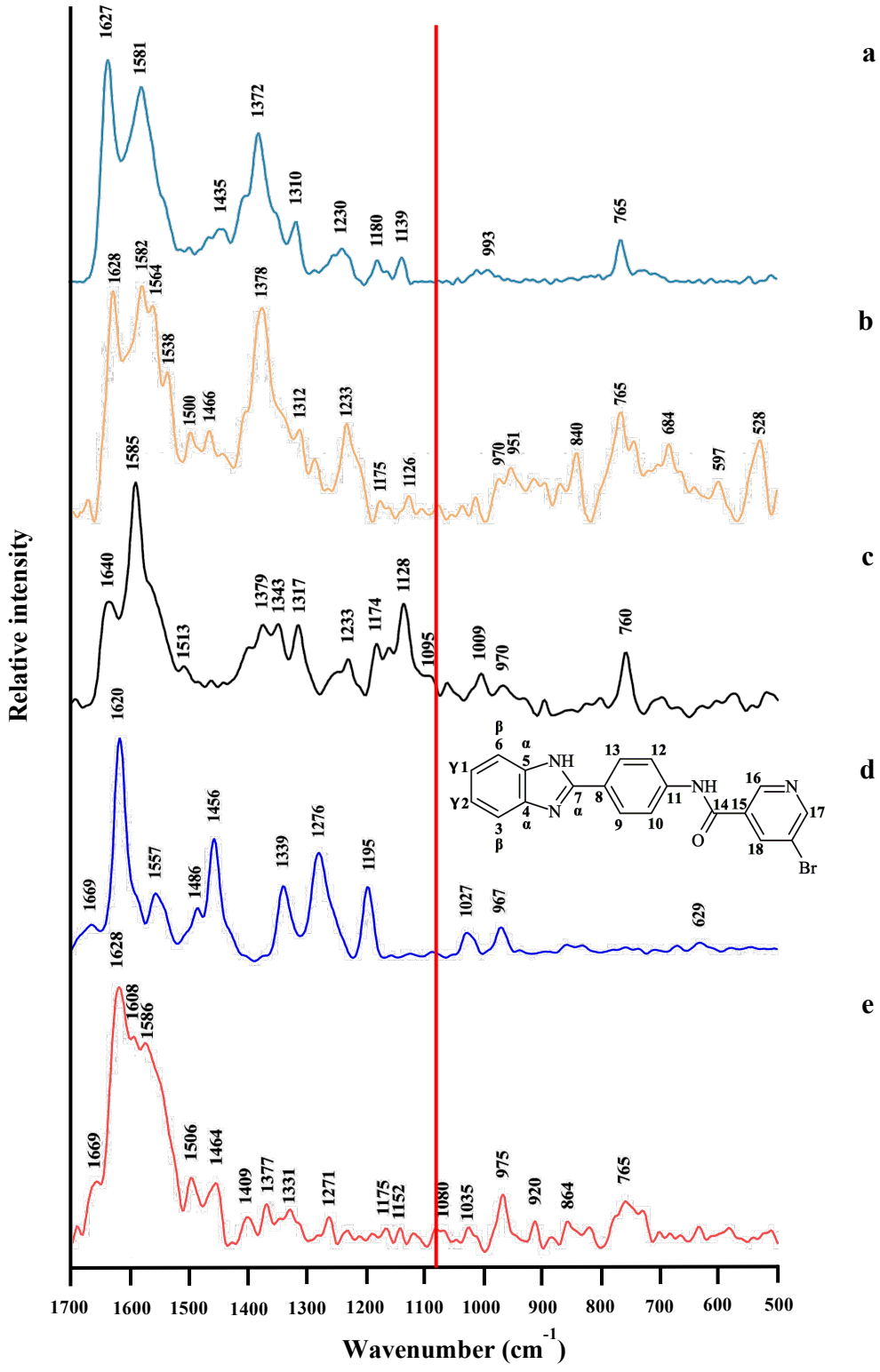

Figure 4-9 a-e: Single scan Raman spectra for synthetic Fe(III)PPIX complexes represented by (a) haematin, (b) haemin, (c) β-haematin, (d) test compound **1** (***inset***), and, (e) haematin-test compound **1** mixture precipitated from aqueous DMSO. The red line represents the possible marker band for the Fe(III)PPIX-test compound **1** complex at 1080 cm^{-1}.

Table 4-5: The observed peak positions, local coordinate, assignments and symmetry terms for synthetic Fe(III)PPIX complexes observed at 532 nm excitation [320,322,405-414]. Labels a-e correspond to haematin, haemin, β-haematin, test compound **1** and the haematin-test compound **1** mixture in DMSO respectively.

a		**b**		**c**		**d**		**e**		**Local coordinate**	**Assignment**	**Symmetry**
-		-		1640	s, b	-		-		$\nu(C_\alpha C_m)_{asym}$	ν_{10}	B_{1g}
1627	s	1628	s	-		-		1628	s, b	$\nu(C_a{=}C_b)$	ν ($C_a{=}C_b$)	
-		-		-		1620	s	-		$\nu(C{=}C)_{Bz}$ and, or $\nu(C{=}N)$	ν_{11}	E_{2g}
1581	s, b	1582	s	1585	s	-		1586	s, sh	$\nu(C_\alpha C_m)_{asym}$	ν_{37}	E_u
-		1564	s, sh	-		-		-		$\nu(C_\beta C_\beta)$	ν_2	A_{1g}
-		-		-		1557	m, b	-		$\nu(C_\beta C_\beta)$ and, or δ(N-H)	ν_{20}	
-		1538	m	-		-		-		$\nu(C_\beta C_\beta)$	ν_{11}	B_{1g}
-		-		-		1486	w, sh	-		$\nu(C{=}C)$	ν (C=C)	
-		-		-		1456	s	1464	w, b	$\nu(C{=}C)_{aromatic\ ring}$	ν_{19}	E_{2g}
1435	w, b	-		-		-		-		$\nu(C_\alpha C_m)_{sym}$	ν_{28}	B_{2g}
1372	s, b	1378	s, b	1379	m, b	-		1377	w	ν(pyr half-ring)$_{sym}$	ν_4	A_{1g}
-		-		1343	m, b	-		1331	w, b	ν(C-N) and, or ν(pyr half-ring)$_{sym}$	ν_{41}	E_u
-		-		-		1339	s, b	-		ν(C-N) and, or ν(C=C)		A_{2g}
1310	m	1312	m, sh	1317	m	-		-		$\delta_{asym}(C_mH)$	ν_{21}	A_{2g}
-		-		-		1276	s, b	1271	w	ν(C-N) and δ(Bz)	a'	
1230	w, b	1233	w, b	1233	w,b	-		-		$\delta(C_mH)$	ν_{13} or ν_{42}	B_{1g}, Eu
-		-		-		1195	m	-		$\nu(C\text{-}H)_{aromatic\ ring}$ and $\delta(C\text{-}H)_{Bz}$		
1180	w	1175	w	1174	m	-		1175	w, b	ν(pyr half-ring)$_{asym}$	ν_{30}	B_{2g}
1139	w, b	1126	w, b	1128	m	-		-		$\nu(C_\alpha N)$ and, or ν(pyr half-ring)$_{asym}$	ν_{22}	A_{2g}
-		-		1095	w,sh	-		-		$\nu(C_\beta C_1)_{asym}$ and, or $\gamma(=C_bH_2)_{sym}$	ν_{23}	A_{2g}
-		-		-		-		1080	w, b	$\nu(C_\beta C_1)_{asym}$ and, or possible marker band	ν_{23}	A_{2g}
-		-		-		1027	w, b	-		δ(Bz) and, or $\nu(C_\beta C_1)_{asym}$		
993	w, b	-		1009	w, b	-		-		$\nu(C_\beta C_1)_{asym}$	ν_{45}	E_u
-		970	w, b	970	w, b	-		975	m	δ(pyr deform)$_{asym}$ and, or $\gamma(=C_bH_2)_{sym}$	ν_{46}	E_u
-		-		-		967	w, b	-		δ(Im) and, or δ(pyr breathing)$_{sym}$	ν_{46}	E_{2u}
765	m	765	m, b	760	m, b	-		765	w, b	ν(pyr breathing)$_{asym}$	ν_{15}	B_{1g}
-		-		-		629	w, b	-		γ(N-H)	ν_{30}	C_s

ν , stretch; δ, in-plane deformation; γ, out-of-plane deformation; Bz, benzene; Im, imidazole; pyr, pyrrole; deform, deformation; asym, asymmetric; sym, symmetric; α, β, m, carbon positions on haem porphyrin; w, weak peak relative to others; m, medium peak relative to others , and, s, strong peak relative to others. Local coordinates, assignments and symmetry terms for the haem labelling scheme were adopted from references 320,322,405-414.

First, haematin was observed to result in a spectrum with peaks showing better signal-to-noise ratio compared to haemin that showed a poor signal-to-noise ratio with broader featureless peaks (***Figure 4-9 a-b***). In particular, for the Fe(III)PPIX porphyrin core size region (***Table 4-5 a-b***), haematin and haemin showed peaks at 1627 cm^{-1}, 1581 cm^{-1}, and, 1628 cm^{-1}, 1582 cm^{-1}, 1564 cm^{-1} and 1538 cm^{-1} respectively. These peaks were assigned to $\nu(C_a{=}C_b)$, ν_{37} (ν $(C_\alpha C_m)_{asym}$), and, $\nu(C_a{=}C_b)$, ν_{37} (ν $(C_\alpha C_m)_{asym}$), ν_2 ($\nu(C_\beta C_\beta)$) and ν_{11} $\nu(C_\beta C_\beta)$ respectively. In the region of the pyrrole-ring stretches and C-H deformations (1500-1200 cm^{-1}), haematin and haemin showed similar peaks with some peaks that were shifted slightly to higher wavenumbers in haemin. Haematin showed peaks at 1435 cm^{-1}, 1372 cm^{-1}, 1310 cm^{-1} and 1230 cm^{-1}, where haemin showed peaks at 1378 cm^{-1} (ν_4 (ν (pyr half-ring)$_{sym}$)), 1312 cm^{-1} (ν_{21} (δ $(C_mH)_{asym}$)) and 1233 cm^{-1} (ν_{13} or ν_{42} (δ (C_mH))). The peaks for haematin were assigned to ν_{28} (ν $(C_\alpha C_m)_{sym}$), ν_4 (ν (pyr half-ring)$_{sym}$), ν_{21} (δ $(C_mH)_{asym}$) and ν_{13} or ν_{42} (δ (C_mH)). On the lower end of the spectra, haematin showed peaks at 1180 cm^{-1}, 1139 cm^{-1}, 993 cm^{-1} and 765 cm^{-1}, where, haemin showed peaks at 1175 cm^{-1}, 1126 cm^{-1}, 970 cm^{-1} and 765 cm^{-1}. These peaks were assigned to pyrrole half-ring stretches and breathing modes which were designated as; ν_{30} (ν (pyr half-ring)$_{asym}$), ν_{22} (ν $(C_\alpha N)$) and, or (ν (pyr half-ring)$_{asym}$)), ν_{45} (ν $(C_\beta$-methyl$)_{asym}$) and ν_{15} (ν (pyr breathing)$_{asym}$). Haemin was observed to have an additional peak at 970 cm^{-1}, which could correspond to ν_{46} (δ(pyr deform)$_{asym}$) and, or ($\gamma(=C_bH_2)$). Both spectra were similar to that obtained by Wood *et al*, who identified haematin to be in the monomeric Fe^{3+} high spin state and haemin in the Fe^{3+} high spin state [416].

The spectrum of β-haematin exhibited peaks at 1640 cm^{-1}, 1585 cm^{-1}, 1379 cm^{-1}, 1343 cm^{-1}, 1317 cm^{-1}, 1233 cm^{-1}, 1174 cm^{-1}, 1128 cm^{-1}, 1095 cm^{-1}, 1009 cm^{-1}, 970 cm^{-1} and 760 cm^{-1} which coincided with the observed peaks for haemozoin (***Table 4-5 c***). These peaks were assigned to ν_{10} (ν $(C_\alpha C_m)_{asym}$), ν_{37} (ν $(C_\alpha C_m)_{asym}$), ν_4 (ν (pyr half-ring)$_{sym}$), ν_{41} (ν (pyr half-ring)$_{sym}$) and, or (ν (C-N)), ν_{21} (δ $(C_mH)_{asym}$)), ν_{13} or ν_{42} (δ (C_mH)), ν_{30} (ν (pyr half-ring)$_{asym}$), ν_{22} (ν $(C_\alpha N)$) and, or (ν (pyr half-ring)$_{asym}$)), ν_{23} (ν $(C_\beta C_1)_{asym}$) and, or $\gamma(=C_bH_2)_{sym}$), ν_{45} (ν $(C_\beta$-methyl$)_{asym}$), ν_{46} (δ(pyr deform)$_{asym}$) and, or ($\gamma(=C_bH_2)$) and ν_{15} (ν (pyr breathing)$_{asym}$) respectively. In β-haematin, a commonly observed peak at 1375 cm^{-1} has been previously reported to be an indication that β-haematin is a high spin Fe(III) species [414]. This appeared to be shifted to 1379 cm^{-1} in this study (***Figure 4-9 c***). Overlay demonstrates how similar the spectra for haemozoin and β-haematin in fact are (***Figure 4-10***).

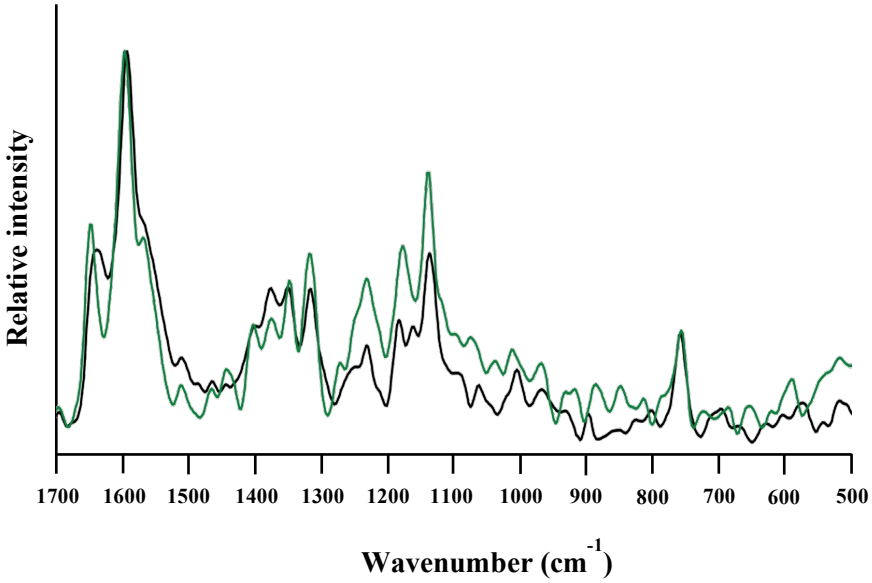

Figure 4-10: Overlay of the single scan Raman spectra for haemozoin in situ in a parasite (green) in test compound 1-treated iRBCs and synthetically prepared β-haematin in DMSO (black).

Figure 4-9 d illustrates the spectrum for test compound **1** in DMSO that showed very good signal-to-noise ratio which coincided with clearly defined peaks, specifically for the spectral range of 1700-1100 cm^{-1} (***Figure 4-9 d, inset***). Peaks at 1620 cm^{-1}, 1557 cm^{-1}, 1486 cm^{-1} and 1456 cm^{-1} were observed, with the strongest peaks being 1620 cm^{-1} and 1456 cm^{-1}. These peaks were assigned to ν_{11} (ν(C=C)$_{Bz}$) and, or (ν(C=N)), ν_{20} ($\nu(C_\beta C_\beta)$ and, or (δ(N-H)), (ν(C=C)) and the aromatic ring stretch ν_{19} (ν(C=C). In the region of 1400-1000 cm^{-1}, test compound **1** showed peaks at 1339 cm^{-1}, 1276 cm^{-1}, 1195 cm^{-1} and 1027 cm^{-1} which were assigned to the vibrational and stretching modes of the benzimidazole which included; ν(C-N) and, or ν(C=C), a' (ν(C-N) and δ(Bz)), ν(C-H)$_{\text{aromatic ring}}$ and δ(C-H)$_{Bz}$, δ(Bz) and, or $\nu(C_\beta C_1)_{asym}$. Towards the lower end of the spectrum, peaks at 967 cm^{-1} and 629 cm^{-1}, assigned to ν_{46} (δ(Im) and, or δ(pyr breathing)$_{sym}$) and ν_{30} (γ(N-H)), were observed to be much broader and weaker compared to the other peaks (***Table 4-5 d***).

The haematin-test compound **1** mixture showed peaks that were related to both haematin and test compound **1** which was suggested to be as a result of the presence of unbound haematin and test compound **1** with bound haematin and test compound **1** in the mixture (***Figure 4-9 e***). Moreover, the peaks that were observed for this haematin-test compound **1** mixture included; 1628 cm^{-1}, 1586 cm^{-1}, 1464 cm^{-1}, 1377 cm^{-1}, 1331 cm^{-1}, 1271 cm^{-1}, 1175 cm^{-1}, 1080 cm^{-1}, 975 cm^{-1} and 765 cm^{-1}. These peaks were designated to $\nu(C_a{=}C_b)$, ν_{37} (ν $(C_\alpha C_m)_{asym}$), aromatic ring stretch ν_{19} (ν(C=C), ν_4 (ν (pyr half-ring)$_{sym}$), ν_{41} (ν (pyr half-ring)$_{sym}$), a' (ν(C-N) and δ(Bz)),

ν_{30} (ν (pyr half-ring)$_{asym}$), ν_{23} (ν ($C_\beta C_1$)$_{asym}$), ν_{46} (δ(pyr deform)$_{asym}$) and ν_{15} (ν (pyr breathing)$_{asym}$) respectively, which are listed in ***Table 4-5 e***. The solution contained a large excess of test compound **1** relative to the amount of haematin. This was in order to drive the equilibrium towards complex formation and to reduce the domination of test compound **1** signals by the signals associated with unbound haematin, which would dominate the spectrum owing to the haem resonance effect. Again, the peak at 1080 cm^{-1} that was observed in the spectrum for the putative Fe(III)PPIX-test compound **1** complex in treated iRBCs was observed in the spectrum for the haematin-test compound **1** mixture, but in none of the other Fe(III)PPIX complexes (red line). From here, it was inferred that this specific peak could indeed be a marker band for the Fe(III)PPIX-test compound **1** complex. However, as presented the spectra differed visibly, where the haematin-test compound **1** mixture showed a much lower signal-to-noise ratio in comparison to the putative Fe(III)PPIX-test compound **1** complex. This was unsurprising given the drastic differences in haematin to test compound **1** ratio.

To reduce this problem, the spectra of these Fe(III)PPIX complexes were overlaid as illustrated in ***Figure 4-11***. For comparison, the spectra for the putative Fe(III)PPIX-test compound **1** complex and test compound **1** in DMSO (black) were added together in the same ratio before overlaying the averaged spectrum with the spectrum of the haematin-test compound **1** mixture (peach). The resulting overlaid spectra showed similarities in most parts of the spectrum, but, this was more apparent in the spectral range of 1700-1400 cm^{-1}. However, the spectra differed in parts of the spectrum that were attributed to the pyrrole-ring stretching region (1400-1000 cm^{-1}) with a poor signal-to-noise ratio.

A disadvantage with the haematin-test compound **1** mixture was that solubility difficulties were encountered with test compound **1** which made it difficult to precipitate the synthetically prepared complex. Multiple experiments were required before it was concluded that the mixture would have to be analyzed in solution rather, which could explain the poor signal-to-noise ratio. Nonetheless, it was inferred that the proposed Fe(III)PPIX-test compound **1** complex observed in treated iRBCs was in fact a complex that formed between Fe(III)PPIX and test compound **1** because peak positions were almost identical, with only intensities varying.

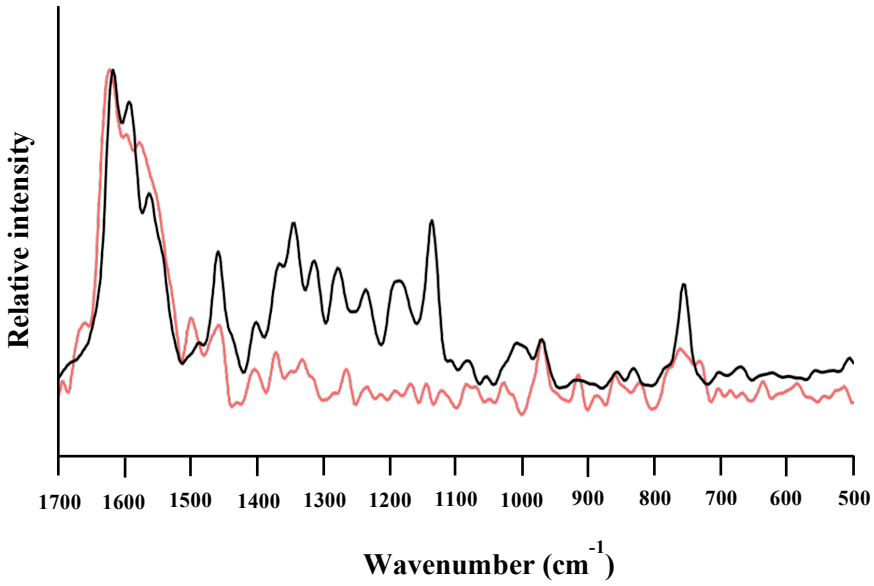

Figure 4-11: Overlay of the Raman spectra for the putative Fe(III)PPIX-test compound **1** complex averaged with the spectrum of test compound **1** in DMSO (black) with the haematin-test compound **1** mixture (peach).

4.4.2.2 Confocal Raman true mapping images

A fast, efficient and non-invasive imaging technique that is rapidly advancing the way in which the variations in chemical and molecular vibrations observed in a Raman spectrum are imaged is, confocal Raman imaging [432]. The images that are obtained are often recorded for a specific region which is defined by the number of lines per image and points per line, where each pixel pertains to a specific spectrum within the image. Here, this allows for the sample to be analyzed for one Fe(III)PPIX complex at a time [433]. Thus, this technique was used to gain further insights into the contribution of a specific Raman peak to the signal distribution for a specific Fe(III)PPIX complex, and thus being able to identify the location of the specific spectra pertaining to each Fe(III)PPIX complex in untreated and treated iRBCs.

In brief, CQS NF54 parasites were treated with test compound **1** (1 × IC_{50}) and incubated at physiological temperature for 30-32 hrs. Cultures were removed after the incubation period, aspirated, then fixed with 25% glutaraldehyde in filtered PBS and stored at 4 °C. An advantage of using an aldehyde as a fixative (e.g. glutaraldehyde), for imaging purposes is that aldehyde fixatives are known to preserve the native composition and components of the cell without the formation of artefacts [435-436]. After 24 hrs, cultures were then left to stand for 15 min at rt. before smearing (2 µl) the samples onto the aluminium foil covered glass microscope slide. The same was applied to untreated iRBCs.

Thus, confocal Raman true mapping images were obtained for the Fe(III)PPIX complexes: oxy-haemoglobin; deoxy-haemoglobin; haemozoin; and the Fe(III)PPIX-test compound **1** complex from LAS image Raman spectra (see ***Section 4.3.2***, ***Figure 4-2***). Briefly, the LAS image Raman spectra were taken through a number of analysis steps using the WITec Project FIVE software. The spectra were analyzed using a built-in true component analysis tool, where, the spectra of each Fe(III)PPIX complex were individually extracted from the residual LAS image. The individually extracted component spectra were averaged and demixed. From here, the spectrum for each Fe(III)PPIX complex was analyzed separately by using the filter tool (width 1 cm^{-1}). This filter viewer was used to generate true mapping images at specific peak positions, including: 754 cm^{-1}; 1080 cm^{-1}; 1090 cm^{-1}; and 1642 cm^{-1} which were color-coded accordingly (red, green, yellow and orange respectively). These specific Raman peaks were chosen based on the observations discussed previously in ***Section 4.4.2.1***, where changes in peak intensities and positions were observed to be apparent in the presence of test compound **1**, as well as investigations into the distribution of the possible marker peak at 1080 cm^{-1} for the Fe(III)PPIX-test compound **1** complex. The results are discussed below.

I. Oxy-haemoglobin

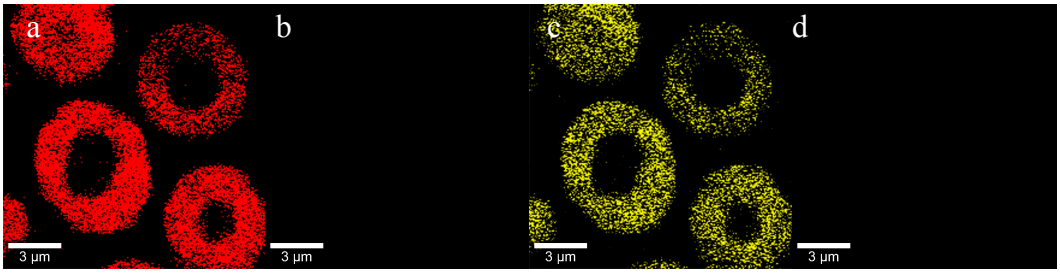

II. Deoxy-haemoglobin

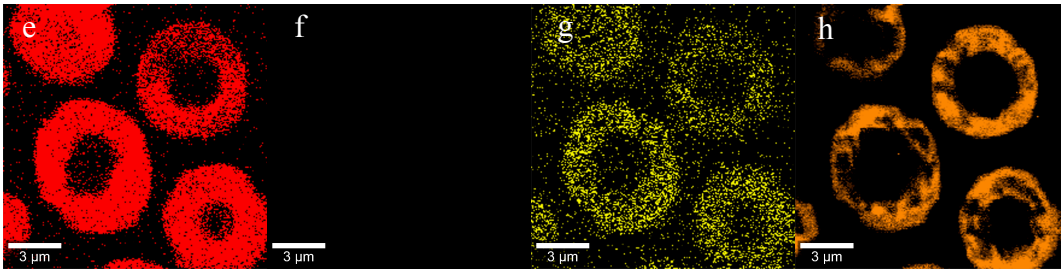

III. Haemozoin

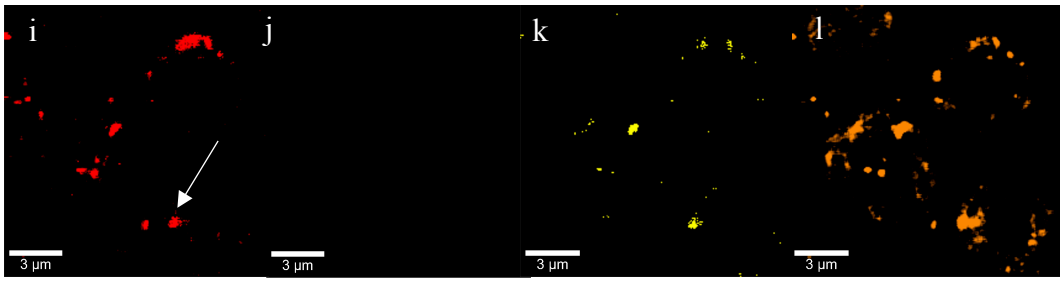

Figure 4-12 I-III: Confocal Raman true mapping images, obtained using true component analysis and filter viewer tools, for untreated iRBCs containing three distinct Fe(III)PPIX complexes which are represented by (I) oxy-haemoglobin, (II) deoxy-haemoglobin and (III) haemozoin which were imaged at specific Raman peaks represented by a, e and i) 754 cm^{-1} (red); b, f and j) 1080 cm^{-1} (green); c, g and k) 1090 cm^{-1} (yellow) and; d, h and l) 1642 cm^{-1} (orange) that were previously assigned to ν_{15} (ν (pyr breathing)$_{asym}$), ν_{23} (ν ($C_\beta C_1$)$_{asym}$), ν_{23} ($\nu(C_\beta C_1)_{asym}$ and, or $\gamma(=C_bH_2)_{sym}$) and ν_{10} ($\nu(C_aC_m)_{asym}$). (15 × 15 points per image and points per line and 0.05 s intergration time with a run time =35 min).

The confocal Raman true mapping images for untreated iRBCs are shown in ***Figure 4-12 I-III*** for three distinct Fe(III)PPIX complexes namely: oxy-haemoglobin; deoxy-haemoglobin; and haemozoin. The images for these Fe(III)PPIX complexes were determined at four specific Raman peaks: 754 cm^{-1} (red); 1080 cm^{-1} (green); 1090 cm^{-1} (yellow); and 1642 cm^{-1} (orange) that were previously assigned to ν_{15} (ν (pyr breathing)$_{asym}$), ν_{23} (ν ($C_\beta C_1$)$_{asym}$) and, or possible marker band, ν_{23} ($\nu(C_\beta C_1)_{asym}$ and, or $\gamma(=C_bH_2)_{sym}$) and ν_{10} ($\nu(C_aC_m)_{asym}$) respectively.

It was observed from the images at the Raman peak of 754 cm^{-1} represented the signal distribution of oxy- and deoxy-haemoglobin in the RBC of the iRBC, where, the image for deoxy-haemoglobin was observed to be more pronounce (***Figure 4-12 a*** and ***e***). For the image pertaining to haemozoin, the signal distribution of haemozoin was observed to be localized in the parasite DV with some haemozoin outside of the RBC (***Figure 4-12 i***, white arrow). This has been observed recently by Kapishnikov *et al* who revealed with X-ray fluorescence microscopy that several isolated haemozoin crystals were observed outside RBCs [291]. At the Raman peak of 1080 cm^{-1}, no signal distribution was observed in the images for all Fe(III)PPIX complexes which was expected, since none showed a peak at this position (***Figure 4-12 b, f*** and ***j***). On the other hand, oxy-haemoglobin, deoxy-haemoglobin and haemozoin produced images at the Raman peak of 1090 cm^{-1}, which, all showed similar signal distributions to that observed for the Raman peak at 754 cm^{-1} (***Figure 4-12 c, g*** and ***k***), although, compared to the images at the Raman peak of 754 cm^{-1}, a more intense signal for oxy-haemoglobin was observed than that for deoxy-haemoglobin. Haemozoin showed a much less intense signal distribution but was consistent with the observations for the Raman peak at 754 cm^{-1}. Additionally, the Raman peak at 1642 cm^{-1} resulted in images illustrated in ***Figure 4-12 d, h*** and ***l*** which showed clear signal distributions for deoxy-haemoglobin and haemozoin, but not oxy-haemoglobin. This was expected since oxy-haemoglobin did not show a peak at this position. The images for deoxy-haemoglobin and haemozoin showed intense signals distributed in the RBC and parasite DV respectively.

To compare, confocal Raman true mapping images for test compound **1**-treated iRBCs were also investigated at the same Raman peaks for untreated iRBCs. ***Figure 4-13 I-IV*** illustrates the true mapping images for four distinct Fe(III)PPIX complexes, including the Fe(III)PPIX-test compound **1** complex, that were observed to result in signal distributions that were similar to untreated parasites.

In more detail, the images for the Raman peak at 754 cm^{-1} showed a strong signal distribution in the RBC of the treated iRBC for oxy- and deoxy-haemolgobin, whereas, haemozoin and the Fe(III)PPIX-test compound **1** complex showed signal distributions within the DV (***Figure 4-13 a, e, i*** and ***m***). Interestingly, the signal distribution for haemozoin and the Fe(III)PPIX-test compound **1** complex were observed to result in similar signal distribution images at this Raman peak, with a less intense signal distribution observed for the Fe(III)PPIX-test compound **1** complex. Similar to the observations for untreated iRBCs, the image for haemozoin revealed haemozoin crystals outside of the RBC of the treated iRBC which may represent material from previous cycles (***Figure 4-13 i***, white arrows). However, for the

Fe(III)PPIX-test compound **1** complex at this particular Raman peak, it was suggested that this vibrational stretch (ν_{15} (ν (pyr breathing)$_{asym}$)) could be associated to both unbound Fe(III)PPIX itself or Fe(III)PPIX attributed to by the Fe(III)PPIX-test compound **1** complex. In addition, part of the signal was observed in the same region as the haemozoin seen outside of the RBC of the treated iRBC (***Figure 4-13 m***, white arrow).

For the Raman peak at 1080 cm^{-1}, none of the Fe(III)PPIX complexes resulted in a signal distribution except the Fe(III)PPIX-test compound **1** complex which was expected (***Figure 4-13 b, f, j*** and ***n***). From this, it was clear from the image illustrated in ***Figure 4-13 n*** that this particular Raman peak was unique for this particular Fe(III)PPIX-test compound **1** complex and could be considered to be marker band.

Images for the Raman peak at 1090 cm^{-1} were observed to result in signal distributions from the RBC for oxy-haemoglobin and deoxy-haemoglobin and the DV for haemozoin, except no signal was observed for the Fe(III)PPIX-test compound **1** complex (***Figure 4-13 c, g, k*** and ***o***). Additionally, oxy-haemoglobin showed a more intense signal than deoxy-haemoglobin, but, both showed a poorer signal-to-noise ratio in comparison to haemozoin.

The images for the Raman peak at 1642 cm^{-1} revealed no signal for oxy-haemoglobin and the Fe(III)PPIX-test compound **1** complex (***Figure 4-13 d*** and ***p***). On the other hand, deoxy-haemoglobin and haemozoin resulted in signal distributions that was localized to the RBC of the treated iRBC and parasite DV respectively (***Figure 4-13 h*** and ***l***).

I. Oxy-haemoglobin

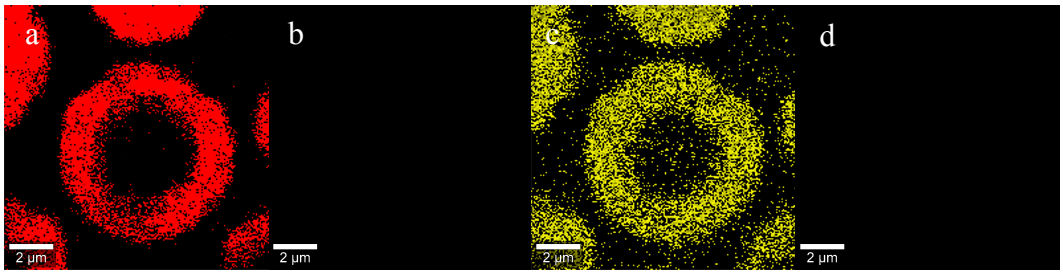

II. Deoxy-haemoglobin

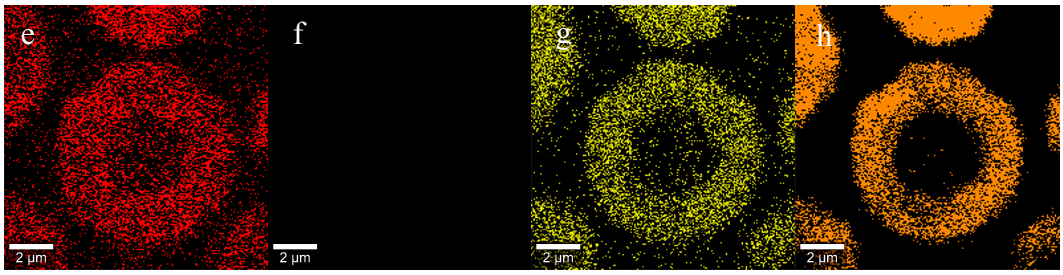

III. Haemozoin

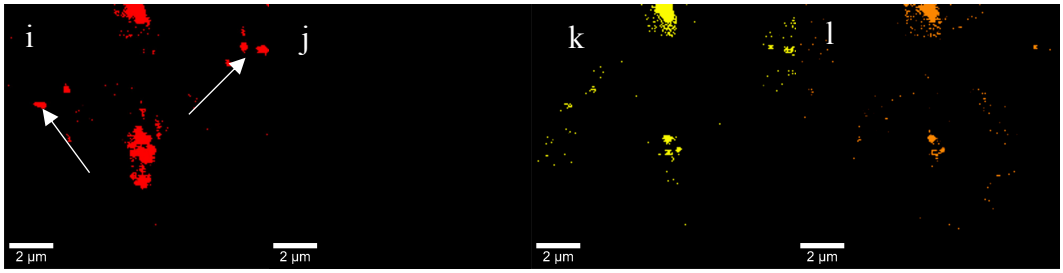

IV. Fe(III)PPIX-test compound 1 complex

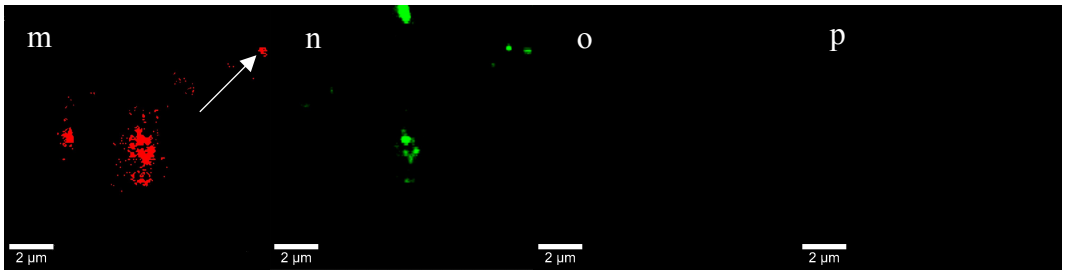

Figure 4-13 I-IV: Confocal Raman true mapping images obtained, using true component analysis and filter viewer tools, for test compound **1**-treated iRBCs containing four distinct Fe(III)PPIX complexes which are represented by (I) oxy-haemoglobin, (II) deoxy-haemoglobin, (III) haemozoin, and, (IV) Fe(III)PPIX-test compound **1** complex which were imaged at specific Raman peaks represented by a, e, i and m) 754 cm^{-1} (red); b, f, j and h)1080 cm^{-1} (green); c, g, k and o) 1090 cm^{-1} (yellow) and; d, h, l and p) 1642 cm^{-1} (orange) that have been previously assigned to ν_{15} (ν (pyr breathing)$_{asym}$), ν_{23} (ν ($C_\beta C_1$)$_{asym}$), ν_{23} ($\nu(C_\beta C_1)_{asym}$ and, or $\gamma(=C_bH_2)_{sym}$) and ν_{10} (ν (C_aC_m)$_{asym}$). (15 × 15 points per image and points per line and 0.05 s intergration time with a run time =35 min).

To better visualize whether the signal distribution of the spectra for haemozoin imaged at the peak position of 754 cm^{-1} and the Fe(III)PPIX-test compound **1** complex at the peak position of 1080 cm^{-1} were localized within the same region of the parasites DV, the true mapping images were overlaid (***Figure 4-10 a-c***). From this observation, it was apparent that the signal distribution of the spectra for haemozoin and the Fe(III)PPIX-test compound **1** complex are co-localized within the parasite DV. This is consistent with the findings from ESI presented above.

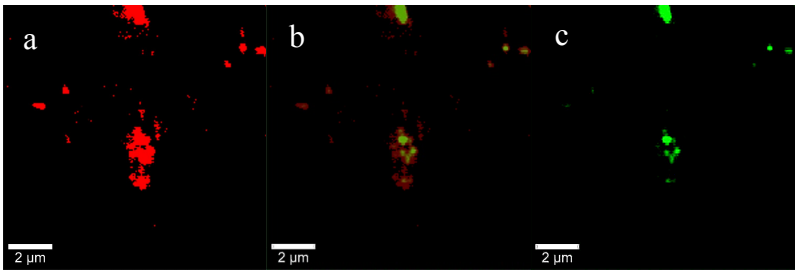

Figure 4-14 a-c: Evidence of the Fe(III)PPIX-test compound **1** complex in the DV of CQS NF54 test compound **1**-treated iRBCs represented by (b) overlaid image of (a) haemozoin at 754 cm^{-1} (red) and (c) Fe(III)PPIX-test compound **1** complex at 1080 cm^{-1} (green).

4.4.2.3 PCA

PCA, a common multidimensional analysis often used in combination with Raman spectroscopy to identify correlations and variability in the Raman spectra, was used in this study [417,431,437-439]. This analysis was used to statistically distinguish between the spectra for the different Fe(III)PPIX complexes based on their peak positions in view of the close similarity of the spectra. In essence, each repeat spectrum can be considered as a point in multidimensional space with a dimension equal to the number of peaks under consideration. These peak positions are then reduced to two dimensions on a set of orthogonal axes (PC1 and PC2). The variance within the spectra of each of the pair of Fe(III)PPIX complexes being considered is represented by a cluster of points on the plot. The replicate spectra for each Fe(III)PPIX complex were obtained from the true mapping images of treated iRBCs (***Figure 4-15 a-d***). The same process as described in ***Section 4.4.2.2***, was used to obtain true mapping images for synthetic Fe(III)PPIX complexes, specifically for performing PCA. Briefly, 150-200 spectra for each Fe(III)PPIX complex investigated in this study for the spectral range of 1700-500 cm^{-1} were collected individually prior to performing a number of analysis steps,

previously described in ***Section 4.3.3***. The eigenvectors with the corresponding eigenvalues were calculated for each Fe(III)PPIX complex being compared using Molegro data analysis tool after which individual PCA plots were constructed in GraphPad Prism v8.2.1. The results are discussed below.

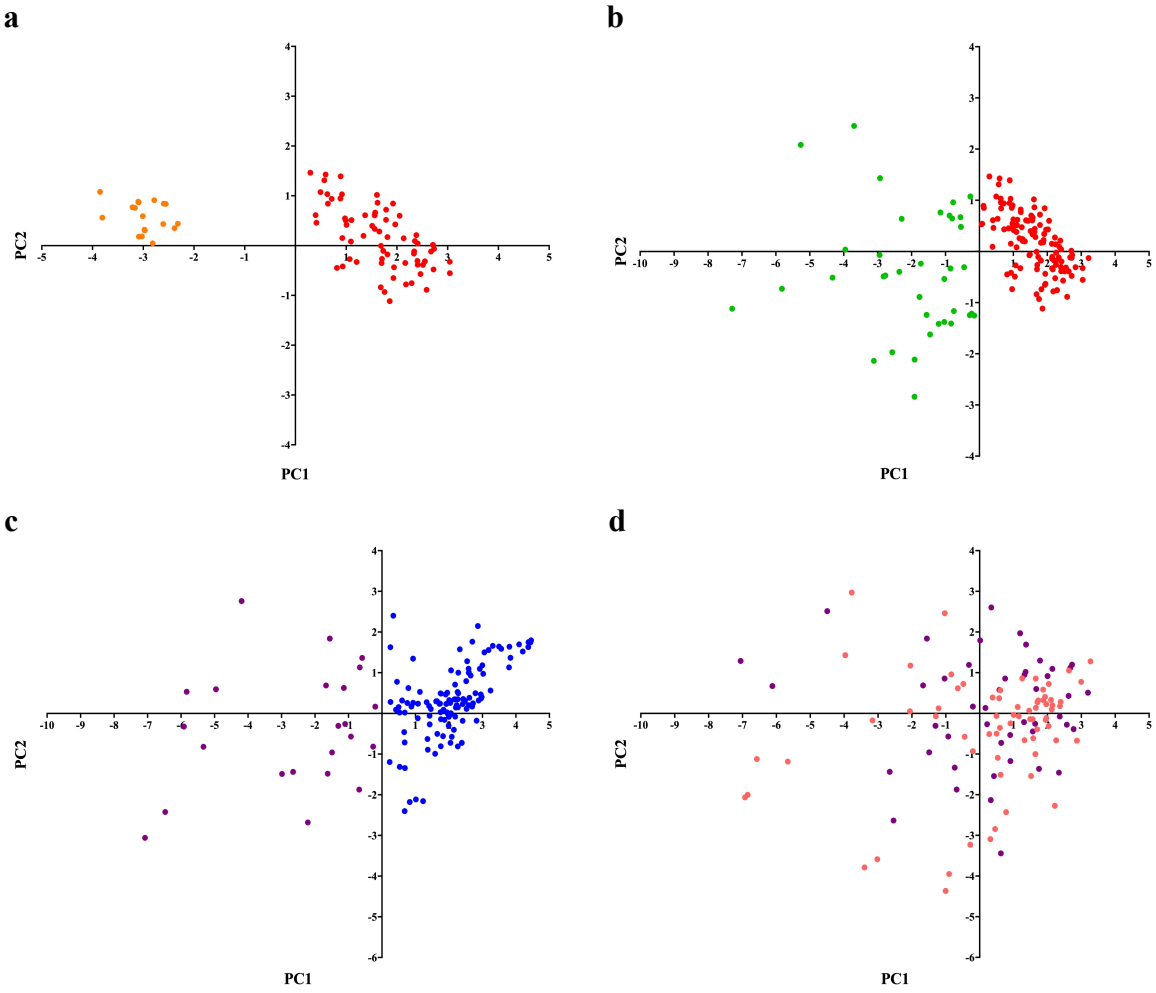

Figure 4-15 a-d: PCA plots for PC1 versus PC2 of Fe(III)PPIX complexes that were compared and are represented by (a) oxy- (red) and deoxy-haemoglobin (orange), (b) oxy-haemoglobin (red) and haemozoin (green), (c) test compound **1** (blue) and Fe(III)PPIX-test compound **1** complex (purple), and, (d) Fe(III)PPIX-test compound **1** complex (purple) and haematin-test compound **1** mixture (peach).

In ***Figure 4-15 a***, the PCA plot for oxy-haemoglobin (red) versus deoxy-haemoglobin (orange) in treated iRBCs showed a significant separation along PC1, where, 86% of the variance was accounted for by PC1 and 8% by PC2. In addition, the cluster for deoxy-haemoglobin was less scattered compared to the cluster for oxy-haemoglobin. A smaller separation between the clusters of oxy-haemoglobin (red) and haemozoin (green) was observed (***Figure 4-15 b***) along PC1. For this plot, 71% of the variance was accounted for by PC1 and 17% for PC2. This was expected as very similar peak positions for oxy-haemoglobin and haemozoin with slight shifts (2-5 cm^{-1}) were observed previously (see ***Section 4.4.2.1***). However, the haemozoin cluster showed a higher degree of scatter compared to that of oxy-haemoglobin which could be as a result of the quality of the replicated spectra for haemozoin. With that said, it was very difficult to obtain high quality spectra for haemozoin as after 30-32 hrs of incubation in the presence of test compound **1**, the haemozoin crystals were observed to be less well-defined (***Figure 4-5 d***) as a result of inhibition of haemozoin formation as well as being intimately mixed with the Fe(III)PPIX-test compound **1** complex thus decreasing the signal-to-noise ratio in the spectra as seen in ***Figure 4-8 e***.

Interestingly, for the PCA plot of test compound **1** (blue) and the Fe(III)PPIX-test compound **1** complex (purple) there was no sign of any overlap in the clusters but rather they were slightly separated along PC1 (***Figure 4-15 c***). About 71% variance was accounted for by PC1 and 16% for PC2 for this specific plot. One possible reason, was that the peaks relating to test compound **1** are dominated by the Fe(III)PPIX peaks as a result of haem resonance, therefore resulting in a separation between the two clusters. In addition, much less scatter was observed for the test compound **1** cluster compared to the Fe(III)PPIX-test compound **1** complex. Again, this could be as a result of the quality of the spectra obtained as well as the signal-to-noise ratio being too low for some of the replicates.

On the other hand, ***Figure 4-15 d*** shows the PC1 (63%) versus PC2 (21%) plot for the Fe(III)PPIX-test compound **1** complex versus the haematin-test compound **1** mixture where no significant separation was observed on either PC1 or PC2. From this, it was inferred that despite the difficulties in visually comparing these spectra, seen in ***Figure 4-11***, PCA confirms that the Fe(III)PPIX-test compound **1** complex is in fact the same as the haematin-test compound **1** mixture, at least with respect to peak positions, confirming that the spectra obtained from the cell almost certainly represent a complex, particularly given the appearance of the unique peak at 1080 cm^{-1} mentioned previously.

4.4.2.4 Welch's t-test analysis

To better establish the significance of the cluster separations observed in the PCA plots for the Fe(III)PPIX complexes, a Welch's t-test analysis was conducted (***Figure 4-16 a-d***). A similar approach called the Mahalanobis distance has been previously reported by Goodpaster *et al*, however, with the clusters being so close to the x axis this more complicated approach was not necessary [440]. The equations previously described in ***Section 4.3.4*** were used instead. This involved shifting the centroids of each cluster and transforming the clusters about the angle between the centroids in order to obtain a new shifted and transformed PCA plot of x versus y such that the centroids of both clusters lay on the x axis with one at the origin. From here, the new data points for the plot of y'' versus x'' were used to perform a Welch's t-test analysis of the x'' values in GraphPad Prism v8.2.1.

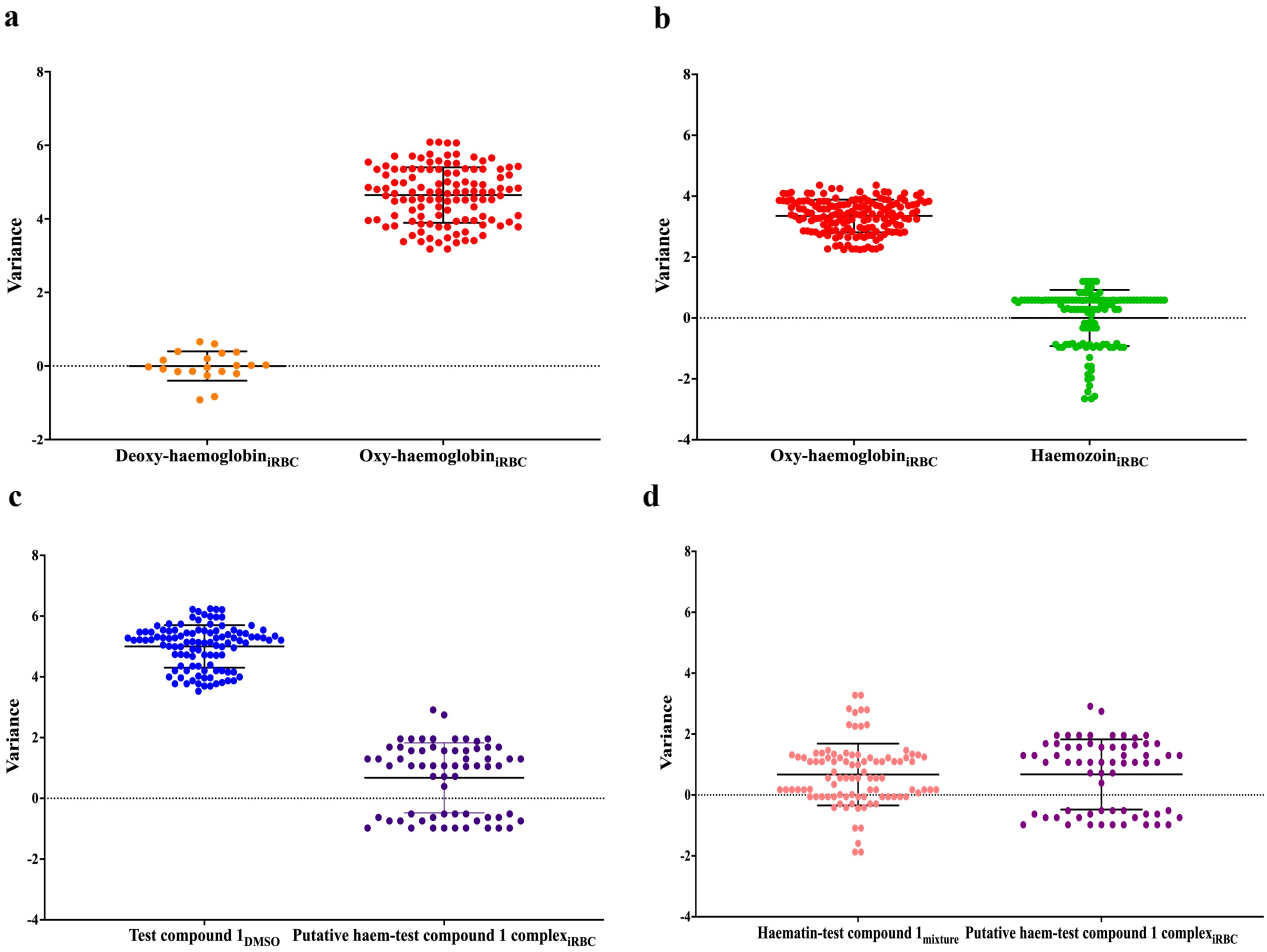

Figure 4-16 a-d: Welch's t-test plots for the PCA plots represented for; (a) oxy-haemoglobin versus deoxy-haemoglobin, (b) oxy-haemoglobin versus haemozoin, (c) test compound **1** versus the Fe(III)PPIX-test compound **1** complex, and, (d) the haematin-test compound **1** mixture versus the Fe(III)PPIX-test compound **1** complex. Using GraphPad Prism v8.2.1, correlation coefficients were calculated to be; $R^2 = 0.9736$, $R^2 = 0.8771$, $R^2 = 0.8889$ and $R^2 = 0.0000022$ respectively.

Figure 4-16 a-d presents the Welch's t-test analysis plots for the PCA plots shown in ***Figure 4-15 a-d***. From the Welch's t-test plots, it was observed that the separation between oxy-haemoglobin and deoxy-haemoglobin was significant at the 99.99% confidence level ($p = <0.0001$) and resulted in a correlation coefficient of $R^2 = 0.9736$. The same was observed for oxy-haemoglobin versus haemozoin ($p = <0.0001$; $R^2 = 0.8771$), and test compound **1** versus the Fe(III)PPIX-test compound **1** complex ($p = <0.0001$; $R^2 = 0.8889$). However, the separation between the Fe(III)PPIX-test compound **1** complex and the haematin-test compound **1** mixture was observed to be not significant ($p = 0.9869$; $R^2 = 0.0000022$). This further verifies that there

is in fact no separation between the clusters of the Fe(III)PPIX-test compound **1** complex and the Fe(III)PPIX-test compound **1** mixture in the PCA plot observed in ***Figure 4-15 d***.

Table 4-6: Statistical comparison of the Fe(III)PPIX-test compound **1** complex in treated iRBCs to all other Fe(III)PPIX complexes analyzed

Fe(III)PPIX complexes compared to Fe(III)PPIX-test compound 1 complex	***p* value**	**R^2 value**
a. oxy-haemoglobin in RBCs	<0.0001	0.7059
b. oxy-haemoglobin in treated iRBCs	<0.0001	0.6082
c. deoxy-haemoglobin in treated iRBCs	<0.0001	0.7523
d. haemozoin in treated iRBCs	<0.0001	0.7729
e. β-haematin	<0.0001	0.8371
f. haematin	<0.0001	0.8267
g. haemin	<0.0001	0.6017

In addition, PCA plots for the Fe(III)PPIX-test compound **1** complex versus all the remaining Fe(III)PPIX complexes were analyzed. From ***Table 4-6***, it was observed that there is a statistically significant separation in the cluster for the Fe(III)PPIX-test compound **1** complex versus all the other Fe(III)PPIX complexes, resulting in correlation coefficients above 0.6 (p = <0.0001). However, haemin was observed to result in the lowest correlation coefficient of R^2=0.6017 (p = <0.0001), but the difference was still highly significant and hence it was concluded to be significantly different from the Fe(III)PPIX-test compound **1** complex.

Table 4-7: Comparison of oxy-haemoglobin in treated iRBCs to all other Fe(III)PPIX complexes analyzed

Fe(III)PPIX complexes compared to oxy-haemoglobin in treated iRBCs	***p* value**	**R^2 value**
a. oxy-haemoglobin in RBCs	0.0026	0.03082
b. deoxy-haemoglobin in treated iRBCs	<0.0001	0.8771
c. haemozoin in treated iRBCs	<0.0001	0.6501
d. β-haematin	<0.0001	0.7411
e. haematin	<0.0001	0.3467
f. haemin	<0.0001	0.3933
g. haematin-test compound **1** mixture	<0.0001	0.8793

In order to further explore whether this method was reliable, oxy-haemoglobin in treated iRBCs was compared to all other Fe(III)PPIX complexes analyzed. In ***Table 4-7***, it was observed that there is a statistically significant separation between the cluster for oxy-haemoglobin in treated iRBCs and the clusters of the other Fe(III)PPIX complexes at the 99.99% confidence level (p = <0.0001), with the exception of oxy-haemoglobin in RBCs (p = 0.0026; R^2 = 0.03082). These were, however, still not significantly different at the 99.99% confidence level. Interestingly, haematin and haemin resulted in the lowest correlation coefficients of R^2 = 0.3467 and R^2 = 0.3933 respectively. This indicated that the separation between the clusters of oxy-haemoglobin in treated iRBCs and haematin or haemin was smaller compared to the other Fe(III)PPIX complexes. This could be as a result of overlapping peak positions for oxy-haemoglobin in treated iRBCs, haematin and haemin, which agrees with reports by Wood *et al* who showed that Fe(III)PPIX associated peaks are similar in the spectra for these Fe(III)PPIX complexes [416].

The same was investigated for haemozoin and the other Fe(III)PPIX complexes. From ***Table 4-8***, it was observed that there is a statistically significant separation between the cluster for haemozoin and the other Fe(III)PPIX complexes, except β-haematin. This further confirmed the observations discussed in ***Section 4.4.2.1*** where the spectra for haemozoin and β-haematin were observed to be very similar as expected (***Figure 4-10***).

Table 4-8: Comparison of haemozoin in treated iRBCs to all other Fe(III)PPIX complexes analyzed

Fe(III)PPIX complexes compared to haemozoin in treated iRBCs	***p* value**	**R^2 value**
a. oxy-haemoglobin in RBCs	<0.0001	0.8377
b. oxy-haemoglobin in treated iRBCs	<0.0001	0.8364
c. deoxy-haemoglobin in treated iRBCs	<0.0001	0.8887
d. β-haematin	0.8528	0.0001228
e. haematin	<0.0001	0.8104
f. haemin	<0.0001	0.8349
g. haematin-test compound **1** mixture	<0.0001	0.7530

4.5 Summary and Conclusions

In summary, evidence for the colocalization of Fe(III)PPIX and test compound **1** as a result of the formation of a Fe(III)PPIX complex in the DV of CQS NF54 iRBCs was successfully obtained in this chapter.

First, the colocalization of Fe(III)PPIX and test compound **1**, a benzimidazole haemozoin inhibitor containing a Br atom, was investigated with TEM and EELS. TEM images of untreated and treated iRBCs, prepared by cryofixation, illustrated intact parasites in RBCs with clear visualization of haemozoin crystals dispersed throughout the parasite DV. For treated iRBCs, less well-defined haemozoin crystals were observed indicating that the formation of haemozoin was inhibited in the presence of test compound **1**. Untreated iRBCs resulted in strong Fe signals attributed to haemozoin consistent with most of the Fe(III)PPIX being haemozoin. Compared to untreated iRBCs, treated iRBCs showed a strong Fe signal for the haemozoin crystals with an increased Fe signal in the RBC cytoplasm. The fact that a significant proportion of the parasite Fe(III)PPIX is in the form of exchangeable haem, this implies that it must be located around the haemozoin. In addition, a strong Br signal was observed in the parasite DV for treated iRBCs. From the overlaid image of the Fe and Br distribution maps, it was clear that co-localization of Fe(III)PPIX and test compound **1** occurs in CQS NF54 parasites, suggestive of complexation.

Second, confocal Raman microspectroscopy was used to investigate the vibrational modes of RBCs, parasite- and synthetic-Fe(III)PPIX complexes. This provided evidence of a putative Fe(III)PPIX-test compound **1** complex. High quality Raman spectra for the Fe(III)PPIX porphyrin dominated region of 1700-500 cm^{-1} at an excitation of 532 nm were obtained for all Fe(III)PPIX complexes including the putative Fe(III)PPIX-test compound **1** complex. From the recorded spectra, it was observed that the spectrum for the putative Fe(III)PPIX-test compound **1** complex was similar to that of the spectrum for the haematin-test compound **1** mixture that showed a unique peak at 1080 cm^{-1}. This was indicative of π- π interactions between the pyrrole-imidazole ring which was expected for a Fe(III)PPIX-test compound **1** complex. It was also observed that the putative Fe(III)PPIX-test compound **1** complex showed peaks that appeared shifted in comparison to the peaks for haemozoin. However, with the absence of the peak at 1160 cm^{-1} in the spectrum for the putative Fe(III)PPIX-test compound **1** complex it was apparent that there was no contribution from the haemozoin spectrum. Additionally, no strong peaks attributed to test compound **1** itself were observed probably as a result of much stronger haem peaks arising from resonance. Spectra for

synthetic Fe(III)PPIX complexes were also investigated for comparison with the spectrum for the putative Fe(III)PPIX-test compound **1** complex, including a haematin-test compound **1** mixture. From this, it was shown that the spectra for haematin (monomer), haemin, β-haematin and test compound **1** were visibly different from the putative Fe(III)PPIX-test compound **1** complex. With respect to β-haematin, the spectrum was observed to be very similar to the spectrum of haemozoin. On the other hand, the spectrum of the haematin-test compound **1** mixture had peak positions similar to the spectrum of the putative Fe(III)PPIX-test compound **1** complex, which was most evident when this spectrum was overlaid with the average spectra of the putative Fe(III)PPIX-test compound **1** complex and test compound **1**. It was similar even with noticeable reductions in the peaks pertaining to the pyrrole half-ring stretching and deformation region. This was concluded to be as a result of the drastic difference in the Fe(III)PPIX and test compound **1** ratio. Interestingly, the same peak at 1080 cm^{-1} was observed in the spectrum of the haematin-test compound **1** mixture and confirmed the possibility that this particular peak could be a marker band for the formation of this putative Fe(III)PPIX-test compound **1** complex.

Confocal Raman true mapping images were obtained to determine the signal distribution of selected Raman peaks in untreated and treated iRBCs. For untreated iRBCs, it was observed that the Raman peak at 754 cm^{-1} was useful for imaging the signal distribution of haemozoin localized in the parasite DV, whilst oxy- and deoxy-haemoglobin were localized to the RBC at the Raman peaks at 754 cm^{-1}, 1090 cm^{-1} and 1642 cm^{-1}. No signal distribution was observed for the images obtained at the Raman peak of 1080 cm^{-1} in untreated iRBCs. For treated iRBCs, similar observations were made, except that, the Fe(III)PPIX-test compound **1** complex was located in the parasite DV. In addition, overlaid true mapping images highlighted that the signal distribution for haemozoin and the Fe(III)PPIX-test compound **1** complex were located in the same region of the parasite DV. This further confirmed the findings obtained with TEM and EELS, and, the uniqueness of the Raman peak at 1080 cm^{-1} for observing the Fe(III)PPIX-test compound **1** complex.

The results obtained from PCA confirmed that there were differences in the peak positions of the spectra for all the Fe(III)PPIX complexes including the Fe(III)PPIX-test compound **1** complex. From the resulting PCA plots, it was observed that the Fe(III)PPIX-test compound **1** complex was different to the spectrum of test compound **1** itself with clusters separated along PC1 rather than PC2. It was also observed that there was no difference in the peak positions of the spectra for the Fe(III)PPIX-test compound **1** complex and the haematin-

test compound **1** mixture. This confirmed the existence of a Fe(III)PPIX-test compound **1** complex in CQS NF54 parasites.

Using a Welch's t-test analysis, the separations of clusters observed in the PCA plots were shown to be statistically significantly for all Fe(III)PPIX complexes being compared to the Fe(III)PPIX-test compound **1** complex with the exception of the haematin-test compound **1** mixture on the one hand and haemozoin versus β-haematin on the other. This method was applied to oxy-haemoglobin and haemozoin in treated iRBCs which showed that this method was very reliable and could be used for future investigations.

In conclusion, this chapter has provided definitive evidence that test compound **1** co-localizes with Fe(III)PPIX, forming a complex in the DV. Most importantly, it was clear from the observations in this chapter that the hypothesis that haemozoin inhibitors, like test compound **1**, act by forming a Fe(III)PPIX-inhibitor complex is true at least in the case of this compound. Presumably, this explains the accumulation of the compound with Fe(III)PPIX which then goes on to cause parasite death.

5

Haemoglobin digestion by aspartic and cysteine proteases

5.1 Introduction

A complete understanding of haemozoin inhibition would require a model of the haem pathway from haemoglobin digestion to haemozoin formation. The formation of haemozoin has been the focal point for understanding the mechanism of action of various antimalarials for many years. This has not only provided a better understanding into the behavior of antimalarials like CQ but also the discovery of new antimalarially active compounds. The first key step in the formation of haemozoin is the degradation of haemoglobin. Haemoglobin degradation occurs in the DV of *P. falciparum* parasites and is vital for its growth, and, is known to be a complex process [79,441-444]. As mentioned in Chapter 1, the RBC content consists of 95% haemoglobin and this is ingested during the blood stage of the parasite via the parasite cytostome and transported into the DV by double-membrane bound transport vesicles [73,123]. Once inside the DV, haemoglobin is digested by a series of known proteases (aspartic and cysteine) which account for 60-80% and 20-40% of haemoglobin digestion respectively [76-78,84,445-449]. In a partly ordered manner, aspartic proteases (Plm I and Plm II, including HAP) have been reported to initially cleave haemoglobin at selected sites which causes the unfolding of native haemoglobin [76,80,445-446]. Plm II is most active thereafter in digesting large globin fragments with the resulting smaller fragments subject to falcipains which result in smaller peptides and amino acids [444,450]. This results in a very large number of amino acids that are to an extent utilized for self-generation of new proteins, but primarily to maintain osmotic stability within the DV by most of the amino acids being exported from the parasite [74,451].

Kinetics have been previously reported by Luker *et al* for aspartic proteases which included the Michealis-Menten (K_m) and turnover constants (k_{cat}). They were able to show that HAP resulted in a much lower K_m (0.29 μM) with a much slower k_{cat} (0.05 s^{-1}) compared to PLM I (0.49 μM; 2.3 s^{-1}) and PLM II (2.6 μM; 11 s^{-1}). With this they inferred that HAP would be 20 times less efficient at digesting haemoglobin than Plm I and II [85]. It has also been previously determined that haemoglobin is digested at a rate of 0.06 fmol/hr per DV in the trophozoite stage [84]. Studies with SDS-PAGE have previously shown that upon addition of inhibitors like pepstatins and E-64, haemoglobin degradation is inhibited in an ordered manner. The reason for this is that pepstatins are specific inhibitors of aspartic proteases where E-64 is specific to cysteine proteases [452-454]. Banjeree *et al* has used indirect immunofluorescence microscopy to analyse which aspartic proteases are present in the blood stage of the parasite and their location within the DV. From this, they were able to show the presence of these

aspartic proteases at different parasite stages, where specifically Plm II and HAP localize with haemozoin. This was similar to the reports by Francis *et al* [80-81].

Estimation of concentrations of these proteases require knowledge of the amount of protein and organelle volume. Various protein quantification assays such as Bradford, bicinchoninic acid (BCA) and Nanodrop, have also been used to quantify the unfolding of falcipain-2, recombinant ookinete micronemal protein chitinase (*Pg*CHT1) and purified mitochondrial dihydroorotate dehydrogenase [455-457]. In 2012, Hanssen *et al* used previously published methods by Rabiner *et al* and Snell *et al* to determine the cell volume and concentration of haemoglobin in iRBCs. They showed that for iRBCs, the volume remained relatively constant from the ring (84 ± 16 fL) to late schizonts stage (68 ± 9 fL) [458-460], while, the haemoglobin concentration decreased slowly during the ring stage and sharply from the trophozoite stage. Additionally, Gligorijevic *et al* was the first to quantitatively determine the rate of haemozoin formation using spinning disk confocal microscopy. They showed that haemozoin first appears at the early trophozoite stage which coincided with the point at which haemoglobin was digested. Also, the rate of haemozoin formation was observed to reach a maximum at the point when haemoglobin digestion stopped which coincided with the late trophozoite stage [205].

In this chapter the prerequisites required for a haem pathway model include the concentrations of aspartic proteases, rate constants for each step and a description of the rate of haemoglobin uptake. In addition, to validate the model, the amount of haemoglobin, exchangeable haem and haemozoin throughout the blood stage of the CQS NF54 parasite is required. To this end, the concentration of proteases was estimated by compiling bioinformatics data for both CQS (NF54) and CQR (Dd2) strain parasites using the protein abundance database, PAXdb. This included collecting the relative abundances for all proteins, and determining their individual molecular weights with the SIB bioinformatics resource portal, ExPASY. From this, the averaged abundance-weighted molecular weight for the entire proteome of Dd2 parasites could be calculated. Next, the mass of the proteins in RBCs, CQS and CQR parasites were analysed using three independent protein quantification methods namely, the Bradford, BCA and NanoDrop spectrophotometric assays With the protein masses and the average abundance-weighted molecular weight for Dd2 parasite proteins, the total number of protein molecules per cell in Dd2 parasites was estimated. Estimates were also made for RBCs and NF54 parasites. Dd2 parasites were found to have a higher number of protein molecules per cell than NF54 parasites. Using the total protein count and PAXdb data, together with estimated volumes of the DV, the concentrations of Plm I, II, HAP and falcipain-2 were

calculated based on their relative abundances. The highest average protease concentration in the Dd2 strain was that of HAP (0.12 μM).

As a basis for future validation, a time point quantification experiment of the haemoglobin amounts present in CQS NF54 parasites throughout the blood stage was performed. This was carried out by first performing an observation experiment to determine the time point 0 in which merozoites invade RBCs so as to accurately determine the time points for the specific parasite stages for the quantification of haemoglobin, exchangeable haem and haemozoin (mass of haem Fe in fg per cell) using a modified pyridine-based parasite haem fractionation plate method. The amount of haemoglobin, exchangeable haem and haemozoin were successfully determined. The results showed a rapid sigmoidal decrease in haemoglobin, while exchangeable haem remained relatively constant and haemozoin increased linearly. Specifically, haemoglobin was observed to decrease in a sigmoidal manner, where, large amounts were observed for early time points than the later stages where it reached a steady state. This sigmoidal decrease suggested that the initial uptake of haemoglobin was larger and could be as a result of an observed increasing concentration of aspartic proteases. This large initial uptake of haemoglobin was further investigated by performing haemoglobin contamination experiments which proved that the method that was used was reliable and efficient for quantifying the amount of haemoglobin, exchangeable haem and haemozoin throughout the blood stage of CQS *P. falciparum* parasites.

5.2 Materials, instrumentation and methods

5.2.1 Materials

General materials, used throughout this study, are detailed in Chapter 2 (see ***Section 2.1***). The commercially purchased materials, used only in this chapter, were all of AR grade or higher and used without further purification unless specified below. Protein quantification kits for Bradford and BCA assays were purchased from Bio-Rad Laboratories and Sigma-Aldrich/Merck respectively. The materials that were specific to this chapter are listed below in ***Table 5-1*** to ***Table 5-2***.

Table 5-1**:** Materials used for Bradford protein quantification kit

Bradford protein quantification kit	
Material	**Supplier**
Bovine serum albumin	Bio-Rad Laboratories
Coomassie® Brilliant Blue G-250 dye (Coomassie dye, phosphoric acid and methanol)	Bio-Rad Laboratories

Table 5-2**:** Materials used for BCA protein quantification kit

BCA protein quantification kit	
Material	**Supplier**
Bovine serum albumin	Sigma Life Science
Reagent A (sodium bicinchoninate, sodium carbonate, sodium tartrate, sodium hydroxide and sodium bicarbonate)	Sigma Life Science
Reagent B (copper(II)sulphate and d.H_2O)	Sigma Life Science

5.2.2 Instrumentation

General instrumentation used throughout this study is discussed in detail in Chapter 2 (see ***Section 2.2***), with the inclusion of one instrument pertaining to this chapter;

NanoDrop Spectrophotometer

Microliter protein samples were measured using a Thermo Scientific NanoDrop™ ND-1000 spectrophotometer, in the Microbiology department at the UCT. It has a Xenon flash lamp excitation source, 0.002 precision and ± 2% accuracy.

5.2.3 Software

The general software used to analyse data and construct graphs is described in detail in Chapter 2 (see ***Section 2.3***). Software pertaining to this chapter included the protein abundance database, PAXdb[4.1], and, the SIB bioinformatics resource portal, ExPASy, were used to obtain *P. falciparum* protein abundances and molecular weights [461-462]. The Nanodrop Protein A280 v3.5.1 was used to quantify protein samples of micro-litre volumes [463].

5.2.4 Preparation of samples and solutions

The preparation of samples and solutions for RBCs, cell culturing of *P. falciparum* cultures, isolation, fixation, counting and the pyridine-based parasite haem fractionation plate method have been previously described in Chapter 2 (see ***Section 2.4.2*** and ***2.4.4.1***). Sample and solution preparation that were specific to this study are described below;

Coomassie® Brilliant Blue dye (Bradford reagent)

The Coomassie® Brilliant Blue dye was diluted 1:4 (v/v) by adding 10 ml of Coomassie® Brilliant Blue dye concentrate to 40 ml of d.H_2O. The diluted solution was stored at 4 ºC until further use with a storage life of a maximum of 2 weeks.

BCA working reagent

The working reagent was prepared by adding 1 ml of reagent B (Copper (KK) sulfate pentahydrate 4 %) to 49 ml of reagent B (BCA solution). The solution was stored at rt. until further use.

5.2.5 Methods

The general experimental method for cell culturing of *P. falciparum* parasites, isolation, fixation and counting used in this chapter are discussed in detail in Chapter 2 (see ***Section 2.5.1***

and ***Section 2.5.3.2***). Throughout this study RBCs, CQS (NF54) and CQR (Dd2) parasite strains were used. The experimental methods used in this chapter are described below.

5.2.5.1 Lysis of RBCs

RBCs were lysed using a modified method previously described by Reed *et al* [464]. Packed RBCs were washed in complete medium and aspirated as described in Chapter 2 (see ***Section 2.4.2***). RBCs were lysed by adding 250 µl of 1% saponin to 1 ml of packed RBCs in 30 ml of filtered PBS. The solution was centrifuged at 750 rpm for 5 min before aspirating the supernatant. The remaining lysed RBCs were divided into Eppendorf tubes of 300 µl in 100 µl of filtered PBS and frozen at -80 °C until further use.

5.2.5.2 *P. falciparum* parasite lysis

CQS and CQR cultures were lysed using methods previously described by Ambele *et al* [372]. Before lysis, the trophozoite pellet was checked by Giemsa smears using a light microscope. From here, the trophozoites were harvested by lysing the iRBCs using 1% saponin (250 µl) in filtered PBS (30 ml) and incubated for 2 min in a water bath. The lysed iRBCs were then centrifuged at 750 rpm for 10 min. The supernatant was aspirated, leaving behind the isolated trophozoite pellet. This pellet was then washed 3 times with filtered PBS (10 ml) by centrifuging at 750 rpm for 10 min. A final volume of 100 µl of filtered PBS was added to the isolated pellet in a 1.5 ml Eppendorf tube. The suspended pellet was counted using a haemocytometer before freezing at -80 °C. After 1 hr, the isolates were thawed at rt. before the isolated DVs were viewed by Giemsa smears. This freeze-thaw process facilitates the rupturing process of the membranes of the isolated trophozoites and was repeated until all trophozoite membranes were lysed. After this, pooled trophozoite lysate and DVs were triturated multiple times using a 26.5 Gauge needle to break open the DVs releasing the proteins and other membrane materials into solution. This process was repeated 4 times to ensure all DVs were completely ruptured, after which, the samples were frozen at -80 °C until further analysis.

5.2.5.3 Protein Quantification methods

The protein quantification for RBCs, CQS and CQR parasites was performed using three well established methods namely, the Bradford, BCA and NanoDrop assay. The Bradford method,

originally determined by Bradford *et al*, is a well-known, time efficient and accurate spectroscopic method for quantitatively determining the concentration of proteins in a sample [465-472]. This method uses a Coomassie® Brilliant Blue G-250 dye that binds to proteins and forms a complex. Upon the formation of a dye-protein complex, the dye shows a red shift in its absorbance from 465 nm to 595 nm which produces a noticeable colour change from reddish brown to blue [466].

Similar to the Bradford method, Smith *et al* developed another spectroscopic assay for quantifying the concentration of proteins in a sample, namely the BCA method [473]. This method utilizes a copper(II) sulphate solution which is reduced to copper (I) in the presence of proteins, however, it is temperature dependent. With this, an observed colour change from blue to purple is observed when two BCA molecules bind to one Cu^{+} cation in the presence of proteins. The amount of complex that is formed is proportional to the concentration of protein which can be spectroscopically assayed at 562 nm [473].

The NanoDrop microvolume spectrophotometer records the absorbance of protein containing samples as small as 0.5 µl. This fast and efficient technique makes use of the principle of surface tension where the sample is analysed between two optical fibres. Light is then passed through the sample from which absorbances at 280 nm are recorded. The spectrophotometer converts the absorbance into a concentration of total protein in a sample based on an average extinction coefficient [474-475]. The methods are described in detail below.

Bradford protein quantification method

The microplate method, described in the Bio-Rad protein quantification kit, was modified for this experiment (***Table 5-1***) [476]. First a bovine serum albumin (BSA) standard curve was established. Briefly, the 30 µM stock solutions (1 ml), provided in the kit, of BSA was used as the control which was diluted to known concentrations in Eppendorf tubes in the ratio of 1:1 (v/v) in filtered PBS by adding 500 µl of the control to 500 µl of filtered PBS. The resulting concentrations for the control stock solutions ranged from 30-0.4 µM. In column 1 of the 96-well plate, 5 µl of filtered PBS was added as a blank. To columns 2-7, 5 µl of the serial diluted control stock solutions were added. All control stock solutions were measured in triplicate. To the plate, 250 µl of Bradford reagent was titrated into all the BSA-containing wells using a micro-multichannel pipette before adding to the blank well (1:20 dilution). This was to ensure that the absorbance of the blank was lower than the control-containing wells. Each well was then gently resuspended using a micro-multichannel pipette and the bubbles were removed

with a 26.5 Gauge needle before leaving the plate to incubate at rt. for 30 min. After the incubation period the plate was spectroscopically assayed at 595 nm using a SpectraMax 340PC plate reader (***Figure 5-1***).

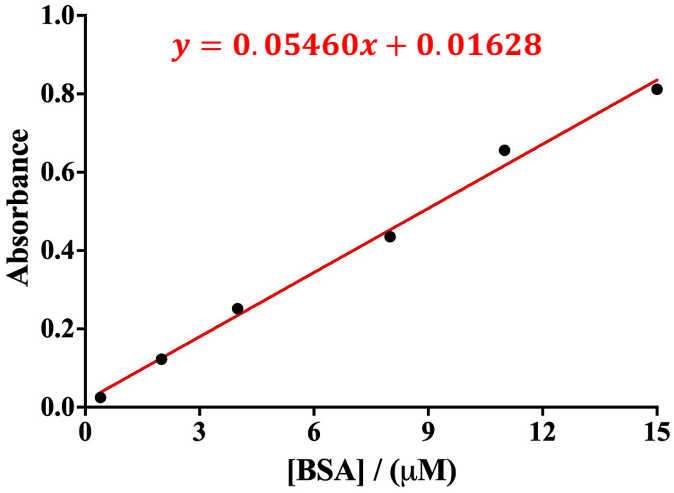

Figure 5-1**:** A standard curve based on the absorbance of BSA determined using the Bradford method at 595 nm for increasing concentrations of BSA, analysed as a protein-dye complex. The standard curve represents a fit to the mean ± SD for data points obtained from four different experiments. A linear regression analysis was performed using GraphPad Prism v8.2.1 to yield a correlation coefficient, $R^2 = 0.9940$ with an average molar adsorption coefficient (ε) of 57,696 ± 3,604 M^{-1} cm^{-1} (ε was calculated for three separate BSA standard curves and averaged).

Next, to quantify the protein concentration for CQS and CQR parasites and RBCs, the same modified microplate method was used. The samples obtained from the lysed cells (see ***Section 5.2.5.1***), were thawed at 37 °C in an incubator before further use. In the same 96-well plate as the BSA standard in column 1, 5 µl of filtered PBS was added as a blank and column 2-6 contained 5 µl of the samples (***Figure 5-2***). All samples were measured in quadruplet for each experiment to ensure reproducibility of results (biological repeats = 3). To the plate, 250 µl of Bradford reagent was titrated into all the sample-containing wells using a micro-multichannel pipette before adding to the blank (1:20 dilution). Each well was gently resuspended with a micro-multichannel pipette, bubbles were removed with a 26.5 Gauge needle before the plate was left to incubate at rt. for 30 min. After 30 minutes, the absorbance was recorded at 595 nm using a SpectraMax 340PC plate reader.

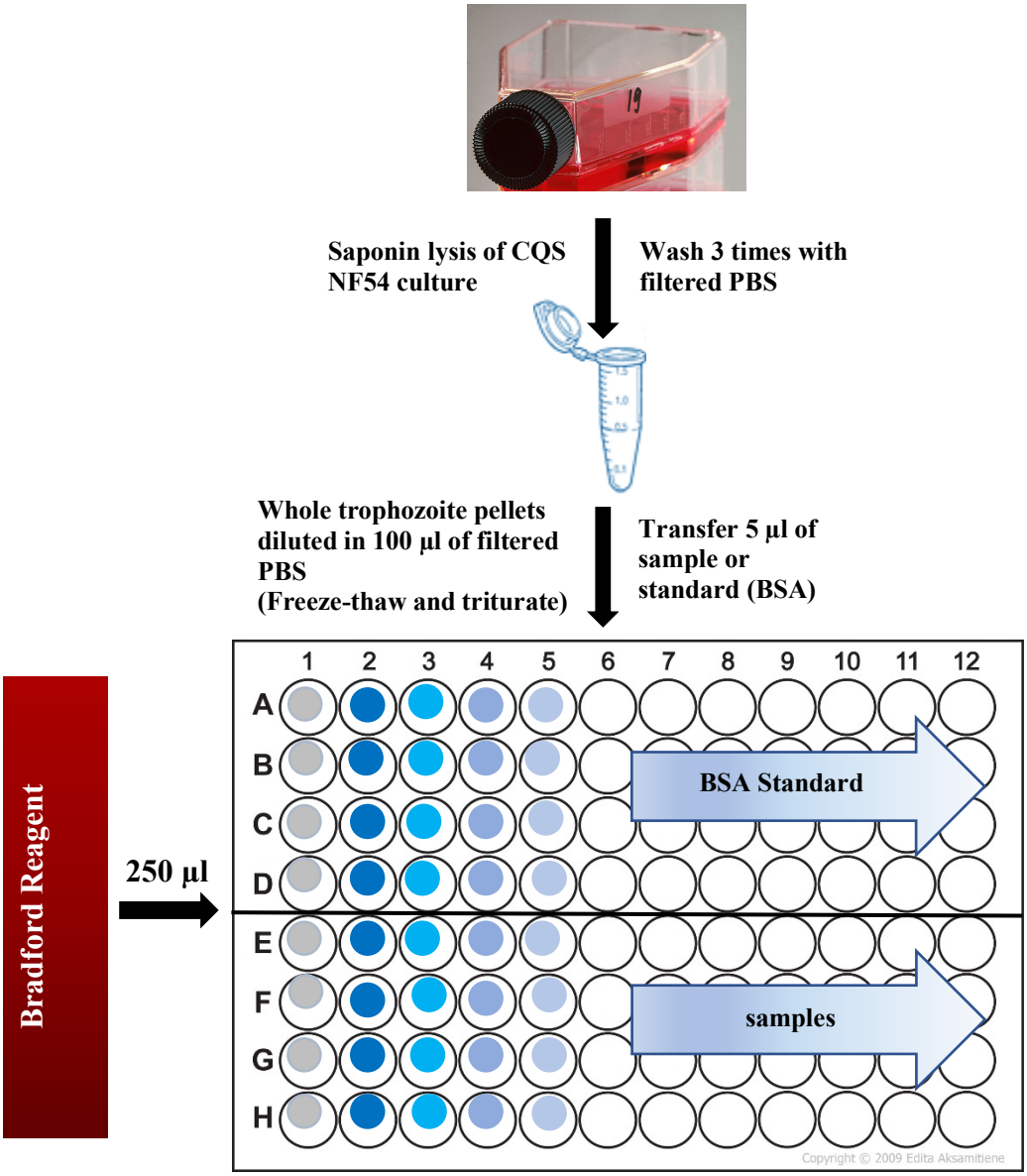

Figure 5-2: Microplate method used for the Bradford protein quantification.

BCA Protein Quantification method

As described in the Sigma-Aldrich protein assay kit, the microplate method was used to determine a BSA standard curve and the protein concentrations for RBCs, CQS and CQR parasites (***Table 5-2***) [477]. Similar to the Bradford protein quantification kit, 30 µM solutions (1 ml) of BSA were provided and used as a control of which further dilutions in Eppendorf tubes were prepared, 15-0.4 µM. Using a 96-well plate, 25 µl of filtered PBS was added to column 1 which was used as a blank. To column 2-7, 25 µl of each diluted control sample was added. All BSA-diluted samples were carried out in triplicate. The BCA working reagent (200 µl) was

titrated into the wells containing the diluted control samples using a micro-multichannel pipette before adding to the blank (1:8 dilution). Each well was gently resuspended with a micro-multichannel pipetted. Before incubating the plates at 37 °C for 15 min, the bubbles were removed using a 26.5 Gauge needle. The absorbance (562 nm) was recorded on a SpectraMax 340PC plate reader (***Figure 5-3***).

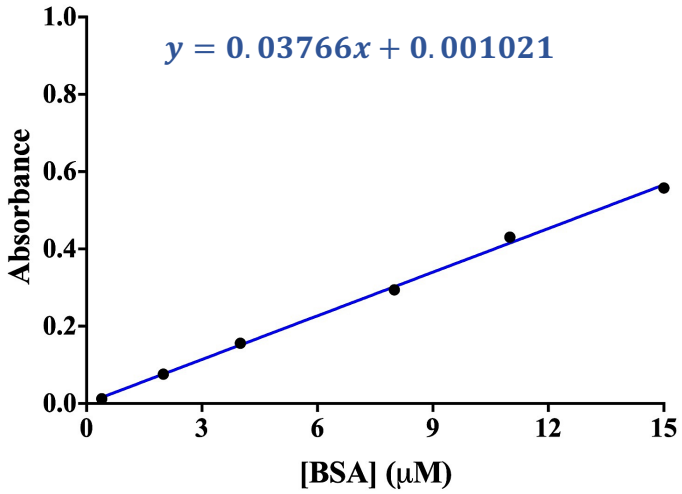

Figure 5-3**:** A standard curve for the absorbance of BSA at 562 nm at increasing concentrations of BSA, analysed as a protein-dye complex. The standard curve represents a fit to the mean ± SD for data points obtained from four different experiments. A linear regression analysis was performed using GraphPad Prism v8.2.1 to yield a correlation coefficient, $R^2 = 0.9982$ with an average molar adsorption coefficient (ε) of 36,901 ± 2,965 M^{-1} cm^{-1} (ε was calculated for three separate BSA standard curves and averaged).

This microplate method was also used to quantify the protein concentration for CQS and CQR iRBCs, including RBCs. Briefly, the samples obtained from the cell lysis method (see ***Section 5.2.5.1***), were thawed at 37 °C in an incubator before further analysis. In the same 96-well plate, 25 µl of filtered PBS (blank) and 25 µl of the samples were added to column 1 and column 2-6 respectively (***Figure 5-4***). All samples were conducted in triplicate (biological repeats = 3). In the plate, 200 µl of working reagent was titrated into all the sample-containing wells using a micro-multichannel pipette before adding to the blank. Each well was gently resuspended using a micro-multichannel pipette, bubbles were removed using a 26.5 Gauge needle and placed in an incubator to incubate at 37 °C for 15 min. After the incubation period, the plate was spectroscopically assayed at 562 nm using a SpectraMax 340PC plate reader.

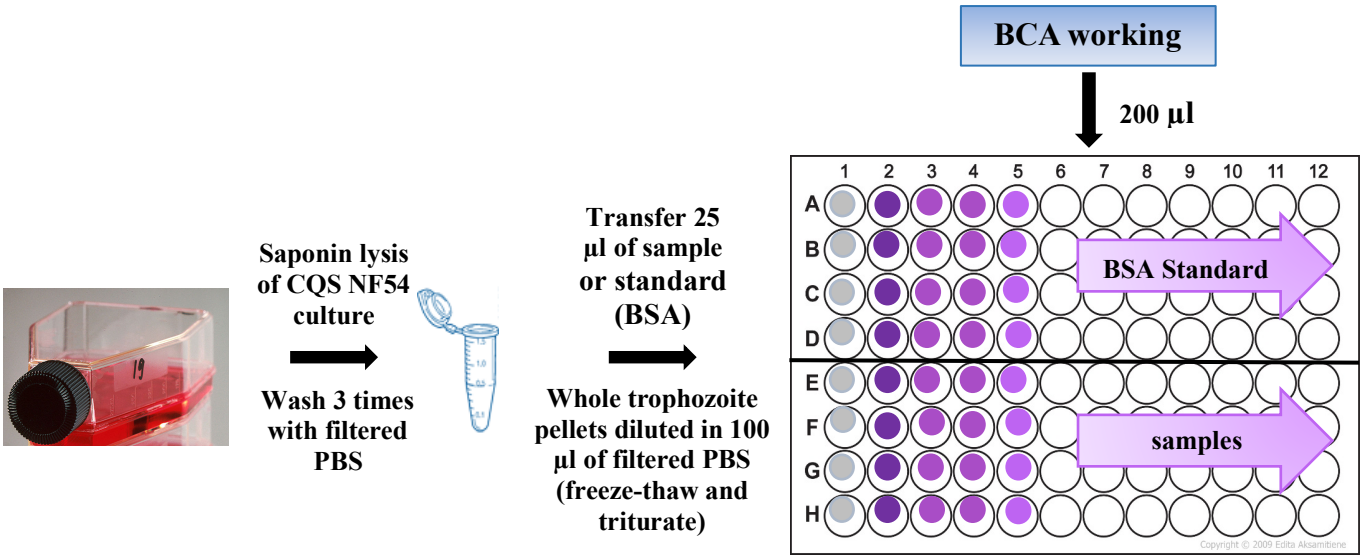

***Figure 5-4*:** Microplate method used for the BCA protein quantification.

Nanodrop analysis

The samples (CQS and CQR iRBCs, including RBCs) obtained after cell lysis (***see Section 5.2.5.1***) were thawed at 37 °C in an incubator. All samples were analysed (2 µl of each sample) using a NanoDrop™ ND-1000 spectrophotometer. The samples were run using the protein A280 module that measures an ultraviolet spectrum, determines the protein absorbance at 280 nm and automatically calculates the protein concentration [474-475]. Samples were tested in triplicate for each experiment (biological repeats = 3).

5.2.5.4 Time point quantification in CQS NF54 cultures

A time point quantification plate method was carried out using a modified method previously described by Combrinck *et al* [263]. In more detail, CQS NF54 strain parasites were cultured according to methods described previously in Chapter 2 (***see Section 2.5.1***). At the start, highly synchronous ring stage cultures (CQS NF54) were confirmed by Giemsa stained smears in order to determine the parasitaemia. From there, the calculated parasitaemia (average of 1000 cells counted) was used to dilute the ring cultures (5% parasitaemia; 2% haematocrit) in 49 ml of complete medium and washed O^+ RBCs. In a 6-well plate (Greiner Bio-One), 5 ml of the diluted ring culture was pipetted into each well where each time point (20-50 hrs) was tested in triplicate. All plates were gassed with 3% O_2, 4% CO_2 and N_2 for 1 min in a sterile gassing

chamber and incubated at 37 °C for the relevant time points. Before removing the plates from the incubator at their respective time points, Giemsa smears were made to confirm the stage of the trophozoite culture. After the confirmation of the different stages, supernatants were aspirated and parasites isolated by saponin lysis of RBCs by adding 250 µl of 1% saponin in 2 ml of filtered PBS (pH 7.5). The iRBC pellets were resuspended to promote lysis and centrifuged at 750 rpm for 10 min. After centrifugation, supernatants were aspirated before washing the isolated pellets with 2 ml of PBS. This process was repeated until a clear supernatant was observed in order to remove excess traces of haemoglobin from RBCs, cell debris and haemozoin from previous cycles [263]. The washed pellets were transferred to a 96-well plate in a 100 µl of filtered PBS. For cell counting, 10 µl of the resuspended mixture was aliquoted into a separate 96-well plate prior to freezing the remaining pellets at -80 °C (stock plate). Isolated trophozoites were glutaraldehyde-fixed, prepared for cell counting and taken through a solvent-mediated plate method for the fractionation of haem species as previously described in Chapter 2 (see ***Section 2.5.5.3*** to ***Section 2.5.5.4***).

5.2.5.5 Haemoglobin contamination experiment

The haemoglobin contamination experiment for the early time points was carried out in 6-well plates (Greiner Bio-One). Briefly, synchronous CQS NF54 cultures (ring stage) were viewed by Giemsa smears to confirm the parasitaemia of the culture. From here, the percentage parasitaemia was used to dilute the culture to 5% parasitaemia and 2% haematocrit in 49 ml of complete medium and packed RBCs. Cultures were incubated at 37 °C for 24 hrs and 27 hrs in a sterile gas chamber (3% O_2, 4% CO_2 and N_2), before, the plates were removed. The plates were removed at their respective time point and Giemsa smears were made in order to confirm the stage of the parasite. After confirmation from the Giemsa smears, the supernatant was removed via aspiration. The remaining pellet was then spiked with 250 µl of packed RBCs and left to stand for 5 min. After 5 min, 250 µl of saponin (1%) was added to the pellet with 2 ml of filtered PBS and left to incubate at rt. for 15 min. Using a pipette, the lysed pellet was transferred to a 2.5 ml deep well plate and centrifuged at 750 rpm for 10 min. The remaining isolated trophozoite pellet was then continuously washed (3 times) until a clear supernatant was observed to remove excess undigested haemoglobin [263]. A 100 µl aliquot of filtered PBS was added to the washed pellet, mixed to ensure a homogenous mixture and transferred to a 96-well plate. For cell counting, 10 µl of the resuspended mixture was aliquoted into a separate 96-well plate prior to freezing the remaining pellet at -80 °C (stock plate). Isolated trophozoites

were glutaraldehyde-fixed, prepared for cell counting and taken through a solvent-mediated plate method for the fractionation of haem species as previously described in Chapter 2 (see ***Section 2.5.5.3*** to ***Section 2.5.5.4***).

5.3 Data analysis

5.3.1 Average abundance-weighted molecular weight of all proteins in the *P. falciparum* proteome

The average abundance-weighted molecular weight (Ab_{MW_t}) for Dd2 parasites was calculated from the sum of the product of the protein abundance (P_{Ab}) and protein molecular weight (P_{MW}) of each protein. The following equation was used (***Eq. 1***);

$$Ab_{MW_t} = \left(\sum_{i=1}^{n} \frac{P_{Ab,i} \times P_{MW,i}}{10^6}\right)_n \qquad \textbf{\textit{Eq. 1}}$$

where n is the total number of proteins in the proteome

5.3.2 Protein concentration

BSA standard curves were constructed for the concentration range of 15-0.4 µM as described in ***Section 5.2.5.3*** using both the Bradford and BCA methods. Considering that the standard curve for BSA is linear for this concentration range, the Beer-Lambert law was applied. This states that the absorbance (A) at any wavelength is equal to the product of the absorptivity in $g^{-1}cm^{-1}$ (ε), mass concentration (c) of the sample and path length (l) equation (***Eq. 2***) [478-479]:

$$A = \varepsilon c l \qquad \textbf{\textit{Eq. 2}}$$

Therefore, the protein concentration could be calculated from the respective linear equations of the BSA standard curves where the concentration of protein (c) is equal to the absorbance(A) minus the y-intercept (A_0) and divided by the slope of the standard curve (ε) (***Eq. 3***):

$$A = \varepsilon c + A_0$$

Which was rearranged to;

$$c = \left(\frac{A-A_0}{\varepsilon}\right) \qquad \textbf{\textit{Eq. 3}}$$

The protein mass per cell (m') was calculated by dividing the mass concentration (c) by the total number of trophozoites (T_t) counted using the haemocytometer, and multiplying by the volume of analyte, V (***Eq. 4***):

$$m' = \frac{c \times V}{T_t} \qquad \textbf{\textit{Eq. 4}}$$

5.3.3 Total number of proteins

Based on the average abundance-weighted molecular weight (Ab_{MW_t}) obtained for the proteins in Dd2 parasites, the protein mass per cell (m') and Avogadro's' constant ($N_a = 6.022 \times 10^{23}$), the total number of proteins per cell ($P_{t/cell}$) for RBCs, CQS (NF54) and CQR (Dd2) strains were calculated using ***Eq. 5***:

$$P_{t/cell} = \left(\frac{m'}{Ab_{MW_t}} \times N_a\right) \qquad \textbf{\textit{Eq. 5}}$$

5.3.4 Aspartic and cysteine protease concentrations

The concentrations for both aspartic and cysteine proteases (Pt_x) were calculated based on their individual relative abundances (Ab_{ppm}), the volume of the DV ($Dv_v = 3.5 \times 10^{-15}\ L$) [205], the total number of proteins per trophozoite ($P_{t/cell}$) for Dd2 parasites and Avogadro's constant (N_a) using ***Eq. 6***:

$$[Pt_x] = \left(\frac{Ab_{ppm} \times P_{t/cell}}{N_a \times 10^6}\right) \times Dv_v \qquad \textbf{\textit{Eq. 6}}$$

5.4 Results and Discussion

To determine the concentration of the four major aspartic (Plm I, II and HAP) and cysteine (falcipain-2) proteases involved in haemoglobin digestion in the DV of *P. falciparum* parasites, the variables discussed below were determined [76,81,444,450,480].

5.4.1 Average abundance-weighted molecular weight of Dd2 parasites

The average abundance-weighted molecular weight of the proteins that are present in NF54 and Dd2 strain parasites was determined by compiling a list of the known relative abundances and molecular weights for the individual proteins. The relative protein abundance and their individual molecular weights are available in the protein abundance database (PAXdb) and SIB bioinformatics resource portal (ExPASy) respectively. However, with the limited bioinformatics data available for NF54 proteins, the average abundance-weighted molecular weight could not be determined. On the other hand, 1337 proteins obtained from the list of Dd2 proteins expressed in the trophozoite stage and previously reported by Tao *et al* consisted of 226 proteins (17%) which were attributed to conserved *Plasmodium* proteins of unknown function and 1111 (83%) of known proteins [481]. From this, the relative abundances and their individually determined molecular weights were used to calculate the average abundance-weighted molecular weight for Dd2 proteins (see ***Section 5.3.1***, ***Eq. 1***) which was calculated to be 40,483 ± 77 g/mol.

5.4.2 Protein concentration and total number of proteins

The protein concentration for NF54 and Dd2 parasites, including RBCs as a control, was determined using the Bradford microplate method that has been previously described in ***Section 5.2.5.3***. In brief, NF54 and Dd2 trophozoites were isolated by saponin lysis and centrifugation before the isolated trophozoites were freeze-thawed. From this, pooled trophozoite lysate and DVs were triturated with a 2.6 Gauge needled multiple times, diluted in 1 ml of filtered PBS and frozen at -80 °C. In a 96-well plate; 5 µl of filtered PBS was added as a blank and 5 µl of the thawed samples were added to the respective columns. A 1:20 dilution was done by titrating 250 µl of Bradford reagent into all the sample-containing wells before adding to the blank. Before recording the absorbance at 595 nm, using a SpectraMax 340PC plate reader, each well resuspended, the bubbles were removed and the plate was left to

incubate at rt. for 30 min. Similar protein quantification methods which included the BCA assay and NanoDrop, previously discussed in ***Section 5.2.5.3***, were included in this study for comparison.

Table 5-3**:** Total protein mass (pg/cell) determined for RBCs, NF54 and Dd2 parasites determined by; (a) Bradford, (b) BCA, and, (c) NanoDrop.

	a	**b**	**c**	**Mean ± SD**
RBC	30.92	32.48	30.65	31.35 ± 0.99
NF54	8.02	8.46	8.01	8.16 ± 0.26
Dd2	12.50	12.72	13.18	12.80 ± 0.35

The protein mass per cell, listed in ***Table 5-3***, were calculated from the BSA standard curves using ***Eq. 3*** and ***Eq. 4*** that have been previously described in ***Section 5.3.2***. From these results, it was observed that the protein masses were relatively constant across all protein quantification methods for RBCs, NF54 and Dd2 parasites. It was, however, observed that that BCA method resulted in slightly higher protein masses compared to the other methods. This could be due to the sensitivity difference between methods, where, the BCA method is known to have much improved sensitivity relative to the Bradford method [482-483]. Looking at the mean protein masses, the protein mass for RBCs was 31 ± 1 pg per cell which was in the accepted range previously reported in the literature [484-485]. For NF54 and Dd2 parasites, the protein mass for Dd2 was observed to be considerably higher than that for NF54 parasites. These data were similar to those previously reported by Wang *et al*, where HB3 strain parasites had a total protein content similar to that of Dd2 strain parasites [486].

Next, the total number of protein molecules per cell was calculated using ***Eq. 5*** (see ***Section 5.3.3***). From these data, listed in ***Table 5-4***, it was observed that the total number of protein molecules per cell was higher for RBCs than NF54 and Dd2 parasites which was expected. On the other hand, the total number of protein molecules per cell for Dd2 parasites resulted in a larger number of protein molecules per cell than for NF54. This was as expected given the observations in ***Table 5-3***. Specifically, Dd2 parasites had 70 million more protein molecules than NF54 parasites which had 121 million per cell.

***Table 5-4*:** Total number of protein molecules per cell for RBCs, NF54 and Dd2 based on (a) the Bradford, (b) BCA, and (c) NanoDrop assays.

	Bradford	**BCA**	**NanoDrop**	**Mean (SD)**
RBC	4.60×10^8	4.83×10^8	4.56×10^8	$4.66\ (15) \times 10^8$
NF54	1.19×10^8	1.26×10^8	1.19×10^8	$1.21\ (4) \times 10^8$
Dd2	1.86×10^8	1.89×10^8	1.96×10^8	$1.90\ (5) \times 10^8$

Based on the average abundance-weighted molecular weight of Dd2 proteins (40,483 ± 77 g/mol) and the relative abundances of Plm I, II, HAP and falcipain-2, the concentration of these proteases was determined using ***Eq. 6*** (see ***Section 5.3.4***). ***Figure 5-5*** illustrates the concentrations of Plm I, II, HAP and falcipain-2 in Dd2 parasites. It can be seen that HAP had the highest concentration at 0.12 µM, Plm I at 0.061 µM, Plm II at 0.051 µM and falcipain-2 at 0.0018 µM. HAP is known to be 60% similar to, but less efficient than Plm I and II, but, its abundance is 2-fold higher than Plm I and II, and 7-fold higher than falcipain-2. This could explain why HAP has a higher concentration than Plm I, II and falcipain-2.

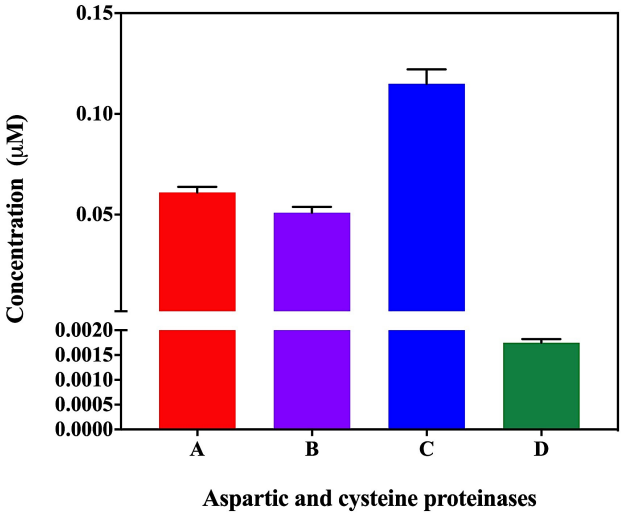

***Figure 5-5*:** Bar graph of the four main protease concentrations in Dd2 parasites which is represented by; (a) Plm I (red), (b) Plm II (purple), (c) HAP (blue), and, (d) falcipain-2 (green).

5.4.3 Time point quantification in CQS NF54 parasites

For future validation of models of the whole haemozoin pathway, the amount of haemoglobin, exchangeable haem and haemozoin was determined throughout the life cycle of CQS *P. falciparum* parasites in the blood stage.

First, a microscopic observation experiment was conducted. This was carried out to determine the relevant time points of the different stages of the parasites and thus the time point at which merozoites invade RBCs, corresponding to time point 0 hrs. Briefly, CQS NF54 cultures were kept in continuous culture and synchronized to the early ring stage as previously described in Chapter 2 (see ***Section 2.5.1***). Cultures were then observed for 48 hrs, where, at 3 hr intervals Giemsa smears were made in order to confirm the stage of the parasites. Throughout the experiment cultures were gassed under sterile conditions (3% O_2, 4% CO_2 and N_2) and incubated at 37 °C in a CO_2 incubator.

Next, using a modified method previously described by Combrinck *et al*, a time point quantification assay was carried out. This was to quantify the haem species (haemoglobin, exchangeable haem and haemozoin) present in CQS NF54 parasites at different time points which can be spectroscopically assayed as low-spin Fe(III)PPIX-pyridine complexes (see ***Section 5.2.5.4***) [263]. Highly synchronous CQS NF54 ring stage cultures were confirmed by viewing Giemsa stained smears. From here, the calculated parasitaemia was used to dilute the ring cultures (5% parasitaemia; 2% haematocrit) in 49 ml of complete medium and washed O^+ RBCs. Diluted Cultures (5 ml) were then transferred to a 6-well plate (Greiner Bio-One), with each time point (20-50 hrs) tested in triplicate. Before incubation at 37 °C for the relevant times, all plates were gassed with 3% O_2, 4% CO_2 and N_2 for a minute in a sterile gassing chamber. The results are discussed below.

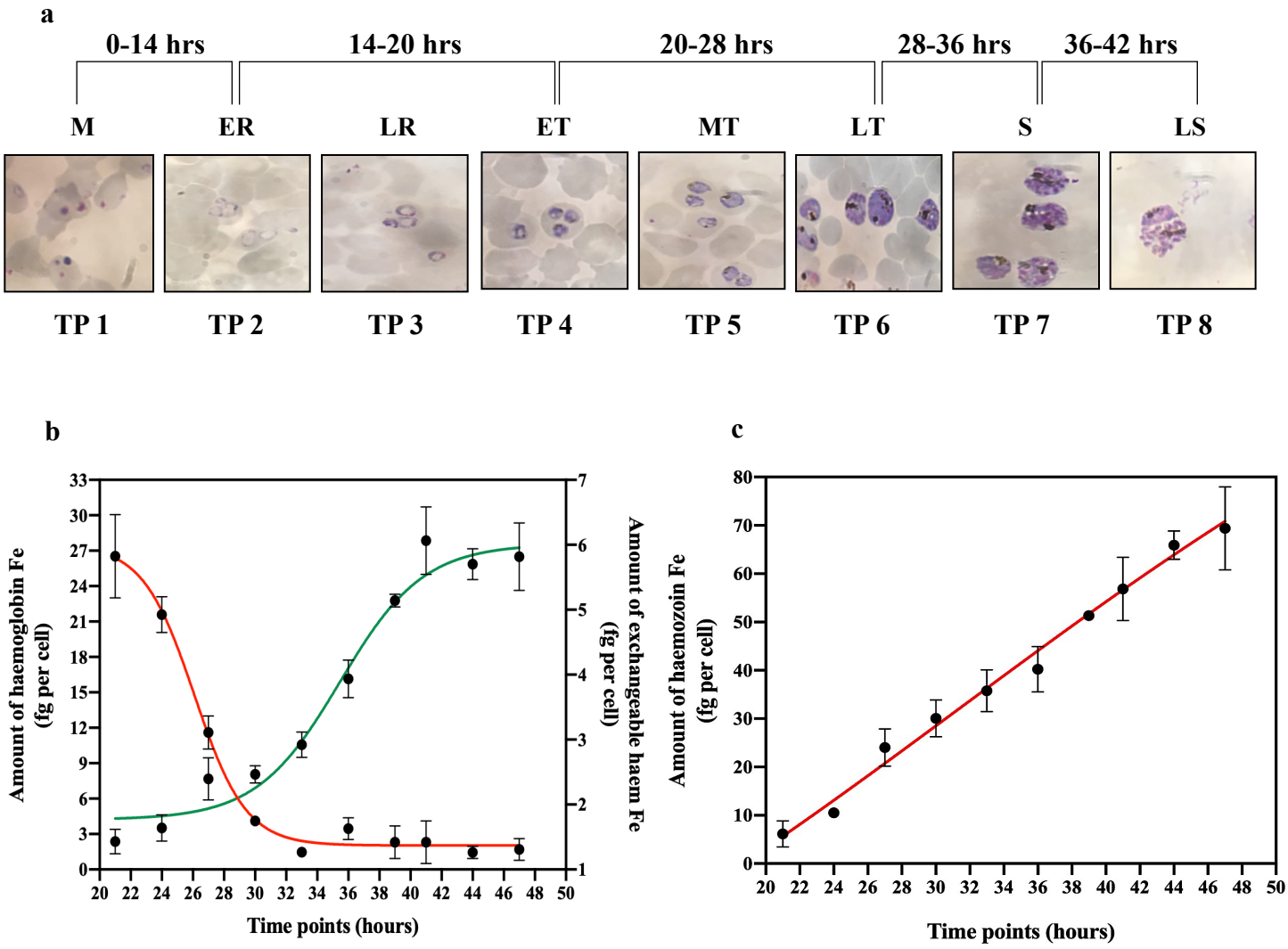

***Figure 5-6 a-d*:** Time point quantification in CQS NF54 parasites represented by, (a) panel of microscope images of Giemsa smears for different time points representing different parasite stages during the intraerythrocytic stage, and (b) the amount of haemoglobin (red) and exchangeable haem (green), and (c) haemozoin expressed as mass of haem Fe in fg per cell at different time points (20-50 h) throughout the life cycle of the parasite. TP = time-point; M = merozoites; ER = early rings; LR = late rings; ET = early trophozoites; MT = mid-trophozoites; LT = late trophozoites; S = schizonts; LS = late schizonts.

Figure 5-6 a illustrates a panel of microscope Giemsa smear images obtained from observing the CQS NF54 cultures over 48 hrs, starting at the merozoite stage (TP 1) to the late schizont stage (TP 8). It was observed from these images that between 0-14 hrs merozoites to early rings were present; 14-20 hrs early rings to early trophozoite were seen; 20-28 hrs early trophozoites to late trophozoites occurred; 28-36 hrs late trophozoites to schizonts were

observed; and 36-42 hrs schizonts to late schizonts were observed. These observations were in close agreement with the observations previously reported by Gligorijevic *et al* whom showed similar Giemsa smear microscope images confirming that at 19 hrs, for example, cultures were in the early trophozoite stage [205].

Figure 5-6 b-d illustrates the quantified time points for the amount of haemoglobin, exchangeable haem and haemozoin throughout the life cycle of CQS NF54 parasites. From this, it was observed that the amount of haem attributed to haemoglobin (***Figure 5-6 b***) decreased in a sigmoidal manner from an initially high value. Compared to the amount of haemoglobin, the amount of exchangeable haem was observed to remain relatively constant throughout the life cycle albeit, with a small sigmoidal increase (***Figure 5-6 c***). Haemozoin amounts, on the other hand, were observed to increase linearly from early to late time points (***Figure 5-6 d***).

In more detail, it was observed that the amount of haemoglobin started to decrease at 20 hrs (TP 4) which corresponded to the early trophozoite stage when the haemozoin was first observed. For the earlier time points (20-28 hrs), corresponding to the early to late trophozoite stage (TP 4-TP 6), a sharp initial decrease in the amount of haemoglobin was observed and corresponded to a steady increase in haemozoin from 10 fg to 30 fg Fe per cell as well as a slight increase in the amount of exchangeable haem. This sharp initial decrease in the amount of haemoglobin agreed with recent reports by Elliott *et al*, who showed that between 6-30 hrs a large volume of haemoglobin is taken up by the parasite [487-490]. A reason could be for this could be as a result of the appearance of Plm I and II, which although from the same group of proteases, have different periods at which they appear in the intraerythrocytic stage of the malaria parasite [491]. During the early stages, (ring stage), Plm I is found to be first synthesized by the parasite and is then continuous throughout the trophozoite stage, which according to Francis *et al* is an indication that Plm I activity in the haemoglobin degradation process is minimal. Plm II, on the other hand, is at its highest concentration only in the trophozoite stage suggesting that its main activity begins after 24 hrs, post invasion [7]. With regards to the amount of haemozoin, these observations agreed with the findings previously reported by Gligorijevic *et al* and Mauritz *et al*, where at the mid to late trophozoite stage the amount of haemozoin was observed to peak [205,491].

After 30 hrs, the amount of haemoglobin remained constant and the amount of exchangeable haem increased by 4 fg Fe per cell whereas the amount of haemozoin continued to increase linearly to 70 fg Fe per cell at 48 hrs. This corresponded to the schizont to late schizont stage (TP 7-TP 8).

With regards to the amount of haemoglobin observed at early time points, between 20-27 hrs specifically, the large error bars that were observed raised some concern. Bearing in mind the limitation of this method which make early time points, especially for the late rings to early trophozoite stage, difficult to measure, there is a difficulty in obtaining reliable results at this stage. This leads to the risk of contamination from the excess haemoglobin of RBCs in the culture. Therefore, a haemoglobin contamination experiment was performed for the early time points of 24 hrs and 27 hrs (see ***Section 5.2.5.5***).

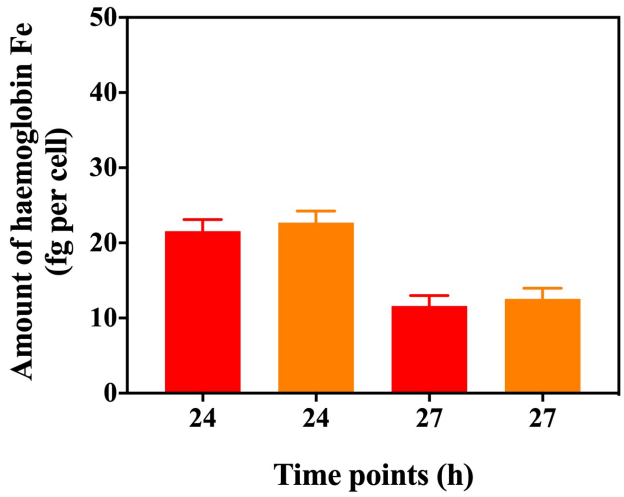

***Figure 5-7*: Bar graph for haemoglobin contamination experiment for early time points of 24 and 27 hrs expressed as mass of haem Fe per cell (fg) for haemoglobin in non-spiked samples (red) and samples spiked with RBCs (orange).**

Figure 5-7 illustrates the haemoglobin contamination experiment that was conducted for non-spiked (red) and RBC-spiked samples (orange) at the early time-points of 24 hrs and 27 hrs post-invasion. From the bar graph, it was inferred that there was no significant haemoglobin contamination from lysed cells at these time points. It also confirmed that the time point quantification method proved to be a reliable and efficient method for quantifying the haem amounts for the different haem species throughout the blood stage of CQS NF54 cultures.

5.6 Summary and conclusions

In summary, the concentration of the aspartic and cysteine proteases (Plm I, II, HAP and falcipain-2) as well as the amount of haemoglobin throughout the life cycle of CQS NF54 parasites was successfully determined for future use in a haem pathway model.

Using the protein abundance database (PAXdb) and SIB bioinformatics resource portal (ExPASy), the average abundance-weighted molecular weight of 1337 proteins in Dd2 strain parasites was calculated to be 40,483 ± 77 g/mol.

Three protein quantification methods, Bradford, BCA and NanoDrop assays, were used to determine the protein mass of NF54 and Dd2 strain parasites with RBCs as a control. The resulting data was observed to be relatively consistent across all three methods. It was observed that Dd2 strain parasites had a higher average protein mass than NF54 strain parasites with RBCs having a similar average protein mass to that reported in the literature. From this, the total number of protein molecules per cell was calculated.

These data combined with the reported volume of the DV and the relative abundances of Plm I, II, HAP and falcipain-2 from PAXdb were used to calculate the concentration of these proteases. From this, it was observed that HAP had a higher concentration than Plm I and II (2-fold) and falcipain-2 (7-fold).

Lastly, a time point quantification assay was successfully performed in order to determine the amount of haemoglobin, exchangeable haem and haemozoin throughout the life cycle of CQS NF54 parasites. It was observed from these data that there was a sigmoidal decrease in the haemoglobin amounts that corresponded to a linear increase in the haemozoin amount and relatively constant exchangeable haem amounts. With this it was noticed that there was a large initial decrease in haemoglobin which was confirmed to not be caused by haemoglobin contamination.

In conclusion, the prerequisites required for the development of a haem pathway model were successfully determined in this study. It was apparent that the protein quantification and time point quantification methods proved to be efficient and reliable in determining the protein masses, total number of protein molecules per cell, protease concentrations as well as the haemoglobin amounts throughout the life cycle of CQS NF54 parasites. From this, it was apparent that Dd2 parasites had a higher protein mass that coincided with a higher number of protein molecules per cell, compared to NF54 parasites. It was also inferred that the concentration of aspartic proteases (Plm I, II and HAP) were 4-fold higher than cysteine proteases (falcipain-2) which was a direct reflection of their relative abundances within Dd2

parasites. Time point quantifications showed significantly high amounts of haemoglobin at early time points (early trophozoite stage) which suggested that the initial intake of haemoglobin by parasites is larger than at later time points (schizont stage) where it is relatively constant. It was, however, not apparent why exchangeable haem amounts remained relatively constant at early time points with the large amounts of haem being releases as a result of haemoglobin being digested. On the contrary, a reason for this could be as a result of the formation of neutral lipids in the parasite DV. These neutral lipids have been previously identified by Jackson *et al*, who showed 100 nm sized particles containing neutral lipids inside the parasite DV using a Nile Red probe and fluorescent imaging [159].

6

Overall conclusions and Future work

6.1 Overall Conclusions

One strategy to deal with drug resistance in *P. falciparum* parasites is the discovery of new inhibitors that are equivalent to or more potent than well-known β-haematin inhibitors like CQ in both CQR and CQS parasites. With the low cost and reliability of CQ, investigations into CQ analogues have proven to show activity against CQ-resistant *P. falciparum* parasites and thus increasing the interest into the discovery of new haemozoin inhibitors [10-12]. An approach has been developed for the discovery of new haemozoin inhibitors that uses a high through-put screening method. This high through-put screening method has proven to select β-haematin inhibitors that are active against the formation of the synthetic counterpart of haemozoin, β-haematin. Ncokazi and Egan developed a cheap and fast β-haematin inhibition assay which has been successful when combined with detergent mediated β-haematin formation in the identification of new β-haematin inhibitors [262]. Like CQ, these β-haematin inhibitors have also been shown to have the ability to disrupt the formation of haemozoin in malaria parasites by increasing exchangeable haem percentages and causing parasite death [144,263,492]. The proposed mechanism in which these β-haematin inhibitors achieve this is through accumulation within the DV of parasites, which is influenced by the phenomenon of pH trapping [269,283,493-495]. Although, the exact mechanism of how these β-haematin inhibitors cross the DV membrane and accumulate is still in question. With this, it has also been proposed that accumulating β-haematin inhibitors have the ability to bind to the μ-oxo dimer of haematin or absorb onto the fastest growing face of haemozoin within the parasite [121,144,251]. Quinoline-derived β-haematin inhibitors have also been claimed to have other mechanisms of action which includes interfering with the process of haemoglobin digestion, reducing the availability of amino acids for protein synthesis by the parasite therefore inhibiting its growth. However, the exact mechanism by which these β-haematin inhibitors inhibit the formation of haemozoin has remained in question.

In this study, investigations into the inhibition of haemozoin formation were carried out in *P. falciparum* parasites using ten selected β-haematin inhibitors and their derivatives. These β-haematin inhibitors (test compounds **1-10**) were chosen across different scaffolds, namely: benzimidazoles (**1-4**), quinazolines (**5-7**), benzothiazoles (**8**), benzoxazoles (**9**), and triarylimidazoles (**10**) including CQ and AQ for comparison. First, the parasite growth inhibition activities of these β-haematin inhibitors in CQS NF54 strain parasites were measured using a p-LDH method. From the sigmoidal dose response curves, micromolar IC_{50} values were determined for these β-haematin inhibitors which were all less active than CQ. Second, a

pyridine-based parasite haem fractionation method was used to measure the effects of these β-haematin inhibitors at increasing inhibitory concentrations (0.5, 1.0, 2.0, 2.5 and 3.0×IC_{50}) on undigested haemoglobin, exchangeable haem and haemozoin present in CQS parasites. Initially, test compound **1** exhibited increasing amounts of exchangeable haem with decreasing amounts of haemozoin, 4- and 3-fold respectively larger than CQ. Similarly, the remaining test compounds (**2-9**) exhibited similar trends at increasing dosage, where, one of the least active test compound (**9**) resulted in the largest increase in the amount of exchangeable haem at the IC_{50} value which coincided with empty parasite DVs containing no visible haemozoin crystals. From these data, it was apparent that the mechanism of action of these β-haematin inhibitors was the inhibition of haemozoin formation, although given the very small change, the quinazoline-containing β-haematin inhibitors could have more than one mechanism of action. This was further confirmed from the observations of the inversely proportional relationship between the decreasing percentage parasite growth and increasing exchangeable haem amounts as a function of increasing dosage of these β-haematin inhibitors. Moreover, a bar plot exhibited a clear but counterintuitive trend between parasite growth inhibition activity and the amount of exchangeable haem at the IC_{50} value of each β-haematin inhibitor, where decreased parasite growth inhibition activity often corresponded to increased exchangeable haem. While it was not apparent as how parasite growth inhibition activities arise, these β-haematin inhibitors could nonetheless be classified as haemozoin inhibitors from this point on.

With suggestions that these haemozoin inhibitors are capable of inhibiting the formation of haemozoin by accumulating in the parasites DV, further investigations to determine their experimental CAR values were carried out. Using an inoculum effect analysis, IC_{50} values were measured at varying parasitaemia. The resulting data showed a linear increase in IC_{50} values as a function of inoculum size, from which the experimental CAR values were calculated. The experimental CAR values for these haemozoin inhibitors were observed to be much lower than the comparative test compounds **11**, **CQ** and **AQ**. From this, it was inferred that pH trapping may contribute but not primarily be the cause for the accumulation of these haemozoin inhibitors. For further analysis, the experimental CAR values were converted to intracellular test compound amounts for all haemozoin inhibitors which was based on their experimental CAR values, volume of an iRBC and their IC_{50} values under standard test conditions. This facilitated direct comparison with exchangeable haem amounts produced by these haemozoin inhibitors which was expressed as femtomoles of exchangeable haem per cell. Remarkably, a plot of femtomoles of exchangeable haem versus the total intracellular test compound amount showed a 1:1 relationship between them. This provided further evidence

that in order for these haemozoin inhibitors to inhibit parasite growth, increase exchangeable haem amounts and inhibit haemozoin formation, they need to accumulate within the parasite's DV.

The suggested rationale for the ability of these haemozoin inhibitors to accumulate in this way was the formation of a 1:1 Fe(III)PPIX-inhibitor complex within the DV of the parasite implying co-localization of Fe(III)PPIX and the inhibitor. Thus, the co-localization of Fe(III)PPIX and a benzimidazole haemozoin inhibitor which incorporated a Br atom (test compound **1**) was investigated using TEM with ESI coupled with EELS for untreated and treated iRBCs. Following cryofixation, TEM images showed parasites within the RBCs with observable structures that included the DV and transport vesicles. For untreated parasites, clearly formed elongated haemozoin crystals were observed. Similar observations were seen for treated iRBCs, however, the haemozoin crystals were less well defined as a result of inhibition by test compound **1** which was observed to be surrounded by what was suggested to be exchangeable haem. Fe distribution maps revealed a strong Fe signal that was attributed to the haemozoin crystals with very little in the RBC cytoplasm for untreated iRBCs. Compared to untreated iRBCs, a slightly less concentrated but still strong Fe signal associated with haemozoin was observed with an increased signal observed in the cytoplasm of the RBC. No Br distribution map was obtained for untreated iRBCs but a strong Br signal attributed to test compound **1** was observed for treated iRBCs in the parasite DV in the same region as the haemozoin crystals. From this, both the Fe and Br distribution maps were overlaid and revealed that Fe(III)PPIX and test compound **1** co-localize in the parasite DV. While this co-localization supported the hypothesis of a Fe(III)PPIX-inhibitor complex forming in the DV, further evidence was obtained using a 532 nm confocal Raman microspectrometer in order to observe changes in the vibrational modes of Fe(III)PPIX complexes in RBCs, untreated and treated parasites. The resulting single scan Raman spectra for the spectral region of 1700-500 cm^{-1} showed subtle shifts in peak positions and increased intensities of certain Fe(III)PPIX peaks for the different Fe(III)PPIX complexes, including the putative Fe(III)PPIX-test compound **1** complex. From the recorded spectrum for the putative Fe(III)PPIX-test compound **1** complex, a unique peak at 1080 cm^{-1} was identified and was observed in the spectrum of its synthetic counterpart in a haematin-test compound **1** mixture. This unique peak was consistent with Fe(III)PPIX pyrrole binding to the imidazole ring via π- π interactions. Upon further inspection, shifted peaks observed in the spectrum for the putative Fe(III)PPIX-test compound **1** complex were seen to be similar to peaks observed in haemozoin. It was, however, inferred from the absence of the peak at 1160 cm^{-1} in the putative Fe(III)PPIX-test compound **1** complex that

there was no contribution from the haemozoin spectrum. In addition, no peaks associated with test compound **1** itself were prominent, probably as a result of haem resonance. On the contrary, the spectrum for β-haematin was observed to be the same as the observed spectrum of haemozoin. Moreover, the spectra for all other Fe(III)PPIX complexes were visually different to that of the putative Fe(III)PPIX-test compound **1** complex which upon overlaying with the haematin-test compound **1** mixture was very similar in peak positions. These data confirmed the possibility that the formation of a Fe(III)PPIX-test compound **1** complex occurs in the DV of CQS parasites and that the peak at 1080 cm^{-1} could be a marker band for this complex. With the observed increased intensities of certain peaks and the possible marker band for the Fe(III)PPIX-test compound **1** complex, confocal Raman true mapping images were obtained for untreated and treated iRBCs at the Raman peaks at 754 cm^{-1}, 1080 cm^{-1}, 1090 cm^{-1} and 1642 cm^{-1}. It was observed that the Raman peak at 754 cm^{-1} was reliable for imaging the signal distribution of haemozoin in the parasite DV, whilst oxy- and deoxy-haemoglobin was localized in the RBC for the remaining Raman peaks for both untreated and treated iRBCs. Interestingly, no signal distribution at the Raman peak at 1080 cm^{-1} was observed for oxy-haemoglobin, deoxy-haemoglobin or haemozoin, but only for the Fe(III)PPIX-test compound **1** complex. Overlaid true mapping images confirmed that the signal distributions of haemozoin and the Fe(III)PPIX-test compound **1** complex co-localized in the parasite DV, consistent with the previous observations for TEM and EELS, highlighting that 1080 cm^{-1} is a marker band for the complex. These spectra were further analysed to identify spectroscopic variations in the spectra of all Fe(III)PPIX complexes using PCA, based on the peak positions. PCA plots exhibited evidence that the Fe(III)PPIX-test compound **1** complex was different to all the other Fe(III)PPIX complexes with cluster separations along PC1, with the exception of the product of the haematin-test compound **1** mixture for which no cluster separation was observed.

Given the central role of haemoglobin degradation within the parasite DV in the mechanism of action of these haemozoin inhibitors, an effort was made to generate experimental input and validation data for the development of a haem pathway model. This included information to determine the concentration of the four main proteases responsible for 60-80% of haemoglobin degradation. To tackle this problem, an abundance-weighted average molecular weight of all *P. falciparum* proteins, calculated from PaxDB, was used to calculate the total number of protein molecules per parasite from a measurement of the total protein mass per parasite. This was then used to determine the cellular concentrations of these haemoglobin-digesting proteases. The abundance-weighted average molecular weights of all *P. falciparum* proteins determined for the CQR Dd2 strain parasite (1337 proteins) was found to be 40,483 ±

77 g/mol. Average total protein mass per cell (Dd2) obtained from three protein quantification assays namely Bradford, BCA and Nanodrop was found to be 12.80 ± 0.35 pg/cell, corresponding to a total of 1.90×10^8 protein molecules per parasite. Intriguingly, Dd2 strain parasites had a higher number of protein molecules per parasite than NF54 strain parasites. From this, the cellular concentration of the haemoglobin-digesting proteases in Dd2 parasites was calculated based on their relative PaxDB abundances, the total number of protein molecules in Dd2 parasites and the estimated DV volume. It was observed that aspartic proteases had a higher average concentration than the cysteine protease, falcipain-2, with HAP having the highest concentration. For future validation purposes, the amount of haemoglobin, exchangeable haem and haemozoin was determined with a time point quantification assay for 20-50 hrs during the blood stage of CQS NF54 parasites. From these data, the amount of trophozoite haemoglobin was observed to decrease in a sigmoidal manner, whilst, haemozoin increased linearly and exchangeable haem remained relatively constant. In early time points the amount of haemoglobin decreased dramatically, and was confirmed to be not as a result of contamination through spiking with excess haemoglobin. These data were also consistent with the early trophozoite to late trophozoite stages that was observed by Giemsa smears.

Therefore in this study, direct evidence of the behaviour of β-haematin inhibitors proved that their mechanism of action is to inhibit the formation of haemozoin and parasite growth by accumulating in the parasite DV, causing a build-up of exchangeable haem involving co-localization of Fe(III)PPIX and the inhibitor (at least for test compound **1**) which forms a Fe(III)PPIX-inhibitor complex. In addition, large initial amounts of haemoglobin were also observed at early time points in the blood stage pertaining to the early trophozoite stage which coincided with 4-fold higher concentrations for aspartic proteases that are known to be involved in the initial stages of haemoglobin degradation.

6.2 Future Work

To fully understand the inhibition of haemozoin formation in the presence of various haemozoin inhibitors for the development of a complete haem pathway model, certain aspects in this study require further investigations.

An initial parameter that has, for a long time, been a reliable indicator of the efficacy of new antimalarials is parasite growth inhibition activity. The widely known p-LDH assay has shown to be consistent and sensitive in determining the parasite growth inhibition activities of new antimalarials, including potential inhibitors that target the formation of haemozoin [496]. However, it is not apparent from this p-LDH assay as to how parasite growth inhibition activity arises. In the case of haemozoin inhibition, it was also unclear how parasite growth inhibition activity is related to the observed variable amounts of exchangeable haem present in parasites, where less active haemozoin inhibitors were observed to often result in larger amounts of exchangeable haem than more active haemozoin inhibitors. Firstly, Wein *et al* showed that the determination of parasite growth inhibition activity by various clinical drug sensitivity assays is dependent on the mechanism of action of these haemozoin inhibitors. Therefore, inoculating parasites at the trophozoite stage and using a SYBR green assay, which is based on DNA levels and independent of the mechanism of action of parasite growth inhibitors, may be more useful in understanding how parasite growth inhibition activity arises [497]. Specifically, this method may be effective for the quinazolines investigated in this study which were suggested to have more than one mode of action. Secondly, the relationship between parasite growth inhibition activity and exchangeable haem amounts could be understood by determining the rate of parasite growth in the presence of these haemozoin inhibitors. In addition, it would also be useful in exploring whether the activities of these inhibitors are stage specificity. A reason for the latter is that Ignatushchenko *et al* used light microscopy to monitor the changes in the stage of parasites at varying times in the presence of xanthone derivatives which are known to inhibit haemozoin formation [307]. From this, the data showed that these derivatives were only toxic at the trophozoite stage, where maximum exchangeable haem levels were observed.

It was observed from cryo-EM studies that a benzimidazole inhibitor containing a Br atom (test compound **1**) co-localized with Fe(III)PPIX in the DV of CQS parasites. TEM images for untreated and test compound **1** treated iRBCs provided clear visualization of parasite structures, which included less well defined haemozoin crystals indicating inhibition. With the EELS distribution images, a clear distinction was made between both the Fe signal associated to exchangeable haem and Br signal corresponding to the haemozoin inhibitor test

compound **1**. However, the Br signal distribution image in comparison to the Fe signal distribution image had a lower signal-to-noise ratio bringing about some concern as to whether the signal observed in the parasite cytoplasm corresponds to test compound **1**. A further limitation to using EELS is that not all haemozoin inhibitors investigated in this study could be analyzed due to the atoms they contain, for example fluorine. It was difficult to distinguish between the elemental distribution of a fluorine-containing haemozoin inhibitor from the Fe signals associated to exchangeable haem as the excitation edges overlapped with that of Fe. Furthermore, the remaining haemozoin inhibitors (test compounds **2-10**) had no suitable elements for distinguishing them from cellular material. To solve this problem and to determine whether the remaining haemozoin inhibitors co-localize with exchangeable haem in the parasites DV, the versatile, fast and efficient confocal Raman true mapping technique that was used in this study would be useful. This would also provide a further understanding of various haemozoin inhibitors and their association with exchangeable haem. At the same time, this technique combined with PCA could be used to determine the changes in the vibrational modes and possible identification of whether or not the remaining haemozoin inhibitors form complexes with Fe(III)PPIX; similar to that observed for the Fe(III)PPIX-test compound **1** complex. With that said, it is still unclear if the formation of these complexes is responsible for parasite death or the unbound exchangeable haem that has been previously reported to be rather insoluble [285]. It could be useful to determine the binding affinities and solubility of these complexes. Although, it may be challenging to determine the binding affinities of these complexes especially with the problems encountered with precipitation of the haematin-test compound **1** mixture as well as low solubility in various solvents of these haemozoin inhibitors.

Finally, haemoglobin digestion is important for the survival of the parasite and it has been shown in this study that large initial amounts of haemoglobin are digested in the early trophozoite stage where as at 30 hrs post-invasion, it is constant. This also corresponded to a relatively constant exchangeable haem amount and linear increase in the amount of haemozoin throughout the blood stage of the parasite. No definite conclusion could be drawn as to why a large amount of haemoglobin is present early in the life cycle which decreases rapidly for early time points while a steady 3-fold increase in exchangeable haem by 30 hrs post-invasion was seen. While the volumes of haemoglobin uptake during the blood stage of the parasite has been previously reported by Elliot *et al*, the rate at which haemoglobin is taken up by the parasite is yet to be determined [490]. Thus, further investigation into the determination of the rate of haemoglobin uptake and digestion could possibly provide reasons for the previously mentioned observed trends. Additionally, a similar assay could be performed from the time of merozoite

invasion to measure the rate of haemoglobin uptake, where Esposito *et al* used Förster resonance energy transfer (FRET) with a calcein fluorophore to determine the concentration of haemoglobin throughout the blood stage of the parasite [498].

Therefore, further investigations will not only be useful in developing a future haem pathway model, but also provide a better understanding of these processes for the development of new antimalarials to aid in the eradication of malaria in the future.

7

References

1. Greenwood, B. and Mutabingwa, T., 2002. Malaria in 2002.
2. WHO, 2015. World malaria report 2015, World Health Organization.
3. Cox-Singh, J., Davis, T.M., Lee, K.S., Shamsul, S.S., Matusop, A., Ratnam, S., Rahman, H.A., Conway, D.J. and Singh, B., 2008. *Plasmodium knowlesi* malaria in humans is widely distributed and potentially life threatening. *Clinical infectious diseases*, *46*(2), pp.165-171.
4. Rowe, J.A., Claessens, A., Corrigan, R.A. and Arman, M., 2009. Adhesion of *Plasmodium falciparum*-infected erythrocytes to human cells: molecular mechanisms and therapeutic implications. *Expert reviews in molecular medicine*, *11*.
5. Caraballo, H. and King, K., 2014. Emergency department management of mosquito-borne illness: malaria, dengue, and West Nile virus. *Emergency medicine practice*, *16*(5), pp.1-23.
6. Snow, R.W., Guerra, C.A., Noor, A.M., Myint, H.Y. and Hay, S.I., 2005. The global distribution of clinical episodes of *Plasmodium falciparum* malaria. *Nature*, *434*(7030), p.214.
7. Francis, S.E., Sullivan Jr, D.J. and Goldberg, A.D.E., 1997. Hemoglobin metabolism in the malaria parasite *Plasmodium falciparum*. *Annual Reviews in Microbiology*, *51*(1), pp.97-123.
8. Wellems, T.E. and Plowe, C.V., 2001. Chloroquine-resistant malaria. *The Journal of infectious diseases*, *184*(6), pp.770-776.
9. Peters, W., Robinson, B.L. and Ellis, D.S., 1987. The chemotherapy of rodent malaria XLII. Halofantrine and halofantrine resistance. *Annals of Tropical Medicine & Parasitology*, *81*(5), pp.639-646.
10. Stocks, P.A., Raynes, K.J., Bray, P.G., Park, B.K., O'Neill, P.M. and Ward, S.A., 2002. Novel short chain chloroquine analogues retain activity against chloroquine resistant K1 *Plasmodium falciparum*. *Journal of medicinal chemistry*, *45*(23), pp.4975-4983.
11. Ridley, R.G., Hofheinz, W., Matile, H., Jaquet, C., Dorn, A., Masciadri, R., Jolidon, S., Richter, W.F., Guenzi, A., Girometta, M.A. and Urwyler, H., 1996. 4-aminoquinoline analogs of chloroquine with shortened side chains retain activity against chloroquine-resistant *Plasmodium falciparum*. *Antimicrobial agents and chemotherapy*, *40*(8), pp.1846-1854.
12. Biot, C., Glorian, G., Maciejewski, L.A., Brocard, J.S., Domarle, O., Blampain, G., Millet, P., Georges, A.J., Abessolo, H., Dive, D. and Lebibi, J., 1997. Synthesis and

antimalarial activity in vitro and in vivo of a new ferrocene−chloroquine analogue. *Journal of medicinal chemistry*, *40*(23), pp.3715-3718.

13. WHO, 2013. World malaria report 2013, World Health Organization.
14. Dondorp, A.M., Nosten, F., Yi, P., Das, D., Phyo, A.P., Tarning, J., Lwin, K.M., Ariey, F., Hanpithakpong, W., Lee, S.J. and Ringwald, P., 2009. Artemisinin resistance in *Plasmodium falciparum* malaria. *New England Journal of Medicine*, *361*(5), pp.455-467.
15. WHO, 2017. World malaria report 2017, World Health Organization.
16. WHO, 2018. World malaria report 2018, World Health Organization.
17. Rogers, W.O., Sem, R., Tero, T., Chim, P., Lim, P., Muth, S., Socheat, D., Ariey, F. and Wongsrichanalai, C., 2009. Failure of artesunate-mefloquine combination therapy for uncomplicated *Plasmodium falciparum* malaria in southern Cambodia. *Malaria journal*, *8*(1), p.10.
18. Leang, R., Barrette, A., Bouth, D.M., Menard, D., Abdur, R., Duong, S. and Ringwald, P., 2013. Efficacy of dihydroartemisinin-piperaquine for treatment of uncomplicated *Plasmodium falciparum* and *Plasmodium vivax* in Cambodia, 2008 to 2010. *Antimicrobial agents and chemotherapy*, *57*(2), pp.818-826.
19. Carrara, V.I., Lwin, K.M., Phyo, A.P., Ashley, E., Wiladphaingern, J., Sriprawat, K., Rijken, M., Boel, M., McGready, R., Proux, S. and Chu, C., 2013. Malaria burden and artemisinin resistance in the mobile and migrant population on the Thai–Myanmar border, 1999–2011: an observational study. *PLoS medicine*, *10*(3), p.e1001398.
20. Bustos, M.D., Wongsrichanalai, C., Delacollette, C. and Burkholder, B., 2013. Monitoring antimalarial drug efficacy in the Greater Mekong Subregion: an overview of in vivo results from 2008 to 2010. *The Southeast Asian journal of tropical medicine and public health*, *44*, pp.201-30.
21. Saunders, D.L., Vanachayangkul, P. and Lon, C., 2014. US Army Military Malaria Research Program. *National Center for Parasitology, Entomology, and Malaria Control (CNM), Royal Cambodian Armed Forces*, pp.484-485.
22. Burrows, J.N., van Huijsduijnen, R.H., Möhrle, J.J., Oeuvray, C. and Wells, T.N., 2013. Designing the next generation of medicines for malaria control and eradication. *Malaria journal*, *12*(1), p.187.
23. Newby, G., Bennett, A., Larson, E., Cotter, C., Shretta, R., Phillips, A.A. and Feachem, R.G., 2016. The path to eradication: a progress report on the malaria-eliminating countries. *The Lancet*, *387*(10029), pp.1775-1784.

24. Wunderlich, J., Rohrbach, P. and Dalton, J.P., 2012. The malaria digestive vacuole. *Front. Biosci*, *4*, pp.1424-1448.
25. Dluzewski, A.R., Ling, I.T., Hopkins, J.M., Grainger, M., Margos, G., Mitchell, G.H., Holder, A.A. and Bannister, L.H., 2008. Formation of the food vacuole in *Plasmodium falciparum*: a potential role for the 19 kDa fragment of merozoite surface protein 1 (MSP119). *PLoS One*, *3*(8).
26. Foley, M. and Tilley, L., 1998. Quinoline antimalarials: mechanisms of action and resistance and prospects for new agents. *Pharmacology & therapeutics*, *79*(1), pp.55-87.
27. Cowman, A.F., Berry, D. and Baum, J., 2012. The cellular and molecular basis for malaria parasite invasion of the human red blood cell. *J Cell Biol*, *198*(6), pp.961-971.
28. Amino, R., Thiberge, S., Martin, B., Celli, S., Shorte, S., Frischknecht, F. and Ménard, R., 2006. Quantitative imaging of *Plasmodium* transmission from mosquito to mammal. *Nature medicine*, *12*(2), p.220.
29. Sinnis, Photini, and Fidel Zavala., 2008. The skin stage of malaria infection: biology and relevance to the malaria vaccine effort. *Future Medicine*, pp.275-278.
30. Yamauchi, L.M., Coppi, A., Snounou, G. and Sinnis, P., 2007. *Plasmodium* sporozoites trickle out of the injection site. *Cellular microbiology*, *9*(5), pp.1215-1222.
31. Ejigiri, I. and Sinnis, P., 2009. *Plasmodium* sporozoite–host interactions from the dermis to the hepatocyte. *Current opinion in microbiology*, *12*(4), pp.401-407.
32. Sturm, A., Amino, R., Van de Sand, C., Regen, T., Retzlaff, S., Rennenberg, A., Krueger, A., Pollok, J.M., Menard, R. and Heussler, V.T., 2006. Manipulation of host hepatocytes by the malaria parasite for delivery into liver sinusoids. *science*, *313*(5791), pp.1287-1290.
33. Greenwood, B.M., Fidock, D.A., Kyle, D.E., Kappe, S.H., Alonso, P.L., Collins, F.H. and Duffy, P.E., 2008. Malaria: progress, perils, and prospects for eradication. *The Journal of clinical investigation*, *118*(4), pp.1266-1276.
34. Tilley, L., Dixon, M.W. and Kirk, K., 2011. The *Plasmodium falciparum*-infected red blood cell. *The international journal of biochemistry & cell biology*, *43*(6), pp.839-842.
35. Baton, L.A. and Ranford-Cartwright, L.C., 2005. How do malaria ookinetes cross the mosquito midgut wall?. *Trends in parasitology*, *21*(1), pp.22-28.
36. Duffy, P.E., Sahu, T., Akue, A., Milman, N. and Anderson, C., 2012. Pre-erythrocytic malaria vaccines: identifying the targets. *Expert review of vaccines*, *11*(10), pp.1261-1280.

37. Moorthy, V.S., Imoukhuede, E.B., Milligan, P., Bojang, K., Keating, S., Kaye, P., Pinder, M., Gilbert, S.C., Walraven, G., Greenwood, B.M. and Hill, A.S., 2004. A randomised, double-blind, controlled vaccine efficacy trial of DNA/MVA ME-TRAP against malaria infection in Gambian adults. *PLoS medicine*, *1*(2), p.e33.
38. Crosnier, J., Jungers, P., Couroucé, A., Laplanche, A., Benhamou, E., Degos, F., Lacour, B., Prunet, P., Cerisier, Y. and Guesry, P., 1981. Randomised placebo-controlled trial of hepatitis B surface antigen vaccine in French haemodialysis units: II, haemodialysis patients. *The Lancet*, *317*(8224), pp.797-800.
39. Medica, D.L. and Sinnis, P., 2005. Quantitative dynamics of *Plasmodium yoelii* sporozoite transmission by infected anopheline mosquitoes. *Infection and immunity*, *73*(7), pp.4363-4369.
40. Mauduit, M., Grüner, A.C., Tewari, R., Depinay, N., Kayibanda, M., Chavatte, J.M., Franetich, J.F., Crisanti, A., Mazier, D., Snounou, G. and Rénia, L., 2009. A role for immune responses against non-CS components in the cross-species protection induced by immunization with irradiated malaria sporozoites. *PloS one*, *4*(11), p.e7717.
41. Oeuvray, C., Theisen, M., Rogier, C., Trape, J.F., Jepsen, S. and Druilhe, P., 2000. Cytophilic immunoglobulin responses to *Plasmodium falciparum* glutamate-rich protein are correlated with protection against clinical malaria in Dielmo, Senegal. *Infection and immunity*, *68*(5), pp.2617-2620.
42. Oeuvray, C., Bouharoun-Tayoun, H., Grass-Masse, H., Iepers, J.P., Ralamboranto, L., Tartar, A. and Druilhe, P., 1994. A novel merozoite surface antigen of *Plasmodium falciparum* (MSP-3) identified by cellular-antibody cooperative mechanism antigenicity and biological activity of antibodies. *Memorias do Instituto Oswaldo Cruz*, *89*, pp.77-80.
43. Chan, J.A., Drew, D.R., Reiling, L., Lisboa-Pinto, A., Dinko, B., Sutherland, C.J., Dent, A., Chelimo, K., Kazura, J.W., Boyle, M.J. and Beeson, J., 2018. Low levels of human antibodies to gametocyte-infected erythrocytes contrasts the *Pf*EMP1-dominant response to asexual stages in *P. falciparum* malaria. *Frontiers in immunology*, *9*, p.3126.
44. Renia, L., Ling, I.T., Marussig, M., Miltgen, F., Holder, A.A. and Mazier, D., 1997. Immunization with a recombinant C-terminal fragment of *Plasmodium yoelii* merozoite surface protein 1 protects mice against homologous but not heterologous *P. yoelii* sporozoite challenge. *Infection and immunity*, *65*(11), pp.4419-4423.

45. Lucantoni, L., Silvestrini, F., Signore, M., Siciliano, G., Eldering, M., Dechering, K.J., Avery, V.M. and Alano, P., 2015. A simple and predictive phenotypic High Content Imaging assay for *Plasmodium falciparum* mature gametocytes to identify malaria transmission blocking compounds. *Scientific reports*, *5*, p.16414.
46. Tanaka, T.Q., Dehdashti, S.J., Nguyen, D.T., McKew, J.C., Zheng, W. and Williamson, K.C., 2013. A quantitative high throughput assay for identifying gametocytocidal compounds. *Molecular and biochemical parasitology*, *188*(1), pp.20-25.
47. Sun, W., Tanaka, T.Q., Magle, C.T., Huang, W., Southall, N., Huang, R., Dehdashti, S.J., McKew, J.C., Williamson, K.C. and Zheng, W., 2014. Chemical signatures and new drug targets for gametocytocidal drug development. *Scientific reports*, *4*, p.3743.
48. Langreth, S.G., Jensen, J.B., Reese, R.T. and Trager, W., 1978. Fine structure of human malaria in vitro. *The Journal of protozoology*, *25*(4), pp.443-452.
49. Stewart, M.J., Schulman, S. and Vanderberg, J.P., 1986. Rhoptry secretion of membranous whorls by *Plasmodium falciparum* merozoites. *The American journal of tropical medicine and hygiene*, *35*(1), pp.37-44.
50. Bannister, L.H. and Mitchell, G.H., 1995. The role of the cytoskeleton in *Plasmodium falciparum* merozoite biology: an electron-microscopic view. *Annals of Tropical Medicine & Parasitology*, *89*(2), pp.105-111.
51. Bannister, L.H., Hopkins, J.M., Fowler, R.E., Krishna, S. and Mitchell, G.H., 2000. A brief illustrated guide to the ultrastructure of *Plasmodium falciparum* asexual blood stages. *Parasitology today*, *16*(10), pp.427-433.
52. Holder, A.A., 1994. Proteins on the surface of the malaria parasite and cell invasion. *Parasitology*, *108*(S1), pp.S5-S18.
53. Ward, G.E., Chitnis, C.E. and Miller, L.H., 1994. The invasion of erythrocytes by malarial merozoites. *Baillieres Clinical Infectious Diseases*, *1*(2), pp.155-190.
54. Barnwell, J.W. and Galinski, M.R., 1998. Invasion of vertebrate cells: erythrocytes. *Science Open*.
55. Aikawa, M., Huff, C.G. and Sprinz, H., 1967. Fine structure of the asexual stages of *Plasmodium elongatum*. *The Journal of cell biology*, *34*(1), pp.229-249.
56. Mikolajczak, S.A. and Kappe, S.H., 2006. A clash to conquer: the malaria parasite liver infection. *Molecular microbiology*, *62*(6), pp.1499-1506.
57. Köhler, S., Delwiche, C.F., Denny, P.W., Tilney, L.G., Webster, P., Wilson, R.J.M., Palmer, J.D. and Roos, D.S., 1997. A plastid of probable green algal origin in Apicomplexan parasites. *Science*, *275*(5305), pp.1485-1489.

58. Stenzel, D.J. and Kara, U.A., 1989. Sorting of malarial antigens into vesicular compartments within the host cell cytoplasm as demonstrated by immunoelectron microscopy. *European journal of cell biology*, *49*(2), pp.311-318.
59. Aikawa, M., Hepler, P.K., Huff, C.G. and Sprinz, H., 1966. The feeding mechanism of avian malarial parasites. *The Journal of cell biology*, *28*(2), pp.355-373.
60. Goldberg, D.E., 1994. Hemoglobin catabolism by intraerythrocytic *plasmodium*. *Baillieres clinical infectious diseases*, *1*(2), pp.319-333.
61. Yayon, A., Timberg, R., Friedman, S. And Ginsburg, H., 1984. Effects of chloroquine on the feeding mechanism of the intraerythrocytic human malarial parasite *plasmodium falciparum* 1. *The Journal of protozoology*, *31*(3), pp.367-372.
62. Slomianny, C. and Prensier, G., 1990. A cytochemical ultrastructural study of the lysosomal system of different species of malaria parasites. *The Journal of Protozoology*, *37*(6), pp.465-470.
63. Ginsburg, H., 1990. Some reflections concerning host erythrocyte-malarial parasite interrelationships. *Blood cells*, *16*(2-3), pp.225-235.
64. Slomianny, C., 1990. Three-dimensional reconstruction of the feeding process of the malaria parasite. *Blood cells*, *16*(2-3), pp.369-378.
65. Elford, B.C., Cowan, G.M. and Ferguson, D.J., 1995. Parasite-regulated membrane transport processes and metabolic control in malaria-infected erythrocytes. *Biochemical journal*, *308*(Pt 2), p.361.
66. Atkinson, C.T. and Aikawa, M., 1990. Ultrastructure of malaria-infected erythrocytes. *Blood cells*, *16*(2-3), pp.351-368.
67. Van Wye, J., Ghori, N., Webster, P., Mitschler, R.R., Elmendorf, H.G. and Haldar, K., 1996. Identification and localization of rab6, separation of rab6 from ERD2 and implications for an 'unstacked'Golgi, in *Plasmodium falciparum*. *Molecular and biochemical parasitology*, *83*(1), pp.107-120.
68. Aikawa, M. and Seed, T.M., 1980. Morphology of plasmodia. *Morphology of plasmodia.*, pp.285-344.
69. Bannister, L.H., Hopkins, J.M., Fowler, R.E., Krishna, S. and Mitchell, G.H., 2000. Ultrastructure of rhoptry development in *Plasmodium falciparum* erythrocytic schizonts. *Parasitology*, *121*(3), pp.273-287.
70. Vickerman, K. and Cox, F.E.G., 1967. Merozoite formation in the erythrocytic stages of the malaria parasite *Plasmodium vinckei*. *Transactions of the Royal Society of Tropical Medicine and Hygiene*, *61*(3), pp.303-312.

71. Jaikaria, N.S., Rozario, C., Ridley, R.G. and Perkins, M.E., 1993. Biogenesis of rhoptry organelles in *Plasmodium falciparum*. *Molecular and biochemical parasitology*, *57*(2), pp.269-279.
72. Egan, T.J., 2008. Recent advances in understanding the mechanism of hemozoin (malaria pigment) formation. *Journal of inorganic biochemistry*, *102*(5-6), pp.1288-1299.
73. Ponsuwanna, P., Kochakarn, T., Bunditvorapoom, D., Kümpornsin, K., Otto, T.D., Ridenour, C., Chotivanich, K., Wilairat, P., White, N.J., Miotto, O. and Chookajorn, T., 2016. Comparative genome-wide analysis and evolutionary history of haemoglobin-processing and haem detoxification enzymes in malarial parasites. *Malaria journal*, *15*(1), p.51.
74. Rosenthal, P.J., 2004. Cysteine proteases of malaria parasites. *International journal for parasitology*, *34*(13-14), pp.1489-1499.
75. Lew, V.L., Macdonald, L., Ginsburg, H., Krugliak, M. and Tiffert, T., 2004. Excess haemoglobin digestion by malaria parasites: a strategy to prevent premature host cell lysis. *Blood Cells, Molecules, and Diseases*, *32*(3), pp.353-359.
76. Gluzman, I.Y., Francis, S.E., Oksman, A., Smith, C.E., Duffin, K.L. and Goldberg, D.E., 1994. Order and specificity of the *Plasmodium falciparum* hemoglobin degradation pathway. *The Journal of clinical investigation*, *93*(4), pp.1602-1608.
77. Gorka, A.P., de Dios, A. and Roepe, P.D., 2013. Quinoline drug–heme interactions and implications for antimalarial cytostatic versus cytocidal activities. *Journal of medicinal chemistry*, *56*(13), pp.5231-5246.
78. Coombs, G.H., Goldberg, D.E., Klemba, M., Berry, C., Kay, J. and Mottram, J.C., 2001. Aspartic proteases of *Plasmodium falciparum* and other parasitic protozoa as drug targets. *Trends in parasitology*, *17*(11), pp.532-537.
79. Goldberg, D.E., Slater, A.F., Beavis, R., Chait, B., Cerami, A. and Henderson, G.B., 1991. Hemoglobin degradation in the human malaria pathogen *Plasmodium falciparum*: a catabolic pathway initiated by a specific aspartic protease. *Journal of Experimental Medicine*, *173*(4), pp.961-969.
80. Francis, S.E., Gluzman, I.Y., Oksman, A., Knickerbocker, A., Mueller, R., Bryant, M.L., Sherman, D.R., Russell, D.G. and Goldberg, D.E., 1994. Molecular characterization and inhibition of a *Plasmodium falciparum* aspartic hemoglobinase. *The EMBO Journal*, *13*(2), pp.306-317.

81. Banerjee, R., Liu, J., Beatty, W., Pelosof, L., Klemba, M. and Goldberg, D.E., 2002. Four plasmepsins are active in the *Plasmodium falciparum* food vacuole, including a protease with an active-site histidine. *Proceedings of the National Academy of Sciences*, *99*(2), pp.990-995.
82. Dame, J.B., Yowell, C.A., Omara-Opyene, L., Carlton, J.M., Cooper, R.A. and Li, T., 2003. Plasmepsin 4, the food vacuole aspartic proteinase found in all *Plasmodium spp.* infecting man. *Molecular and biochemical parasitology*, *130*(1), pp.1-12.
83. Francis, S.E., Gluzman, I.Y., Oksman, A., Banerjee, D. and Goldberg, D.E., 1996. Characterization of native falcipain, an enzyme involved in *Plasmodium falciparum* hemoglobin degradation. *Molecular and biochemical parasitology*, *83*(2), pp.189-200.
84. Goldberg, D.E., Slater, A.F., Cerami, A. and Henderson, G.B., 1990. Hemoglobin degradation in the malaria parasite *Plasmodium falciparum*: an ordered process in a unique organelle. *Proceedings of the National Academy of Sciences*, *87*(8), pp.2931-2935.
85. Luker, K.E., Francis, S.E., Gluzman, I.Y. and Goldberg, D.E., 1996. Kinetic analysis of plasmepsins I and II, aspartic proteases of the *Plasmodium falciparum* digestive vacuole. *Molecular and biochemical parasitology*, *79*(1), pp.71-78.
86. Perutz, M.F., 1987. Molecular anatomy, physiology, and pathology of hemoglobin. *The Molecular basis of blood diseases*, pp.127-178.
87. Francis, S.E., Banerjee, R. and Goldberg, D.E., 1997. Biosynthesis and maturation of the malaria aspartic hemoglobinases plasmepsins I and II. *Journal of Biological Chemistry*, *272*(23), pp.14961-14968.
88. Rosenthal, P.J., 2011. Falcipains and other cysteine proteases of malaria parasites. In *Cysteine Proteases of Pathogenic Organisms* (pp. 30-48). Springer, Boston, MA.
89. Schlagenhauf, P., Adamcova, M., Regep, L., Schaerer, M.T. and Rhein, H.G., 2010. The position of mefloquine as a 21st century malaria chemoprophylaxis. *Malaria journal*, *9*(1), p.357.
90. Wyatt, D.M. and Berry, C., 2002. Activity and inhibition of plasmepsin IV, a new aspartic proteinase from the malaria parasite, *Plasmodium falciparum*. *FEBS letters*, *513*(2-3), pp.159-162.
91. Bjelic, S. and Åqvist, J., 2006. Catalysis and linear free energy relationships in aspartic proteases. *Biochemistry*, *45*(25), pp.7709-7723.

92. Ambele, M.A., Sewell, B.T., Cummings, F.R., Smith, P.J. and Egan, T.J., 2013. Synthetic hemozoin (β-hematin) crystals nucleate at the surface of neutral lipid droplets that control their sizes. *Crystal growth & design*, *13*(10), pp.4442-4452.
93. Klemba, M., Gluzman, I. and Goldberg, D.E., 2004. A *Plasmodium falciparum* dipeptidyl aminopeptidase I participates in vacuolar hemoglobin degradation. *Journal of Biological Chemistry*, *279*(41), pp.43000-43007.
94. Gavigan, C.S., Dalton, J.P. and Bell, A., 2001. The role of aminopeptidases in haemoglobin degradation in *Plasmodium falciparum*-infected erythrocytes. *Molecular and biochemical parasitology*, *117*(1), pp.37-48.
95. Allary, M., Schrevel, J. and Florent, I., 2002. Properties, stage-dependent expression and localization of *Plasmodium falciparum* M1 family zinc-aminopeptidase. *Parasitology*, *125*(1), pp.1-10.
96. Dalal, S. and Klemba, M., 2007. Roles for two aminopeptidases in vacuolar hemoglobin catabolism in *Plasmodium falciparum*. *Journal of Biological Chemistry*, *282*(49), pp.35978-35987.
97. Skinner-Adams, T.S., Lowther, J., Teuscher, F., Stack, C.M., Grembecka, J., Mucha, A., Kafarski, P., Trenholme, K.R., Dalton, J.P. and Gardiner, D.L., 2007. Identification of phosphinate dipeptide analog inhibitors directed against the *Plasmodium falciparum* M17 leucine aminopeptidase as lead antimalarial compounds. *Journal of medicinal chemistry*, *50*(24), pp.6024-6031.
98. Grembecka, J., Mucha, A., Cierpicki, T. and Kafarski, P., 2002. Structure-based design and synthesis of dipeptide analogues as new inhibitors of leucine aminopeptidase. *Phosphorus, Sulfur, and Silicon and the Related Elements*, *177*(6-7), pp.1739-1743.
99. Lamarque, M., Tastet, C., Poncet, J., Demettre, E., Jouin, P., Vial, H. and Dubremetz, J.F., 2008. Food vacuole proteome of the malarial parasite *Plasmodium falciparum*. *PROTEOMICS–Clinical Applications*, *2*(9), pp.1361-1374.
100. Lolupiman, S., Siripurkpong, P. and Yuvaniyama, J., 2014. Disulfide linkages in *Plasmodium falciparum* plasmepsin-i are essential elements for its processing activity and multi-milligram recombinant production yield. *PloS one*, *9*(2), p.e89424.
101. Siripurkpong, P., Yuvaniyama, J., Wilairat, P. and Goldberg, D.E., 2002. Active site contribution to specificity of the aspartic proteases plasmepsins I and II. *Journal of Biological Chemistry*, *277*(43), pp.41009-41013.

102. Tyas, L., Gluzman, I., Moon, R.P., Rupp, K., Westling, J., Ridley, R.G., Kay, J., Goldberg, D.E. and Berry, C., 1999. Naturally-occurring and recombinant forms of the aspartic proteinases plasmepsins I and II from the human malaria parasite *Plasmodium falciparum*. *FEBS letters*, *454*(3), pp.210-214.

103. Liu, P., Marzahn, M.R., Robbins, A.H., Gutiérrez-de-Terán, H., Rodríguez, D., McClung, S.H., Stevens Jr, S.M., Yowell, C.A., Dame, J.B., McKenna, R. and Dunn, B.M., 2009. Recombinant plasmepsin 1 from the human malaria parasite *Plasmodium falciparum*: enzymatic characterization, active site inhibitor design, and structural analysis. *Biochemistry*, *48*(19), pp.4086-4099.

104. Moon, R.P., Tyas, L., Certa, U., Rupp, K., Bur, D., Jacquet, C., Matile, H., Loetscher, H., Grueninger-Leitch, F., Kay, J. and Dunn, B.M., 1997. Expression and characterisation of plasmepsin I from *Plasmodium falciparum*. *European journal of biochemistry*, *244*(2), pp.552-560.

105. Dunn, B.M., Jimenez, M., Parten, B.F., Valler, M.J., Rolph, C.E. and Kay, J., 1986. A systematic series of synthetic chromophoric substrates for aspartic proteinases. *Biochemical Journal*, *237*(3), pp.899-906.

106. Rosenthal, P.J. and Nelson, R.G., 1992. Isolation and characterization of a cysteine proteinase gene of *Plasmodium falciparum*. *Molecular and biochemical parasitology*, *51*(1), pp.143-152.

107. Rosenthal, P.J., McKerrow, J.H., Rasnick, D. and Leech, J.H., 1989. *Plasmodium falciparum*: inhibitors of lysosomal cysteine proteinases inhibit a trophozoite proteinase and block parasite development. *Molecular and biochemical parasitology*, *35*(2), pp.177-183.

108. Salas, F., Fichmann, J., Lee, G.K., Scott, M.D. and Rosenthal, P.J., 1995. Functional expression of falcipain, a *Plasmodium falciparum* cysteine proteinase, supports its role as a malarial hemoglobinase. *Infection and Immunity*, *63*(6), pp.2120-2125.

109. Vander Jagt, D.L., Baack, B.R. and Hunsaker, L.A., 1984. Purification and characterization of an aminopeptidase from *Plasmodium falciparum*. *Molecular and biochemical parasitology*, *10*(1), pp.45-54.

110. Teuscher, F., Lowther, J., Skinner-Adams, T.S., Spielmann, T., Dixon, M.W., Stack, C.M., Donnelly, S., Mucha, A., Kafarski, P., Vassiliou, S. and Gardiner, D.L., 2007. The M18 aspartyl aminopeptidase of the human malaria parasite *Plasmodium falciparum*. *Journal of Biological Chemistry*, *282*(42), pp.30817-30826.

111. Lancisi, G.M., Cramer, J.A. and Perachon, P., 1717. *Jo. Mariae Lancisii ab intimo Cubiculo et archiatro sanctissimi patris Clementis XI. PM De noxiis paludum effluviis eorumque remediis libri duo*. sumptibus Cramer et Perachon.

112. Laveran, C.L.A., Kean, B.H., Mott, K.E. and Russell, A.J., 1982. A newly discovered parasite in the blood of patients suffering from malaria. Parasitic etiology of attacks of malaria. *Reviews of infectious diseases*, pp.908-911.

113. Ross, R., 1897. On some peculiar pigmented cells found in two mosquitos fed on malarial blood. *British medical journal*, *2*(1929), p.1786.

114. Brown, W.H., 1911. Malarial pigment (so-called melanin): its nature and mode of production. *The Journal of experimental medicine*, *13*(2), p.290.

115. Fitch, C.D. and Kanjananggulpan, P., 1987. The state of ferriprotoporphyrin IX in malaria pigment. *Journal of Biological Chemistry*, *262*(32), pp.15552-15555.

116. Lemberg, R. and Legge, J.W., 1949. Hematin compounds and bile pigments.

117. Sullivan, D.J., 2002. Theories on malarial pigment formation and quinoline action. *International journal for parasitology*, *32*(13), pp.1645-1653.

118. Slater, A.F., Swiggard, W.J., Orton, B.R., Flitter, W.D., Goldberg, D.E., Cerami, A. and Henderson, G.B., 1991. An iron-carboxylate bond links the heme units of malaria pigment. *Proceedings of the National Academy of Sciences*, *88*(2), pp.325-329.

119. Ghosh, B.N. and Nath, M.C., 1934. The Chemical Composition of Malaria Pigment (Haemozoin). *Records of the Malaria Survey of India*, *4*(3).

120. Brémard, C., Girerd, J.J., Kowalewski, P., Merlin, J.C. and Moreau, S., 1993. Spectroscopic investigations of malaria pigment. *Applied spectroscopy*, *47*(11), pp.1837-1842.

121. Pagola, S., Stephens, P.W., Bohle, D.S., Kosar, A.D. and Madsen, S.K., 2000. The structure of malaria pigment β-haematin. *Nature*, *404*(6775), p.307.

122. Bohle, D.S., Kosar, A.D. and Stephens, P.W., 2002. Phase homogeneity and crystal morphology of the malaria pigment β-hematin. *Acta Crystallographica Section D: Biological Crystallography*, *58*(10), pp.1752-1756.

123. Egan, T.J., 2008. Haemozoin formation. *Molecular and biochemical parasitology*, *157*(2), pp.127-136.

124. de Villiers, K.A., Marques, H.M. and Egan, T.J., 2008. The crystal structure of halofantrine–ferriprotoporphyrin IX and the mechanism of action of arylmethanol antimalarials. *Journal of inorganic biochemistry*, *102*(8), pp.1660-1667.

125. Buisine, E., de Villiers, K., Egan, T.J. and Biot, C., 2006. Solvent-induced effects: self-association of positively charged π systems. *Journal of the American Chemical Society*, *128*(37), pp.12122-12128.

126. Solomonov, I., Osipova, M., Feldman, Y., Baehtz, C., Kjaer, K., Robinson, I.K., Webster, G.T., McNaughton, D., Wood, B.R., Weissbuch, I. and Leiserowitz, L., 2007. Crystal nucleation, growth, and morphology of the synthetic malaria pigment β-hematin and the effect thereon by quinoline additives: the malaria pigment as a target of various antimalarial drugs. *Journal of the American Chemical Society*, *129*(9), pp.2615-2627.

127. Yayon, A., Cabantchik, Z.I. and Ginsburg, H., 1984. Identification of the acidic compartment of *Plasmodium falciparum*-infected human erythrocytes as the target of the antimalarial drug chloroquine. *The EMBO journal*, *3*(11), pp.2695-2700.

128. Krogstad, D.J., Schlesinger, P.H. and Gluzman, I.Y., 1985. Antimalarials increase vesicle pH in *Plasmodium falciparum*. *The Journal of Cell Biology*, *101*(6), pp.2302-2309.

129. Koenig, D.F., 1965. The structure of α-chlorohemin. *Acta crystallographica*, *18*(4), pp.663-673.

130. Bohle, D.S., Dinnebier, R.E., Madsen, S.K. and Stephens, P.W., 1997. Characterization of the products of the heme detoxification pathway in malarial late trophozoites by X-ray diffraction. *Journal of Biological Chemistry*, *272*(2), pp.713-716.

131. Bohle, D.S. and Helms, J.B., 1993. Synthesis of β-hematin by dehydrohalogenation of hemin. *Biochemical and biophysical research communications*, *193*(2), pp.504-508.

132. Fitch, C.D., 1983, January. Mode of action of antimalarial drugs. In *Ciba Found Symp* (Vol. 94, pp. 222-232).

133. Egan, T.J., Chen, J.Y., de Villiers, K.A., Mabotha, T.E., Naidoo, K.J., Ncokazi, K.K., Langford, S.J., McNaughton, D., Pandiancherri, S. and Wood, B.R., 2006. Haemozoin (β-haematin) biomineralization occurs by self-assembly near the lipid/water interface. *FEBS letters*, *580*(21), pp.5105-5110.

134. Hempelmann, E., 2007. Hemozoin biocrystallization in *Plasmodium falciparum* and the antimalarial activity of crystallization inhibitors. *Parasitology research*, *100*(4), pp.671-676.

135. Slater, A.F.G. and Cerami, A., 1992. Inhibition by chloroquine of a novel haem polymerase enzyme activity in malaria trophozoites. *Nature*, *355*(6356), p.167.

136. Sullivan, D.J., Gluzman, I.Y. and Goldberg, D.E., 1996. *Plasmodium* hemozoin formation mediated by histidine-rich proteins. *Science*, *271*(5246), pp.219-222.

137. Jani, D., Nagarkatti, R., Beatty, W., Angel, R., Slebodnick, C., Andersen, J., Kumar, S. and Rathore, D., 2008. HDP—a novel heme detoxification protein from the malaria parasite. *PLoS pathogens*, *4*(4), p.e1000053.

138. Pal, P., Balaban, A.E., Diamond, M.S., Sinnis, P., Klein, R.S. and Goldberg, D.E., 2017. *Plasmodium falciparum* histidine-rich protein II causes vascular leakage and exacerbates experimental cerebral malaria in mice. *PloS one*, *12*(5), p.e0177142.

139. Pisciotta, J.M., Coppens, I., Tripathi, A.K., Scholl, P.F., Shuman, J., Bajad, S., Shulaev, V. and Sullivan, D.J., 2007. The role of neutral lipid nanospheres in *Plasmodium falciparum* haem crystallization. *Biochemical Journal*, *402*(1), pp.197-204.

140. Jani, D., Nagarkatti, R., Beatty, W., Angel, R., Slebodnick, C., Andersen, J., Kumar, S. and Rathore, D., 2008. HDP—a novel heme detoxification protein from the malaria parasite. *PLoS pathogens*, *4*(4).

141. Chugh, M., Sundararaman, V., Kumar, S., Reddy, V.S., Siddiqui, W.A., Stuart, K.D. and Malhotra, P., 2013. Protein complex directs hemoglobin-to-hemozoin formation in *Plasmodium falciparum*. *Proceedings of the National Academy of Sciences*, *110*(14), pp.5392-5397.

142. Kapishnikov, S., Grolimund, D., Schneider, G., Pereiro, E., McNally, J.G., Als-Nielsen, J. and Leiserowitz, L., 2017. Unraveling heme detoxification in the malaria parasite by in situ correlative X-ray fluorescence microscopy and soft X-ray tomography. *Scientific reports*, *7*(1), p.7610.

143. Egan, T.J., Ross, D.C. and Adams, P.A., 1994. Quinoline anti-malarial drugs inhibit spontaneous formation of β-haematin (malaria pigment). *FEBS letters*, *352*(1), pp.54-57.

144. Dorn, A., Vippagunta, S.R., Matile, H., Jaquet, C., Vennerstrom, J.L. and Ridley, R.G., 1998. An assessment of drug-haematin binding as a mechanism for inhibition of haematin polymerisation by quinoline antimalarials. *Biochemical pharmacology*, *55*(6), pp.727-736.

145. Dorn, A., Stoffel, R., Matile, H., Bubendorf, A. and Ridley, R.G., 1995. Malarial haemozoin/β-haematin supports haem polymerization in the absence of protein. *Nature*, *374*(6519), p.269.

146. Bendrat, K., Berger, B.J. and Cerami, A., 1995. Haem polymerization in malaria. *Nature*, *378*(6553), p.138.

147. Wellems, T.E. and Howard, R.J., 1986. Homologous genes encode two distinct histidine-rich proteins in a cloned isolate of *Plasmodium falciparum*. *Proceedings of the National Academy of Sciences*, *83*(16), pp.6065-6069.

148. Panton, L.J., McPhie, P., Maloy, W.L., Wellems, T.E., Taylor, D.W. and Howard, R.J., 1989. Purification and partial characterization of an unusual protein of *Plasmodium falciparum*: histidine-rich protein II. *Molecular and biochemical parasitology*, *35*(2), pp.149-160.

149. Papalexis, V., Siomos, M.A., Campanale, N., Guo, X.G., Kocak, G., Foley, M. and Tilley, L., 2001. Histidine-rich protein 2 of the malaria parasite, *Plasmodium falciparum*, is involved in detoxification of the by-products of haemoglobin degradation. *Molecular and biochemical parasitology*, *115*(1), pp.77-86.

150. Akompong, T., Kadekoppala, M., Harrison, T., Oksman, A., Goldberg, D.E., Fujioka, H., Samuel, B.U., Sullivan, D. and Haldar, K., 2002. Trans expression of a *Plasmodium falciparum* histidine-rich protein II (HRPII) reveals sorting of soluble proteins in the periphery of the host erythrocyte and disrupts transport to the malarial food vacuole. *Journal of Biological Chemistry*, *277*(32), pp.28923-28933.

151. Pandey, A.V., Babbarwal, V.K., Okoyeh, J.N., Joshi, R.M., Puri, S.K., Singh, R.L. and Chauhan, V.S., 2003. Hemozoin formation in malaria: a two-step process involving histidine-rich proteins and lipids. *Biochemical and biophysical research communications*, *308*(4), pp.736-743.

152. Fitch, C.D., Cai, G.Z., Chen, Y.F. and Shoemaker, J.D., 1999. Involvement of lipids in ferriprotoporphyrin IX polymerization in malaria. *Biochimica et Biophysica Acta (BBA)-Molecular Basis of Disease*, *1454*(1), pp.31-37.

153. Ambele, M.A. and Egan, T.J., 2012. Neutral lipids associated with haemozoin mediate efficient and rapid β-haematin formation at physiological pH, temperature and ionic composition. *Malaria journal*, *11*(1), p.337.

154. Coppens, I. and Vielemeyer, O., 2005. Insights into unique physiological features of neutral lipids in Apicomplexa: from storage to potential mediation in parasite metabolic activities. *International journal for parasitology*, *35*(6), pp.597-615.

155. Nawabi, P., Lykidis, A., Ji, D. and Haldar, K., 2003. Neutral-lipid analysis reveals elevation of acylglycerols and lack of cholesterol esters in *Plasmodium falciparum*-infected erythrocytes. *Eukaryotic cell*, *2*(5), pp.1128-1131.

156. Vial, H.J. and Ancelin, M.L., 1992. Malarial lipids. *In Intracellular Parasites*. Springer, Boston, MA, pp. 259-306.

157. Fitch, C.D., Cai, G.Z. and Shoemaker, J.D., 2000. A role for linoleic acid in erythrocytes infected with *Plasmodium berghei*. *Biochimica et Biophysica Acta (BBA)-Molecular Basis of Disease*, *1535*(1), pp.45-49.

158. Hoang, A.N., Sandlin, R.D., Omar, A., Egan, T.J. and Wright, D.W., 2010. The neutral lipid composition present in the digestive vacuole of *Plasmodium falciparum* concentrates heme and mediates β-hematin formation with an unusually low activation energy. *Biochemistry*, *49*(47), pp.10107-10116.

159. Jackson, K.E., Klonis, N., Ferguson, D.J., Adisa, A., Dogovski, C. and Tilley, L., 2004. Food vacuole-associated lipid bodies and heterogeneous lipid environments in the malaria parasite, *Plasmodium falciparum*. *Molecular microbiology*, *54*(1), pp.109-122.

160. Stiebler, R., Majerowicz, D., Knudsen, J., Gondim, K.C., Wright, D.W., Egan, T.J. and Oliveira, M.F., 2014. Unsaturated glycerophospholipids mediate heme crystallization: biological implications for hemozoin formation in the kissing bug Rhodnius prolixus. *PloS one*, *9*(2), p.e88976.

161. Kapishnikov, S., Weiner, A., Shimoni, E., Guttmann, P., Schneider, G., Dahan-Pasternak, N., Dzikowski, R., Leiserowitz, L. and Elbaum, M., 2012. Oriented nucleation of hemozoin at the digestive vacuole membrane in Plasmodium falciparum. *Proceedings of the National Academy of Sciences*, *109*(28), pp.11188-11193.

162. Oliveira, M.F., Kycia, S.W., Gomez, A., Kosar, A.J., Bohle, D.S., Hempelmann, E., Menezes, D., Vannier-Santos, M.A., Oliveira, P.L. and Ferreira, S.T., 2005. Structural and morphological characterization of hemozoin produced by Schistosoma mansoni and Rhodnius prolixus. *Febs letters*, *579*(27), pp.6010-6016.

163. Kapishnikov, S., Berthing, T., Hviid, L., Dierolf, M., Menzel, A., Pfeiffer, F., Als-Nielsen, J. and Leiserowitz, L., 2012. Aligned hemozoin crystals in curved clusters in malarial red blood cells revealed by nanoprobe X-ray Fe fluorescence and diffraction. *Proceedings of the National Academy of Sciences*, *109*(28), pp.11184-11187.

164. Pukrittayakamee, S., Supanaranond, W., Looareesuwan, S., Vanijanonta, S. and White, N.J., 1994. Quinine in severe falciparum malaria: evidence of declining efficacy in Thailand. *Transactions of the Royal Society of Tropical Medicine and Hygiene*, *88*(3), pp.324-327.

165. Jelinek, T., Schelbert, P., Loescher, T. and Eichenlaub, D., 1995. Quinine resistant *falciparum* malaria acquired in east Africa. *Tropical medicine and parasitology: official organ of Deutsche Tropenmedizinische Gesellschaft and of Deutsche Gesellschaft fur Technische Zusammenarbeit (GTZ)*, *46*(1), pp.38-40.

166. Segurado, A.A.C., Santi, S.M.D. and Shiroma, M., 1997. In vivo and in vitro *Plasmodium falciparum* resistance to chloroquine, amodiaquine and quinine in the Brazilian Amazon. *Revista do Instituto de Medicina Tropical de São Paulo*, *39*, pp.85-90.

167. Rathore, D., McCutchan, T.F., Sullivan, M. and Kumar, S., 2005. Antimalarial drugs: current status and new developments. *Expert Opinion on Investigational Drugs*, *14*(7), pp.871-883.

168. Loeb, R.F., 1946. Activity of a new antimalarial agent, pentaquine (Sn 13,276): Statement approved by the board for coordination of malarial studies. *Journal of the American Medical Association*, *132*(6), pp.321-323.

169. Krafts, K., Hempelmann, E. and Skórska-Stania, A., 2012. From methylene blue to chloroquine: a brief review of the development of an antimalarial therapy. *Parasitology research*, *111*(1), pp.1-6.

170. Coatney, G.R., 1963. Pitfalls in a discovery: the chronicle of chloroquine. *The American journal of tropical medicine and hygiene*, *12*(2), pp.121-128.

171. Jensen, M. and Mehlhorn, H., 2009. Seventy-five years of Resochin® in the fight against malaria. *Parasitology research*, *105*(3), p.609.

172. Fidock, D.A., Nomura, T., Talley, A.K., Cooper, R.A., Dzekunov, S.M., Ferdig, M.T., Ursos, L.M., Naudé, B., Deitsch, K.W., Su, X.Z. and Wootton, J.C., 2000. Mutations in the *P. falciparum* digestive vacuole transmembrane protein *Pf*CRT and evidence for their role in chloroquine resistance. *Molecular cell*, *6*(4), pp.861-871.

173. Smrkovski, L.L., Buck, R.L., Alcantara, A.K., Rodriguez, C.S. and Uylangco, C.V., 1985. Studies of resistance to chloroquine, quinine, amodiaquine and mefloquine among Philippine strains of *Plasmodium falciparum*. *Transactions of the Royal Society of Tropical Medicine and Hygiene*, *79*(1), pp.37-41.

174. Smrkovski, L., Buck, R., Alcantara, A., Rodriguez, C. and Uylanco, C., 1982. In vitro mefloquine resistant *Plasmodium falciparum* from the Philippines. *In vitro mefloquine resistant Plasmodium falciparum from the Philippines.*, *2*.

175. O'Neill, P.M., Mukhtar, A., Stocks, P.A., Randle, L.E., Hindley, S., Ward, S.A., Storr, R.C., Bickley, J.F., O'Neil, I.A., Maggs, J.L. and Hughes, R.H., 2003. Isoquine and related amodiaquine analogues: a new generation of improved 4-aminoquinoline antimalarials. *Journal of medicinal chemistry*, *46*(23), pp.4933-4945.

176. Atteke, C., Ndong, J.M.M., Aubouy, A., Maciejewski, L., Brocard, J., Lébibi, J. and Deloron, P., 2003. In vitro susceptibility to a new antimalarial organometallic analogue, ferroquine, of *Plasmodium falciparum* isolates from the Haut-Ogooue region of Gabon. *Journal of Antimicrobial Chemotherapy*, *51*(4), pp.1021-1024.

177. Yang, H., Yang, Y., Yang, P., Li, X., Gao, B., Zhang, Z., Yang, Z. and Cui, L., 2008. Monitoring *Plasmodium falciparum* chloroquine resistance in Yunnan province, China, 1981–2006. *Acta tropica*, *108*(1), pp.44-49.

178. Yang, Z., Zhang, Z., Sun, X., Wan, W., Cui, L., Zhang, X., Zhong, D., Yan, G. and Cui, L., 2007. Molecular analysis of chloroquine resistance in *Plasmodium falciparum* in Yunnan Province, China. *Tropical Medicine & International Health*, *12*(9), pp.1051-1060.

179. Lan, C.X., Lin, X., Huang, Z.S., Chen, Y.S. and Guo, R.N., 1989. In vivo sensitivity of *Plasmodium falciparum* to piperaquine phosphate assayed in Linshui and Baisha counties, Hainan Province. *Zhongguo ji sheng chong xue yu ji sheng chong bing za zhi= Chinese journal of parasitology & parasitic diseases*, *7*(3), pp.163-165.

180. Huang, F., Tang, L., Yang, H., Zhou, S., Liu, H., Li, J. and Guo, S., 2012. Molecular epidemiology of drug resistance markers of *Plasmodium falciparum* in Yunnan Province, China. *Malaria journal*, *11*(1), p.243.

181. Davis, T.M., Hung, T.Y., Sim, K., Karunajeewa, H.A. and Ilett, K.F., 2005. Piperaquine. *Drugs*, *65*(1), pp.75-87.

182. Croft, A.M., 2007. A lesson learnt: the rise and fall of Lariam and Halfan. *Journal of the Royal Society of Medicine*, *100*(4), pp.170-174.

183. Pradines, B., Fusai, T., Daries, W., Laloge, V., Rogier, C., Millet, P., Panconi, E., Kombila, M. and Parzy, D., 2001. Ferrocene-chloroquine analogues as antimalarial agents: in vitro activity of ferrochloroquine against 103 Gabonese isolates of *Plasmodium falciparum*. *Journal of Antimicrobial Chemotherapy*, *48*(2), pp.179-184.

184. Dlugónska, H., 2015. The Nobel Prize 2015 in physiology or medicine for highly effective antiparasitic drugs. *Annals of parasitology*, *61*(4).

185. Zishiri, V.K., Hunter, R., Smith, P.J., Taylor, D., Summers, R., Kirk, K., Martin, R.E. and Egan, T.J., 2011. A series of structurally simple chloroquine chemosensitizing dibemethin derivatives that inhibit chloroquine transport by PfCRT. *European journal of medicinal chemistry*, *46*(5), pp.1729-1742.

186. O'neill, P.M., Barton, V.E. and Ward, S.A., 2010. The molecular mechanism of action of artemisinin—the debate continues. *Molecules*, *15*(3), pp.1705-1721.

187. Wang, J., Zhang, C.J., Chia, W.N., Loh, C.C., Li, Z., Lee, Y.M., He, Y., Yuan, L.X., Lim, T.K., Liu, M. and Liew, C.X., 2015. Haem-activated promiscuous targeting of artemisinin in *Plasmodium falciparum*. *Nature communications*, *6*, p.10111.

188. Tilley, L., Straimer, J., Gnädig, N.F., Ralph, S.A. and Fidock, D.A., 2016. Artemisinin action and resistance in *Plasmodium falciparum*. *Trends in parasitology*, *32*(9), pp.682-696.

189. Walliker, D., Hunt, P. and Babiker, H., 2005. Fitness of drug-resistant malaria parasites. *Acta tropica*, *94*(3), pp.251-259.

190. Shandilya, A., Chacko, S., Jayaram, B. and Ghosh, I., 2013. A plausible mechanism for the antimalarial activity of artemisinin: a computational approach. *Scientific reports*, *3*, p.2513.

191. Mok, S., Ashley, E.A., Ferreira, P.E., Zhu, L., Lin, Z., Yeo, T., Chotivanich, K., Imwong, M., Pukrittayakamee, S., Dhorda, M. and Nguon, C., 2015. Population transcriptomics of human malaria parasites reveals the mechanism of artemisinin resistance. *Science*, *347*(6220), pp.431-435.

192. Mbengue, A., Bhattacharjee, S., Pandharkar, T., Liu, H., Estiu, G., Stahelin, R.V., Rizk, S.S., Njimoh, D.L., Ryan, Y., Chotivanich, K. and Nguon, C., 2015. A molecular mechanism of artemisinin resistance in *Plasmodium falciparum* malaria. *Nature*, *520*(7549), p.683.

193. Amato, R., Pearson, R.D., Almagro-Garcia, J., Amaratunga, C., Lim, P., Suon, S., Sreng, S., Drury, E., Stalker, J., Miotto, O. and Fairhurst, R.M., 2018. Origins of the current outbreak of multidrug-resistant malaria in southeast Asia: a retrospective genetic study. *The Lancet Infectious Diseases*, *18*(3), pp.337-345.

194. Eastman, R.T. and Fidock, D.A., 2009. Artemisinin-based combination therapies: a vital tool in efforts to eliminate malaria. *Nature Reviews Microbiology*, *7*(12), p.864.

195. Harrison, T.S., Griffin, G.E. and Levitz, S.M., 2000. Conditional lethality of the diprotic weak bases chloroquine and quinacrine against Cryptococcus neoformans. *The journal of infectious diseases*, *182*(1), pp.283-289.

196. Yayon, A., Cabantchik, Z.I. and Ginsburg, H., 1985. Susceptibility of human malaria parasites to chloroquine is pH dependent. *Proceedings of the National Academy of Sciences*, *82*(9), pp.2784-2788.

197. Saliba, K.J., Folb, P.I. and Smith, P.J., 1998. Role for the *Plasmodium falciparum* digestive vacuole in chloroquine resistance. *Biochemical pharmacology*, *56*(3), pp.313-320.

198. Fitch, C.D., 2004. Ferriprotoporphyrin IX, phospholipids, and the antimalarial actions of quinoline drugs. *Life sciences*, *74*(16), pp.1957-1972.

199. Bray, P.G., Martin, R.E., Tilley, L., Ward, S.A., Kirk, K. and Fidock, D.A., 2005. Defining the role of *Pf*CRT in *Plasmodium falciparum* chloroquine resistance. *Molecular microbiology*, *56*(2), pp.323-333.

200. Packard, R.M., 2014. The origins of antimalarial-drug resistance. *New England Journal of Medicine*, *371*(5), pp.397-399.

201. Trape, J.F., Pison, G., Preziosi, M.P., Enel, C., du Loû, A.D., Delaunay, V., Samb, B., Lagarde, E., Molez, J.F. and Simondon, F., 1998. Impact of chloroquine resistance on malaria mortality. *Comptes Rendus de l'Académie des Sciences-Series III-Sciences de la Vie*, *321*(8), pp.689-697.

202. Okie, S., 2008. A new attack on malaria. *New England Journal of Medicine*, *358*(23), pp.2425-2428.

203. Fitch, C.D., 1969. Chloroquine resistance in malaria: a deficiency of chloroquine binding. *Proceedings of the National Academy of Sciences*, *64*(4), pp.1181-1187.

204. Krogstad, D.J. and Schlesinger, P.H., 1987. The basis of antimalarial action: non-weak base effects of chloroquine on acid vesicle pH. *The American journal of tropical medicine and hygiene*, *36*(2), pp.213-220.

205. Gligorijevic, B., McAllister, R., Urbach, J.S. and Roepe, P.D., 2006. Spinning disk confocal microscopy of live, intraerythrocytic malarial parasites. 1. Quantification of hemozoin development for drug sensitive versus resistant malaria. *Biochemistry*, *45*(41), pp.12400-12410.

206. Ginsburg, H. and Krugliak, M., 1992. Quinoline-containing antimalarials—mode of action, drug resistance and its reversal an update with unresolved puzzles. *Biochemical pharmacology*, *43*(1), pp.63-70.

207. Martiney, J.A., Cerami, A. and Slater, A.F., 1995. Verapamil reversal of chloroquine resistance in the malaria parasite *Plasmodium falciparum* is specific for resistant parasites and independent of the weak base effect. *Journal of Biological Chemistry*, *270*(38), pp.22393-22398.

208. Bray, P.G., Mungthin, M., Ridley, R.G. and Ward, S.A., 1998. Access to hematin: the basis of chloroquine resistance. *Molecular Pharmacology*, *54*(1), pp.170-179.

209. Cooper, R.A., Hartwig, C.L. and Ferdig, M.T., 2005. pfcrt is more than the *Plasmodium falciparum* chloroquine resistance gene: a functional and evolutionary perspective. *Acta tropica*, *94*(3), pp.170-180.

210. Summers, R.L., Nash, M.N. and Martin, R.E., 2012. Know your enemy: understanding the role of *Pf*CRT in drug resistance could lead to new antimalarial tactics. *Cellular and Molecular Life Sciences*, *69*(12), pp.1967-1995.

211. Martin, R.E. and Kirk, K., 2004. The malaria parasite's chloroquine resistance transporter is a member of the drug/metabolite transporter superfamily. *Molecular biology and evolution*, *21*(10), pp.1938-1949.

212. Ginsburg, H. and Stein, W.D., 1991. Kinetic modelling of chloroquine uptake by malaria-infected erythrocytes: assessment of the factors that may determine drug resistance. *Biochemical pharmacology*, *41*(10), pp.1463-1470.

213. Bennett, T.N., Kosar, A.D., Ursos, L.M., Dzekunov, S., Sidhu, A.B.S., Fidock, D.A. and Roepe, P.D., 2004. Drug resistance-associated *Pf*CRT mutations confer decreased *Plasmodium falciparum* digestive vacuolar pH. *Molecular and biochemical parasitology*, *133*(1), pp.99-114.

214. Dzekunov, S.M., Ursos, L.M.B. and Roepe, P.D., 2000. Digestive vacuolar pH of intact intraerythrocytic *P. falciparum* either sensitive or resistant to chloroquine. *Molecular and biochemical parasitology*, *110*(1), pp.107-124.

215. Ursos, L.M.B., Dzekunov, S.M. and Roepe, P.D., 2000. The effects of chloroquine and verapamil on digestive vacuolar pH of *P. falciparum* either sensitive or resistant to chloroquine. *Molecular and biochemical parasitology*, *110*(1), pp.125-134.

216. Wissing, F., Sanchez, C.P., Rohrbach, P., Ricken, S. and Lanzer, M., 2002. Illumination of the Malaria Parasite *Plasmodium falciparum* Alters Intracellular pH Implications for live cell imaging. *Journal of biological chemistry*, *277*(40), pp.37747-37755.

217. Krogstad, D.J., Gluzman, I.Y., Herwaldt, B.L., Schlesinger, P.H. and Wellems, T.E., 1992. Energy dependence of chloroquine accumulation and chloroquine efflux in *Plasmodium falciparum*. *Biochemical pharmacology*, *43*(1), pp.57-62.

218. Pulcini, S., Staines, H.M., Lee, A.H., Shafik, S.H., Bouyer, G., Moore, C.M., Daley, D.A., Hoke, M.J., Altenhofen, L.M., Painter, H.J. and Mu, J., 2015. Mutations in the *Plasmodium falciparum* chloroquine resistance transporter, *Pf*CRT, enlarge the parasite's food vacuole and alter drug sensitivities. *Scientific reports*, *5*, p.14552.

219. Cooper, R.A., Hartwig, C.L. and Ferdig, M.T., 2005. pfcrt is more than the *Plasmodium falciparum* chloroquine resistance gene: a functional and evolutionary perspective. *Acta tropica*, *94*(3), pp.170-180.

220. Guan, J., Kyle, D.E., Gerena, L., Zhang, Q., Milhous, W.K. and Lin, A.J., 2002. Design, Synthesis, and Evaluation of New Chemosensitizers in Multi-Drug-Resistant *Plasmodium falciparum*. *Journal of medicinal chemistry*, *45*(13), pp.2741-2748.

221. Juge, N., Moriyama, S., Miyaji, T., Kawakami, M., Iwai, H., Fukui, T., Nelson, N., Omote, H. and Moriyama, Y., 2015. *Plasmodium falciparum* chloroquine resistance transporter is a H+-coupled poly-specific nutrient and drug exporter. *Proceedings of the National Academy of Sciences*, *112*(11), pp.3356-3361.

222. Johnson, D.J., Fidock, D.A., Mungthin, M., Lakshmanan, V., Sidhu, A.B.S., Bray, P.G. and Ward, S.A., 2004. Evidence for a central role for *Pf*CRT in conferring *Plasmodium falciparum* resistance to diverse antimalarial agents. *Molecular cell*, *15*(6), pp.867-877.

223. Martin, R.E., Marchetti, R.V., Cowan, A.I., Howitt, S.M., Bröer, S. and Kirk, K., 2009. Chloroquine transport via the malaria parasite's chloroquine resistance transporter. *science*, *325*(5948), pp.1680-1682.

224. Bitonti, A.J., Sjoerdsma, A., McCann, P.P., Kyle, D.E., Oduola, A.M., Rossan, R.N., Milhous, W.K. and Davidson, D.E., 1988. Reversal of chloroquine resistance in malaria parasite *Plasmodium falciparum* by desipramine. *Science*, *242*(4883), pp.1301-1303.

225. Tilley, L., Davis, T.M. and Bray, P.G., 2006. Prospects for the treatment of drug-resistant malaria parasites.

226. van Schalkwyk, D.A. and Egan, T.J., 2006. Quinoline-resistance reversing agents for the malaria parasite *Plasmodium falciparum*. *Drug resistance updates*, *9*(4-5), pp.211-226.

227. Plouffe, D., Brinker, A., McNamara, C., Henson, K., Kato, N., Kuhen, K., Nagle, A., Adrián, F., Matzen, J.T., Anderson, P. and Nam, T.G., 2008. In silico activity profiling reveals the mechanism of action of antimalarials discovered in a high-throughput screen. *Proceedings of the National Academy of Sciences*, *105*(26), pp.9059-9064.

228. Gamo, F.J., Sanz, L.M., Vidal, J., De Cozar, C., Alvarez, E., Lavandera, J.L., Vanderwall, D.E., Green, D.V., Kumar, V., Hasan, S. and Brown, J.R., 2010. Thousands of chemical starting points for antimalarial lead identification. *Nature*, *465*(7296), p.305.

229. Mayr, L.M. and Fuerst, P., 2008. The future of high-throughput screening. *Journal of biomolecular screening*, *13*(6), pp.443-448.

230. Fox, S., Farr-Jones, S., Sopchak, L., Boggs, A., Nicely, H.W., Khoury, R. and Biros, M., 2006. High-throughput screening: update on practices and success. *Journal of biomolecular screening*, *11*(7), pp.864-869.

231. Fox, S., Farr-Jones, S., Sopchak, L., Boggs, A. and Comley, J., 2004. High-throughput screening: searching for higher productivity. *Journal of biomolecular screening*, *9*(4), pp.354-358.

232. Pereira, D.A. and Williams, J.A., 2007. Origin and evolution of high throughput screening. *British journal of pharmacology*, *152*(1), pp.53-61.

233. Ridley, R.G., Dorn, A., Vippagunta, S.R. and Vennerstrom, J.L., 1997. Haematin (haem) polymerization and its inhibition by quinoline antimalarials. *Annals of Tropical Medicine & Parasitology*, *91*(5), pp.559-566.

234. Kurosawa, Y., Dorn, A., Kitsuji-Shirane, M., Shimada, H., Satoh, T., Matile, H., Hofheinz, W., Masciadri, R., Kansy, M. and Ridley, R.G., 2000. Hematin polymerization assay as a high-throughput screen for identification of new antimalarial pharmacophores. *Antimicrobial agents and chemotherapy*, *44*(10), pp.2638-2644.

235. Rush, M.A., Baniecki, M.L., Mazitschek, R., Cortese, J.F., Wiegand, R., Clardy, J. and Wirth, D.F., 2009. Colorimetric high-throughput screen for detection of heme crystallization inhibitors. *Antimicrobial agents and chemotherapy*, *53*(6), pp.2564-2568.

236. Huy, N.T., Uyen, D.T., Maeda, A., Oida, T., Harada, S. and Kamei, K., 2007. Simple colorimetric inhibition assay of heme crystallization for high-throughput screening of antimalarial compounds. *Antimicrobial agents and chemotherapy*, *51*(1), pp.350-353.

237. Guiguemde, W.A., Shelat, A.A., Bouck, D., Duffy, S., Crowther, G.J., Davis, P.H., Smithson, D.C., Connelly, M., Clark, J., Zhu, F. and Jiménez-Díaz, M.B., 2010. Chemical genetics of *Plasmodium falciparum*. *Nature*, *465*(7296), p.311.

238. Sandlin, R.D., Carter, M.D., Lee, P.J., Auschwitz, J.M., Leed, S.E., Johnson, J.D. and Wright, D.W., 2011. Use of the NP-40 detergent-mediated assay in discovery of inhibitors of β-hematin crystallization. *Antimicrobial agents and chemotherapy*, *55*(7), pp.3363-3369.

239. Carter, M.D., Phelan, V.V., Sandlin, R.D., Bachmann, B.O. and Wright, D.W., 2010. Lipophilic mediated assays for β-hematin inhibitors. *Combinatorial chemistry & high throughput screening*, *13*(3), pp.285-292.

240. Johnson, J.D., Dennull, R.A., Gerena, L., Lopez-Sanchez, M., Roncal, N.E. and Waters, N.C., 2007. Assessment and continued validation of the malaria SYBR green I-based fluorescence assay for use in malaria drug screening. *Antimicrobial agents and chemotherapy*, *51*(6), pp.1926-1933.

241. Sandlin, R.D., Fong, K.Y., Wicht, K.J., Carrell, H.M., Egan, T.J. and Wright, D.W., 2014. Identification of β-hematin inhibitors in a high-throughput screening effort reveals scaffolds with in vitro antimalarial activity. *International Journal for Parasitology: Drugs and Drug Resistance*, *4*(3), pp.316-325.

242. Combrinck, J.M., Mabotha, T.E., Ncokazi, K.K., Ambele, M.A., Taylor, D., Smith, P.J., Hoppe, H.C. and Egan, T.J., 2012. Insights into the role of heme in the mechanism of action of antimalarials. *ACS chemical biology*, *8*(1), pp.133-137.

243. Peters, W., 1970. The chemotherapy of rodent malaria, X: Dynamics of drug resistance, part 2: Acquisition and loss of chloroquine resistance in *Plasmodium berghei* observed by continuous bioassay. *Annals of Tropical Medicine & Parasitology*, *64*(1), pp.25-40.

244. Loria, P., Miller, S., Foley, M. and Tilley, L., 1999. Inhibition of the peroxidative degradation of haem as the basis of action of chloroquine and other quinoline antimalarials. *Biochemical Journal*, *339*(2), pp.363-370.

245. Ginsburg, H., Famin, O., Zhang, J. and Krugliak, M., 1998. Inhibition of glutathione-dependent degradation of heme by chloroquine and amodiaquine as a

possible basis for their antimalarial mode of action. *Biochemical pharmacology*, *56*(10), pp.1305-1313.

246. Garavito, G., Monje, M.C., Maurel, S., Valentin, A., Nepveu, F. and Deharo, E., 2007. A non-radiolabeled heme–GSH interaction test for the screening of antimalarial compounds. *Experimental parasitology*, *116*(3), pp.311-313.

247. Parker, F.S. and Irvin, J.L., 1952. The interaction of chloroquine with the albumin of bovine plasma. *Journal of Biological Chemistry*, *199*(2), pp.889-895.

248. Cohen, S.N. and Yielding, K.L., 1965. Inhibition of DNA and RNA polymerase reactions by chloroquine. *Proceedings of the National Academy of Sciences of the United States of America*, *54*(2), p.521.

249. Marquez, V.E., Cranston, J.W., Ruddon, R.W. and Burckhalter, J.H., 1974. Binding to deoxyribonucleic acid and inhibition of ribonucleic acid polymerase by analogs of chloroquine. *Journal of medicinal chemistry*, *17*(8), pp.856-862.

250. Fitch, C.D., 1986. Antimalarial schizontocides: ferriprotoporphyrin IX interaction hypothesis. *Parasitology today*, *2*(12), pp.330-331.

251. Sullivan, D.J., Gluzman, I.Y., Russell, D.G. and Goldberg, D.E., 1996. On the molecular mechanism of chloroquine's antimalarial action. *Proceedings of the National Academy of Sciences*, *93*(21), pp.11865-11870.

252. Ziegler, J., Pasierb, L., Cole, K.A. and Wright, D.W., 2003. Metalloporphyrin probes for antimalarial drug action. *Journal of inorganic biochemistry*, *96*(4), pp.478-486.

253. Parapini, S., Basilico, N., Pasini, E., Egan, T.J., Olliaro, P., Taramelli, D. and Monti, D., 2000. Standardization of the physicochemical parameters to assess in vitro the β-hematin inhibitory activity of antimalarial drugs. *Experimental parasitology*, *96*(4), pp.249-256.

254. Baelmans, R., Deharo, E., Bourdy, G., Muñoz, V., Quenevo, C., Sauvain, M. and Ginsburg, H., 2000. A search for natural bioactive compounds in Bolivia through a multidisciplinary approach: Part IV. Is a new haem polymerisation inhibition test pertinent for the detection of antimalarial natural products?. *Journal of Ethnopharmacology*, *73*(1-2), pp.271-275.

255. Kalkanidis, M., Klonis, N., Tilley, L. and Deady, L.W., 2002. Novel phenothiazine antimalarials: synthesis, antimalarial activity, and inhibition of the formation of β-haematin. *Biochemical pharmacology*, *63*(5), pp.833-842.

256. Egan, T.J., 2003. Haemozoin (malaria pigment): a unique crystalline drug target. *Targets*, *2*(3), pp.115-124.

257. Egan, T.J., 2006. Interactions of quinoline antimalarials with hematin in solution. *Journal of inorganic biochemistry*, *100*(5-6), pp.916-926.

258. Egan, T.J., 2004. Haemozoin formation as a target for the rational design of new antimalarials. *Drug Design Reviews-Online*, *1*(1), pp.93-110.

259. Tekwani, B.L. and Walker, L.A., 2005. Targeting the hemozoin synthesis pathway for new antimalarial drug discovery: technologies for in vitro β-hematin formation assay. *Combinatorial chemistry & high throughput screening*, *8*(1), pp.63-79.

260. Vippagunta, S.R., Dorn, A., Matile, H., Bhattacharjee, A.K., Karle, J.M., Ellis, W.Y., Ridley, R.G. and Vennerstrom, J.L., 1999. Structural specificity of chloroquine−hematin binding related to inhibition of hematin polymerization and parasite growth. *Journal of medicinal chemistry*, *42*(22), pp.4630-4639.

261. Kaschula, C.H., Egan, T.J., Hunter, R., Basilico, N., Parapini, S., Taramelli, D., Pasini, E. and Monti, D., 2002. Structure−activity relationships in 4-aminoquinoline antiplasmodials. The role of the group at the 7-position. *Journal of medicinal chemistry*, *45*(16), pp.3531-3539.

262. Ncokazi, K.K. and Egan, T.J., 2005. A colorimetric high-throughput β-hematin inhibition screening assay for use in the search for antimalarial compounds. *Analytical biochemistry*, *338*(2), pp.306-319.

263. Combrinck, J.M., Fong, K.Y., Gibhard, L., Smith, P.J., Wright, D.W. and Egan, T.J., 2015. Optimization of a multi-well colorimetric assay to determine haem species in *Plasmodium falciparum* in the presence of anti-malarials. *Malaria journal*, *14*(1), p.253.

264. Macomber, P.B., O'Brien, R.L. and Hahn, F.E., 1966. Chloroquine: physiological basis of drug resistance in *Plasmodium berghei*. *Science*, *152*(3727), pp.1374-1375.

265. Homewood, C.A., Moore, G.A., Warhurst, D.C. and Atkinson, E.M., 1975. Purification and some properties of malarial pigment. *Annals of Tropical Medicine & Parasitology*, *69*(3), pp.283-287.

266. Aikawa, M., 1972. High-resolution autoradiography of malarial parasites treated with 3H-chloroquine. *The American journal of pathology*, *67*(2), p.277.

267. Hayward, R., Saliba, K.J. and Kirk, K., 2006. The pH of the digestive vacuole of *Plasmodium falciparum* is not associated with chloroquine resistance. *Journal of cell science*, *119*(6), pp.1016-1025.

268. Bray, P.G., Hawley, S.R., Mungthin, M. and Ward, S.A., 1996. Physicochemical properties correlated with drug resistance and the reversal of drug resistance in *Plasmodium falciparum*. *Molecular pharmacology*, *50*(6), pp.1559-1566.

269. Hawley, S.R., Bray, P.G., O'Neill, P.M., Park, B.K. and Ward, S.A., 1996. The role of drug accumulation in 4-aminoquinoline antimalarial potency: the influence of structural substitution and physicochemical properties. *Biochemical pharmacology*, *52*(5), pp.723-733.

270. Warhurst, D.C., Craig, J.C., Adagu, I.S., Meyer, D.J. and Lee, S.Y., 2003. The relationship of physico-chemical properties and structure to the differential antiplasmodial activity of the cinchona alkaloids. *Malaria Journal*, *2*(1), p.26.

271. De Duve, C., De Barsy, T., Poole, B. and Tulkens, P., 1974. Lysosomotropic agents. *Biochemical pharmacology*, *23*(18), pp.2495-2531.

272. Egan, T.J., 2001. Structure-function relationships in chloroquine and related 4-aminoquinoline antimalarials. *Mini reviews in medicinal chemistry*, *1*(1), pp.113-123.

273. Wicht, K.J., 2015. Discovery of benzamides and triarylimidazoles active against Plasmodium falciparum via haemozoin inhibition: high throughput screening, synthesis and structure-activity relationships (*Doctoral dissertation*, University of Cape Town).

274. Geary, T.G., Jensen, J.B. and Ginsburg, H., 1986. Uptake of [3H] chloroquine by drug-sensitive and-resistant strains of the human malaria parasite *Plasmodium falciparum*. *Biochemical pharmacology*, *35*(21), pp.3805-3812.

275. Ginsburg, H., Nissani, E. and Krugliak, M., 1989. Alkalinization of the food vacuole of malaria parasites by quinoline drugs and alkylamines is not correlated with their antimalarial activity. *Biochemical pharmacology*, *38*(16), pp.2645-2654.

276. Geary, T.G., Divo, A.D., Jensen, J.B., Zangwill, M. and Ginsburg, H., 1990. Kinetic modelling of the response of *Plasmodium falciparum* to chloroquine and its experimental testing in vitro: implications for mechanism of action of and resistance to the drug. *Biochemical pharmacology*, *40*(4), pp.685-691.

277. Krogstad, D.J. and Schlesinger, P.H., 1986. A perspective on antimalarial action: effects of weak bases on *Plasmodium falciparum*. *Biochem Pharmacol*, *35*(4), pp.547-552.

278. Schlesinger, P.H., Krogstad, D.J. and Herwaldt, B.L., 1988. Antimalarial agents: mechanisms of action. *Antimicrobial agents and chemotherapy*, *32*(6), p.793.

279. Fitch, C.D., Yunis, N.G., Chevli, R. and Gonzalez, Y., 1974. High-affinity accumulation of chloroquine by mouse erythrocytes infected with *Plasmodium berghei*. *The Journal of clinical investigation*, *54*(1), pp.24-33.

280. Diribe, C.O. and Warhurst, D.C., 1980, January. Inhibitors of chloroquine uptake. In *Transactions of the Royal Society of Tropical Medicine and Hygiene*, 74(5), pp.675-676.

281. Fitch, C.D., 1973. Chloroquine-resistant Plasmodium falciparum: difference in the handling of 14C-amodiaquine and 14C-chloroquine. *Antimicrobial agents and chemotherapy*, *3*(5), pp.545-548.

282. Wünsch, S., Sanchez, C.P., Gekle, M., Große-Wortmann, L., Wiesner, J. and Lanzer, M., 1998. Differential stimulation of the Na+/H+ exchanger determines chloroquine uptake in *Plasmodium falciparum*. *The Journal of cell biology*, *140*(2), pp.335-345.

283. Bray, P.G., Janneh, O., Raynes, K.J., Mungthin, M., Ginsburg, H. and Ward, S.A., 1999. Cellular uptake of chloroquine is dependent on binding to ferriprotoporphyrin IX and is independent of NHE activity in *Plasmodium falciparum*. *The Journal of cell biology*, *145*(2), pp.363-376.

284. Schmitt, T.H., Frezzatti, W.A. and Schreier, S., 1993. Hemin-induced lipid membrane disorder and increased permeability: a molecular model for the mechanism of cell lysis. *Archives of biochemistry and biophysics*, *307*(1), pp.96-103.

285. Orjih, A.U., Banyal, H.S., Chevli, R. and Fitch, C.D., 1981. Hemin lyses malaria parasites. *Science*, *214*(4521), pp.667-669.

286. Fulton, J.D. and Rimington, C., 1953. The pigment of the malaria parasite *Plasmodium berghei*. *Microbiology*, *8*(1), pp.157-159.

287. Egan, T.J., Combrinck, J.M., Egan, J., Hearne, G.R., Marques, H.M., Ntenteni, S., Sewell, B.T., Smith, P.J., Taylor, D., van Schalkwyk, D.A. and Walden, J.C., 2002. Fate of haem iron in the malaria parasite *Plasmodium falciparum*. *Biochemical Journal*, *365*(Pt 2), p.343.

288. Bohórquez, E.B., Chua, M. and Meshnick, S.R., 2012. Quinine localizes to a non-acidic compartment within the food vacuole of the malaria parasite *Plasmodium falciparum*. *Malaria journal*, *11*(1), p.350.

289. Purfield, A.E., Tidwell, R.R. and Meshnick, S.R., 2009. The diamidine DB75 targets the nucleus of *Plasmodium falciparum*. *Malaria journal*, *8*(1), p.104.

290. Dubar, F., Bohic, S., Slomianny, C., Morin, J.C., Thomas, P., Kalamou, H., Guérardel, Y., Cloetens, P., Khalife, J. and Biot, C., 2012. In situ nanochemical imaging of label-free drugs: a case study of antimalarials in *Plasmodium falciparum*-infected erythrocytes. *Chemical Communications*, *48*(6), pp.910-912.

291. Kapishnikov, S., Staalsø, T., Yang, Y., Lee, J., Pérez-Berná, A.J., Pereiro, E., Werner, S., Guttmann, P., Leiserowitz, L. and Als-Nielsen, J., 2019. Mode of action of quinoline antimalarial drugs in red blood cells infected by *Plasmodium falciparum* revealed in vivo. *Proceedings of the National Academy of Sciences*, *116*(46), pp.22946-22952.

292. Ridley, R.G., 2002. Introduction. Antimalarial drug resistance: ramifications, explanations and challenges. *Microbes and infection*, *4*(2), p.155.

293. Egan, T.J., Hunter, R., Kaschula, C.H., Marques, H.M., Misplon, A. and Walden, J., 2000. Structure−function relationships in aminoquinolines: effect of amino and chloro groups on quinoline−hematin complex formation, inhibition of β-hematin formation, and antiplasmodial activity. *Journal of medicinal chemistry*, *43*(2), pp.283-291.

294. Wood, B.R., Langford, S.J., Cooke, B.M., Lim, J., Glenister, F.K., Duriska, M., Unthank, J.K. and McNaughton, D., 2004. Resonance Raman spectroscopy reveals new insight into the electronic structure of β-hematin and malaria pigment. *Journal of the American Chemical Society*, *126*(30), pp.9233-9239.

295. Fong, K.Y. and Wright, D.W., 2013. Hemozoin and antimalarial drug discovery. *Future medicinal chemistry*, *5*(12), pp.1437-1450.

296. Slater, A.F., 1993. Chloroquine: mechanism of drug action and resistance in *Plasmodium falciparum*. *Pharmacology & therapeutics*, *57*(2-3), pp.203-235.

297. Egan, T.J. and Marques, H.M., 1999. The role of haem in the activity of chloroquine and related antimalarial drugs. *Coordination Chemistry Reviews*, *190*, pp.493-517.

298. de Villiers, K.A., Kaschula, C.H., Egan, T.J. and Marques, H.M., 2007. Speciation and structure of ferriprotoporphyrin IX in aqueous solution: spectroscopic and diffusion measurements demonstrate dimerization, but not μ-oxo dimer formation. *JBIC Journal of Biological Inorganic Chemistry*, *12*(1), pp.101-117.

299. Chou, A.C. and Fitch, C.D., 1981. Mechanism of hemolysis induced by ferriprotoporphyrin IX. *The Journal of clinical investigation*, *68*(3), pp.672-677.

300. Blauer, G., 1986. Optical properties of complexes of antimalarial drugs with ferriprotoporphyrin IX in aqueous medium: II. The system ferriprotoporphyrin IX-quinidine. *Archives of biochemistry and biophysics*, *251*(1), pp.315-322.

301. Balasubramanian, D., Rao, C.M. and Panijpan, B., 1984. The malaria parasite monitored by photoacoustic spectroscopy. *Science*, *223*(4638), pp.828-830.

302. Bauminger, E.R., Kowitt, M., Felner, I. and Nowik, I., 1988. Mössbauer spectroscopy of 57Fe in high Tc superconductors YBa2Fe3xCu3 (1− x) O7− δ. *Solid state communications*, *65*(2), pp.123-127.

303. Blauer, G., Akkawi, M. and Bauminger, E.R., 1993. Further evidence for the interaction of the antimalarial drug amodiaquine with ferriprotoporphyrin IX. *Biochemical pharmacology*, *46*(9), pp.1573-1576.

304. Adams, P.A., Egan, T.J., Ross, D.C., Silver, J. and Marsh, P.J., 1996. The chemical mechanism of β-haematin formation studied by Mössbauer spectroscopy. *Biochemical Journal*, *318*(1), pp.25-27.

305. Ziegler, J., Linck, R. and Wright, D.W., 2001. Heme Aggregation Inhibitors Antimalarial Drugs Targeting an Essential Biomineralization Process. *Current medicinal chemistry*, *8*(2), pp.171-189.

306. Olliaro, P.L. and Trigg, P.I., 1995. Status of antimalarial drugs under development. *Bulletin of the World Health Organization*, *73*(5), p.565.

307. Ignatushchenko, M.V., Winter, R.W. and Riscoe, M, 2000. Xanthones as antimalarial agents: stage specificity. *The American journal of tropical medicine and hygiene*, *62*(1), pp.77-81.

308. Dodean, R.A., Kelly, J.X., Peyton, D., Gard, G.L., Riscoe, M.K. and Winter, R.W., 2008. Synthesis and heme-binding correlation with antimalarial activity of 3, 6-bis-(ω-N, N-diethylaminoamyloxy)-4, 5-difluoroxanthone. *Bioorganic & medicinal chemistry*, *16*(3), pp.1174-1183.

309. Kelly, J.X., Winter, R.W., Cornea, A., Peyton, D.H., Hinrichs, D.J. and Riscoe, M., 2002. The kinetics of uptake and accumulation of 3, 6-bis-ω-diethylamino-amyloxyxanthone by the human malaria parasite *Plasmodium falciparum*. *Molecular and biochemical parasitology*, *123*(1), pp.47-54.

310. de Villiers, K.A., Gildenhuys, J. and le Roex, T., 2012. Iron (III) protoporphyrin IX complexes of the antimalarial cinchona alkaloids quinine and quinidine. *ACS chemical biology*, *7*(4), pp.666-671.

311. Frosch, T., Küstner, B., Schlücker, S., Szeghalmi, A., Schmitt, M., Kiefer, W. and Popp, J., 2004. In vitro polarization-resolved resonance Raman studies of the interaction of hematin with the antimalarial drug chloroquine. *Journal of Raman Spectroscopy*, *35*(10), pp.819-821.

312. Frosch, T., Meyer, T., Schmitt, M. and Popp, J., 2007. Device for Raman difference spectroscopy. *Analytical chemistry*, *79*(16), pp.6159-6166.

313. Wood, B.R. and McNaughton, D., 2002. Raman excitation wavelength investigation of single red blood cells in vivo. *Journal of Raman Spectroscopy*, *33*(7), pp.517-523.

314. Spiro, T.G., 1988. Resonance Raman spectroscopy of metalloporphyrins. *Biological applications of Raman spectroscopy*, *3*, pp.1-37.

315. Petry, R., Schmitt, M. and Popp, J., 2003. Raman spectroscopy—a prospective tool in the life sciences. *ChemPhysChem*, *4*(1), pp.14-30.

316. Wood, B.R., Hammer, L., Davis, L. and McNaughton, D., 2005. Raman microspectroscopy and imaging provides insights into heme aggregation and denaturation within human erythrocytes. *Journal of biomedical optics*, *10*(1), p.014005.

317. Tang, J. and Albrecht, A.C., 1970. Developments in the theories of vibrational Raman intensities. In *Raman spectroscopy* (pp. 33-68). Springer, Boston, MA.

318. Coolidge, A.S., James, H.M. and Present, R.D., 1936. A Study of the Franck-Condon Principle. *The Journal of Chemical Physics*, *4*(3), pp.193-211.

319. Ong, C.W., Shen, Z.X., Ang, K.K.H., Kara, U.A.K. and Tang, S.H., 1999. Resonance Raman microspectroscopy of normal erythrocytes and *Plasmodium berghei*-infected erythrocytes. *Applied spectroscopy*, *53*(9), pp.1097-1101.

320. Wood, B.R., Langford, S.J., Cooke, B.M., Glenister, F.K., Lim, J. and McNaughton, D., 2003. Raman imaging of hemozoin within the food vacuole of *Plasmodium falciparum* trophozoites. *FEBS letters*, *554*(3), pp.247-252.

321. Pinzaru, S.C., Peica, N., Kustner, B., Schlucker, S., Schmitt, M., Frosch, T., Popp, J. and Kiefer, W., 2006. Surface-enhanced Raman spectroscopy employed in antimalarial mechanism of chloroquine drug upon haematin. *Romanian J. Biophys*, *16*, pp.57-62.

322. Webster, G.T., Tilley, L., Deed, S., McNaughton, D. and Wood, B.R., 2008. Resonance Raman spectroscopy can detect structural changes in haemozoin (malaria pigment) following incubation with chloroquine in infected erythrocytes. *FEBS letters*, *582*(7), pp.1087-1092.

323. Bro, R. and Smilde, A.K., 2014. Principal component analysis. *Analytical Methods*, *6*(9), pp.2812-2831.

324. Reese, S.E., Archer, K.J., Therneau, T.M., Atkinson, E.J., Vachon, C.M., De Andrade, M., Kocher, J.P.A. and Eckel-Passow, J.E., 2013. A new statistic for identifying batch effects in high-throughput genomic data that uses guided principal component analysis. *Bioinformatics*, *29*(22), pp.2877-2883.

325. Kozicki, M., Creek, D.J., Sexton, A., Morahan, B.J., Wesełucha-Birczyńska, A. and Wood, B.R., 2015. An attenuated total reflection (ATR) and Raman spectroscopic investigation into the effects of chloroquine on *Plasmodium falciparum*-infected red blood cells. *Analyst*, *140*(7), pp.2236-2246.

326. Vander Jagt, D.L., Hunsaker, L.A. and Campos, N.M., 1987. Comparison of proteases from chloroquine-sensitive and chloroquine-resistant strains of *Plasmodium falciparum*. *Biochemical pharmacology*, *36*(19), pp.3285-3291.

327. Ginsburg, H. and Demel, R.A., 1984. Interactions of hemin, antimalarial drugs and hemin-antimalarial complexes with phospholipid monolayers. *Chemistry and physics of lipids*, *35*(4), pp.331-347.

328. GraphPad Prism, v8.2.1, 2019, *GraphPad Software, Inc.* San Diego California USA, http://www.graphpad.com.

329. MarvinSketch, v19.1, 2019, *ChemAxon Ltd.* http://www.chemaxon.com.

330. Microsoft Office Home student package, v16.16.18, *Microsoft*®. https://microsoftoffice.store.

331. FlowJo, v10.6.1, *FlowJo Inc*. http://www.flowjo.com.

332. Becton and Dickerson, *Biosceinces*, http://www.bd.com.

333. SoftMax Pro, 2013, *Molecular Devices*, USA. http://www.moleculardevices.com.

334. Wicht, K.J., Combrinck, J.M., Smith, P.J., Hunter, R. and Egan, T.J., 2016. Identification and SAR evaluation of hemozoin-inhibiting benzamides active against *Plasmodium falciparum*. *Journal of medicinal chemistry*, *59*(13), pp.6512-6530.

335. L'abbate, F.P., Müller, R., Openshaw, R., Combrinck, J.M., de Villiers, K.A., Hunter, R. and Egan, T.J., 2018. Hemozoin inhibiting 2-phenylbenzimidazoles active against malaria parasites. *European journal of medicinal chemistry*, *159*, pp.243-254.

336. Benjamin, S.J., 2016. Synthesis and SAR investigation of haemozoin-inhibiting quinazolines active against *Plasmodium falciparum*. *Doctoral dissertation*, University of Cape Town).

337. Wainwright, L., 2014. The synthesis of benzothioazole and benzoxazole derivatives as novel β-haematin inhibiting antimalarials. *Honours dissertation*, University of Cape Town.

338. Wicht, K.J., Combrinck, J.M., Smith, P.J., Hunter, R. and Egan, T.J., 2017. Identification and Mechanistic Evaluation of Hemozoin-Inhibiting Triarylimidazoles Active against *Plasmodium falciparum*. *ACS medicinal chemistry letters*, *8*(2), pp.201-205.

339. Guinet, F., Dvorak, J.A., Fujioka, H., Keister, D.B., Muratova, O., Kaslow, D.C., Aikawa, M., Vaidya, A.B. and Wellems, T.E., 1996. A developmental defect in *Plasmodium falciparum* male gametogenesis. *The Journal of cell biology*, *135*(1), pp.269-278.

340. Antony, H.A., Pathak, V., Parija, S.C., Ghosh, K. and Bhattacherjee, A., 2016. Transcriptomic analysis of chloroquine-sensitive and chloroquine-resistant strains of *Plasmodium falciparum*: toward malaria diagnostics and therapeutics for global health. *Omics: a journal of integrative biology*, *20*(7), pp.424-432.

341. Cowman, A.F., Morry, M.J., Biggs, B.A., Cross, G.A. and Foote, S.J., 1988. Amino acid changes linked to pyrimethamine resistance in the dihydrofolate reductase-thymidylate synthase gene of *Plasmodium falciparum*. *Proceedings of the National Academy of Sciences*, *85*(23), pp.9109-9113.

342. Su, X.Z., 2014. Tracing the geographic origins of *Plasmodium falciparum* malaria parasites. *Pathogens and global health*, *108*(6), p.261.

343. Trager, W. and Jensen, J.B., 1976. Human malaria parasites in continuous culture. *Science*, *193*(4254), pp.673-675.

344. Makler, M.T., Ries, J.M., Williams, J.A., Bancroft, J.E., Piper, R.C., Gibbins, B.L. and Hinrichs, D.J., 1993. Parasite lactate dehydrogenase as an assay for *Plasmodium falciparum* drug sensitivity. *The American journal of tropical medicine and hygiene*, *48*(6), pp.739-741.

345. Shafariatul, A.I., Sidek, H.M. and Surif, S., 2012, September. Comparison of the Makler & Hinrichs (1993) Technique Versus Application Of Hepes Lysis Solvent In Determining The Activities Of Plasmodium Lactate Dehydrogenase (pLDH) In *Plasmodium berghei*-Infected Erythrocytes. In *International Conference on Applied Life Sciences*. IntechOpen.

346. Combrinck, J.M., 2016. The role of haem in the mechanism of action of antimalarials in *Plasmodium falciparum*. *Doctoral dissertation*, University of Cape Town.

347. Brown, S.B., Dean, T.C. and Jones, P., 1970. Aggregation of ferrihaems. Dimerization and protolytic equilibria of protoferrihaem and deuteroferrihaem in aqueous solution. *Biochemical Journal*, *117*(4), pp.733-739.

348. Paulat, F., Praneeth, V.K.K., Näther, C. and Lehnert, N., 2006. Quantum chemistry-based analysis of the vibrational spectra of five-coordinate metalloporphyrins [M (TPP) Cl]. *Inorganic chemistry*, *45*(7), pp.2835-2856.

349. Asakura, T., Minakata, K., Adachi, K., Russell, M.O. and Schwartz, E., 1977. Denatured hemoglobin in sickle erythrocytes. *The Journal of clinical investigation*, *59*(4), pp.633-640.

350. Okafor, U.E., Tsoka-Gwegweni, J.M., Bibirigea, A., Irimie, A. and Tomuleasa, C., 2016. Parasitaemia and haematological changes in malaria-infected refugees in South Africa. *South African Medical Journal*, *106*(4), pp.413-416.

351. Pandey, A.V. and Chauhan, V.S., 1998. Heme polymerization by malarial parasite: A potential target for antimalarial drug. *Current Science*, *75*(9).

352. Egan, T.J. and Ncokazi, K.K., 2005. Quinoline antimalarials decrease the rate of β-hematin formation. *Journal of inorganic biochemistry*, *99*(7), pp.1532-1539.

353. O'Neill, P.M., Bray, P.G., Hawley, S.R., Ward, S.A. and Park, B.K., 1998. 4-Aminoquinolines—Past, present, and future; A chemical perspective. *Pharmacology & therapeutics*, *77*(1), pp.29-58.

354. Fong, K.Y., Sandlin, R.D. and Wright, D.W., 2015. Identification of β-hematin inhibitors in the MMV Malaria Box. *International Journal for Parasitology: Drugs and Drug Resistance*, *5*(3), pp.84-91.

355. Fitch, C.D., 1970. Plasmodium falciparum in owl monkeys: drug resistance and chloroquine binding capacity. *Science*, *169*(3942), pp.289-290.

356. Chou, A.C., Chevli, R. and Fitch, C.D., 1980. Ferriprotoporphyrin IX fulfills the criteria for identification as the chloroquine receptor of malaria parasites. *Biochemistry*, *19*(8), pp.1543-1549.

357. Hawley, S.R., Bray, P.G., Mungthin, M., Atkinson, J.D., O'Neill, P.M. and Ward, S.A., 1998. Relationship between antimalarial drug activity, accumulation, and inhibition of heme polymerization in *Plasmodium falciparum* in vitro. *Antimicrobial agents and chemotherapy*, *42*(3), pp.682-686.

358. Warhurst, D.C., Craig, J.C., Adagu, I.S., Guy, R.K., Madrid, P.B. and Fivelman, Q.L., 2007. Activity of piperaquine and other 4-aminoquinoline antiplasmodial drugs against chloroquine-sensitive and resistant blood-stages of *Plasmodium falciparum*: role of β-haematin inhibition and drug concentration in vacuolar water-and lipid-phases. *Biochemical pharmacology*, *73*(12), pp.1910-1926.

359. Brook, I., 1989. Inoculum effect. *Reviews of infectious diseases*, *11*(3), pp.361-368.

360. Gluzman, I.Y., Schlesinger, P.H. and Krogstad, D.J., 1987. Inoculum effect with chloroquine and *Plasmodium falciparum*. *Antimicrobial agents and chemotherapy*, *31*(1), pp.32-36.

361. Ginsburg, H. and Geary, T.G., 1987. Current concepts and new ideas on the mechanism of action of quinoline-containing antimalarials. *Biochemical pharmacology*, *36*(10), pp.1567-1576.

362. Surolia, N. and Padmanaban, G., 1991. Chloroquine inhibits heme-dependent protein synthesis in *Plasmodium falciparum*. *Proceedings of the National Academy of Sciences*, *88*(11), pp.4786-4790.

363. O'Neill, P.M., Bishop, L.P., Searle, N.L., Maggs, J.L., Ward, S.A., Bray, P.G., Storr, R.C. and Park, B.K., 1997. The biomimetic iron-mediated degradation of arteflene (Ro-42-1611), an endoperoxide antimalarial: implications for the mechanism of antimalarial activity. *Tetrahedron letters*, *38*(24), pp.4263-4266.

364. Fitch, C.D., 1989. Ferriprotoporphyrin IX: role in chloroquine susceptibility and resistance in malaria. *Progress in clinical and biological research*, *313*, pp.45-52.

365. Geary, T.G., Divo, A.A. and Jensen, J.B., 1986. Effect of calmodulin inhibitors on viability and mitochondrial potential of *Plasmodium falciparum* in culture. *Antimicrobial agents and chemotherapy*, *30*(5), pp.785-788.

366. Macomber, P.B., Sprinz, H. and Tousimis, A.J., 1967. Morphological effects of chloroquine on *Plasmodium berghei* in mice. *Nature*, *214*(5091), p.937.

367. Saha, S.J., Siddiqui, A.A., Pramanik, S., Saha, D., De, R., Mazumder, S., Debsharma, S., Nag, S., Banerjee, C. and Bandyopadhyay, U., 2018. Hydrazonophenol, a Food Vacuole-Targeted and Ferriprotoporphyrin IX-Interacting Chemotype Prevents Drug-Resistant Malaria. *ACS infectious diseases*, *5*(1), pp.63-73.

368. Vippagunta, S.R., Dorn, A., Ridley, R.G. and Vennerstrom, J.L., 2000. Characterization of chloroquine-hematin μ-oxo dimer binding by isothermal titration calorimetry. *Biochimica et Biophysica Acta (BBA)-General Subjects*, *1475*(2), pp.133-140.

369. Rees, R.W., Russell, P.B., Foell, T.J. and Bright, R.E., 1972. Antimalarial activities of some 3, 5-diamino-as-triazine derivatives. *Journal of medicinal chemistry*, *15*(8), pp.859-861.

370. Pandey, A.V., Bisht, H., Babbarwal, V.K., Srivastava, J., Pandey, K.C. and Chauhan, V.S., 2001. Mechanism of malarial haem detoxification inhibition by chloroquine. *Biochemical Journal*, *355*(2), pp.333-338.

371. Perez-Guaita, D., Kochan, K., Batty, M., Doerig, C., Garcia-Bustos, J., Espinoza, S., McNaughton, D., Heraud, P. and Wood, B.R., 2018. Multispectral atomic force microscopy-infrared nano-imaging of malaria infected red blood cells. *Analytical chemistry*, *90*(5), pp.3140-3148.

372. Ambele, M.A., 2013. The role of lipid in malaria pigment (Haemozoin) formation under biomimetic conditions (*Doctoral dissertation*, University of Cape Town).

373. Li, X.Y. and Spiro, T.G., 1988. Is bound carbonyl linear or bent in heme proteins? Evidence from resonance Raman and infrared spectroscopic data. *Journal of the American Chemical Society*, *110*(18), pp.6024-6033.

374. Tarcea, N., Frosch, T., Rösch, P., Hilchenbach, M., Stuffler, T., Hofer, S., Thiele, H., Hochleitner, R. and Popp, J., 2008. Raman spectroscopy—A powerful tool for in situ planetary science. In *Strategies of Life Detection* (pp. 281-292). Springer, Boston, MA.

375. Bohle, D.S., Conklin, B.J., Cox, D., Madsen, S.K., Paulson, S., Stephens, P.W. and Yee, G.T., 1994. Structural and spectroscopic studies of β-hematin (the heme coordination polymer in malaria pigment). *Inorganic and Organometallic Polymers II: Advanced Materials and Intermediates*, *572*, pp.497-515.

376. Tempera, C., Franco, R., Caro, C., André, V., Eaton, P., Burke, P. and Hänscheid, T., 2015. Characterization and optimization of the haemozoin-like crystal

(HLC) assay to determine Hz inhibiting effects of anti-malarial compounds. *Malaria journal*, *14*(1), p.403.

377. Koontz, L., 2013. Agarose gel electrophoresis. *Methods Enzymol*, *529*, pp.35-45.

378. Yamada, H., Yamaguchi, M., Chikamatsu, K., Aono, A. and Mitarai, S., 2015. Structome analysis of virulent Mycobacterium tuberculosis, which survives with only 700 ribosomes per 0.1 fl of cytoplasm. *PLoS One*, *10*(1), p.e0117109.

379. Yamada, H., Mitarai, S., Chikamatsu, K., Mizuno, K. and Yamaguchi, M., 2010. Novel freeze-substitution electron microscopy provides new aspects of virulent Mycobacterium tuberculosis with visualization of the outer membrane and satisfying biosafety requirements. *Journal of microbiological methods*, *80*(1), pp.14-18.

380. Yamada, H., Chikamatsu, K., Aono, A. and Mitarai, S., 2014. Pre-fixation of virulent Mycobacterium tuberculosis with glutaraldehyde preserves exquisite ultrastructure on transmission electron microscopy through cryofixation and freeze-substitution with osmium-acetone at ultralow temperature. *Journal of microbiological methods*, *96*, pp.50-55.

381. Image J v1.8.0_172, v219, 2019, *National Institute of Health*, imagej.nih.gov/ij/download/.

382. Control FIVE software, v5.0.0, 2017, *WITec GmbH in Germany*, www.witec.de.

383. Project FIVE software, v5.0.0.40, 2017, *WITec GmbH in Germany*, www.witec.de.

384. Molegro Data Modeller executive, v3.0, 2013. *CLC bio*, www.clcbio.com.

385. Cui, L., Butler, H.J., Martin-Hirsch, P.L. and Martin, F.L., 2016. Aluminium foil as a potential substrate for ATR-FTIR, transflection FTIR or Raman spectrochemical analysis of biological specimens. *Analytical methods*, *8*(3), pp.481-487.

386. Diem, M., Mazur, A., Lenau, K., Schubert, J., Bird, B., Miljković, M., Krafft, C. and Popp, J., 2013. Molecular pathology via IR and Raman spectral imaging. *Journal of biophotonics*, *6*(11-12), pp.855-886.

387. Kamemoto, L.E., Misra, A.K., Sharma, S.K., Goodman, M.T., Luk, H., Dykes, A.C. and Acosta, T., 2010. Near-infrared micro-Raman spectroscopy for in vitro detection of cervical cancer. *Applied spectroscopy*, *64*(3), pp.255-261.

388. Berry, D., Mader, E., Lee, T.K., Woebken, D., Wang, Y., Zhu, D., Palatinszky, M., Schintlmeister, A., Schmid, M.C., Hanson, B.T. and Shterzer, N., 2015. Tracking heavy water (D2O) incorporation for identifying and sorting active microbial cells. *Proceedings of the National Academy of Sciences*, *112*(2), pp.E194-E203.

389. Li, M., Canniffe, D.P., Jackson, P.J., Davison, P.A., FitzGerald, S., Dickman, M.J., Burgess, J.G., Hunter, C.N. and Huang, W.E., 2012. Rapid resonance Raman microspectroscopy to probe carbon dioxide fixation by single cells in microbial communities. *The ISME journal*, *6*(4), p.875.

390. Pahlow, S., Kloß, S., Blaettel, V., Kirsch, K., Hübner, U., Cialla, D., Roesch, P., Weber, K. and Popp, J., 2013. Isolation and Enrichment of Pathogens with a Surface-Modified Aluminium Chip for Raman Spectroscopic Applications. *ChemPhysChem*, *14*(15), pp.3600-3605.

391. Ramser, K., Bjerneld, E.J., Fant, C. and Kall, M., 2002, March. Raman imaging and spectroscopy of single functional erythrocytes: a feasibility study. In *Biomedical Vibrational Spectroscopy II* (Vol. 4614, pp. 20-27). International Society for Optics and Photonics.

392. Ramser, K.K., Bjerneld, E.J., Fant, C. and Kaell, M., 2003. Importance of substrate-and photo-induced effects in Raman spectroscopy of single functional erythrocytes. *Journal of biomedical optics*, *8*(2), pp.173-179.

393. WITec manual, 2017, *WITec GmbH in Germany*, www.witec.de.

394. Barnes, R.J., Dhanoa, M.S. and Lister, S.J., 1989. Standard normal variate transformation and de-trending of near-infrared diffuse reflectance spectra. *Applied spectroscopy*, *43*(5), pp.772-777.

395. Wayne, W., 1988. [27] Rapid colorimetric micromethod for the quantitation of complexed iron in biological samples. In *Methods in enzymology* (Vol. 158, pp. 357-364). Academic Press.

396. Passchier, A.A., Christian, J.D. and Gregory, N.W., 1967. The ultraviolet-visible absorption spectrum of bromine between room temperature and 440. degree. *The Journal of Physical Chemistry*, *71*(4), pp.937-942.

397. Ripper, D., Schwarz, H. and Stierhof, Y.D., 2008. Cryo-section immunolabelling of difficult to preserve specimens: advantages of cryofixation, freeze-substitution and rehydration. *Biology of the Cell*, *100*(2), pp.109-123.

398. Shami, G., Cheng, D., Henriquez, J. and Braet, F., 2014. An assessment of high-pressure freezing and freeze substitution protocols for cultured cells.

399. Love, M.S., Millholland, M.G., Mishra, S., Kulkarni, S., Freeman, K.B., Pan, W., Kavash, R.W., Costanzo, M.J., Jo, H., Daly, T.M. and Williams, D.R., 2012. Platelet factor 4 activity against *P. falciparum* and its translation to nonpeptidic mimics as antimalarials. *Cell host & microbe*, *12*(6), pp.815-823.

400. Bleck, C.K.E., Merz, A., Gutierrez, M.G., Walther, P., Dubochet, J., Zuber, B. and Griffiths, G., 2010. Comparison of different methods for thin section EM analysis of Mycobacterium smegmatis. *Journal of microscopy*, *237*(1), pp.23-38.

401. Frosch, T., Koncarevic, S., Zedler, L., Schmitt, M., Schenzel, K., Becker, K. and Popp, J., 2007. In situ localization and structural analysis of the malaria pigment hemozoin. *The Journal of Physical Chemistry B*, *111*(37), pp.11047-11056.

402. Egan, T.J., Hempelmann, E. and Mavuso, W.W., 1999. Characterisation of synthetic β-haematin and effects of the antimalarial drugs quinidine, halofantrine, desbutylhalofantrine and mefloquine on its formation. *Journal of inorganic biochemistry*, *73*(1-2), pp.101-107.

403. Ridley, R.G., Matile, H., Jaquet, C., Dorn, A., Hofheinz, W., Leupin, W., Masciadri, R., Theil, F.P., Richter, W.F., Girometta, M.A. and Guenzi, A., 1997. Antimalarial activity of the bisquinoline trans-N1, N2-bis (7-chloroquinolin-4-yl) cyclohexane-1, 2-diamine: comparison of two stereoisomers and detailed evaluation of the S, S enantiomer, Ro 47-7737. *Antimicrobial agents and chemotherapy*, *41*(3), pp.677-686.

404. Baelmans, R., Deharo, E., Munoz, V., Sauvain, M. and Ginsburg, H., 2000. Experimental conditions for testing the inhibitory activity of chloroquine on the formation of β-hematin. *Experimental parasitology*, *96*(4), pp.243-248.

405. Abe, M., Kitagawa, T. and Kyogoku, Y., 1978. Resonance Raman spectra of octaethylporphyrinato-Ni (II) and meso-deuterated and 15N substituted derivatives. II. A normal coordinate analysis. *The Journal of Chemical Physics*, *69*(10), pp.4526-4534.

406. Hu, S., Smith, K.M. and Spiro, T.G., 1996. Assignment of protoheme resonance Raman spectrum by heme labeling in myoglobin. *Journal of the American Chemical Society*, *118*(50), pp.12638-12646.

407. Szczerbowska-Boruchowska, M., Dumas, P., Kastyak, M.Z., Chwiej, J., Lankosz, M., Adamek, D. and Krygowska-Wajs, A., 2007. Biomolecular investigation of human substantia nigra in Parkinson's disease by synchrotron radiation Fourier

transform infrared microspectroscopy. *Archives of biochemistry and biophysics*, *459*(2), pp.241-248.

408. Socrates, G., 1980. Infrared characteristic group frequencies. Infrared spectrometry.

409. Dines, T.J., MacGregor, L.D. and Rochester, C.H., 2002. IR spectroscopic investigation of the interaction of quinoline with acidic sites on oxide surfaces. *Langmuir*, *18*(6), pp.2300-2308.

410. Marzec, K.M., Wrobel, T.P., Rygula, A., Maslak, E., Jasztal, A., Fedorowicz, A., Chlopicki, S. and Baranska, M., 2014. Visualization of the biochemical markers of atherosclerotic plaque with the use of Raman, IR and AFM. *Journal of biophotonics*, *7*(9), pp.744-756.

411. Suwaiyan, A., Zwarich, R. and Baig, N., 1990. Infrared and Raman spectra of benzimidazole. *Journal of Raman spectroscopy*, *21*(4), pp.243-249.

412. Mohan, S., Sundaraganesan, N. and Mink, J., 1991. FTIR and Raman studies on benzimidazole. *Spectrochimica Acta Part A: Molecular Spectroscopy*, *47*(8), pp.1111-1115.

413. Wesełucha-Birczyńska, A., Frączek-Szczypta, A., Długoń, E., Paciorek, K., Bajowska, A., Kościelna, A. and Błażewicz, M., 2014. Application of Raman spectroscopy to study of the polymer foams modified in the volume and on the surface by carbon nanotubes. *Vibrational Spectroscopy*, *72*, pp.50-56.

414. Wood, B.R. and McNaughton, D., 2006. Resonance Raman spectroscopy in malaria research. *Expert review of proteomics*, *3*(5), pp.525-544.

415. Wood, B.R., Caspers, P., Puppels, G.J., Pandiancherri, S. and McNaughton, D., 2007. Resonance Raman spectroscopy of red blood cells using near-infrared laser excitation. *Analytical and bioanalytical chemistry*, *387*(5), pp.1691-1703.

416. Wood, B.R., Tait, B. and McNaughton, D., 2001. Micro-Raman characterisation of the R to T state transition of haemoglobin within a single living erythrocyte. *Biochimica et Biophysica Acta (BBA)-Molecular Cell Research*, *1539*(1-2), pp.58-70.

417. Dasgupta, R., Verma, R.S., Ahlawat, S., Uppal, A. and Gupta, P.K., 2011. Studies on erythrocytes in malaria infected blood sample with Raman optical tweezers. *Journal of biomedical optics*, *16*(7), p.077009.

418. Strekas, T.C. and Spiro, T.G., 1973. Hemoglobin resonance Raman excitation profiles with a tunable dye laser. *Journal of Raman Spectroscopy*, *1*(4), pp.387-392.

419. Brunner, H., Mayer, A. and Sussner, H., 1972. Resonance Raman scattering on the haem group of oxy-and deoxyhaemoglobin. *Journal of molecular biology*, *70*(1), pp.153-156.

420. Ozaki, Y., Cho, R., Ikegaya, K., Muraishi, S. and Kawauchi, K., 1992. Potential of near-infrared Fourier transform Raman spectroscopy in food analysis. *Applied Spectroscopy*, *46*(10), pp.1503-1507.

421. Venkatesh, B., Ramasamy, S., Mylrajan, M., Asokan, R., Manoharan, P.T. and Rifkind, J.M., 1999. Fourier transform Raman approach to structural correlation in hemoglobin derivatives. *Spectrochimica Acta Part A: Molecular and Biomolecular Spectroscopy*, *55*(7-8), pp.1691-1697.

422. Asghari-Khiavi, M., Mechler, A., Bambery, K.R., McNaughton, D. and Wood, B.R., 2009. A resonance Raman spectroscopic investigation into the effects of fixation and dehydration on heme environment of hemoglobin. *Journal of Raman Spectroscopy: An International Journal for Original Work in all Aspects of Raman Spectroscopy, Including Higher Order Processes, and also Brillouin and Rayleigh Scattering*, *40*(11), pp.1668-1674.

423. Cohen, S.N., Phifer, K.O. and Yielding, K.L., 1964. Complex formation between chloroquine and ferrihaemic acid in vitro and its effect on the antimalarial action of chloroquine. *Nature*, *202*(4934), pp.805-806.

424. Yamamoto, T., Palmer, G., Gill, D., Salmeen, I.T. and Rimai, L., 1973. The valence and spin state of iron in oxyhemoglobin as inferred from resonance Raman spectroscopy. *Journal of Biological Chemistry*, *248*(14), pp.5211-5213.

425. Lanir, A., Yu, N.T. and Felton, R.H., 1979. Conformational transitions and vibronic couplings in acid ferricytochrome c: a resonance Raman study. *Biochemistry*, *18*(9), pp.1656-1660.

426. Rimai, L., Salmeen, I. and Petering, D.H., 1975. Comparison of the resonance Raman spectra of carbon monoxy and oxy hemoglobin and myoglobin. Similarities and differences in heme electron distribution. *Biochemistry*, *14*(2), pp.378-382.

427. Johjima, T., Wariishi, H. and Tanaka, H., 1996. The effect of ligand field strength on nonresonance Raman characteristics of hemoproteins. *Biochemical and biophysical research communications*, *226*(3), pp.601-606.

428. Spiro, T.G., Stong, J.D. and Stein, P., 1979. Porphyrin core expansion and doming in heme proteins. New evidence from resonance Raman spectra of six-

coordinate high-spin iron (III) hemes. *Journal of the American Chemical Society*, *101*(10), pp.2648-2655.

429. Schweitzer-Stenner, R., Eker, F., Griebenow, K., Cao, X. and Nafie, L.A., 2004. The conformation of tetraalanine in water determined by polarized Raman, FT-IR, and VCD spectroscopy. *Journal of the American Chemical Society*, *126*(9), pp.2768-2776.

430. Huber, C.P., Ozaki, Y., Pliura, D.H., Storer, A.C. and Carey, P.R., 1982. Precise structural information for transient enzyme-substrate complexes by a combined X-ray crystallographic-resonance Raman spectroscopic approach. *Biochemistry*, *21*(13), pp.3109-3115.

431. Hobro, A.J., Konishi, A., Coban, C. and Smith, N.I., 2013. Raman spectroscopic analysis of malaria disease progression via blood and plasma samples. *Analyst*, *138*(14), pp.3927-3933.

432. Dieing, T. and Hollricher, O., 2008. High-resolution, high-speed confocal Raman imaging. *Vibrational Spectroscopy*, *48*(1), pp.22-27.

433. Wilson, T. ed., 1990. *Confocal microscopy*. Academic press.

434. Srinivasan, M., Sedmak, D. and Jewell, S., 2002. Effect of fixatives and tissue processing on the content and integrity of nucleic acids. *The American journal of pathology*, *161*(6), pp.1961-1971.

435. Troiano, N.W., Ciovacco, W.A. and Kacena, M.A., 2009. The effects of fixation and dehydration on the histological quality of undecalcified murine bone specimens embedded in methylmethacrylate. *Journal of histotechnology*, *32*(1), pp.27-31.

436. Hobro, A.J. and Smith, N.I., 2017. An evaluation of fixation methods: Spatial and compositional cellular changes observed by Raman imaging. *Vibrational Spectroscopy*, *91*, pp.31-45.

437. Chen, F., Flaherty, B.R., Cohen, C.E., Peterson, D.S. and Zhao, Y., 2016. Direct detection of malaria infected red blood cells by surface enhanced Raman spectroscopy. *Nanomedicine: Nanotechnology, Biology and Medicine*, *12*(6), pp.1445-1451.

438. Khoshmanesh, A., Dixon, M.W., Kenny, S., Tilley, L., McNaughton, D. and Wood, B.R., 2014. Detection and quantification of early-stage malaria parasites in laboratory infected erythrocytes by attenuated total reflectance infrared spectroscopy and multivariate analysis. *Analytical chemistry*, *86*(9), pp.4379-4386.

439. Wood, B.R., Bailo, E., Khiavi, M.A., Tilley, L., Deed, S., Deckert-Gaudig, T., McNaughton, D. and Deckert, V., 2011. Tip-enhanced Raman scattering (TERS) from hemozoin crystals within a sectioned erythrocyte. *Nano letters*, *11*(5), pp.1868-1873.

440. Goodpaster, A.M. and Kennedy, M.A., 2011. Quantification and statistical significance analysis of group separation in NMR-based metabonomics studies. *Chemometrics and Intelligent Laboratory Systems*, *109*(2), pp.162-170.

441. Sherman, I.W., 1977. Transport of amino acids and nucleic acid precursors in malarial parasites. *Bulletin of the World Health Organization*, *55*(2-3), p.211.

442. Sherman, I.W., 1977. Amino acid metabolism and protein synthesis in malarial parasites. *Bulletin of the World Health Organization*, *55*(2-3), p.265.

443. Zarchin, S., Krugliak, M. and Ginsburg, H., 1986. Digestion of the host erythrocyte by malaria parasites is the primary target for quinolinecontaining antimalarials. *Biochemical pharmacology*, *35*(14), pp.2435-2442.

444. Goldberg, D.E., 2005. Hemoglobin degradation. In *Malaria: Drugs, Disease and Post-genomic Biology* (pp. 275-291). Springer, Berlin, Heidelberg.

445. Silva, A.M., Lee, A.Y., Gulnik, S.V., Maier, P., Collins, J., Bhat, T.N., Collins, P.J., Cachau, R.E., Luker, K.E., Gluzman, I.Y. and Francis, S.E., 1996. Structure and inhibition of plasmepsin II, a hemoglobin-degrading enzyme from *Plasmodium falciparum*. *Proceedings of the National Academy of Sciences*, *93*(19), pp.10034-10039.

446. Dame, J.B., Reddy, G.R., Yowell, C.A., Dunn, B.M., Kay, J. and Berry, C., 1994. Sequence, expression and modeled structure of an aspartic proteinase from the human malaria parasite *Plasmodium falciparum*. *Molecular and biochemical parasitology*, *64*(2), pp.177-190.

447. Ball, E.G., McKee, R.W., Anfinsen, C.B., Cruz, W.O. and Geiman, Q.M., 1948. Studies on Malarial Parasites. IX. Chemical and Metabolic Changes during Growth and Multiplication in vivo and in vitro. *Journal of biological chemistry*, *175*(2), pp.547-71.

448. Morrison, D.B. and Jeskey, H.A., 1948. Alterations in some constituents of the monkey erythrocyte infected with *Plasmodium knowlesi* as related to pigment formation. *Journal of the National Malaria Society*, *7*(4), pp.259-64.

449. Nene, V., Gobright, E., Musoke, A.J. and Lonsdale-Eccles, J.D., 1990. A single exon codes for the enzyme domain of a protozoan cysteine protease. *Journal of Biological Chemistry*, *265*(30), pp.18047-18050.

450. Rosenthal, P.J., Sijwali, P.S., Singh, A. and Shenai, B.R., 2002. Cysteine proteases of malaria parasites: targets for chemotherapy. *Current pharmaceutical design*, *8*(18), pp.1659-1672.

451. Lew, V.L., Tiffert, T. and Ginsburg, H., 2003. Excess hemoglobin digestion and the osmotic stability of *Plasmodium falciparum*–infected red blood cells. *Blood*, *101*(10), pp.4189-4194.

452. Bailly, E., Jambou, R., Savel, J. and Jaureguiberry, G., 1992. *Plasmodium falciparum*: differential sensitivity in vitro to E-64 (cysteine protease inhibitor) and Pepstatin A (aspartyl protease inhibitor). *The Journal of protozoology*, *39*(5), pp.593-599.

453. Yoshida, H., Okamoto, K., Iwamoto, T., Sakai, E., Kanaoka, K., Hu, J.P., Shibata, M., Hotokezaka, H., Nishishita, K., Mizuno, A. and Kato, Y., 2006. Pepstatin A, an aspartic proteinase inhibitor, suppresses RANKL-induced osteoclast differentiation. *Journal of biochemistry*, *139*(3), pp.583-590.

454. Koelsch, G., 2017. BACE1 function and inhibition: implications of intervention in the amyloid pathway of Alzheimer's disease pathology. *Molecules*, *22*(10), p.1723.

455. Sijwali, P.S., Shenai, B.R. and Rosenthal, P.J., 2002. Folding of the *Plasmodium falciparum* cysteine protease falcipain-2 is mediated by a chaperone-like peptide and not the prodomain. *Journal of Biological Chemistry*, *277*(17), pp.14910-14915.

456. Li, F., Patra, K.P. and Vinetz, J.M., 2005. An Anti-Chitinase Malaria Transmission–Blocking Single-Chain Antibody as an Effector Molecule for Creating a *Plasmodium falciparum*–Refractory Mosquito. *The Journal of infectious diseases*, *192*(5), pp.878-887.

457. Krungkrai, J., Learngaramkul, P., Kanjanarithisak, R. and Krungkrai, S.R., 1994. Mitochondrial function of human malarial parasite *Plasmodium falciparum* cultivated in vitro: implications for antimalarial drug design. *Chula Med J*, *38*, pp.315-23.

458. Hanssen, E., Knoechel, C., Dearnley, M., Dixon, M.W., Le Gros, M., Larabell, C. and Tilley, L., 2012. Soft X-ray microscopy analysis of cell volume and hemoglobin content in erythrocytes infected with asexual and sexual stages of *Plasmodium falciparum*. *Journal of structural biology*, *177*(2), pp.224-232.

459. Rabiner, S.F., Helbert, J.R., Lopas, H. and Friedman, L.H., 1967. Evaluation of a stroma-free hemoglobin solution for use as a plasma expander. *Journal of Experimental Medicine*, *126*(6), pp.1127-1142.

460. Snell, S.M. and Marini, M.A., 1988. A convenient spectroscopic method for the estimation of hemoglobin concentrations in cell-free solutions. *Journal of biochemical and biophysical methods*, *17*(1), pp.25-33.

461. Wang, M., Herrmann, C.J., Simonovic, M., Szklarczyk, D. and von Mering, C., 2015. Version 4.0 of PaxDb: protein abundance data, integrated across model organisms, tissues, and cell-lines. *Proteomics*, *15*(18), pp.3163-3168.

462. Artimo, P., Jonnalagedda, M., Arnold, K., Baratin, D., Csardi, G., De Castro, E., Duvaud, S., Flegel, V., Fortier, A., Gasteiger, E. and Grosdidier, A., 2012. ExPASy: SIB bioinformatics resource portal. *Nucleic acids research*, *40*(W1), pp.W597-W603.

463. NanoDrop, v3.5.1. *Thermo Fisher Scientific*. www.thermofisher.com.

464. Reed, K.W. and Yalkowsky, S.H., 1985. Lysis of human red blood cells in the presence of various cosolvents. *PDA Journal of Pharmaceutical Science and Technology*, *39*(2), pp.64-69.

465. Bradford, M.M., 1976. A rapid and sensitive method for the quantitation of microgram quantities of protein utilizing the principle of protein-dye binding. *Analytical biochemistry*, *72*(1-2), pp.248-254.

466. Reisner, A.H., Nemes, P. and Bucholtz, C., 1975. The use of Coomassie Brilliant Blue G250 perchloric acid solution for staining in electrophoresis and isoelectric focusing on polyacrylamide gels. *Analytical biochemistry*, *64*(2), pp.509-516.

467. Groth, F.D.S., S., Webster, RG, and Datyner, A.(1963) Two new staining procedures for quantitative estimation of proteins on electrophoretic strips. *Biochim. Biophys. Acta*, *71*, pp.377-391.

468. Sedmak, J.J. and Grossberg, S.E., 1977. A rapid, sensitive, and versatile assay for protein using Coomassie brilliant blue G250. *Analytical biochemistry*, *79*(1-2), pp.544-552.

469. Compton, S.J. and Jones, C.G., 1985. Mechanism of dye response and interference in the Bradford protein assay. *Analytical biochemistry*, *151*(2), pp.369-374.

470. Spector, T., 1978. Refinement of the Coomassie blue method of protein quantitation: A simple and linear spectrophotometric assay for≤ 0.5 to 50 µg of protein. *Analytical biochemistry*, *86*(1), pp.142-146.

471. Duhamel, R.C., Meezan, E. and Brendel, K., 1981. The addition of SDS to the Bradford dye-binding protein assay, a modification with increased sensitivity to collagen. *Journal of biochemical and biophysical methods*, *5*(2), pp.67-74.

472. Macart, M. and Gerbaut, L., 1982. An improvement of the Coomassie Blue dye binding method allowing an equal sensitivity to various proteins: application to cerebrospinal fluid. *Clinica Chimica Acta*, *122*(1), pp.93-101.

473. Smith, P.K., Krohn, R.I., Hermanson, G.T., Mallia, A.K., Gartner, F.H., Provenzano, M., Fujimoto, E.K., Goeke, N.M., Olson, B.J. and Klenk, D.C., 1985. Measurement of protein using bicinchoninic acid. *Analytical biochemistry*, *150*(1), pp.76-85.

474. Desjardins, P., Hansen, J.B. and Allen, M., 2009. Microvolume protein concentration determination using the NanoDrop 2000c spectrophotometer. *JoVE (Journal of Visualized Experiments)*, (33), p.e1610.

475. Desjardins, P. and Conklin, D., 2010. NanoDrop microvolume quantitation of nucleic acids. *JoVE (Journal of Visualized Experiments)*, (45), p.e2565.

476. Bio-Rad quick start protein assay kit, www.biorad.com.

477. Sigma-Aldrich quick start protein assay kit, www.sigmaaldrich.com.

478. Swinehart, D.F., 1962. The beer-lambert law. *Journal of chemical education*, *39*(7), p.333.

479. Zor, T. and Selinger, Z., 1996. Linearization of the Bradford protein assay increases its sensitivity: theoretical and experimental studies. *Analytical biochemistry*, *236*(2), pp.302-308.

480. McKerrow, J.H., Sun, E., Rosenthal, P.J. and Bouvier, J., 1993. The proteases and pathogenicity of parasitic protozoa. *Annual review of microbiology*, *47*(1), pp.821-853.

481. Tao, D., Ubaida-Mohien, C., Mathias, D.K., King, J.G., Pastrana-Mena, R., Tripathi, A., Goldowitz, I., Graham, D.R., Moss, E., Marti, M. and Dinglasan, R.R., 2014. Sex-partitioning of the *Plasmodium falciparum* stage V gametocyte proteome provides insight into *falciparum*-specific cell biology. *Molecular & Cellular Proteomics*, *13*(10), pp.2705-2724.

482. Sorensen, K. and Brodbeck, U., 1986. A sensitive protein assay method using micro-titer plates. *Experientia*, *42*(2), pp.161-162.

483. Hinson, D.L. and Webber, R.J., 1988. Miniaturization of the BCA protein assay. *BioTechniques*, *6*(1), pp.14-16.

484. Orjih, A.U. and Fitch, C.D., 1993. Hemozoin production by *Plasmodium falciparum*: variation with strain and exposure to chloroquine. *Biochimica et Biophysica Acta (BBA)-General Subjects*, *1157*(2), pp.270-274.

485. Tycko, D.H., Metz, M.H., Epstein, E.A. and Grinbaum, A., 1985. Flow-cytometric light scattering measurement of red blood cell volume and hemoglobin concentration. *Applied optics*, *24*(9), pp.1355-1365.

486. Wang, P., Nirmalan, N., Wang, Q., Sims, P.F. and Hyde, J.E., 2004. Genetic and metabolic analysis of folate salvage in the human malaria parasite *Plasmodium falciparum*. *Molecular and biochemical parasitology*, *135*(1), pp.77-87.

487. Banerjee, R., Das, K., Ravishankar, R., Suguna, K., Surolia, A. and Vijayan, M., 1996. Conformation, protein-carbohydrate interactions and a novel subunit association in the refined structure of peanut lectin-lactose complex. *Journal of molecular biology*, *259*(2), pp.281-296.

488. Bhaumik, P., Horimoto, Y., Xiao, H., Miura, T., Hidaka, K., Kiso, Y., Wlodawer, A., Yada, R.Y. and Gustchina, A., 2011. Crystal structures of the free and inhibited forms of plasmepsin I (PMI) from *Plasmodium falciparum*. *Journal of structural biology*, *175*(1), pp.73-84.

489. Berry, C., Humphreys, M.J., Matharu, P., Granger, R., Horrocks, P., Moon, R.P., Certa, U., Ridley, R.G., Bur, D. and Kay, J., 1999. A distinct member of the aspartic proteinase gene family from the human malaria parasite *Plasmodium falciparum*. *FEBS letters*, *447*(2-3), pp.149-154.

490. Elliott, D.A., McIntosh, M.T., Hosgood, H.D., Chen, S., Zhang, G., Baevova, P. and Joiner, K.A., 2008. Four distinct pathways of hemoglobin uptake in the malaria parasite *Plasmodium falciparum*. *Proceedings of the National Academy of Sciences*, *105*(7), pp.2463-2468.

491. Mauritz, J.M., Seear, R., Esposito, A., Kaminski, C.F., Skepper, J.N., Warley, A., Lew, V.L. and Tiffert, T., 2011. X-ray microanalysis investigation of the changes in Na, K, and hemoglobin concentration in *Plasmodium falciparum*-infected red blood cells. *Biophysical journal*, *100*(6), pp.1438-1445.

492. Chou, A.C. and Fitch, C.D., 1992. Heme polymerase: modulation by chloroquine treatment of a rodent malaria. *Life sciences*, *51*(26), pp.2073-2078.

493. Verdier, F., Le Bras, J., Clavier, F., Hatin, I. and Blayo, M.C., 1985. Chloroquine uptake by *Plasmodium falciparum*-infected human erythrocytes during in vitro culture and its relationship to chloroquine resistance. *Antimicrobial agents and chemotherapy*, *27*(4), pp.561-564.

494. Krogstad, D.J., Gluzman, I.Y., Kyle, D.E., Oduola, A.M., Martin, S.K., Milhous, W.K. and Schlesinger, P.H., 1987. Efflux of chloroquine from *Plasmodium falciparum*: mechanism of chloroquine resistance. *Science*, *238*(4831), pp.1283-1285.

495. Sanchez, C.P., Wünsch, S. and Lanzer, M., 1997. Identification of a chloroquine importer in *Plasmodium falciparum* Differences in import kinetics are genetically linked with the chloroquine-resistant phenotype. *Journal of Biological Chemistry*, *272*(5), pp.2652-2658.

496. Makler, M.T., Palmer, C.J. and Ager, A.L., 1998. A review of practical techniques for the diagnosis of malaria. *Annals of tropical medicine and parasitology*, *92*(4), pp.419-434.

497. Wein, S., Maynadier, M., Bordat, Y., Perez, J., Maheshwari, S., Bette-Bobillo, P., Tran Van Ba, C., Penarete-Vargas, D., Fraisse, L., Cerdan, R. and Vial, H., 2012. Transport and pharmacodynamics of albitiazolium, an antimalarial drug candidate. *British journal of pharmacology*, *166*(8), pp.2263-2276.

498. Esposito, A., Tiffert, T., Mauritz, J.M., Schlachter, S., Bannister, L.H., Kaminski, C.F. and Lew, V.L., 2008. FRET imaging of hemoglobin concentration in *Plasmodium falciparum*-infected red cells. *PLoS One*, *3*(11), p.e3780.